



UNIVERSITY OF
LIVERPOOL

Fluids Engineering Research Group

School of Engineering

Adam Yuile

Swept Boundary Layer Transition

by

Adam Yuile

Thesis submitted in accordance with the requirements of the
University of Liverpool for a PhD degree

September 2013

Statement of Originality

This thesis has been submitted by Adam Yuile to be examined as part of a PhD research degree for the School of Engineering at the University of Liverpool.

The research material reported herein was carried out solely by the author, under the primary supervision of Dr. Mark W. Johnson, for the Fluids Engineering Research Group at the University of Liverpool over a period of 4 years, starting in October 2009.

No part of this thesis has been submitted for a degree to any other university or educational establishment.

Acknowledgements

The first person I wish to express my gratitude to is **Dr. Mark W. Johnson** for his invaluable supervision, encouragement and enthusiasm to help deliver this project to completion. **Dr. Mark W. Johnson** is not only an excellent source of knowledge, particularly on boundary layer transition, but also radiates an infectious happiness which brings fun into the workplace. I will forever be grateful for his support in allowing me to suspend my studies for a single semester placement in Hong Kong.

I must also thank those responsible at the **University of Liverpool** for giving me the opportunity to conduct my studies here and, despite my vociferous grumblings about long delivery times, for eventually producing everything I needed to adequately conduct research in boundary layer transition. On the issue of delays I would like to extend a special thanks to **Prof. Ieuan Owen** (former secondary supervisor) for the help he provided in our attempts to realise the manufacture of equipment as quickly as possible.

In terms of support from technical staff I would like to extend thanks to **Derek Neary, John Curran** and **Steve Bode**, as well as **Marc Bratley, Bob Seamans** and **Martin Jones** who (between them) helped manufacture and assemble the test sections on the wind tunnel for each pressure gradient, as well as the traverse and all its associated ancillary equipment.

I've been a member of the **Fluids Engineering Research Group** for 4 years and have seen a lot of students graduate from within, in addition to having shared discussions with them on our research projects and social matters. Some people I've been fortunate enough to work with in this group were (my former housemate) **Dr. Chris Kaaria, Dr. James Forrest, Dr. Sean Malkeson, Dr. Mohit Katragadda, Dr. Dimitris Tsovolos, Dr. Richard Whalley** and **Miss. Siân Tedds** (soon to be doctor!).

I must also give special thanks for the support of my family, particularly my mother and father, who have always been there for what has been a long journey.

Abstract

Boundary layer transition has been investigated for incompressible three-dimensional mean flows on a flat plate with a 60° swept leading edge for a nominally zero, a positive, and a negative pressure gradient for three freestream turbulence intensities using a low speed blower tunnel with a 1.22 x 0.61 m working section at the University of Liverpool. The freestream turbulence intensities were generated using grids upstream of the leading edge, producing turbulence levels of approximately 0.2 %, 1.25 % and 3.25 %.

For each of these nine (3 x 3) test cases detailed boundary layer traverses were obtained at ten streamwise measurement stations, at a fixed spanwise location, using single-wire constant temperature hot-wire anemometry techniques and digital signal processing. The location for the onset and end of transition was obtained for each case, in terms of distance from the leading edge and local momentum thickness Reynolds number. These results are compared with the 2-D unswept empirical transition correlations of Abu-Ghannam and Shaw (1980) and the differences in the results between the two flows are highlighted. It was found that transition starts and ends earlier than for similar unswept flows, complementing the transition observations of Gray (1952) for swept wings.

Further to this the receptivity of the swept boundary layers to freestream turbulence (in the bypass transition regime) was determined by comparing near wall and local freestream spectra, for the pre-transitional boundary layers. These experimental results were compared with numerical predictions from a fourth order accurate computational fluid dynamics method which considered a multitude of perturbation waveforms. This numerical approach was also able to identify the waveform frequency and orientation combinations which drive receptivity in swept boundary layer transition and indicate the manner in which receptivity scales with momentum thickness Reynolds number. It was found that the most receptive waveforms correspond to the streamwise streaks which are frequently

observed in flow visualisations and direct numerical simulation studies of pre-transitional boundary layers.

Additionally it was also found that the numerical receptivities to freestream turbulence were highest for the positive pressure gradient and, in contrast, lowest for the negative pressure gradient – a similar finding to that in 2-D boundary layers. Transition was seen to commence prior to the advent of the intended non-zero pressure gradients in the experiments and thus direct comparisons are not strictly available.

The results obtained, and synthesis undertaken for this thesis, contribute towards an improved understanding of the transition process, particularly with respect to receptivity, in regard to flat plates with swept leading edges in various pressure gradients and highlight the differences between swept and unswept flows. Furthermore, additional avenues have been identified for future work on more complicated topologies where potential problems have also been highlighted.

Contents – Swept Boundary Layer Transition

Statement of Originality	i
Acknowledgements	ii
Abstract	iii
Contents – Swept Boundary Layer Transition.....	v
Nomenclature.....	ix
Abbreviations	xii
1 Chapter 1 – Introduction	1
2 Chapter 2 – Literature Review of Swept Boundary Layer Transition	4
2.1 Introduction to Boundary Layer Transition.....	4
2.2 Fundamental Boundary Layer Parameters	5
2.3 Boundary Layer Transition Processes	9
2.3.1 Intermittency Effect	15
2.3.2 Influence of Freestream Turbulence on Transition – Intensity and Length Scale	18
2.3.3 Influence of Pressure Gradient on Transition	19
2.4 Boundary Layer Theory.....	22
2.4.1 Laminar Boundary Layers.....	22
2.4.2 Transitional Boundary Layers.....	23
2.4.3 Turbulent Boundary Layers.....	25
2.5 3-D Boundary Layers.....	30
2.5.1 Falkner-Skan-Cooke Boundary Layer Example	33
2.5.2 Instability Mechanisms for Swept Transition	37
2.5.3 Receptivity in 3-D Boundary Layers	42
3 Chapter 3 – Experimental Procedures, Apparatus and Data Processing	44
3.1 Blower Wind Tunnel	44
3.2 Swept Flat Plate and Leading Edge Control Flap.....	49
3.3 Turbulent Grids.....	55
3.4 Section Sidewall Profiles and Design	58
3.5 Inclined Manometer	67
3.6 Cathetometer	69
3.7 Traverse Gear and Template.....	70

3.8	Pitot-Static Tube (Validyne)	75
3.9	Constant Temperature Hot-Wire Anemometry – CTA Boxes (54T30 & StreamlinePro)	76
3.9.1	54T30 Miniature CTA Experimental Configuration	77
3.9.2	StreamLine Pro CTA Experimental Configuration	79
3.10	Main Data Acquisition Card (USB 6210).....	81
3.11	Static Pressure Tappings	83
3.12	Hot-Wire Systems, Calibration and Corrective Procedures	85
3.12.1	Advantages and Disadvantages of Hot-Wire Anemometry Systems	86
3.12.2	Hot-Wire Calibration	88
3.12.3	Wall-Proximity Effect and Initial Probe Height.....	90
3.12.4	Corrective Procedures for Ambient Drift	92
3.13	Data Processing	95
3.14	Intermittency Algorithm	96
3.14.1	High Pass Filter Setting for Intermittency Algorithm	98
3.14.2	Window Size for Intermittency Algorithm	100
3.14.3	Residence Time for Intermittency Algorithm.....	101
3.15	Experimental Procedure	101
3.16	Measurement Uncertainties.....	104
3.16.1	Calibration Uncertainty.....	105
3.16.2	Uncertainty in Alignment of Probe	105
4	Chapter 4 – Swept Boundary Layer Transition Experimental Results	107
4.1	Streamwise Static Pressure Distributions	107
4.2	Nominally Zero Pressure Gradient (GxZ)	111
4.2.1	Wall Normal Profiles under Zero Pressure Gradient (G0Z)	111
4.2.2	Streamwise Parameters under Zero Pressure Gradient (G0Z)	118
4.2.3	Flow Angles (G0Z)	124
4.2.4	Falkner-Skan-Cooke Comparisons (G0Z)	128
4.2.5	G1Z.....	134
4.2.6	G3Z.....	136
4.3	Positive Pressure Gradient (GxP)	138
4.3.1	G0P.....	138
4.3.2	G1P.....	143
4.3.3	G3P.....	146
4.4	Negative Pressure Gradient (GxN)	148

4.4.1	G0N	148
4.4.2	G1N	151
4.4.3	G3N	152
4.5	Collective Analysis of Results	155
4.6	Spanwise Flow Quality Issues	159
4.7	Receptivities of Pre-Transitional Boundary Layers (Experiments)	165
4.7.1	ZPG Receptivities	166
4.7.2	PPG Receptivities	169
4.7.3	NPG Receptivities.....	170
5	Chapter 5 – Crossflow Boundary Layer Receptivity Code	172
5.1	3-D Steady Code	172
5.1.1	3-D Steady Code Results	174
5.2	3-D Unsteady Code	178
5.2.1	3-D Unsteady Code Results.....	184
5.3	Comparisons between Numerical and Experimental Results	192
5.3.1	Non-Dimensional Numerical Receptivities.....	194
5.3.2	Non-Dimensional Experimental Receptivities.....	199
5.4	Comparisons with 2-D Results	204
6	Chapter 6 – Conclusions and Suggestions for Future Work.....	206
6.1	Conclusions.....	206
6.2	Recommendations and Suggestions for Future Work	207
7	List of Tables	210
8	List of Figures.....	211
9	References	217
10	Appendix A – OpenFOAM and ANSYS Fluent Receptivity	228
10.1	Derivation of Real Inflow Velocity Components	228
10.2	OpenFOAM Case Library Files.....	230
10.3	OpenFOAM Results.....	247
10.4	NACA 0002 Test Case.....	250
11	Appendix B – LabVIEW Codes (Experimental)	256
11.1	Record Wire Velocities and King’s Law with Temperature Correction	256
11.2	U and Delta Seek.....	258
11.3	Intermittency	259
11.4	Integral Parameters	261

11.5	Full Program.....	265
------	-------------------	-----

Nomenclature

Symbol	Function	Dimensions
A	King's law coefficient	
a	overheat ratio	
a_x	streamwise frequency	rad/m
a_y	wall normal frequency	rad/m
a_z	spanwise frequency	rad/m
B	King's law coefficient	
C_f	skin friction coefficient	
E	hot-wire voltage	V
E_{corr}	temperature corrected hot-wire voltage	V
g	acceleration due to gravity	m/s ²
G_x	streamwise coordinate (unswept)	m
G_y	wall-normal coordinate (unswept)	m
G_z	spanwise coordinate (unswept)	m
h	local height of tunnel section	m
h₀	inlet height of tunnel section	m
H	shape factor	
L	characteristic length (for Reynolds number)	m
L_x	streamwise coordinate (swept - normal to leading edge)	m
L_y	wall-normal coordinate (swept)	m
L_z	spanwise coordinate (swept - parallel with leading edge)	m
m	Hartree parameter	
n	King's law coefficient	
n	arbitrary parameter for skew angle cosine fit	
p	surface static pressure	Pa
P	ambient pressure	Pa
R	ideal gas constant	J/kgK
R	receptivity	
R_{uv}	u'v' receptivity	
R_{vw}	v'w' receptivity	
R_{amb}	wire ambient resistance	Ω
Re_c	corrected Reynolds number (Wills method)	
Re_{cf}	critical crossflow Reynolds number	
Re_m	measured Reynolds number (Wills method)	
Re_x	streamwise Reynolds number	
Re_δ	boundary layer thickness Reynolds number	
Re_{δ*}	displacement thickness Reynolds number	
Re_θ	momentum thickness Reynolds number	
R_w	wire hot resistance	Ω
\overline{R}_{yz}	integral averaged receptivity (fixed streamwise frequency)	
T_{amb}	ambient temperature	K

T_l	laminar signal time	s
TI	turbulence intensity	%
T_t	turbulent signal time	s
T_{ref}	calibration reference temperature	K
T_w	sensor wire temperature	K
u	streamwise velocity	m/s
u_{corr}	corrected velocity (Wills method)	m/s
u'	standard deviation in streamwise velocity	m/s
U_0	inviscid inlet velocity	m/s
U_1	inviscid local velocity	m/s
U_∞	freestream velocity	m/s
u_τ	friction velocity	m/s
v	wall-normal velocity	m/s
v'	standard deviation in wall-normal velocity	m/s
w	spanwise velocity	m/s
w'	standard deviation in spanwise velocity	m/s
x_0	datum location for FSC profile	m
x_t	location for start of transition (Narasimha)	m
$x_{\gamma 25\%}$	streamwise location for 25% intermittency	m
$x_{\gamma 75\%}$	streamwise location for 75% intermittency	m
α	roof convergence angle	°
β	perturbation decay rate	m^{-1}
γ	intermittency	%
γ_1	raw intermittency	%
γ_2	Wills corrected intermittency	%
δ	boundary layer thickness	m
δ^*	displacement thickness	m
θ	momentum thickness	m
λ	skew angle (probe angular position)	°
Λ	arbitrary Narasimha parameter	m
Ω	non-dimensional temporal frequency	
Ω_x	non-dimensional x frequency	
Ω_y	non-dimensional y frequency	
Ω_z	non-dimensional z frequency	
μ	fluid dynamic viscosity	kg/ms
μ_t	artificial eddy/turbulent viscosity	kg/ms
ν	fluid kinematic viscosity	m^2/s
ρ	density	kg/m^3
τ	turbulence intensity (u'/u) - local mean	%
τ_w	near-wall shear stress	Pa
ϕ	leading edge sweep angle	°
χ	mean flow direction	°
ψ	stream function	m^2/s
ω	temporal frequency	rad/s

ω_x	spatial x frequency	rad/m
ω_y	spatial y frequency	rad/m
ω_z	spatial z frequency	rad/m

Abbreviations

Abbreviation	Long name
ADC	Analogue to Digital Converter
ANSI	American National Standards Institute
ASCII	American Standard Code for Information Exchange
ASU	Arizona State University (US)
CFL	Courant-Friedrichs-Lewy
CNC	Computer Numerical Control
CTA	Constant Temperature Anemometer
DAQ	Data Acquisition (USB-DAQ)
DLR	German Aerospace Center (Germany)
DNS	Direct Numerical Simulation
DSO	Digital Storage Oscilloscope
ERCOFTAC	European Research Community On Flow, Turbulence and Combustion
FFT	Fast Fourier Transform
FP	Flat Plate
HWA	Hot-Wire Anemometry
ITAM	Institute of Theoretical and Applied Mechanics (Russia)
LabVIEW	Laboratory Virtual Instrument Engineering Workbench
MATLAB	Matrix Laboratory
MFA	Mean Flow Angle
MPI	Message Passing Interface
NACA	National Advisory Committee for Aeronautics
NAL	National Aerospace Laboratory (Japan)
ODE	Ordinary Differential Equation
NPG	Negative Pressure Gradient
PPG	Positive Pressure Gradient
RANS	Reynolds-Averaged Navier-Stokes Equations
TS	Tollmien-Schlichting
TTL	Transistor-Transistor Logic
USB	Universal Serial Bus
VI	Virtual Instrument (LabVIEW)
ZPG	Zero Pressure Gradient

1 Chapter 1 – Introduction

The onset of turbulent structures in shear flows has intrigued investigators for more than a century (Kachanov (1994)). A tremendous volume of effort continues to be directed towards improving the understanding of the inception and evolution of turbulent structures in boundary layer flows, owing to the potential improvements, in terms of performance and efficiency, for the likes of aircraft wings and gas turbine engines. This is particularly important given that the majority of flows occurring in nature and engineering are turbulent (Tennekes and Lumley (1972)). In Tempelmann (2011) it is stated that around 20% of the drag on modern aeroplanes can typically be attributed to skin friction acting on the wing surfaces alone. However, in Kohama (1987) it was stated that the boundary layers over swept wings are generally turbulent and can account for up to 50% of the total drag on an aircraft at cruise. The difference between these two quoted figures can perhaps be attributed to the increased use of natural laminar flow wings. The primary advantage of sweeping a wing (backwards or forwards) is a net reduction in wave drag, Pearcey (1962), with the compromise of less favourable stall characteristics, which must be managed accordingly.

Furthermore, in gas turbine engines, the boundary layer flow on the turbomachinery blade surfaces is said to be transitional for 50 – 80 % of the chord length, Brandt (2003). For turbomachinery designers it is important to accurately quantify the fraction of blade chord that is turbulent as this will not only have implications in terms of potential losses through increased skin friction, but also in terms of being able to reliably quantify the cooling requirements for the high pressure turbine in a large axial turbofan for example, owing to the higher heat transfer rates associated with turbulent flows (through Reynolds analogy, see Anderson (2010)).

This issue is further complicated in such engines by the tendency of designers to bypass air from compressor stages for use in film cooling, as well as additional complications such as compressibility, rotor-stator interaction, wake-induced transition, thermal barrier coatings etc. (Han et al. (2012)).

Sweep is commonly used by designers of turbomachinery, see the backswept centrifugal impeller of Eckardt (1979) for example, to control tip Mach numbers and to optimise aerothermodynamic performance.

Technically speaking, a boundary layer is a momentum deficient region of flow in a viscous fluid which is manifested in the immediate vicinity of a solid surface (such as a duct wall or fuselage skin) as that fluid translates with respect to the surface, which itself may or may not itself be at rest. Boundary layer transition, however, can be considered as the process between laminar and turbulent parts of the boundary layer. This robust description of transition, as a process, can be broken down into forward transition (laminar to turbulent) or reverse transition (turbulent to laminar) also known as (re)laminarisation. Laminar flow (from the Latin “lamina” meaning layer, sheet or leaf) is characterised as being ordered, predictable and layered - Brandt (2003). Turbulent flow or turbulence, on the other hand, is characterised as being chaotic and inherently three-dimensional (Versteeg and Malalasekera (2007)).

There are many examples of generic boundary layer transition work which has been conducted both internally (at the University of Liverpool) and throughout the world (example research programmes include ASU, DLR, KTH, ITAM and NAL), an excellent review of such experimental studies in swept transition is provided by Bippes (1999). In relatively recent times this work has been primarily focused on two-dimensional flat plates from which there has been considerable return on investment which has translated to both empirical correlations for predicting the start and end of transition (e.g. Abu-Ghannam and Shaw (1980)) and physical models of transition, such as the receptivity transition model of Johnson and Ercan (1996).

As such similar efforts are now being extended to 3-D flows, as with the swept flat plate boundary layers discussed in this thesis. 3-D boundary layer studies are not entirely new at the University of Liverpool and have been investigated in the past notably by Ramadan (2000) and Riley (1985). Ramadan (2000) used a flat plate with a 60° swept leading edge, which has subsequently been

inherited for this research, to study relaminarisation with the justification for 60° of sweep being that the effects were likely to be readily observable at such a high angle. The latter author, Riley (1985), highlighted a 'paucity' in terms of the amount of work in this area present within the research community, but this has subsequently been addressed in the intervening three decades. Nevertheless there still would appear to be a shortage of research specific to bypass transition in 3-D mean flows, hence this area is the focus of this thesis, with the main deliverable objective being to quantify boundary layer receptivity in swept flows and to highlight the underlying physical differences with respect to unswept 2-D flat plate flows.

The layout of this thesis is as follows **Chapter 2 – Literature Review of Swept Boundary Layer Transition** offers a literature review of the general boundary layer transition process and attempts to provide a brief overview of the current state of the art in terms of most of the concepts and physical knowledge mostly specific to the case of transition on swept flat plates. More detailed descriptions and analyses of the important parameters and flow features observed in each of the flow regimes are also discussed. **Chapter 3 – Experimental Procedures, Apparatus and Data Processing** as the name suggests covers the methodologies from which the transition experiments were conducted and how the resulting data acquired was processed. **Chapter 4 – Swept Boundary Layer Transition Experimental Results** and **Chapter 5 – Crossflow Boundary Layer Receptivity Code** comprise detailed presentations and reviews of research undertaken both experimentally and numerically for each of the different test configurations; namely analysis of zero, negative and positive pressure gradient cases. The main body of the thesis is brought to an end with **Chapter 6 – Conclusions** which presents the main concluding statements and also provides suggestions for future work and the outlook for how things are likely to develop in the field of swept boundary layer transition.

2 Chapter 2 – Literature Review of Swept Boundary Layer Transition

2.1 Introduction to Boundary Layer Transition

The transition from laminar to turbulent flow is fundamental for understanding fluid dynamics, particularly given that the overwhelming majority of engineering fluid field problems, both internal and external, involve turbulence (Cant (2002)) and the genesis of such research is attributed to Osbourne Reynolds, as stated by Schlichting (1968). In order for transition to turbulent flow to take place there need to be circumstances which allow for breakdown in stability. In general terms the probability of breakdown to turbulence is proportional to the ratio of inertial and viscous forces, a non-dimensional parameter which is attributed to Osbourne Reynolds as being the Reynolds number (Equation 2-1) owing to his work in the late 19th century on tube flows (Reynolds (1883)). One of these experiments involved adding streaks of “highly coloured water” (dye) to the colourless water and tracking the development of the flow patterns downstream, where the initially laminar streaks were (after some critical distance) observed to curl up and the dye was observed to diffuse throughout the water in the pipe, in other words transition as we know it today was witnessed.

Reynolds experiments, performed at the hydraulics laboratory of Manchester University, were devised such that the bulk water velocity (driven by pressure - Reynolds (1895)) and kinematic viscosity (implicitly from varying the water temperature from 5 to 22°C) could be parametrically studied with respect to the fixed glass tube diameter. Typically one is taught to simply assume that fluid behaviour can be strictly characterised (as laminar or turbulent) for a given geometrical scenario (e.g. pipe flow) effectively digitally switched either side of a critical Reynolds number. However, Reynolds himself was aware that there wasn't a single critical Reynolds number above which transition uniquely occurs and that the situation was far more complicated than that.

Reynolds was also aware of the importance of the incoming flow and found that the critical Reynolds number effectively was inversely proportional to the magnitude of the disturbances of the inlet flow. Similarly, in terms of the classical literature, in 1914 Ludwig Prandtl, often termed the ‘father of modern aerodynamics’, published his paper detailed his experiments with spheres, demonstrating both laminar and turbulent regimes and furthermore highlighting the problem of separation and that in such cases the overall drag is governed by the transition - Prandtl (1914) and reported in Schlichting (1968).

$$Re = \frac{\rho U_{\infty} L}{\mu} \quad \text{Equation 2-1}$$

In the field of transition it is no longer possible to be utterly comprehensive, given the rapid expansion of knowledge which is constantly occurring, and the time span for which the subject has already been intensely studied. As such, this thesis tackles the specific case of incompressible boundary layer transition over swept flat plate topologies and hence, the literature review is restricted to general transition theories and a concise literature review of swept flat plate transition, which will naturally draw content from transition studies on swept wings, given the overlap between the two sub-genres and the commercial appeal of such research in aerospace.

2.2 Fundamental Boundary Layer Parameters

A classic two dimensional boundary layer, with the leading edge aligned perpendicular to the approach flow, is depicted in Figure 2-1 which graphically illustrates some of the fundamental boundary layer parameters which are discussed in this section.

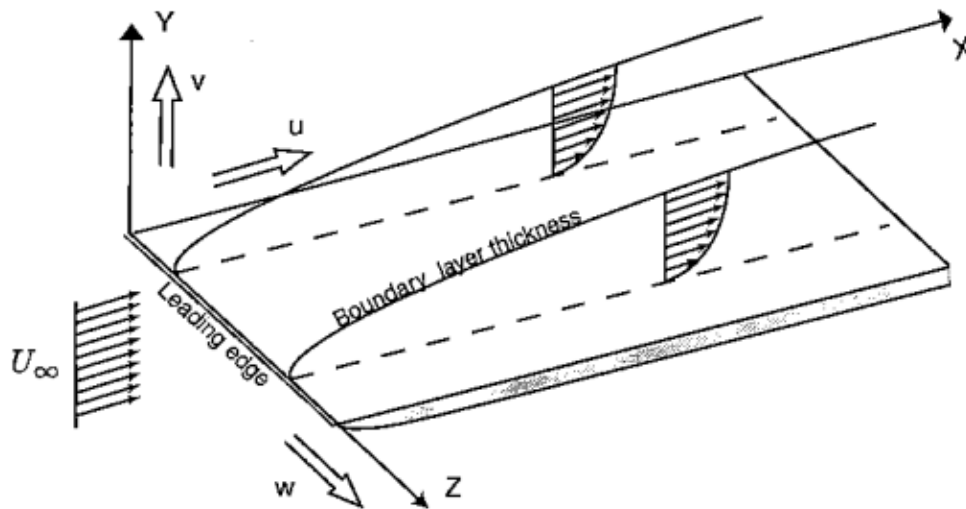


Figure 2-1 - Two dimensional flat plate boundary layer flow depicting freestream velocity, local velocity components, boundary layer thickness, freestream approach flow and typical coordinate system, from Andersson (1999)

As previously mentioned this section discusses the fundamental parameters of boundary layer theory and those which derive from what's known as the momentum integral equation (Schlichting and Gersten (2000)), known as the boundary layer integral parameters;

- Freestream velocity, U_∞ - the freestream velocity, in an ideal scenario, equates to the velocity upstream of a particular object under consideration, such as an automobile model placed on a rolling road in a wind tunnel under test conditions. See the approach flow indicated in Figure 2-1.
- Boundary layer thickness, δ – the boundary layer thickness is defined as the normal displacement from the wall at which the local mean velocity reaches an arbitrary threshold (usually 99%) of the freestream velocity. Logically, the boundary layer is contained within the limits of the boundary layer thickness and, hence, in this region the effects of viscosity are significant. Beyond the boundary layer thickness the effects of viscosity can usually be ignored, this is certainly the case for all classical/theoretical boundary layer problems. A

typical value for δ on the bonnet of a car travelling at 100 km/h is approximately 1 mm (Andersson (1999))

- Displacement thickness, δ^* – this parameter (Equation 2-2) equates to the offset through which a wall boundary would have to be displaced, normal to the direction of the potential flow, proportional to the reduction in volumetric flow rate of an inviscid fluid caused by the retardation due to viscosity in the boundary layer. In other words it's an index proportional to the 'missing mass flow', Anderson (2010).

$$\delta^* = \int_0^{\infty} \left(1 - \frac{u}{U_{\infty}}\right) dy \quad \text{Equation 2-2}$$

- Momentum thickness, θ – similarly to the displacement thickness, the momentum thickness (Equation 2-3) is a representation of the decrement in the flow of momentum accounted for by the presence of the boundary layer.

$$\theta = \int_0^{\infty} \frac{u}{U_{\infty}} \left(1 - \frac{u}{U_{\infty}}\right) dy \quad \text{Equation 2-3}$$

- Shear stress (wall), τ_w – Equation 2-4; shear stress exists where there is a velocity gradient across streamlines (Anderson (2010)) and has the most significant effect where the aforementioned gradients are their most substantial. In fact Prandtl (1904) himself discriminated between regions of significant and insignificant shear stress, these are often termed viscous and inviscid regions of flow where the viscous region itself is the boundary layer and the inviscid region corresponding to the freestream flow. In the absence of viscosity, there would be no boundary layer flows and the streamline on the surface of a body (such as a wing) would slip without any retardation.

$$\tau_w = \mu \left(\frac{\delta u}{\delta y} \right)_w$$

Equation 2-4

- Skin friction coefficient, C_f – the skin friction coefficient (Equation 2-5) represents a non-dimensionalised version of the shear stress near the wall, normalised by the dynamic pressure of the adjoining freestream velocity. In practical terms it is a representation of the friction generated during the interaction of the air and the respective wall surface. The skin friction coefficient is markedly different for laminar and turbulent flows, owing to the larger velocity gradients and therefore shear stresses present in the latter regime.

$$C_f = \frac{\tau_w}{\frac{1}{2} \rho U_\infty^2}$$

Equation 2-5

- Shape factor, H – The shape factor of a boundary layer is defined as the ratio of the displacement and momentum thicknesses - Equation 2-6. In practical terms the shape factor can be used as an indicator for characterising properties of the flow. For example in a 2-D laminar boundary layer (under zero pressure gradient conditions) the shape factor is around 2.6 and 1.3 - 1.4 for turbulent flows.

$$H = \frac{\delta^*}{\theta}$$

Equation 2-6

- Intermittency factor, γ – The intermittency is defined, for a continuous signal, as the fraction of time for which the signal trace is turbulent (Equation 2-7). That is to say 0% intermittency is representative of laminar flow, 100% intermittency can be considered as fully turbulent and anywhere between these extremes resides the flow is transitional. This parameter (defined in Equation 2-7) is revisited in greater detail in section 3.14. It's interesting to note,

that from the point of view of the intermittency factor, that fully turbulent flow can in some sense be considered as a saturated transitional one. This is a point of view which is supported by the fact that with sufficient stabilisation a fully turbulent flow can be relaminarised, where one will observe a drop in the intermittency.

$$\gamma = \frac{T_t}{T_t + T_l} \quad \text{Equation 2-7}$$

2.3 Boundary Layer Transition Processes

Many experiments return boundary layer profiles which are laminar, transitional and fully turbulent in nature. As such many of the characteristics and important flow structures are briefly discussed in the following sections, where they are later identified and analysed in specific results in Chapter 4 and Chapter 5. This review only provides a brief overview of general transition theory but also attempts to provide guidance as to where the interested reader would be able to find out more in-depth analyses regarding these respective structures and characteristics.

Boundary layer transition is the process by which fluid flow develops between different regime states. Laminar and turbulent flows are regimes of developed flow for which the state of knowledge in simple flow configurations can be regarded as somewhat mature, where one regime is universal or, rather, dominant. However, even in simplistic topologies such as flat plates, the understanding and prediction of transition between these two states is still very much under development. That is to say that where the transition begins and ends, should full transition to turbulence be obtained, is in most cases either poorly understood and or difficult to extrapolate between problems of different scales/nature. Furthermore, transition evolves through several paths (see Figure 2-2) depending on what disturbance conditions are prevalent. One such path is natural transition which evolves through the mechanisms detailed in Figure 2-3.

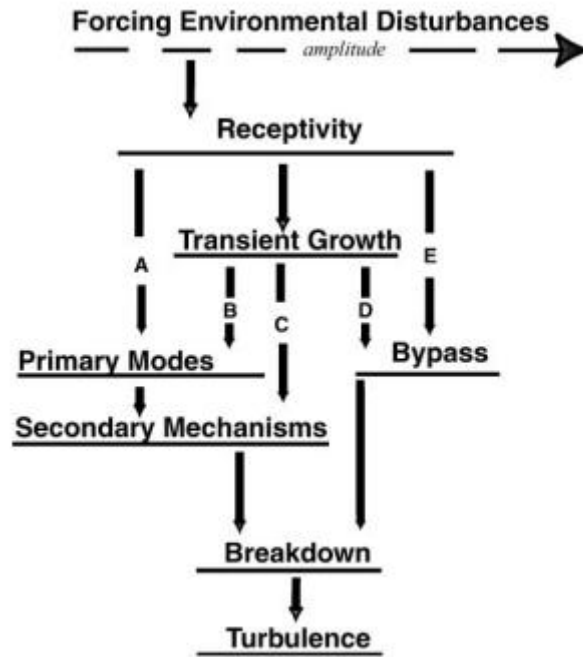


Figure 2-2 - Transition paths following receptivity (Saric et al. (2002))

The following represents a description of what is known as the ‘natural’ transition process which corresponds to path A in Figure 2-2.

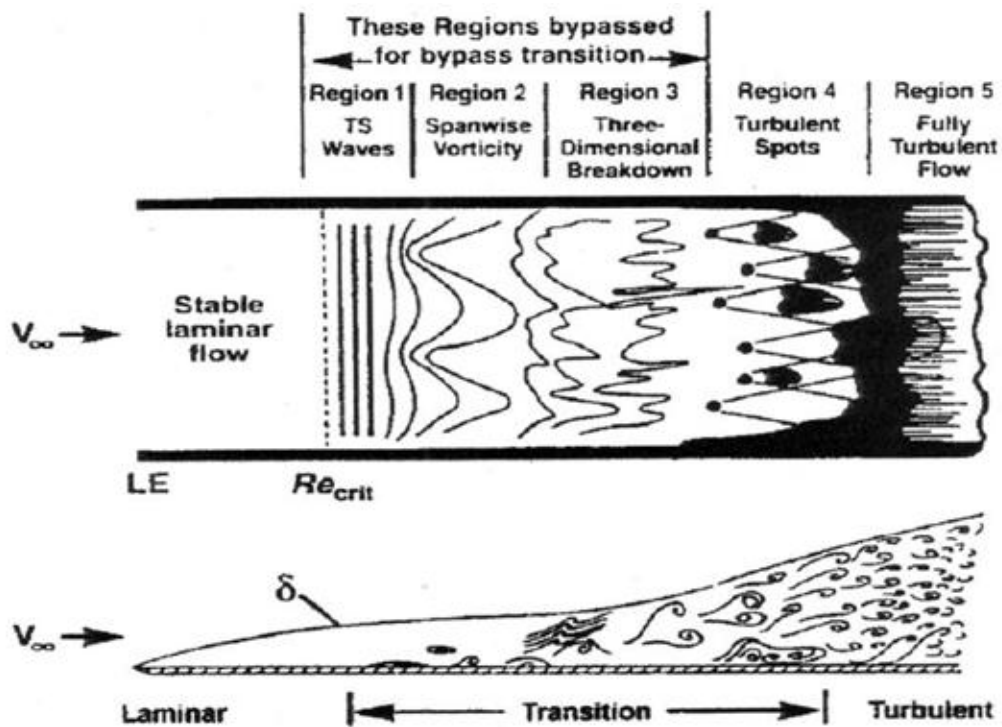


Figure 2-3 - Natural transition process in a flat plate boundary layer Schlichting (1979)

Thereafter an overview of path E ('bypass') transition is provided. Consideration of these two paths will provide a good overview of the transition process less the potential transition triggering phenomenon of transient growth where transition can occur even if the exponentially growing perturbations are damped, see Brandt (2003) for example.

Natural transition on a 2-D flat plate (Path A) proceeds through the following stages;

- Receptivity – receptivity is the initial phase of transition and concerns the transformation of freestream disturbances into small perturbations within the boundary layer, hereafter the growth (or decay) of these perturbations will depend on the base flow and the nature of the disturbance, with respect to its characteristic frequencies and propagation direction.
- Primary modes – these modes of growth apply when the perturbations are sufficiently small that the disturbances can grow (or decay) in accordance with linear stability theory. An example of such a primary mode is Tollmien-Schlichting waves which propagate in the streamwise direction on a 2-D unswept flat plate, whereas in swept flows crossflow instability modes propagate in the spanwise direction.
- Secondary mechanisms (spanwise vorticity and 3-D breakdown, see Figure 2-3) – some primary instability modes can eventually grow to such an extent that the linear theories governing their growth are no longer physically applicable. Furthermore the magnitudes of the disturbances become so large that they significantly distort the mean flow which can lead to inflection points in the velocity profile, and hence an absolute instability in the boundary layer, which will rapidly lead to the next stage of transition - breakdown into turbulence.
- Breakdown into turbulence – this phase of transition is said to commence with the generation of turbulent spots and thereafter will typically lead to saturation as a fully turbulent flow with increasing Reynolds number.

Depending on the transition path some of these stages are said to be skipped/bypassed but there is evidence to say that each of the mechanisms is present, in some form or another, albeit at negligible intensities with respect to the dominant mechanism, see for example Hughes and Walker (2001) who observed TS activity in their spectral analysis of flows with upstream streaky structures which would normally correlate with the observations of bypass transition. In Andersson (1999) it is claimed that streamwise streaks are ubiquitous in transitional boundary layers, furthermore Klebanoff et al. (1962) were able to show that the onset of three-dimensionality is rapidly followed by the breakdown of the laminar flow.

The approximate freestream turbulence intensity for digitally switching between natural and bypass paths is usually considered to be 1% (Mayle (1991)) but as will be discussed in the following sub-sections, and indeed in other chapters, transition is affected heavily by more than just the turbulence intensity – pressure gradient and turbulence length scale to name just two additional parameters.

An equation describing the linear stability of parallel shear flows, known now as the Orr-Sommerfeld equation, was first presented by Orr (1907) and then Sommerfeld (1908), where the equation was considered to be derived independently, hence the shared attribution. This equation was an enhancement of the approach devised by Rayleigh (1880) who developed equations which described the evolution of a disturbance linearised around a mean velocity profile for inviscid flow, where the aforementioned Orr-Sommerfeld equation was extended to include viscous effects and is stated as Equation 2-8 in Schlichting and Gersten (2000).

$$(U - c)(\varphi'' - \alpha^2 \varphi) - U''\varphi = -\frac{i}{\alpha Re}(\varphi''' - 2\alpha^2 \varphi'' + \alpha^4 \varphi) \quad \text{Equation 2-8}$$

Where $U(y)$ is the velocity of the basic flow in the x direction and single partial perturbations/modes are superimposed and propagate in the x direction, with the assumption that their magnitude is

small compared to the basic flow and the following also applies for the stream function of the two-dimensional perturbation, which satisfies continuity of the perturbed boundary layer.

$$\psi(x, y, t) = \varphi(y)e^{i(\alpha x - \beta t)} \quad \text{Equation 2-9}$$

Where $\lambda = \frac{2\pi}{\alpha}$ is the wavelength of the perturbation, $\beta = \beta_r + i\beta_i$ represents the mode and

$c = \frac{\beta}{\alpha} = c_r + ic_i$ is the combined quantity expressing the phase velocity c_r and

amplification/damping via c_i , with respect to the polarity of the latter ($c_i > 0$ = amplification).

Note Equation 2-8 reduces to the Rayleigh equation for the limit when the Reynolds number tends to infinity. In summary, the theoretical disturbances/perturbations involved assume a wave-like form and through a Fourier transformation the Orr-Sommerfeld equation is effectively an eigenvalue problem for exponentially growing or decaying disturbances.

Using the Orr-Sommerfeld equation Tollmien (1929) and Schlichting (1933) were able to predict the growth of two-dimensional wave-like disturbances, which have subsequently been termed Tollmien-Schlichting waves, in (laminar) flat plate boundary layers. Schlichting (1933) was also able to demonstrate that such waveforms would theoretically become unstable above a critical momentum thickness Reynolds number of 162, for zero pressure gradient. Close comparisons of the results of this theoretical work were then observed experimentally by Schubauer and Skramstad (1947) where they tracked the development of 2-D disturbances excited through an oscillating thin, flat ribbon (made from phosphor bronze) placed a few thousandths of an inch from the flat plate surface in a NACA National Bureau of Standards facility with significantly reduced turbulence intensity of the freestream, through judicious use of damping screens. The ribbon was driven to and from the surface by subjecting an electromagnet, placed on the opposite side of the plate, to a small current at the desired frequency. It was also stated in Schubauer and Skramstad (1947) that the ribbon was observed to have a negligible effect on the rest of the flow in its passive state. Unfortunately such

theoretical models do not exist for bypass transition which is perhaps due to the fact that the structures upstream of bypass transition in the pre-transitional boundary layer are three-dimensional and composed of many frequencies (Johnson (2011a)).

Nevertheless, continuing on with a description of the remainder of the natural transition process, once the Tollmien-Schlichting waves reach a streamwise standard deviation of around 1% of the freestream velocity, secondary instabilities are born (Brandt (2001)). The disturbances, by this stage, will now develop in a three-dimensional manner which results in a complex, unstable mean flow. Eventually, the flow will locally breakdown into turbulence and form regions which are commonly known as “turbulent spots”. In plan view, turbulent spots are arrowhead shaped (Wygnanski et al. (1976)) bursts of turbulence which originate from the non-linear growth of disturbances breaking down into a hairpin vortex. This vortex elongates and can spawn multiple child vortices, some of which are concurrently aligned with the parent vortex and are displaced in the spanwise direction. Should this process continue then more vortices will form and interact, developing into the highly disturbed flow known as the turbulent spot. In Johnson and Fashifar (1994) it was suggested that a turbulent spot is generated when there’s a local transient separation of the flow in the near-wall region which they estimated to occur when the instantaneous velocity drops below 50% of the mean.

Figure 2-4 illustrates most of the salient features with respect to the topology of turbulent spots. These comprise the origin, spreading half-angle, α and the relative propagation velocities at the extremities of the spot. The turbulent spots, in the instance of Schubauer and Klebanoff (1955), were generated artificially by means of discharging an electric spark normal to the flat plate under zero pressure gradient. The half-angle is around 10° and whilst the leading edge of the spot propagates at near enough the freestream velocity, the trailing edge does so at only 50% of that value, hence the propensity for the spot to grow. Another interesting observation was that the wake of a spot corresponds to a “calmed region” of flow which actually acts to attenuate transitional

disturbances. This is arguably one of the only aspects of turbulence which offers self-stabilising characteristics resulting in a lengthening of the transition region, however, the effect is usually somewhat drowned out by the sheer number of spots which consume the wake region (Schubauer and Klebanoff (1955)). It has been shown experimentally by Gostelow et al. (1996) and numerically by Johnson (2001) that the boundary layer thickness in proximity of a calmed region was found to be reduced with respect to the surrounding flow, which is indicative of stabilisation.

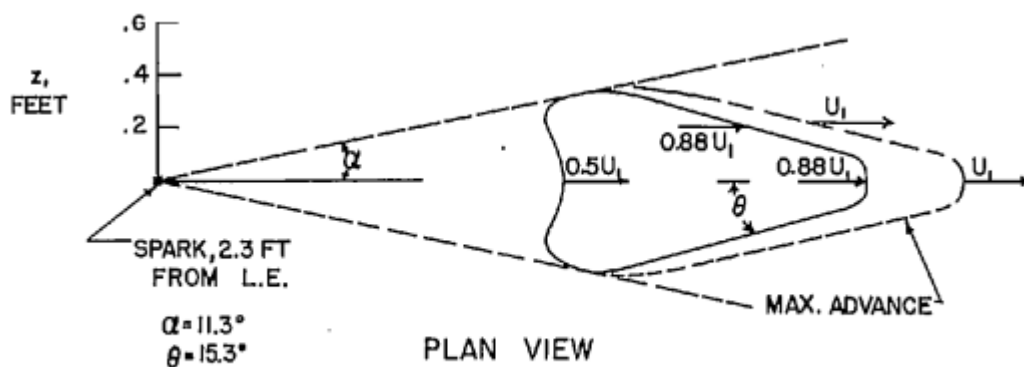


Figure 2-4 - Turbulent spot generated by spark (Schubauer and Klebanoff (1955))

Prior to the water table experiments of Emmons (1951) there was a school of thought that transition occurred instantaneously. However this hypothesis has been disproved as it has been shown many times that regions of laminar flow can coexist downstream of turbulent bursts concurrently as well as consecutively at an identical streamwise location. As such transition is now formally regarded as taking place over a defined region, between the streamwise coordinates where turbulent spots first appear to where they have merged to form a continuous front (Dhawan and Narasimha (1958)).

2.3.1 Intermittency Effect

In Figure 2-5 typical unfiltered signal traces are shown for boundary layers from their laminar to fully turbulent state, with transitional signals in between and these are seen to be qualitatively similar

(with respect to γ) to the similarly unfiltered hot-wire signal traces of Figure 2-6 by Fasihfar and Johnson (1992). Figure 2-7 also provides a demonstration of how the filtered near wall hot-wire velocity profiles vary with increasing streamwise displacement (and therefore intermittency). Please note that these signals have been arbitrarily offset (by their integer count index $\times 5$ m/s, where the filtered signals have been amplified by a factor of 3) such that they are stratified, rather than overlaid, for the sake of clarity. Additionally the quoted intermittency values in the plot legend are representative of the intermittencies experienced over the entire flow signal (of 30 seconds) but, again for the sake of clarity, only a small portion of the signal (the first 1 second) is shown such that discrete bursts are clearly visible.

Furthermore, each of the signal traces in the aforementioned demonstrative figure have been produced at a fixed height with each boundary layer rather than at self-similar non-dimensional wall normal displacements, with respect to the boundary layer thickness.

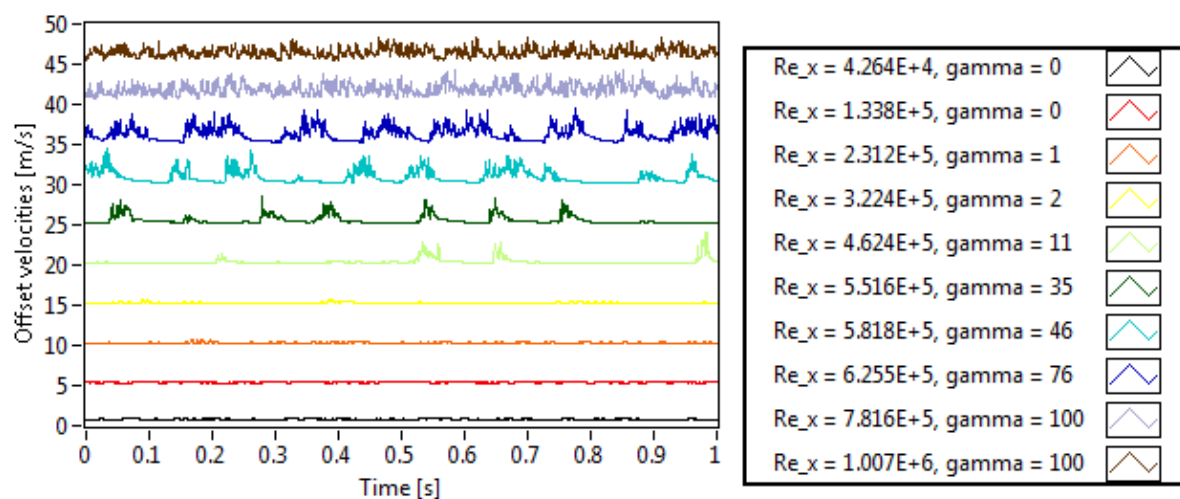


Figure 2-5 - Unfiltered hot-wire velocity signals demonstrating intermittency effect (offset for clarity)

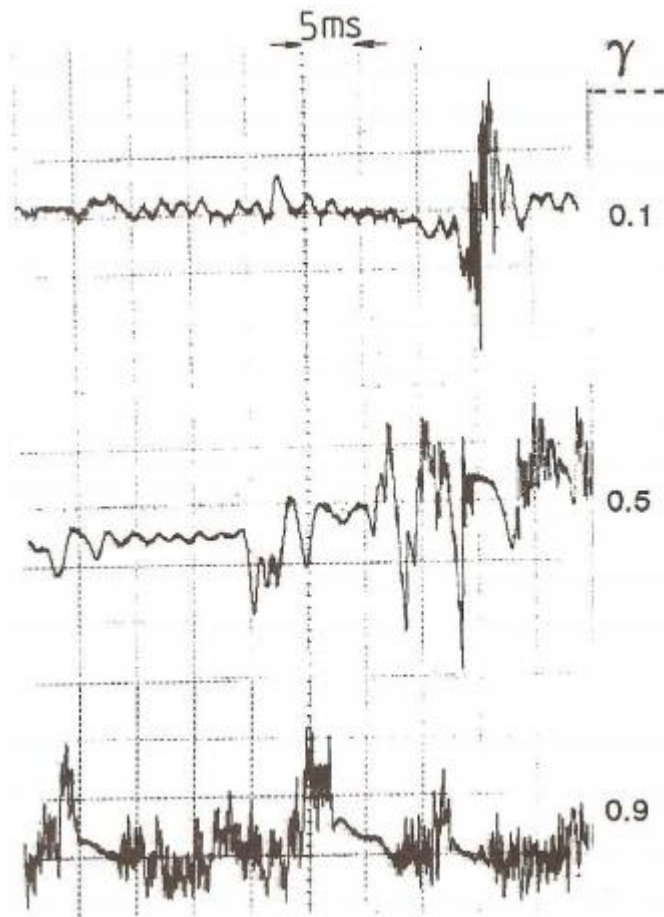


Figure 2-6 - Unfiltered hot-wire signal traces Fasihfar and Johnson (1992)

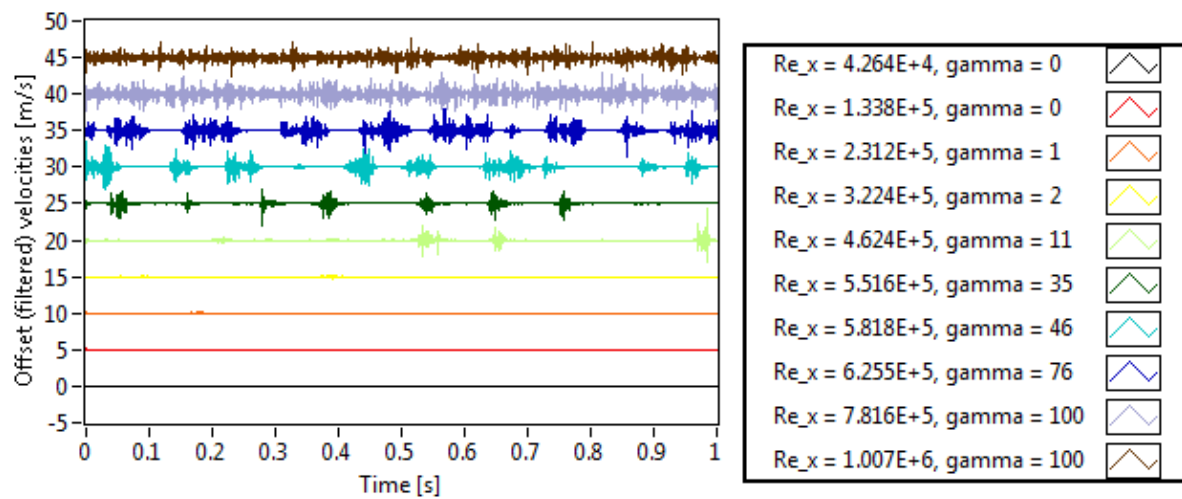


Figure 2-7 - Filtered hot-wire velocity signals demonstrating intermittency effect (positive pressure gradient, square grid)

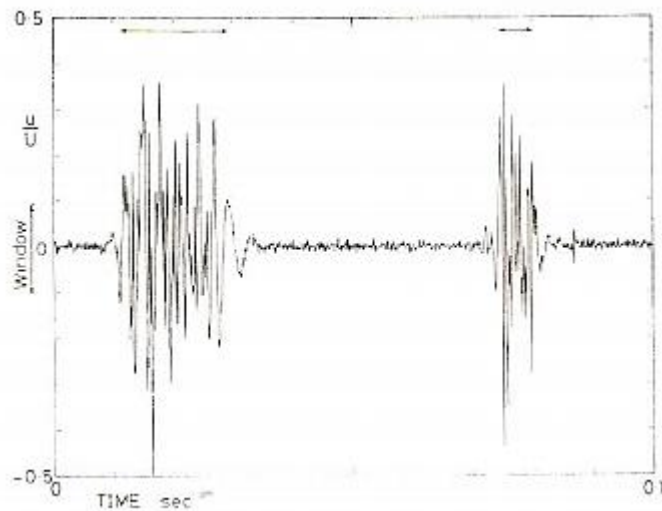


Figure 2-8 - Filtered velocity for intermittent signal (Fasihfar and Johnson (1992))

In addition to the advent of turbulent bursts for signals with non-zero intermittency, one can also observe from Figure 2-7 that the burst frequency (as in the rate at which bursts occur as opposed to frequencies associated with the burst structures themselves) increases with Reynolds number until the flow signal is effectively saturated with turbulent bursts at 100% intermittency – the end of transition.

2.3.2 Influence of Freestream Turbulence on Transition – Intensity and Length Scale

In the past many researchers, such as Hall and Gibbings (1972) and Abu-Ghannam and Shaw (1980), have investigated the effects of freestream turbulence intensity on the onset and propagation of transition in flat plate two dimensional boundary layers. They have typically produced empirical transition correlations which predict the momentum thickness Reynolds numbers for the start and end of transition based on the freestream turbulence intensity.

These empirical correlations have also been extended to account for the effects of pressure gradient but fundamentally relying on empirical correlations in the field of transition is only suitable for

preliminary design because transition is an extremely complex phenomenon and is highly dependent on the environment in which the tests were conducted. As such results can differ markedly from one testing environment to another and replicating the results of others is not something which is readily achievable. This is further compounded, particularly for low turbulence intensity environments, by the effects of surface roughness in that no two plates or wings have identical roughness profiles and, as such, results for the same specification can be significantly different if, that is, the surfaces are not hydraulically smooth, albeit this is usually the case if so desired.

Jonáš et al. (2000) point out that when it comes to turbulence intensity and length scales it is the former which has benefited from the greatest degree of attention, in terms of the research undertaken, but there are reasons to expect that length scale imposes a significant influence also. This largely stems from the fact that the larger the length scale of the freestream turbulence, the lesser the dissipation/decay, with the opposite holding true. As a consequence the boundary layer is perturbed in a different manner downstream even if two initially dissimilar flows happen to match at the leading edge. Correlations do exist which characterise the flow in terms of both turbulence intensity and length scale and these have been applied with some success, see Jonáš et al. (2000).

2.3.3 Influence of Pressure Gradient on Transition

The effect of pressure gradient on the evolution of the transition process is very much dependent on the flow configuration itself. The significance of pressure gradients is most often taught within the context of incompressible 2-D boundary layer theory. That is typically to say that a positive pressure gradient in the streamwise direction will have an adverse effect on stability and, similarly, a negative pressure gradient conforms to favourable conditions, enhancing stability.

This is perhaps best understood by careful consideration of the streamwise momentum equation (Equation 2-14) at a wall where all of the velocity components are zero and hence;

$$\frac{\delta p}{\delta x} = \mu \left(\frac{\delta^2 u}{\delta x^2} + \frac{\delta^2 u}{\delta y^2} + \frac{\delta^2 u}{\delta z^2} \right) \quad \text{Equation 2-10}$$

If one considers a 2-D flow then $\frac{\delta^2 u}{\delta z^2}$ is zero and since $\frac{\delta^2 u}{\delta y^2} \gg \frac{\delta^2 u}{\delta x^2}$ (for a flat surface, where $u = 0$) then

$\frac{\delta^2 u}{\delta x^2}$ can be neglected, thus leaving Equation 2-11 as expressing the pressure gradient;

$$\frac{\delta p}{\delta x} = \mu \left(\frac{\delta^2 u}{\delta y^2} \right) \quad \text{Equation 2-11}$$

Henceforth it is understood that the pressure gradient, both in its magnitude and polarity, will go a long way towards determining the shape of the velocity profile in the near wall region of a flat plate laminar boundary layer. For a negative pressure gradient causing the flow to accelerate in the streamwise direction, $\frac{\delta p}{\delta x} < 0$, $\frac{\delta^2 u}{\delta y^2}$ must also be negative and this negative magnitude actually persists until $y \rightarrow \infty$. A negative pressure gradient has the effect of filling out the velocity profiles, due to the increased curvature, and hence the boundary layer thickness, displacement thickness and momentum thickness will be reduced for the trade-off that the shear stress on the fluid will be higher in the near wall region owing to the increased velocity gradients. All of which conspire to increase the stability of the boundary layers under the influence of such pressure gradients, hence in 2-D flows these are often termed favourable pressure gradients.

For the opposite case of decelerating streamwise flow, $\frac{\delta p}{\delta x} > 0$, the $\frac{\delta^2 u}{\delta y^2}$ term will also be positive in the near wall region. However once more, with increasing wall normal displacement, $\frac{\delta^2 u}{\delta y^2}$ will eventually become negative and hence a point of inflection, where $\frac{\delta^2 u}{\delta y^2} = 0$, will be present. This point of inflection was shown by Rayleigh to be a source of instability where it will typically result in

reduced stability and accelerate the transition process. As such positive streamwise pressure gradients in 2-D boundary layers are termed as being adverse pressure gradients. Should such an adverse pressure gradient be of sufficient severity, or persist for sufficient spatial duration, it is likely that separation would be instigated. Separation of the mean flow occurs when the shear stress, and therefore the wall normal velocity gradient, drops to 0.

The severity of adverse pressure gradient which a boundary layer can sustain without separation also depends on the nature (laminar, turbulent or indeed transitional) of the boundary layer itself. Turbulent boundary layers are known to be less susceptible to the effects of adverse pressure gradients owing to the enhanced mixing associated with turbulence which act to suppress separation by producing a continuous flux of momentum towards the wall which effectively keeps the boundary layer energised and therefore attached.

This is perhaps best illustrated with the practical example of dimples on a golf ball where the Reynolds numbers are sufficiently high that separation occurs. The dimples act to turbulate the flow, maintaining flow attachment for longer, relative to the smooth, laminar counterpart of a perfect sphere and thus keeping pressure drag to a minimum by increasing the separation to approximately 130° from 80° in the laminar case and therefore minimising the size of the wake. Note that the separation angles quoted here are merely demonstrative figures and, in reality, the actual separation angles will vary depending on Reynolds number and the background environment.

In a swept flat plate boundary layer the crossflow in the mean flow profile leads to an inflectional instability on its own and in contrast to 2-D boundary layer flows a negative pressure gradient has a destabilising effect (Bippes (1999)). This aspect, specific to three dimensional boundary layers in non-zero pressure gradients is covered in more detail in section 2.5. However, the situation reverses with respect to flows which are critical (from a stability perspective) only to crossflow instabilities (Bippes (1999)).

2.4 Boundary Layer Theory

The following section provides a brief overview of the theoretical frameworks for which boundary layer theory has developed from, in strict relation to laminar, transitional and turbulent boundary layer flows. These are initially considered from the classical 2-D unswept viewpoint, whereafter (in section 2.5) the focus shifts towards 3-D boundary layers and Falkner-Skan-Cooke mean velocity profiles which are closely correlated to the flow fields which were present in the experimental and numerical work presented in Chapter 4 and Chapter 5.

2.4.1 Laminar Boundary Layers

In laminar flows the fluid particles tend to move in parallel layers (laminae) but in the boundary layer each laminate layer propagates at different relative velocities as the motion is restricted by the action of shear stress, initiated by the lack of slip (usually no slip) at the solid boundary.

For all flows considered in this thesis there are two (classical) physical conservation arguments which are abided by. These being; firstly that mass is conserved and secondly momentum is conserved.

The continuity equation, in three-dimensional Cartesian notation, for steady incompressible flow, where source terms and body forces due to gravity can be ignored (where air is considered to be the fluid medium) is as follows in Equation 2-12.

$$\frac{\delta u}{\delta x} + \frac{\delta v}{\delta y} + \frac{\delta w}{\delta z} = 0 \quad \text{Equation 2-12}$$

or, in vector notation;

$$\nabla \cdot \mathbf{u} = 0$$

Equation 2-13

Likewise the momentum equations are;

$$\rho \left(u \frac{\delta u}{\delta x} + v \frac{\delta u}{\delta y} + w \frac{\delta u}{\delta z} \right) = -\frac{\delta p}{\delta x} + \mu \left(\frac{\delta^2 u}{\delta x^2} + \frac{\delta^2 u}{\delta y^2} + \frac{\delta^2 u}{\delta z^2} \right)$$

Equation 2-14

$$\rho \left(u \frac{\delta v}{\delta x} + v \frac{\delta v}{\delta y} + w \frac{\delta v}{\delta z} \right) = -\frac{\delta p}{\delta y} + \mu \left(\frac{\delta^2 v}{\delta x^2} + \frac{\delta^2 v}{\delta y^2} + \frac{\delta^2 v}{\delta z^2} \right)$$

Equation 2-15

$$\rho \left(u \frac{\delta w}{\delta x} + v \frac{\delta w}{\delta y} + w \frac{\delta w}{\delta z} \right) = -\frac{\delta p}{\delta z} + \mu \left(\frac{\delta^2 w}{\delta x^2} + \frac{\delta^2 w}{\delta y^2} + \frac{\delta^2 w}{\delta z^2} \right)$$

Equation 2-16

again, in vector notation;

$$\rho(\mathbf{u} \cdot \nabla \mathbf{u}) = -\nabla p + \mu \nabla^2 \mathbf{u}$$

Equation 2-17

Note that, subject to the inclusion of the transient term; $\frac{\delta \mathbf{u}}{\delta t}$, the above equations are those which are solved for direct numerical simulations (DNS) in incompressible flows, in that no modelling of the fluctuating terms is used for solution time brevity, at the expense of accuracy/physicality.

2.4.2 Transitional Boundary Layers

The spatial extremities of transition should technically be where transition is first observed, and the intermittency becomes non-zero, and where the transition first saturates at 100%. However determining these exact points is impractical and hence the established approach of Narasimha (1957) is utilised.

This approach involves quantifying the positions, with respect to the streamwise displacements from the leading edge and their respective target intermittencies for unskewed boundary layer profiles.

The following streamwise positions can then be trapped through linear interpolation of the near wall data points; at 1%, 25%, 75% and 99% intermittency. 1% is considered to be where the transition starts and 99% where transition is completed and the difference between these two parameters represents the streamwise displacement over which the transition takes place – i.e. the transition length.

Dhawan and Narasimha (1958) then postulated the following relationship (Equation 2-19) for the distribution of intermittency with respect to a flat plate zero pressure gradient boundary layer in the near wall region, where Equation 2-18 provides the definition of the arbitrary λ parameter.

$$\lambda = x_{\gamma|75\%} - x_{\gamma|25\%} \quad \text{Equation 2-18}$$

$$\gamma(x) = 1 - \exp\left(-\frac{0.412(x - x_t)^2}{\lambda^2}\right) \quad \text{Equation 2-19}$$

Thereafter transitional boundary layer parameters can be approximated as an intermittency weighted average of laminar and turbulent profiles, as suggested by Emmons (1951), for example for the skin friction coefficient where L and T denote laminar and turbulent portions;

$$C_f = (1 - \gamma)C_{fL} + \gamma C_{fT} \quad \text{Equation 2-20}$$

Similar relationships can be drawn for other parameters and in fact some relatively primitive transitional CFD models exist which are effectively laminar-RANS hybrids with additional transport equation(s) for intermittency. See Steelant and Dick (1996) for example who incorporate an intermittency transport equation into Wilcox's low Reynolds k- ω model Wilcox (1994) using the

empirical correlation of Abu-Ghannam and Shaw (1980) – Equation 2-21 to predict the start of transition.

$$Re_{\theta_s} = 163 + \exp(6.91 - \tau) \quad \text{Equation 2-21}$$

Unfortunately, the computational effort required to directly solve the Navier-Stokes equations at relevant Reynolds numbers using DNS is large and so the use of empirically based RANS methods are more commonplace. Such approaches are perhaps valid (and have certainly proven to be successful commercially) and to a limited extent physically realistic, where one does not deviate significantly from simple test cases (for example the T3 ERCOFTAC test cases zero pressure gradient test cases from Savill (1992) as in Steelant and Dick (1996)) but reliable, robust general transition models which span a wide variety of problems don't exist, as of yet.

In Johnson (2002) a method of predicting transition without empiricism or DNS is presented by studying the receptivity of Poulhausen boundary layer profiles to various vortex orientations. This was subsequently improved to similar studies on developing laminar boundary layer profiles in Johnson (2011a). One of the objectives of the current thesis is to extend this to non-zero pressure gradients and swept flows.

2.4.3 Turbulent Boundary Layers

The mathematical complexities of turbulence prohibit exact analyses of turbulent flows (except through the use of DNS which is extremely computationally expensive) and therefore analytical solutions for turbulent boundary layers are not available. This is due to turbulence consisting of random fluctuations of the flow properties and hence a statistical approach is adopted for analysis. This statistical approach is optimised by using the procedures introduced by Reynolds (1895) who

expressed all properties as the sum of mean and fluctuating components, therefore, in the case of incompressible, isothermal flows, forming the time-averaged continuity and Navier Stokes equations. Furthermore, since virtually all engineering problems involve inhomogeneous turbulence, time-averaging represents the most appropriate form of Reynolds averaging (Wilcox (1998)). There are several statistical averaging choices available, but given that hot-wire measurements are frequently recorded with single component hot-wires resolving the Reynolds stresses is not something which can be achieved from single wire data. This is clear with the following explanation of the Reynolds-averaged Navier-Stokes equations (RANS) in the case of spatially stationary turbulence.

To start with we formally express the instantaneous velocity, $u_i(x, t)$, of such a flow as;

$$u_i(x, t) = U_i(x) + u'_i(x, t) \quad \text{Equation 2-22}$$

This is to say that the instantaneous velocity is the sum of the mean and the fluctuating component where the mean is time-averaged, as in Equation 2-23;

$$U_i(x) = \lim_{T \rightarrow \infty} \frac{1}{T} \int_t^{t+T} u_i(x, t) dt \quad \text{Equation 2-23}$$

Whilst in reality the sampling time will never be of infinite length it is sufficient to choose a sampling time which is much longer than the maximum wavelength (period) of the velocity fluctuations and as such this should also be adhered to for hot-wire sampling time selection. Furthermore, there are flows in engineering where the longest period of oscillations are not down to the turbulence itself but rather due to low frequency oscillations, for example residual oscillations stemming from a wind tunnel motor speed controller set-up.

The time-average of the fluctuating component, on the other hand, is zero, owing to the mean and time-average of the mean being equivalent. However, there is no a priori reason for the product of different fluctuating properties to be zero, such as is in turbulent flows where ‘apparent stresses’ – i.e. the Reynolds stresses, are observed (Wilcox (1998)).

For the reader interested in studying turbulent flows the book by Tennekes and Lumley (1972) offers insight into most of the salient macroscopic features of such flows which are listed below;

Irregularity - Turbulent flows are irregular and chaotic. They are the product of a broad spectrum of different eddy-sizes/length scales. It is however, contrary to popular misconceptions, deterministic and fully described by the Navier-Stokes equations. That is to say for two separate ‘numerical experiments’ with the same set of input conditions that identical results will be produced. However, the background acoustic noise that one may observe during physical experimentation may, on the other hand, essentially be random. In order to sufficiently resolve such issues a valid DNS approach may have to include the full wind tunnel and possibly the laboratory environment itself in the calculation, which would of course be exceptionally (and prohibitively) expensive. As such many of the inflow boundary conditions on numerical simulations, which solve some form of the Navier-Stokes equations, utilise random algorithms to superimpose turbulent structures on the incoming mean flow to represent freestream turbulence, see the synthetic-eddy-method of Jarrin et al. (2006) for example. Theoretically, with a well-designed synthetic inflow boundary condition, which is representative of the complementary experimental set-up, it would be possible to obtain convergence with the statistically steady mean properties. This would hold true if the Reynolds averaged results for solution time tending towards infinity and, likewise, an infinite number of ensemble averaged experiments/Reynolds averaged experiments over infinite sampling time.

Diffusivity – The enhanced diffusion which is achieved with turbulent flows greatly increases the transfer of mass, momentum, energy and species. This effect of turbulence is often exploited with the use of devices, termed ‘turbulators’, such as in heat exchangers with the likely trade-off of

pressure losses due to increased 'blockage'. Furthermore, owing to the enhanced diffusivity, the fluid stress can be several orders of magnitude greater than that of a corresponding laminar flow field.

Three-dimensionality - Turbulent flows are inherently three-dimensional, as discussed previously in chapter 1 and in Versteeg and Malalasekera (2007).

Dissipation - Turbulent flows dissipate their energy through a cascade process. The largest eddies, operating at the integral length scale, which are on the order of the flow geometry (e.g. mesh spacing size), extract their kinetic energy from the freestream. Smaller eddies consume their energy from the larger eddies, and the kinetic energy of the smallest eddies (operating at the Kolmogorov lengthscale) are dissipated as heat/internal energy through the action of molecular viscosity. This process of energy transferral, from the largest to the smallest eddies, is called the cascade process.

Continuum – The smallest turbulent eddies are typically much larger than the molecular scale and, hence, classical continuum assumptions, analogous to those in classical mechanics, are applicable. That is to say for turbulent flows, in the case of numerical simulations, there is no necessity to model discrete particle collisions although there are methods which model the particle collisions, such as Lattice-Boltzmann methods.

When it comes to the analysis of turbulent boundary layers the total boundary layer thickness is typically divided into sub-layers. These sub-layers are comprised of the viscous sub-layer, a buffer layer and a region where a log-law whose applicability is often the subject of debate, see George (2007) for example. There are numerous formulations and coefficients for the log-law (or law of the wall) as it is more commonly known, each reputed to have their own respective applicability in various fields, e.g. in pipe flow and flat plate boundary layers. The emphasis in this thesis mainly regards transitional and pre-transitional boundary layers but comparisons with the empirical turbulence laws are useful for validating data in any case. The law (and respective coefficients) chosen for later comparisons is that of the form offered by Clauser (1956) as per Equation 2-24;

$$u^+ = 2.44 \ln(y^+) + 4.9 \quad \text{Equation 2-24}$$

where the empirical coefficient 2.44 is the reciprocal of von Karman's constant κ of 0.41, attributed to Von Karman (1930) and the latter coefficient (often termed the 'additive constant' as in Marusic et al. (2010)) of 4.9 (or C^+) is typical of those expressed for smooth walls, e.g. in Schlichting and Gersten (2000) the value 5.0 is quoted. Furthermore u^+ and y^+ are defined as follows, with u_τ , also known as the friction velocity, given in Equation 2-27;

$$u^+ = \frac{u}{u_\tau} \quad \text{Equation 2-25}$$

$$y^+ = \frac{u_\tau y}{\nu} \quad \text{Equation 2-26}$$

where;

$$u_\tau = \sqrt{\frac{\tau_w}{\rho}} \quad \text{Equation 2-27}$$

The law of the wall (in the form of Equation 2-24) effectively states that the mean velocity in the form of u^+ in a turbulent flow is proportional to the natural logarithmic distance from the boundary within a certain range of y^+ values. The empirical law is generally found to be applicable for y^+ values greater than 70, Schlichting and Gersten (2000), although some sources observe collapse in their data down to y^+ of 30, e.g. Kline et al. (1967).

Beneath the law of the wall region resides the viscous sublayer, with a buffer layer in between. In Schlichting and Gersten (2000) the viscous sublayer is said to exist for y^+ values below 5, with the buffer layer spanning the gap to the log law region. In the viscous sublayer the u^+ and y^+ values are observed to be equal in magnitude, i.e;

$$u^+ = y^+ \quad \text{Equation 2-28}$$

However, in the buffer layer Equation 2-24 and Equation 2-25 are not applicable. Nevertheless the buffer layer is still considered as part of the near wall region, which was defined as being $y^+ \leq 100$ by Cantwell (1981) within which region the majority of turbulent energy production is contained so it is therefore not to be considered an insignificant region.

2.5 3-D Boundary Layers

There are many forms of classical 3-D (including axisymmetrical) boundary layers, as in boundary layers where the direction of the mean flow forms a function of the normal coordinate, Schmid and Henningson (2001), which have been the subject of several high quality research studies. The majority of these classical problems are discussed in Schlichting's Boundary Layer Theory (Schlichting (1968)) and include the boundary layers on yawed cylinders, rotating disks, cones, spheres, ellipsoids, various combinations of geometrical intersections ('interference drag') and of course flat plates, with and without sweep. Gregory et al. (1955) were able to arrive at the conclusion that the flow over a rotating disk is similar to that of swept wing flow, given that the crossflow vortices are corotating in both cases.

Typically the laminar base flows of many such configurations are well understood, where the flow remains attached, however the transition process towards fully turbulent flow remains a significant challenge in each of these fields. Schmid and Henningson (2001) attribute the realisation of the majority of improvements in the understanding of three-dimensionality (in the mean flow) to studies which have been carried out on swept wings. In Gray (1952) it was observed for wing sections covered with substantial regions of laminar flow, that this advanced to almost fully turbulent over the chord for sweep angles larger than 20 degrees. Gray also observed the growth of stationary vortices which were approximately oriented along an inviscid streamline at low Reynolds numbers Boiko (2012). Thereafter similar vortices were found in analogous three-dimensional flows Boiko

(2012), such as rotating discs (see Gregory et al. (1955)), rotating cones (see Kobayashi et al. (1983)) and swept cylinders (see Poll (1985)).

Similarly, two such well-studied flow configurations are boundary layers over swept wings and internally within turbomachinery, as previously discussed. Such cases are well described by a family of solutions to the boundary layer equations known as the Falkner-Skan-Cooke similarity solutions Kurian et al. (2011). These solutions are stable to the development of Tollmien-Schlichting waves but are sensitive to, and often governed by, crossflow instabilities Kurian et al. (2011). Crossflow instabilities exist as stationary or travelling waves and the transition process, where all other instability mechanisms (such as centrifugal and TS) remain sub-critical, will be governed by either waveform mode Kurian et al. (2011). Typically more effort is spent trying to replicate circumstances where stationary crossflow modes (as opposed to travelling) are deemed responsible for the transition process as this is the scenario most often seen in free-flight conditions Kurian et al. (2011) on aircraft.

In order for this to be achieved there is a drive towards minimising freestream turbulence levels in wind tunnels. For instance at the MTL (Minimum Turbulence Level or Mårten Theodore Landahl, named after its late creator Lindgren and Johansson (2002b)) facility at KTH – Royal Institute of Technology in Sweden the streamwise freestream turbulence intensity is quoted as less than 0.025% (when high-pass filtered) at 35m/s in Lindgren and Johansson (2002b). It is interesting to note that similar readings were observed at the MTL facility a decade previously in Johansson (1992). Ideally (from their perspective) these turbulence intensities would tend towards 0% which would allow something of a replication of quiescent atmospheric conditions, in the relative frame of reference moving at the freestream velocity, similar to that experienced in free-flight. In Kachanov (2000a) it is stated that the main problem with all such low-turbulence facilities is that they don't actually possess low-turbulence characteristics below 1 or 0.1 Hz. Furthermore in Yokota et al. (1967) and Schubauer and Skramstad (1947) it is stated that hot-wire velocity measurements at such low levels

of freestream turbulence are susceptible to errors caused by vibration. Thereafter changes in the freestream turbulence intensities, and often other important parameters such as turbulent length scale etc., can be successfully modulated through judicious choice and installation of turbulent generating grids upstream of the test section. Similarly, several experiments have been performed in water towing tank facilities, such as in Bippes (1990) – on cylinders in this case, following a similar rationale regarding freestream turbulence intensity.

Although crossflow instability has been studied extensively it is still not well described by the e^N method Kurian et al. (2011), which has been used successfully with 2-D boundary layer flows, see for example Arnal (1994) and other work on the parabolised stability equations (PSE) such as Herbert (1997). As with 2-D boundary layers, reliable prediction of the transition process is dependent upon detailed knowledge of the disturbance environment and, hence, accurate predictions require an understanding of the receptivity process (Kurian et al. (2011)). As such this is the area in which the efforts exerted for the current work have been channelled towards, both in terms of the experimental and numerical receptivity work.

Similarly with many non-3-D configurations, there are several methods employed in order to study these flow problems. These can be summarised as firstly, direct numerical simulations (DNS), where the Navier-Stokes equations are solved numerically across the entire spectrum of scales (integral to Kolmogorov) with respect to the characteristic Reynolds number of the problem being analysed. Secondly, one can perform a linear stability analysis of the governing equations, similar to those of Orr-Sommerfeld in 2-D flat plate boundary layer flows. Furthermore, there are many instances, particularly since 1985 (in the case of swept flat plate transition Saric and Yeates (1985)) where researchers have used experimental set-ups in aerodynamic/hydrodynamic facilities by physically measuring and tracking the development of transition. Each of these approaches has its merits and drawbacks but with every approach (arguably) the most significant limiting factor, in terms of the quality of the output, is resources, particularly when it comes to DNS, where even researchers who

are blessed with the best resources are limited to Reynolds numbers which typically aren't comparable with what would be observed in 'real-world' scenarios. In general terms one can now reach realistic Reynolds numbers for bypass, albeit not for natural transition. For example Johnson (2013) performed a DNS on a flat plate boundary layer for $Re_\theta = 2240$ using a grid with up to 140 million grid points, solving through a spectral method whilst utilising a periodic boundary condition in the streamwise direction. Such approximations are effectively necessary owing to the (present) prohibitively expensive nature of the process and, as with most modelling, each present their own numerical artefacts.

2.5.1 Falkner-Skan-Cooke Boundary Layer Example

Mathematically speaking, an approximation of the velocity profiles in swept three-dimensional boundary layers are successfully provided by the Falkner-Skan-Cooke similarity solutions derived by Cooke (1950). These similarity solutions effectively extend the von Karman-Pohlhausen method Pohlhausen (1921) to another dimension Cooke (1950) using the Falkner-Skan third order ordinary differential equation (ODE) for wedge flows attributed to Falkner and Skan (1931) as a starting point. The Falkner-Skan-Cooke boundary layer is frequently used as the base for swept wing analyses since it comprises both a pressure gradient and sweep angle, Tempelmann et al. (2010). Three dimensional laminar boundary layers on swept wings with a pressure gradient are well described by these Falkner-Skan-Cooke similarity solutions to the boundary layer equations (Kurian et al. (2011)). Please note that the Falkner-Skan-Cooke general solutions can be reduced back to the special case of Blasius flow in the absence of crossflow and pressure gradient - Chevalier et al. (2007).

In order to obtain these solutions it is first assumed that the freestream velocity obeys a power law in the following form of Equation 2-29 and that W_∞ , the freestream crossflow velocity, is invariant in the spanwise direction;

$$U_{\infty} = U_0 \left(\frac{x}{x_0} \right)^m \quad \text{Equation 2-29}$$

where;

$$m = \frac{\beta_H}{2 - \beta_H} \quad \text{Equation 2-30}$$

therefore;

$$\beta_H = \frac{2m}{m + 1} \quad \text{Equation 2-31}$$

The non-dimensional boundary layer thickness is also given by the similarity variable η as;

$$\eta = y \sqrt{\left(\frac{m+1}{2} \right) \frac{U(x)}{\nu x}} \quad \text{Equation 2-32}$$

and when $y \rightarrow \infty$; $u = U_{\infty}$ and $w = W_{\infty}$, i.e tending towards potential flow outside of the boundary layer.

Using the stream function approach to implicitly solve continuity gives a stream function, ψ , of the following form;

$$\psi(x, y) = \sqrt{\left(\frac{2U\nu x}{m+1} \right)} f(\eta) \quad \text{Equation 2-33}$$

eventually yielding the following differential equations for Falkner-Skan-Cooke flow;

$$f''' + ff'' + \beta_H(1 - f'^2) = 0 \quad \text{Equation 2-34}$$

$$g'' + fg' = 0 \quad \text{Equation 2-35}$$

where $f''' = \frac{\delta^3 f}{\delta \eta^3}$ and $g'' = \frac{\delta^2 g}{\delta \eta^2}$ etc.

The effects of the β_H parameter (in Equation 2-34) on the Falkner-Skan equation were investigated by Hartree (1937) who found that physical solutions, using a shooting method approach, were viable for the range;

$$-0.0908 \leq m \leq 1$$

This was because values of m greater than unity resulted in floating point errors and, on the other periphery, too low a value of m will physically instigate flow separation. Stewartson (1954) suggested that the Falkner-Skan equation can be thought of (qualitatively) as analogous to non-zero pressure gradient flows where the pressure gradient is prescribed by the β_H parameter, hence the corresponding separation which occurs when the m (or β_H) parameters are too severe and, by analogy, so too would be the pressure gradient.

The second of the two ODE's (Equation 2-35) and, in essence, the contribution of Cooke (1950) utilises the previous solution for f in the Falkner-Skan equation and, once solved, allows for computation of the streamwise and crossflow velocities as follows;

$$u(y) = f' \cos^2 \theta + g \sin^2 \theta \quad \text{Equation 2-36}$$

$$w(y) = (g - f') \cos \theta \sin \theta \quad \text{Equation 2-37}$$

where θ is relative to the leading edge and;

$$\theta = \tan^{-1} \frac{W(x)}{U_\infty} \quad \text{Equation 2-38}$$

Furthermore, the boundary layer thickness of the Falkner-Skan-Cooke velocity profile can be determined through;

$$\delta = \sqrt{\left(\frac{m+1}{2}\right) \frac{U(x)}{2\nu x} \int_0^\infty (1-f') dy} \quad \text{Equation 2-39}$$

The Falkner-Skan-Cooke equations can't be solved analytically and, as such, approximate numerical methods are utilised to obtain solutions, in conjunction with the following boundary conditions for this boundary value problem;

$$f'(0) = f(0) = 0$$

$$f'(\infty) \rightarrow 1$$

$$g(0) = 0$$

$$g(\infty) \rightarrow 1$$

The results of Stemmer (2010) are presented here for Falkner-Skan-Cooke profiles at two different β_H values, -0.1 and 1.0, in Figure 2-9. These results are later replicated in section 4.2.4.

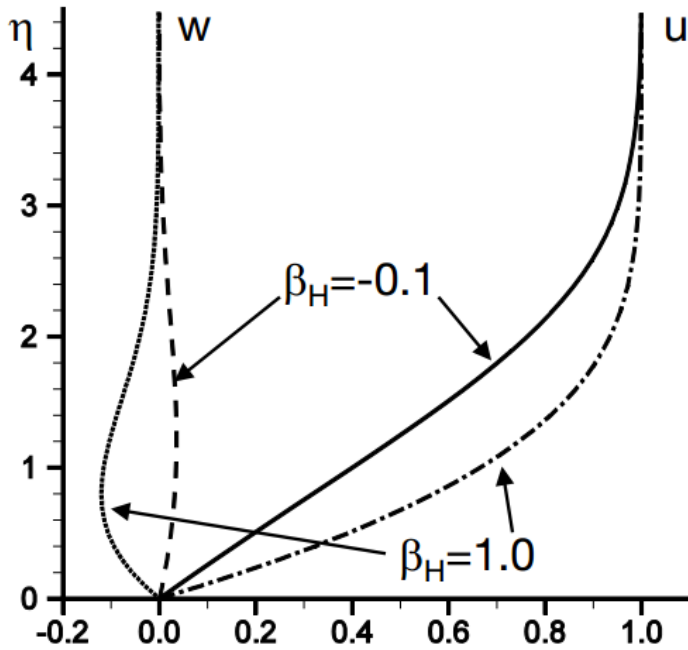


Figure 2-9 - Falkner-Skan-Cooke velocity profiles for two β_H values - Stemmer (2010)

2.5.2 Instability Mechanisms for Swept Transition

There are four fundamental instability modes present on a swept (wing) laminar boundary layer flow and these comprise; attachment line, streamwise (Tollmien Schlichting), crossflow and centrifugal instabilities, Dagenhart and Saric (1999), and these are depicted in Figure 2-10, relative to their principal area of action. When dealing with flat plates, centrifugal instability, which can lead to the production of Görtler vortices in concave regions of wings, does not feature and, therefore, is afforded no additional consideration here.

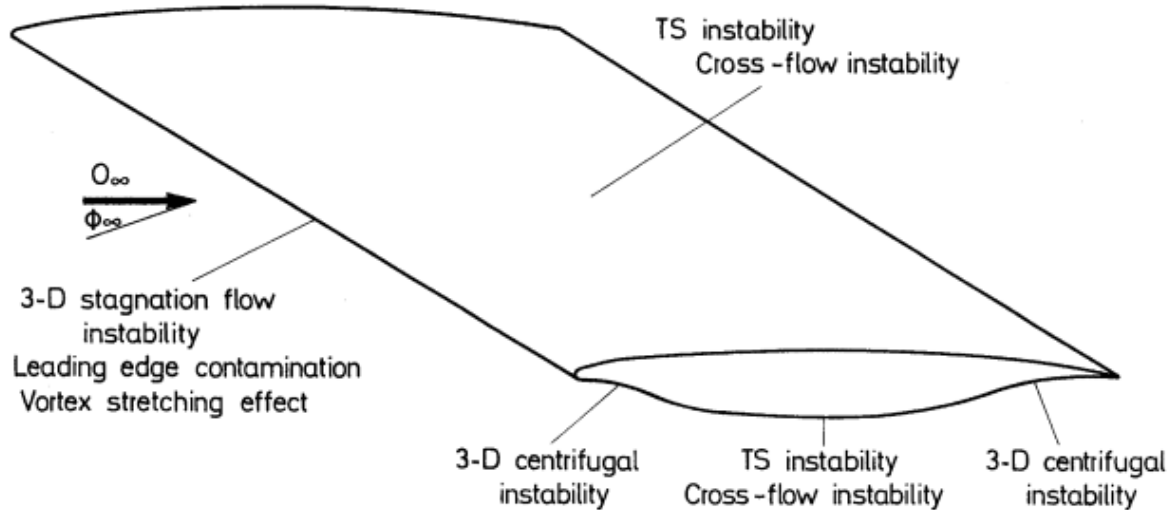


Figure 2-10 - Possible instability mechanisms acting on a swept wing and their prevalent locations (Bippes (1999))

At the leading edge of a swept wing there are two classes of primary flow instabilities which are observed; these comprise attachment line instability and crossflow instability as stated, for example, by Sesterhenn and Friedrich in the lecture note series of Gad-el-Hak and Tsai (2005) who further indicate that crossflow instability is observed at several viscous lengthscales downstream of the leading edge. Crossflow instabilities are a primary instability which propagate approximately in the leading edge tangential direction on a swept plate and are somewhat analogous to the Tollmien-Schlichting waves which propagate in the streamwise direction (see Figure 2-11)

In Uranga et al. (2011) the parameters which are stated to be important in crossflow stability studies are the height of the inflection point, the velocity gradient at this point and the maximum crossflow velocity. An example of a critical Reynolds number for crossflow instability is given in Zurigat and Malik (1995) as Equation 2-40.

$$Re_{cf} = \frac{\bar{U}_c \delta_{0.1}}{\nu} \quad \text{Equation 2-40}$$

where \bar{U}_c is the magnitude of the maximum crossflow velocity and $\delta_{0.1}$ is the boundary layer thickness, within which the crossflow velocity is less than 10% of \bar{U}_c . Other forms of critical Re_{cf} exist and can even be compared with similar criteria for Tollmien-Schlichting natural transition, to estimate the extent and influence of the respective regions for a given scenario.

The baseflow of attachment line instability is a swept Hiemenz flow, that is to say a stagnation flow with a superimposed crossflow/spanwise component (Gad-el-Hak and Tsai (2005)). Attachment-line instability is a linear viscous instability, Gad-el-Hak and Tsai (2005), whereas crossflow instabilities (whilst similarly linear) are of the inviscid type. As a consequence, passive suction methods (on which significant work has been conducted along with other transition control methodologies) for controlling transition in swept wing flows are less effective where crossflow instability dominates, owing to crossflow instabilities being inflectional in nature. This is in contrast to Tollmien-Schlichting instabilities, which are more conducive to such control, given their viscous instability nature (Reed and Saric (1989)).

In Gaster (1967) it is stated that attachment-line instability can be prevented through the use of a carefully designed bump at the leading edge towards the wing root. Attachment line instability, however, should only be significant on wings with large leading edge radii – again something which is typically of negligible significance in any flat plate boundary layer and, hence, once more they are not described in substantial detail.

Downstream of the crossflow instability region at the leading edge streamwise instability (basically Tollmien Schlichting activity) tends to dominate swept natural transition processes, as depicted in Figure 2-11. In Saric and Yeates (1985) it is stated that for the mid-chord region of a swept wing the stability is governed by Tollmien-Schlichting waves, but this would only be applicable in cases where the freestream turbulence intensity is lower than that for bypass transition to take place, as is typically the case in free flight conditions.

In swept-wing boundary layers Tollmien-Schlichting instability waves can also play a significant role in the process of transition (Kachanov (2000a)). However, the most important mechanism responsible for natural 3-D transition is associated with the crossflow instability (Kachanov (2000a)). Similar to swept wings, swept flat plate boundary layers are also known to exhibit strongly inflectional (crossflow) instabilities (Tempelmann (2011)).

The reason why crossflow instability dominates towards the leading edge in (swept) natural transition is because the Tollmien Schlichting activity is attenuated by the initially favourable pressure gradient and, generally speaking, crossflow instability is the dominant instability mechanism for swept wing flows in regions of non-zero pressure gradient Reed and Saric (1989). Hence, near the leading edge the stability of a swept wing boundary layer is dominated by the behaviour of the crossflow vortices (Saric and Yeates (1985)). Dagenhart and Saric (1999) discuss operating their swept wing at an angle of attack of -4° such that crossflow instability drives the transition process, through producing a long extent of negative pressure gradient which is favourable for the Tollmien Schlichting waves but strongly amplifies crossflow vortices.

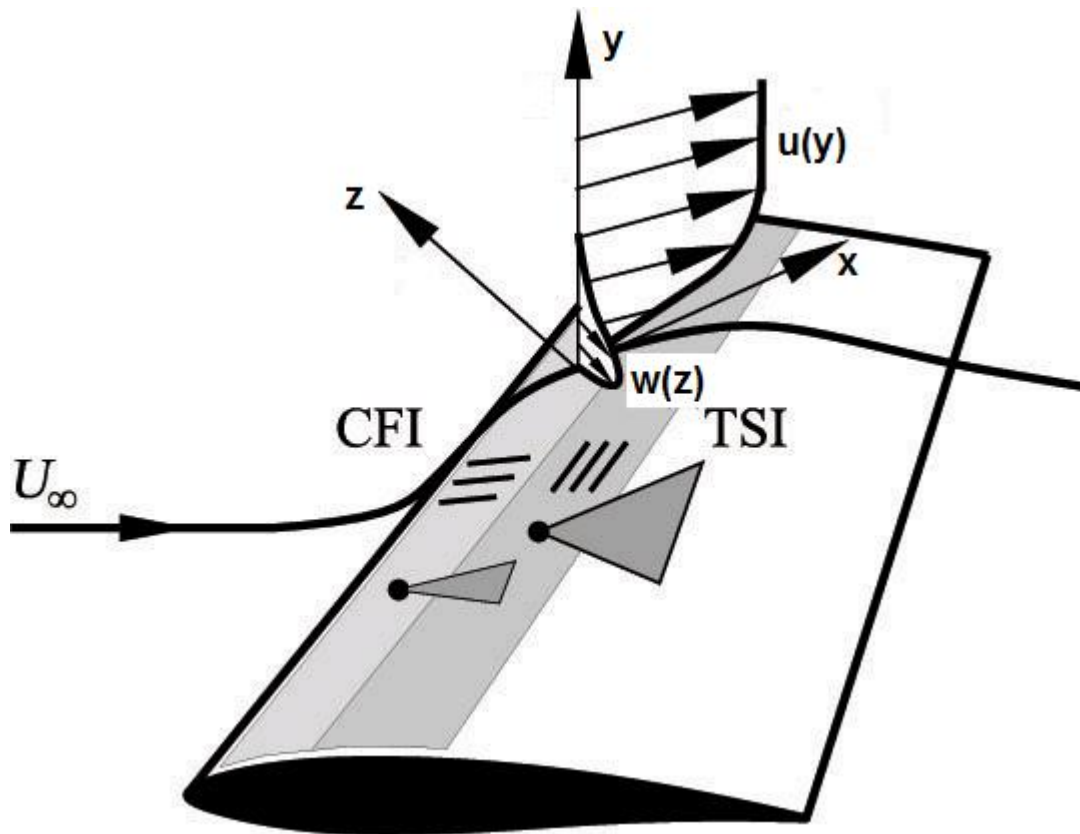


Figure 2-11 - Crossflow and Tollmien Schlichting instability waves on a swept wing - Oertel (2010)

Transition initiated through crossflow instability has been studied extensively but is still not well described by the e^N method, which has been implemented successfully in unswept flows (Kurian et al. (2011)), as highlighted earlier in section 2.5. The highlights of work on crossflow instabilities are largely covered in the review papers of Bippes (1999) and Saric et al. (2003) where the former goes into some detail on the experimental configurations at ASU, ITAM, NAL and DLR which cover a wide range of topologies, such as swept wings, flat plates, cylinders etc. where three-dimensionality in the mean flow is present. As has been mentioned previously in section 2.5 much of the work covered in swept transition has been geared towards disturbance growth through the primary instability mechanisms outlined within this sub-section. The main focus being on stationary crossflow vortices, which are of course associated with very low freestream turbulence levels and therefore free flight conditions in aviation.

However, with significantly increased freestream turbulence intensity these primary instability modes will largely be bypassed and the transition will take place through a bypass mechanism. For a boundary layer transitioning through a bypass mechanism the flow is characterised by the growth of high and low speed streaks which are generated through what's known as the Klebanoff mode (Kendall (1985)). These streaks are also observed in the near wall region of fully turbulent flow.

In Brandt (2003) it is stated that streaks are seen to appear with boundary layers that are subject to significantly high free-stream turbulence levels, as such attention is now drawn to streaky structures and Klebanoff modes. Klebanoff modes appear to be caused by freestream turbulence and take the form of streamwise streaks (Kudar et al. (2006)). Klebanoff modes are fundamentally different to TS instability modes in that the former grows algebraically, as opposed to the latter which grow in an exponential fashion (Kudar et al. (2006)). Klebanoff modes are, therefore, not wavelike in form.

It was observed by Gray (1952) (in both real flight and wind tunnel conditions on swept wings - Kohama (1987)) that regularly-aligned streaks appear almost along the outer streamline of the boundary layer. These flow patterns are also observed in non-zero pressure gradients on swept flat plates, as in Saric and Yeates (1985). It is thought that these streaks are caused via the action of co-rotating stationary vortices (Kohama (1987)) and, as such, are perhaps limited to cases where the freestream turbulence intensity is below the order of magnitude where the vortices become unsteady

Kudar et al. (2006) presented a study of Klebanoff modes, in the context of 3-D transition, through a simplified DNS study, with the high values of turbulence intensity approximated through a fictitious body force, using the aforementioned Falkner-Skan-Cooke family of velocity profiles as their respective base flow. They concluded that the evolution of Klebanoff modes in the swept boundary layer is much more complex than unswept flows and that their development scales with respect to the angle of sweep. Klebanoff modes have also been studied through forced spanwise-periodic wall-suction in both theoretical and computational domains and furthermore others, such as Fransson et

al. (2004), have artificially generated similar streaks using spanwise arrays of cylindrical roughness elements.

2.5.3 Receptivity in 3-D Boundary Layers

Receptivity as a term, if not a concept, was first coined in Morkovin (1969) and represents the first stage of the transition process Jahanmiri (2011) – see Figure 2-2. It is first of all important to understand that no flow in nature, or indeed in engineering applications, is free from disturbances Jahanmiri (2011) and that true transition prediction is dependent upon understanding/quantifying the disturbance environment and receptivity processes which trigger disturbances inside the boundary layer that subsequently grow Kurian et al. (2011).

The receptivity process, or mechanism, is that in which disturbances in the freestream enter, and have the effect of, exciting instability waves inside wall-bounded and free-shear layers (Kerschen (1993)). It is known that the nature of the stability of these respective layers (free vs. bounded) are fundamentally different (Saric et al. (2002)). In Kerschen (1993) receptivity is sub-divided into two categories – that of natural and forced receptivity. In natural receptivity the aforementioned waves are excited by acoustic and vortical disturbances which, as the name suggests, appear naturally in freestream flows.

Forced receptivity concerns the use of artificial perturbation methods manifested through localised disturbances, such as small surface-mounted cylindrical roughness elements, as in Kurian et al. (2011), where roughness elements (stamped out from brass sheets) were attached to flat plates (with swept leading edges) through adhesive spray. Lasseigne et al. (1999) also allocate a third category, termed naturally forced receptivity, where the natural freestream disturbances are scattered by the localised surface irregularities. In Kachanov (2000a) it is stated that there are two main approaches for forcing the excitation of crossflow instabilities. These are through the

application of surface non-uniformities, as per the theoretical studies of Fyodorov (1988) (in Russian) Kachanov (2000b) and the respective experimental studies and comparisons thereafter such as Ivanov and Kachanov (1994) and Crouch et al. (1997), or by introducing spanwise non-uniformity of the potential flow.

Since these freestream disturbances take the form of vorticity, sound, vibrations or surface roughness, the influences are incompletely understood (Saric et al. (2002)). What is known however is that these disturbances can penetrate into the boundary layer via its respective boundaries Jahanmiri (2011), such as the horizon of the boundary layer thickness, at the boundary layer origin (such as the leading edge of a wing - Kachanov (2000a)) or the surface itself, such as a flat plate. Some combined methods of the above are also possible (Kachanov (2000a)).

The theoretical approach of Goldstein (1983) was able to show that boundary layers are most receptive (to external disturbances and surface roughness) in regions where non-parallel effects are significant. Such non-parallel regions would, for example, include corners in a wind tunnel and at the leading edges of flat plate topologies. The optimal disturbances in swept flat plate boundary layers, as discussed by Tempelmann (2011) using the approach of solving the parabolised stability equations, are considered to take the form of tilted streamwise vortices. Streamwise vortices strongly influence the behaviour of other disturbances in a boundary layer, Reed (1987), however it is known that attachment-line instability does not produce streamwise vortices of the crossflow type (Reed and Saric (1989)). During convection downstream the streamwise vortices develop into streamwise streaks and experience strong non-modal growth, eventually turning into crossflow disturbances and undergoing exponential growth (Tempelmann (2011)).

3 Chapter 3 – Experimental Procedures, Apparatus and Data Processing

3.1 Blower Wind Tunnel

In Johansson (1992) it is stated that there are four main categories of wind tunnels, these being;

- Subsonic or low-speed
- Transonic
- Supersonic
- Hypersonic

Each experiment for this thesis has been conducted in what is referred to as the 'large blower tunnel facility' at the University of Liverpool and is pictured in both an isometric computer aided design (CAD) screenshot - Figure 3-1 and an actual panoramic photo of the tunnel – Figure 3-2. This is a subsonic blower tunnel which operates in an open-circuit configuration, and was designed by Gibson (1960), within which thesis the author provides both their rationale for design choices and detailed tunnel specifications. This tunnel was primarily designed for boundary layer research, Gibson (1960), and comprises a 4' x 2' (1.22 m x 0.61 m) outlet from its compressor which is then extended approximately 700mm, via a uniform cross-section settling chamber, less an approximately 25 mm gap (see Figure 3-3) for the placement of turbulence generating grids upstream of the leading edge. The swept flat plate is positioned such that there is 500 mm below the top and 100 mm above the base of the cross section and is mounted on adjustable feet. These dimensions are similar to those used in the swept transition work of Kurian et al. (2011) only their plate was more centrally located within the test section.

Air is drawn radially through the tunnel inlet and then pushed by a propeller fan, which is driven by a constant speed 50hp 3-phase induction motor. The freestream velocity in the working section is

administered by adjusting a PI motor controller which, in turn, adjusts the slip on the respective electromagnetic coupler (eddy current clutch), with respect to the tachometer (RPM) feedback of the blower fan. This tunnel design is one of many which were featured in Bradshaw and Pankhurst (1964) which is highlighted as being a very useful reference point by Lindgren and Johansson (2002a) for those designing and constructing low-speed subsonic wind tunnels.

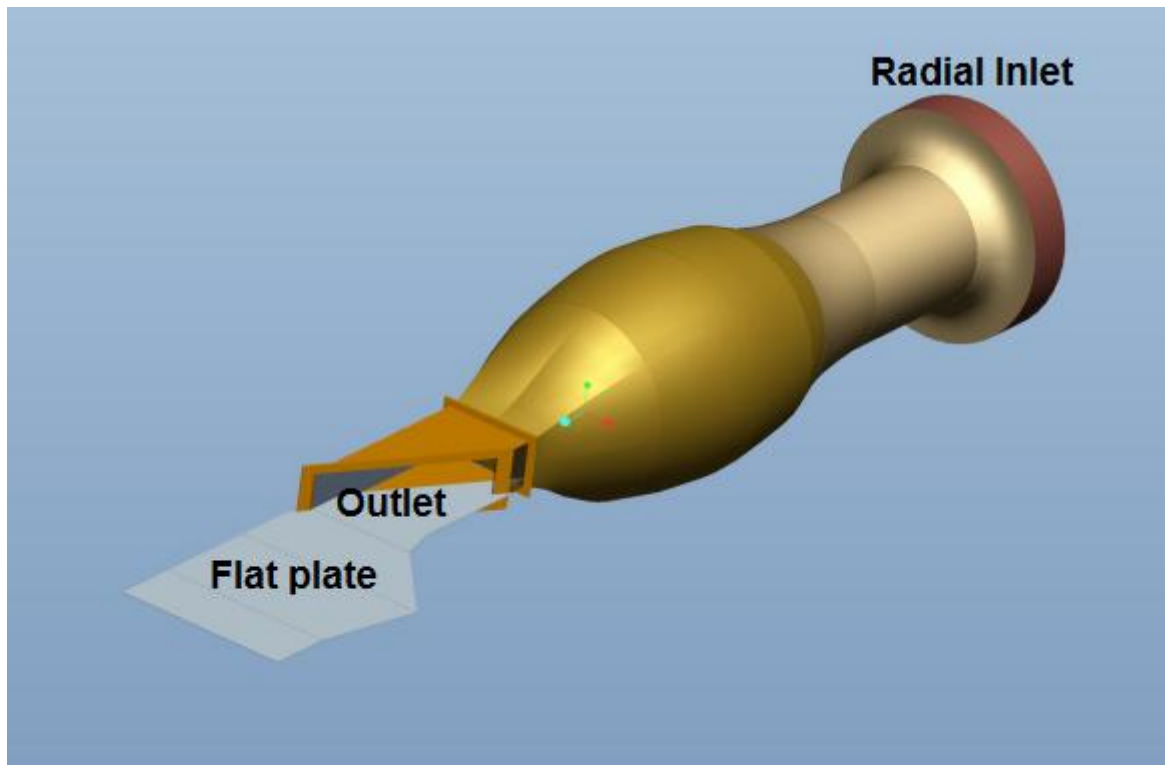


Figure 3-1 - Isometric CAD drawing of tunnel and plate with no section fitted above plate



Figure 3-2 - Panoramic view of the tunnel, measuring and ancillary equipment with the positive pressure gradient section fitted

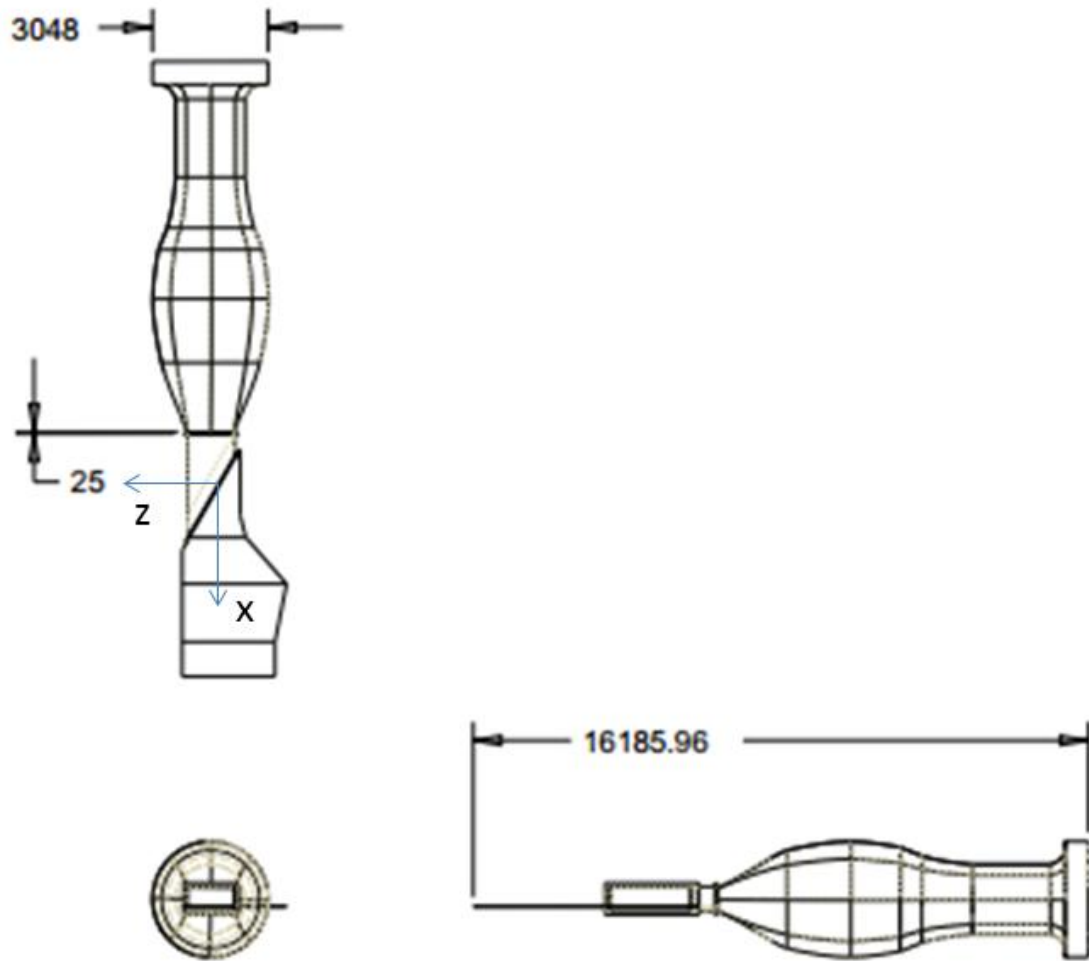


Figure 3-3 - Third angle projection of University of Liverpool large blower tunnel with significant dimensions only (no test section fitted at outlet) [mm]

The following comprises a detailed list of the main components of the experimental apparatus available at the University of Liverpool large blower tunnel facility, each of which are detailed in the following sections of this thesis;

- 3-phase 50 horsepower open circuit radial inflow, axial outflow blower tunnel
- 60° Swept flat plate (see Figure 3-4 for details). As previously stated the plate topology was inherited from the relaminarisation work of Ramadan (2000)
- Bleed control flap (see Figure 3-5)

- Pitot-static tube
- Inclined manometer
- 2x Validyne differential pressure transducers – one for measuring freestream velocity and the other for recording the streamwise pressure gradient
- Cathetometer (travelling microscope) – see Figure 3-2
- Dantec 54T30 Miniature CTA and StreamLine Pro CTA systems, the former used only for the straight, nominally zero pressure gradient section.
- 16-bit USB-6210 and 2x USB-6009 (14-bit - differential analogue input) National Instruments data acquisition devices
- DISA 55P15 Miniature Hot-Wire “Boundary Layer” Probes (Figure 3-6)
- Desktop PC (2GHz single-core, 2GB RAM)
- Elliptical pitching traverse assembly with 35NCLA-B01 stepper motor MCP (2012), complete with Dantec 55H20 probe holder
- Stepper motor controller with MSD415 driver MCP (2009)
- Template for skewing elliptical traverse assembly
- 2x Turbulent grids, immediately upstream of leading edge (resulting in three freestream turbulence intensities)

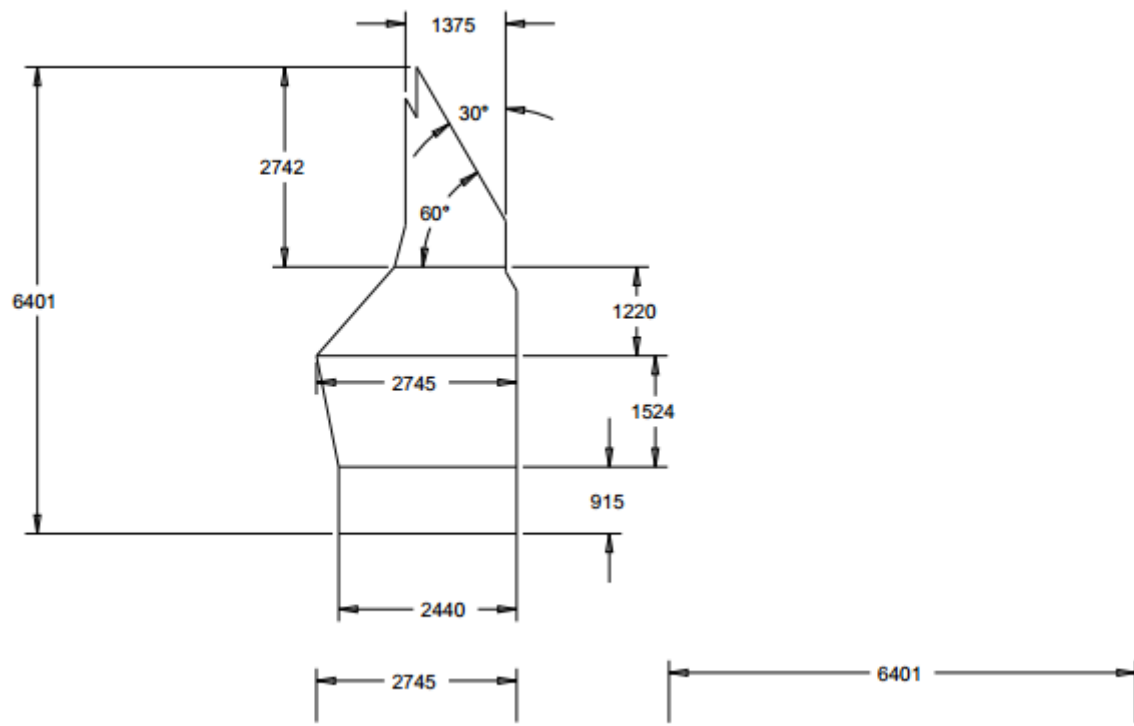


Figure 3-4 - Dimensioned CAD drawing of flat plate section in third angle projection [mm]

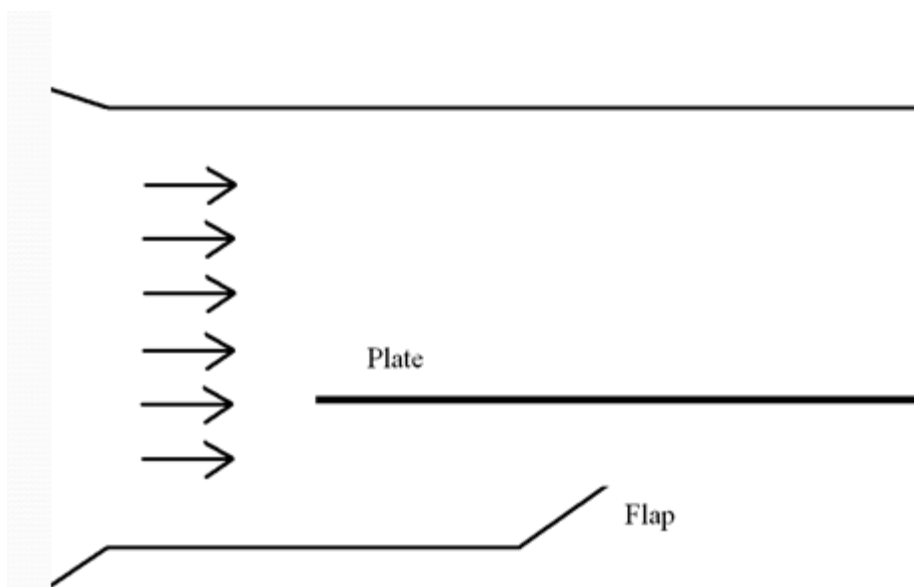


Figure 3-5 - Schematic of wind tunnel flat plate and control flap for bleeding air under the leading edge

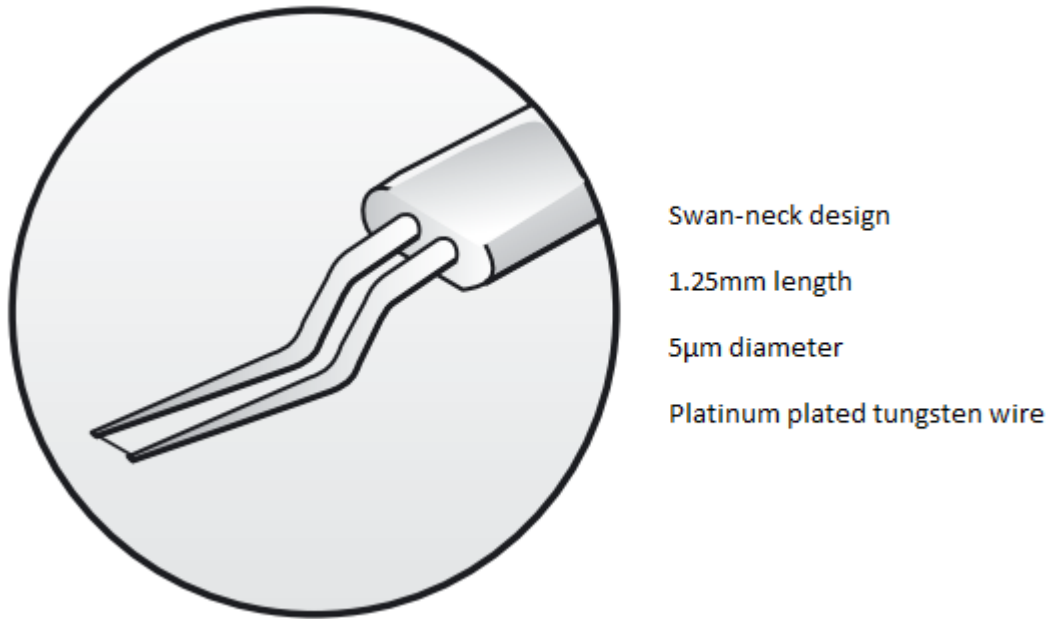


Figure 3-6 - 55P15 miniature boundary layer hot-wire probe

3.2 Swept Flat Plate and Leading Edge Control Flap

Flat plates have been used extensively for experimental boundary layer research, see for example Hall and Gibbings (1972) and Abu-Ghannam and Shaw (1980), owing to their topology being, from a practical perspective, both simple to interact with and manufacture and, furthermore, because they allow comparisons with theoretical postulates to be made; for example a Blasius solution for a laminar boundary layer in a zero pressure gradient, see Blasius (1907) or the respective English translation Blasius (1950). This research thesis is based on flat plates with the leading edge swept back by 60°, a configuration used previously at the University of Liverpool for relaminarisation research carried out principally by Ashraf Ramadan, see Ramadan (2000) and Escudier et al. (2001).

The plate is 10 mm thick and was chosen for its high flatness tolerance (less than 0.375 mm over 2.438 m, Ramadan (2000)). The plate was ground to an M2 (2 micron) finish on the measuring (top) surface, making it hydraulically smooth Ramadan (2000), and has subsequently been maintained

through regular cleaning which, on an additional note, is important for protecting hot-wires from damage caused by dust and large particles made airborne through operation of the tunnel. The plate was levelled to a target of ± 0.5 mm tolerance.

The plate was approximately 6.4 m long, spans 2745 mm in its widest region and is composed of 4 sub-sections, as detailed in Figure 3-4. The joins were achieved using rectangular alignment blocks bolted to the underside of the plate structure. The use of sub-sections offered the possibility of using a variety of leading edge sweep profiles but, whilst alternatives (15, 30 and 45°) are held as assets within the department, this possibility, in this instance, hasn't been realised and all experimentation was carried out with 60° sweep. Tests were performed immediately upstream and downstream of the joins along the measurement plane to ascertain whether or not the joins were tripping the boundary layer. It was found from these tests that there was no discernible difference in the mean profiles or intermittency between these test stations and as such it was determined that the influence of the joins was negligible. Hence it was insured, both immediately fore and aft of the joins, that the filling material used to join sub-sections together was done so with sufficient care such that the effect of joins was negligible.

An elliptical leading edge of the swept flat plate was achieved through CNC, comprising 10 mm and 5 mm semi-major (a) and semi-minor (b) axes. Such a leading edge has an aspect ratio (a/b) of 2 which is 10 times smaller than the swept leading edge of Kurian et al. (2011) at KTH in Sweden who quote their value of 20 as being a common choice in similar experimental setups. In Schrader et al. (2010) comparisons were made numerically between two leading edges of differing aspect ratio – one 6 and the other 20, which were termed 'blunt' and 'sharp', in order to evaluate the significance of the aspect ratio on receptivity. On the basis that an aspect ratio of 2 is significantly less than 6, the leading edge may be considered to be relatively blunt for the large blower tunnel swept flat plate.

The large blower tunnel facility also has a flap (5" in length with a structural aluminium Guernsey flap running along the trailing edge) running across the span of the leading edge, parallel to it, this is depicted in the schematic of Figure 3-5. This flap was installed as part of the previous relaminarisation work carried out by Ramadan (2000) and its purpose is to control where the stagnation line resides on the leading edge. This is achieved by modulating the diffusion underneath the plate with the objective of ideally matching that which is experienced on the upper surface. If this is achieved then, in effect, a symmetry boundary condition (in terms of the mean flow) has been achieved about the plane of the flat plate, a process which is far more cost efficient than manufacturing two identical pressure sections on either side of the plate for every configuration that is tested.

In Ramadan (2000) flow alignment was achieved by following the procedure of Launder (1963). This involved using a vertical column stand with 200 mm cotton strands at 25 mm pitch and then adjusting the flap angle (for a given tunnel speed) until the tufts were parallel with the leading edge of the flat plate. Thereafter Ramadan tripped the boundary layer through the use of rivets and a strip of aluminium oxide abrasive paper glued 35 mm from the leading edge of the plate on the measuring surface. The objective in this case was to provide a turbulent boundary layer with the objective of then relaminarising it. However, reverse transition was not of interest in this case and as such these trips were removed with the leading edge restored as close as possible to its original condition.

For this research similar procedures were adopted, only an Ate-AEROTECH smoke generator for flow visualisation was utilised by inserting the smoke generator probe through the gap between the outlet of the wind tunnel and the straight section. The flap was then similarly adjusted until a separation bubble could no longer be observed along the measuring plane at the desired tunnel speed. Figure 3-7 and Figure 3-8, are outputs of a demonstrative simulation performed in Fluent 6.2. This simulation was designed to illustrate the sensitivity of the leading edge in terms of the evolution

of the transition process. They are a 2-D representation of the leading edge (and its respective elliptical profile) of the swept flat plate with a streamwise inflow velocity of 3m/s, where the diffusion is in this case obtained by adjusting the target mass flow rates on the outflow boundary conditions, such as to artificially force asymmetry about the leading edge. The solution was performed on a relatively coarse grid comprising 14706 paved quadrilateral cells modelled with a sizing function in Gambit 2.4 such that the demonstrative solution would be provided quickly whilst allowing for the plate thickness and leading edge geometry to be captured by the mesh design. This asymmetry in the pressure distribution causes the stagnation point on the leading edge migrating to the underside of the flat plate. This in turn can have the effect of causing a separation bubble on the top surface. As such it is desirable to aim for a slightly negative angle of attack of the approach flow to maintain an attached flow on the side of the plate where measurements are recorded.

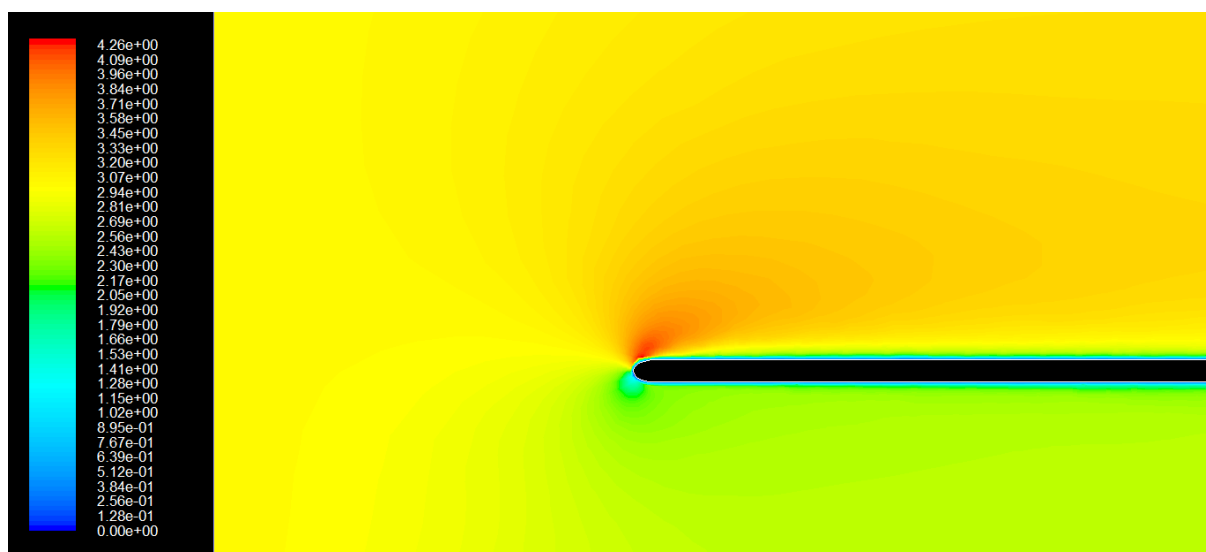


Figure 3-7 - Velocity contours for stagnation migration example [m/s]

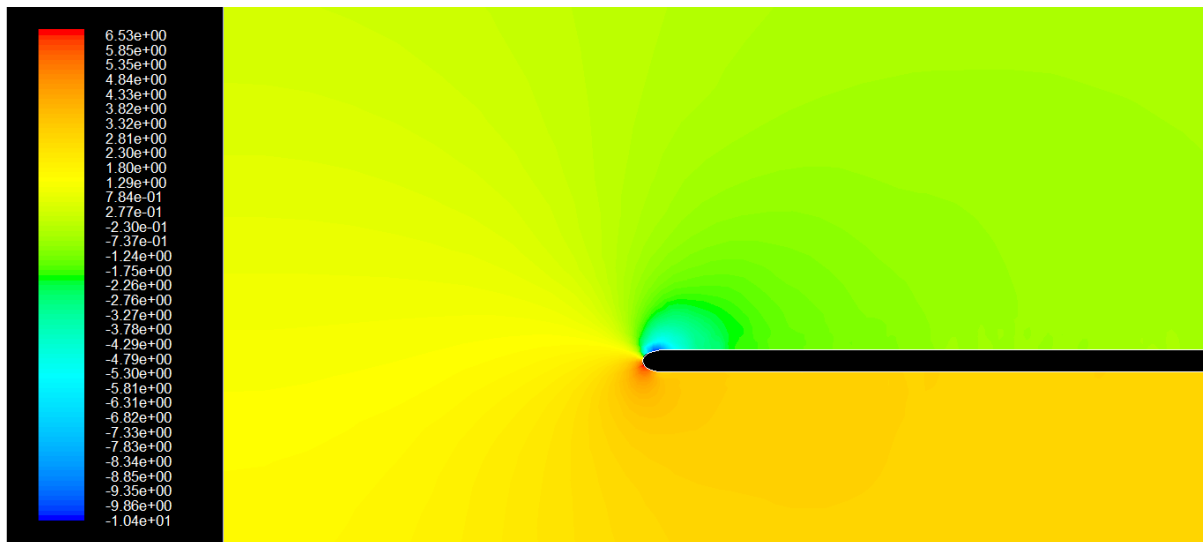


Figure 3-8 - Pressure contours for stagnation migration example [Pa - gauge]

However, once the flap was locked in the location determined by following the procedure outlined with the smoke generator, it was found that turbulent spots were observed towards the leading edge in the hot-wire signal traces. These turbulent spots may have been the result of an undetectable separation bubble, or perhaps the effects of local separation elsewhere on the span propagating across to the measurement plane. As such an alternative approach was adopted for the zero and negative pressure gradient sections where the tunnel was set to a target velocity and then the flap adjusted until the flow signal traces at the leading edge were void of turbulent spots. In reality this method was more robust and more practical and didn't have the drawback of polluting the laboratory with smoke which in turn would instil downtime and have an adverse effect on other users of the laboratory.

The flap design was unable to provide adequate diffusion for the positive pressure gradient section and, as such, grids were placed at the outlet of the tunnel in order to offset the pressure gradient by the pressure loss generated by the grids themselves. This had the immediate effect of migrating the stagnation line to the measuring surface, which could then be realigned with respect to the major

axis of the elliptical leading edge by adjusting the aforementioned flap and hence modulating the angle of attack of the approach flow.

The main features of the swept flat plate are summarised in the following schematic of Figure 3-9 where the spanwise location relative to the spanwise datum of each of the measuring planes (for pressure and the hot-wire measurements) have been clearly indicated.

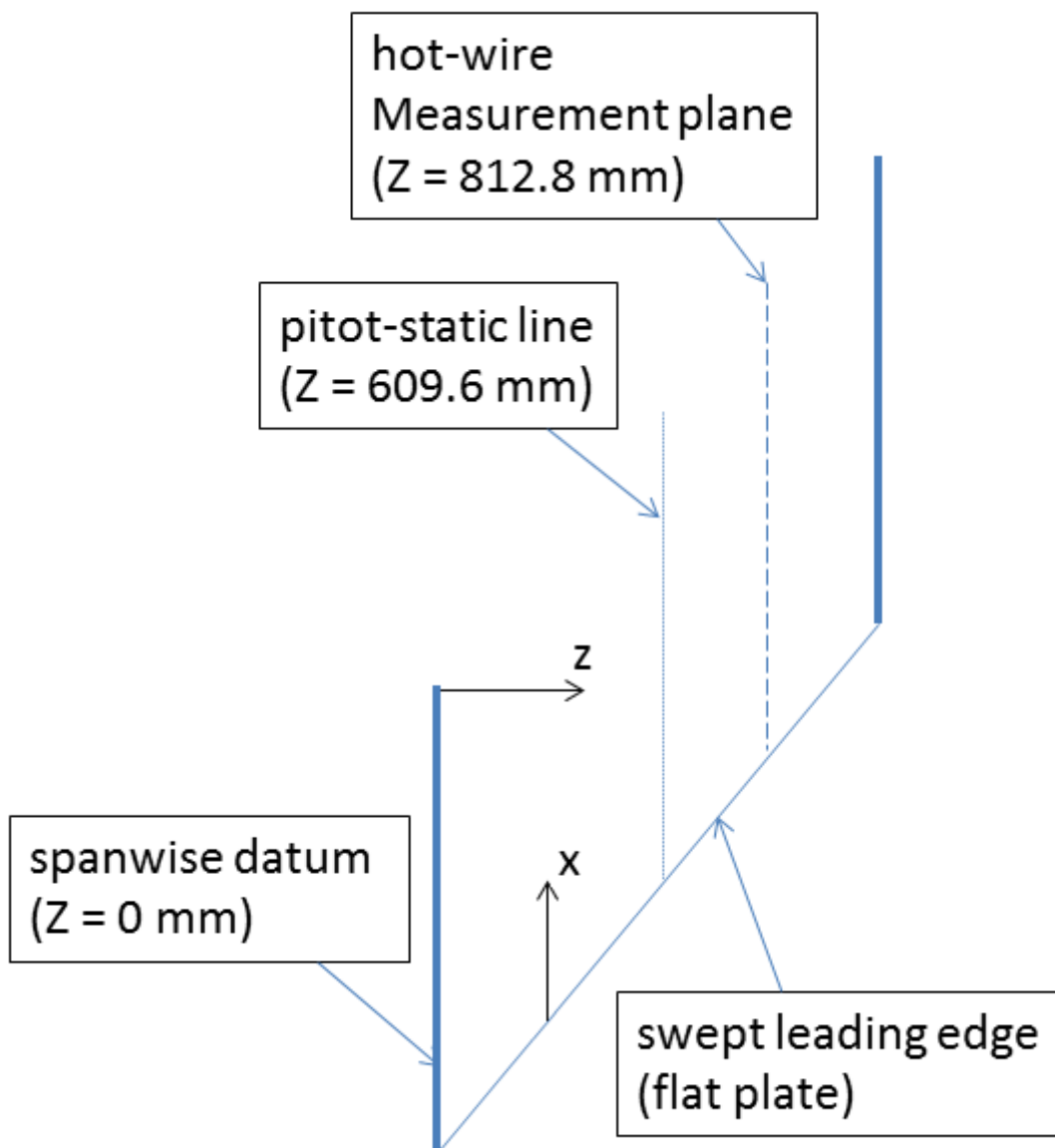


Figure 3-9 - Schematic highlighting the main features, reference and measurement locations for the swept flat plate

3.3 Turbulent Grids

All experimentation was carried out using three 'grid' configurations. These are referred to as the 'vertical', 'square' and 'zero' grid cases (G3, G1 and G0 as their coded titles) which correspond to approximately 3.25, 1.25 and 0.25% freestream turbulence intensity at the leading edge along the measuring plane; hence $X = 0\text{mm}$, $Y \rightarrow 44\text{ mm}$ (maximum traverse displacement, y_{\max}), $Z = 812.8\text{ mm}$. Given that the cut off for bypass transition is generally considered to occur at 1% turbulence intensity (Mayle (1991)) these tests can be compartmentalised into two cases of bypass transition ('vertical' and 'square') and one of natural transition ('zero').

The 'zero' grid configuration, as the name suggests, was simply where the gap between the exit of the compressor and the entrance of the test section settling chamber was left open.

The bypass turbulent grids, 'vertical' and 'square', were housed within frameworks constructed to the specification detailed in Figure 3-10. Each framework was held firmly in place by clamping the protruding support legs to the main framework of the tunnel with 40 mm wooden packers wedged in such that the free cross-section of the grid support frame was concurrently aligned with the exit of the compressor and the inlet to the test section.

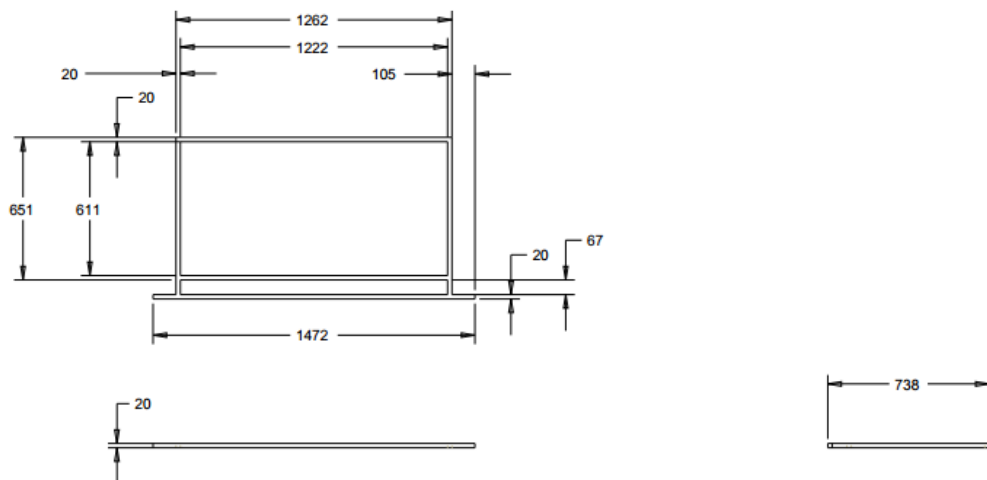


Figure 3-10 - Grid assembly for housing meshes [mm]

The 'square' grid (Figure 3-11) contained 3.175 mm (1/8") rods oriented both vertically and horizontally in the frame with 15.875 mm (5/8") pitch – both with 12.7 mm open spacing, whereas the 'vertical' grid (Figure 3-12) housed steel rods of 15.875 mm diameter (5/8") oriented vertically only and spaced at 50 mm pitch horizontally. Rather than 'zero', 'square' and 'vertical' a naming convention of G0, G1 and G3 has been adopted for the presentation of the results in Chapter 4.

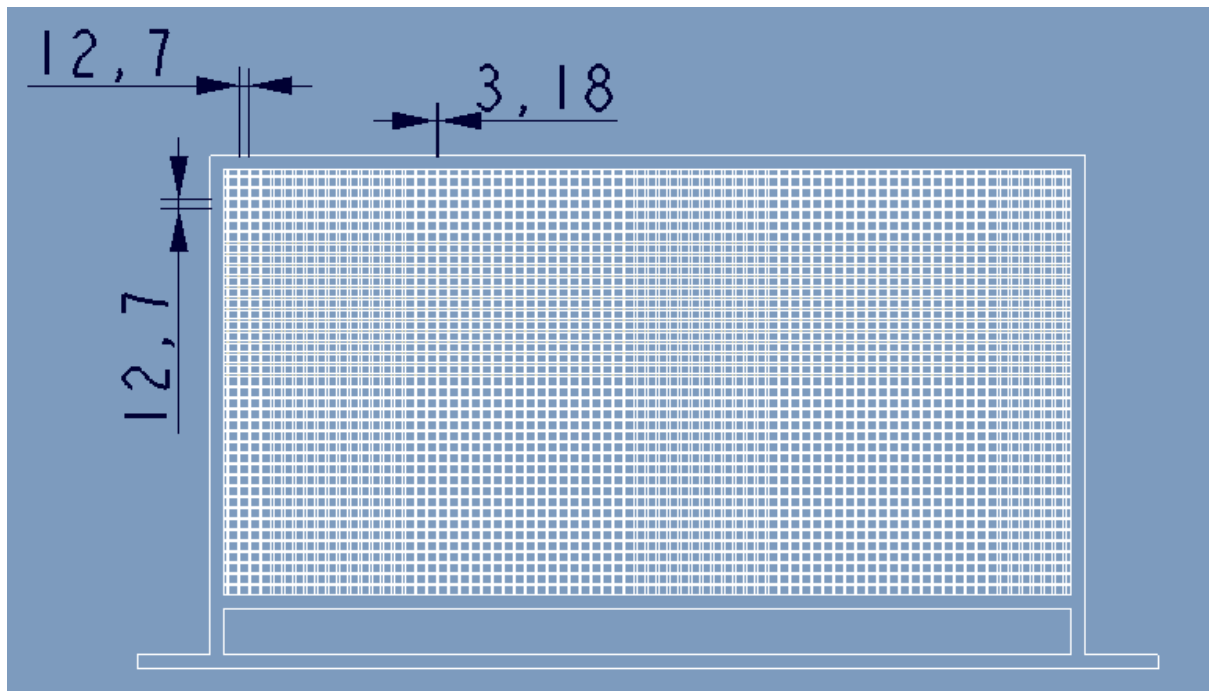


Figure 3-11 - Square mesh dimensions inside grid framework [mm]

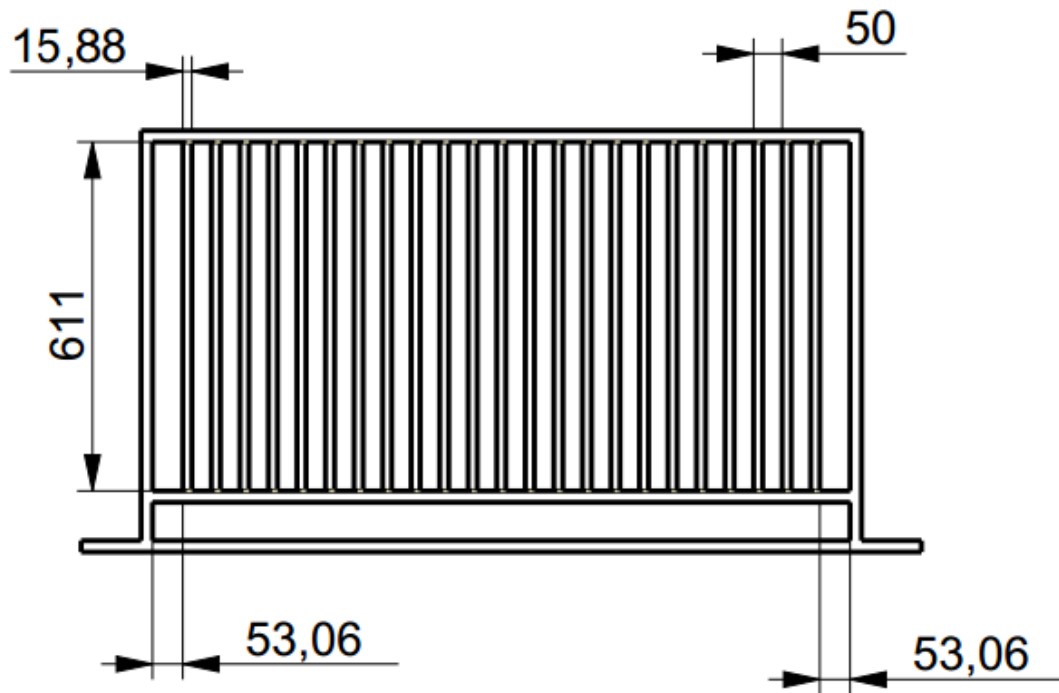


Figure 3-12 - Vertical mesh dimensions inside grid framework [mm]

As mentioned in section 3.2 the flap for controlling the approach flow direction with respect to the leading edge was unable to provide sufficient diffusion and hence extra turbulent grids at the outflow of the tunnel were utilised. The mesh dimensions for the outflow grids were to the same specification as those of the 'square' grid only some felt was sewed around the perimeter of the outflow grids owing to the sharpness of the elements. The felt acted as a barrier primarily to protect the user from injury and to prevent scratches or grooves being carved into the flat plate. The outlet grids were held in place through 4 x 8" (20.32 cm) G-clamps.

3.4 Section Sidewall Profiles and Design

This section provides details regarding the aerodynamic specifications of the sidewall profiles for each of the pressure gradient sections and, in addition, some of the mechanical considerations, mainly regarding rigidity and accessibility.

Earlier it has been indicated that there were three pressure gradient sections considered for the experiments in this thesis; these being the straight, diverging and converging sections from a topological perspective. Aerodynamically these are then referred to as the nominally zero (Z), positive (P) and negative (N) streamwise pressure gradients. These names are specifically chosen to be aerodynamically neutral from the perspective that the dominant primary modes of transition were unknown a priori and as such the use of 'adverse' and 'favourable' terminology, as is common in unswept boundary layer transition, is avoided. As a complete example the case for positive pressure gradient (P) with the square mesh (G1) was assigned the code G1P.

The straight section comprised two parallel sidewalls made from 12 mm thick plywood of 500 mm in height and 2.8 m in length. These were assembled in an aluminium framework which was fitted with a gasket of felt fabric fitted between the framework and the plate such as to avoid scratching the plate. This felt gasket was also originally installed so that the entire framework could be hinged both for gaining access to the plate section and also such that the framework could readily be adjusted depending on which section was fitted at that moment in time. However, in eventuality this system was not employed and individual assemblies were manufactured for each section.

Each section was fitted with its own straight roof each of which were comprised of sub-sections and screwed into the sidewalls in order to be firmly fixed in place. The joins of the roof sub-sections were spanned by lateral supports external to the working section flow to increase rigidity. The entire straight section assembly is rendered in the Pro/ENGINEER CAD drawing of Figure 3-13.

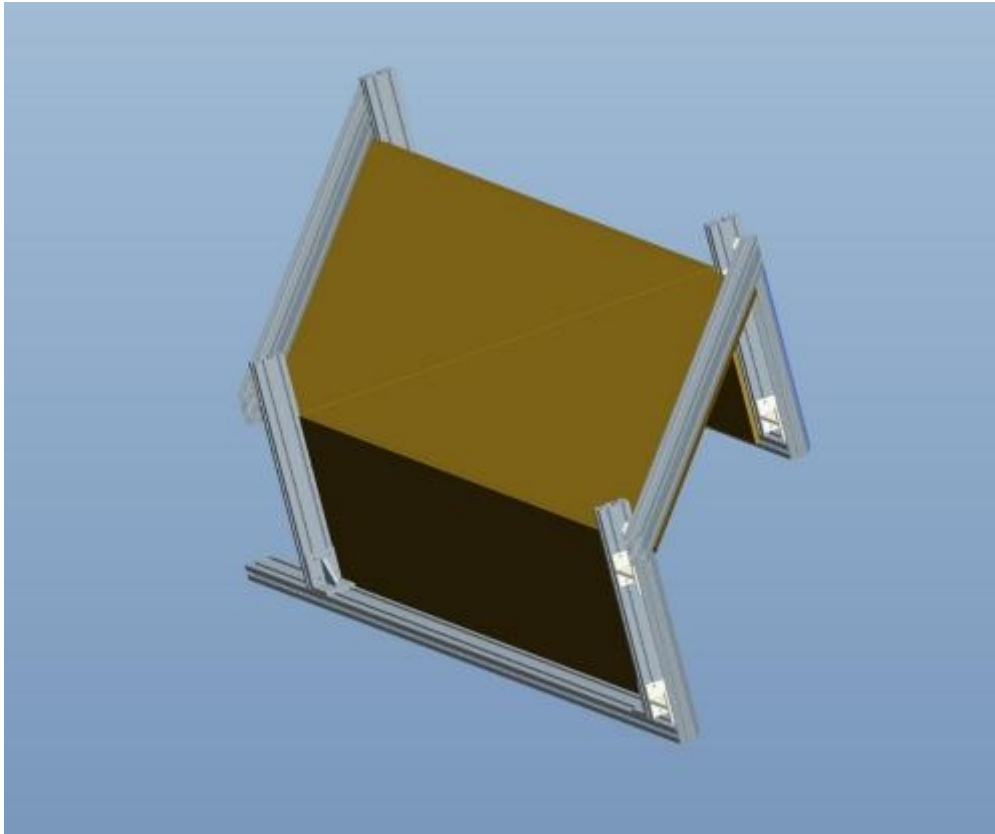


Figure 3-13 - Straight section framework with roof and sidewalls

The two non-orthogonal sections – i.e. the diverging and converging sections require more detailed explanation from a design perspective. One of these sections is displayed in the Pro/ENGINEER CAD model in Figure 3-14. The curved sidewalls were braced externally to the flow inside the working section and the sidewalls fitted to the bracing by screws from within the test section.

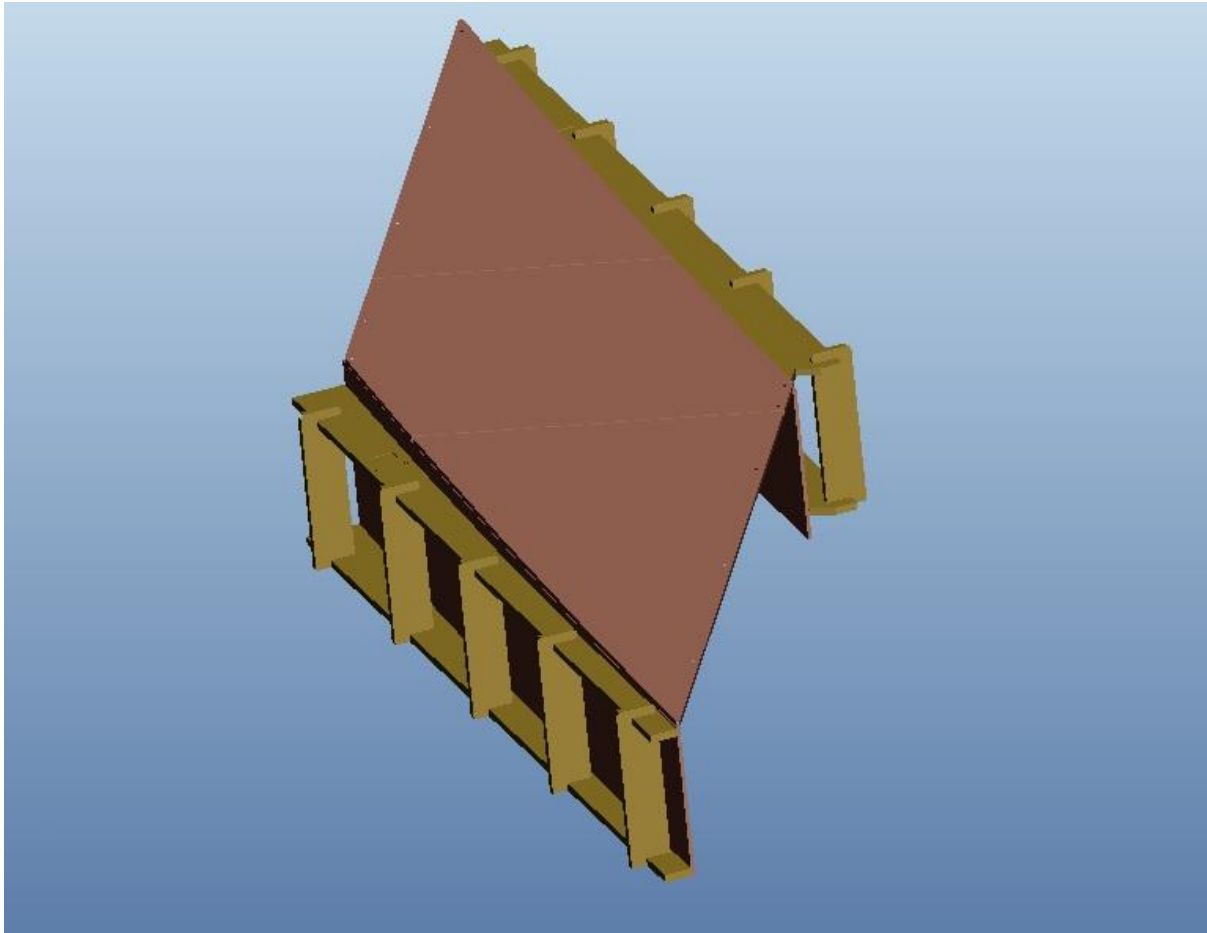


Figure 3-14 - Curved sidewall framework for diverging (positive) section with roof sub-sections

One can observe from Figure 3-14 in addition to the curved sidewalls that the roof is also diverging from the plate and hence there is an increase in the free cross-sectional area which for an inviscid steady subsonic flow will result in diffusion (deceleration). It should also be noted that although the sidewalls are curved they remain parallel to each other with respect to the sweep angle of the leading edge of the flat plate.

The parallel nature of the sidewalls is a direct result of how the test sections were designed using the following procedure which aims to maintain a constant crossflow velocity tangential to the leading edge but impose an acceleration or otherwise with respect to the velocity magnitude normal to the leading edge.

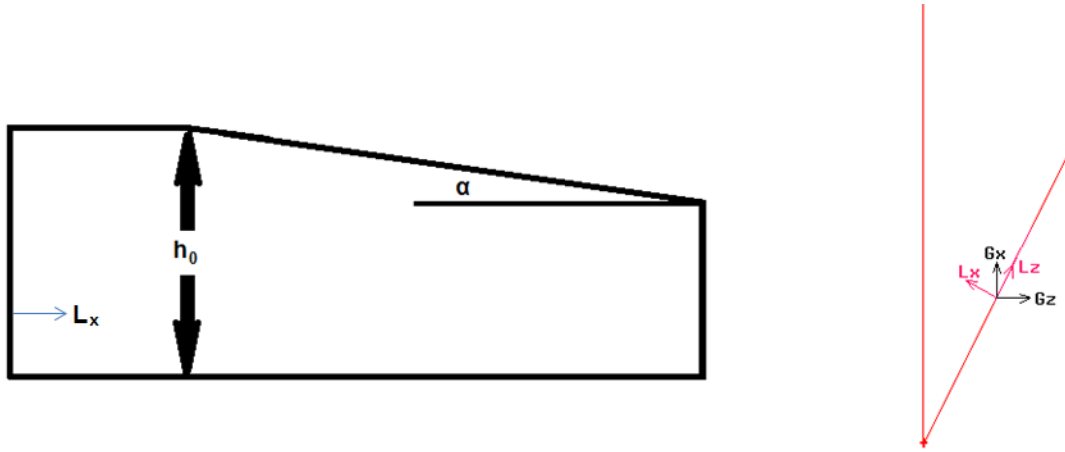


Figure 3-15 - Tunnel roof profile (left) with freestream and tunnel Cartesian coordinate systems (right)

When deriving the curvature of the mean line of each section firstly one must consider the most convenient choice of coordinate systems and these are illustrated in Figure 3-15 as (G_x , G_y , G_z) and (L_x , L_y , L_z) where the 'L' Cartesian coordinate system has been rotated 60° around the y axis such that L_z is tangential with the leading edge of the 60° swept plate (i.e. $\phi = 60^\circ$).

$$G_x = L_x \cos \phi + L_z \sin \phi \quad \text{Equation 3-1}$$

$$G_z = L_x \sin \phi - L_z \cos \phi \quad \text{Equation 3-2}$$

$$h(L_x) = h_0 - L_x \tan \alpha \quad \text{Equation 3-3}$$

Appealing to a conservation of mass equation (with spanwise invariance in the profile, i.e. fixed width relative to the leading edge) yields;

$$U_1 h = U_0 h_0 \cos \phi \quad \text{Equation 3-4}$$

$$U_1 = \frac{dL_x}{dt} = \frac{U_0 h_0 \cos \phi}{h} = \frac{U_0 h_0 \cos \phi}{h_0 - L_x \tan \phi} \quad \text{Equation 3-5}$$

$$\int_0^{L_x} (h_0 - L_x \tan \phi) dL_x = U_0 h_0 \cos \phi \int_0^t dt \quad \text{Equation 3-6}$$

$$\frac{L_x^2}{2} \tan \alpha - h_0 L_x + U_0 h_0 t \cos \phi = 0 \quad \text{Equation 3-7}$$

Where the pertinent solution to this quadratic equation is;

$$L_x = \frac{h_0 - \sqrt{h_0^2 - 2U_0 h_0 t \cos \phi \tan \alpha}}{\tan \phi} \quad \text{Equation 3-8}$$

and

$$L_z = U_0 t \sin \phi \quad \text{Equation 3-9}$$

When the L coordinates are calculated with respect to the chosen convergence angle, α , initial section height, $h_0 = 500mm$, and inlet velocity then these values can be substituted back into the G coordinate equation system so as to what extent the mean span of a converging or diverging section will deviate from the approach flow direction upstream and any change in cross section.

Just from observing the coordinate systems alone one can understand that accelerating the flow normal to the leading edge will result in the freestream turning to the portside, whereas a deceleration will produce the opposite effect.

The sections were carefully chosen with the following constraints in mind;

- Avoid separation in the diverging case by setting $\alpha > -8^\circ$
- Try to make use of as much of the plate as possible
- Minimum outlet height of 400 mm to allow for physical access to the test section by the user
- Only 15 cm of plate was available on the diverging side relative to the straight section settling chamber since this plate was originally designed for very strong converging sections which turn in the opposite direction
- Ideally the same convergence angles would be utilised

Eventually it was decided that 3° was the most suitable choice of convergence angle (-3° for the diverging case) based on an equivalent residence time for the flow through each section. This choice of convergence angle was somewhat conservative from a purely aerodynamic perspective but practically speaking it was ideal for two main reasons. Firstly space was very limited on the starboard side of the plate (from the perspective of the approach flow) and as such a more severe negative convergence angle would restrict the length of the section further. Secondly this choice utilised a relatively high proportion of the plate and, in the converging case, still was able to afford sufficient space for access to the test section such that the traverse could be positioned in its appropriate station for each measurement.

The following figures, Figure 3-16 and Figure 3-17, outline the topological distributions throughout the two non-zero pressure gradient test sections.

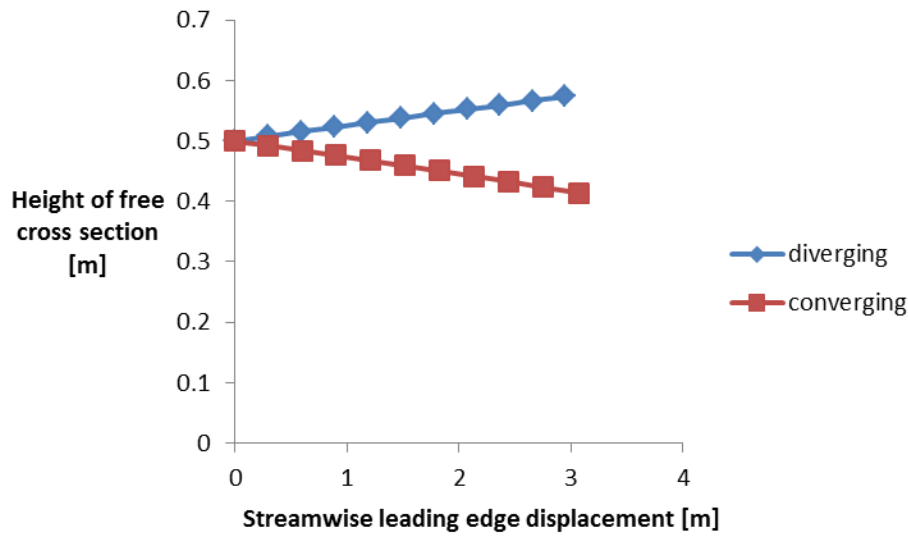


Figure 3-16 - Free cross section height profile

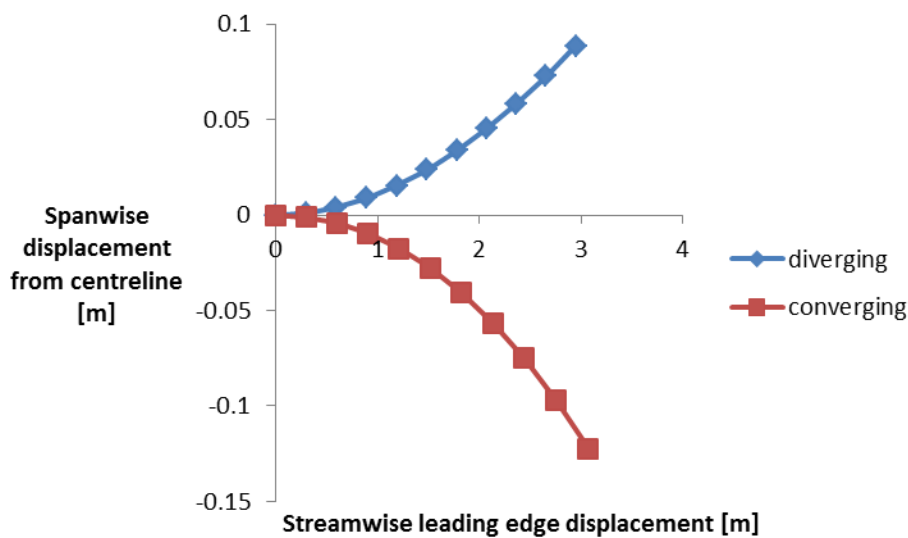


Figure 3-17 - Spanwise profile for meanline of sections

One can observe from Figure 3-16 that the length of the converging section is slightly longer than the diverging section, owing to the residence time being fixed in the design phase and continuity dictating that fluid particles will travel further for the same time period in the converging section. Furthermore one can observe that the height of the section varies in a linear manner and as such a straight roof section was easily fitted. Additionally one can also observe in Figure 3-17 that the sections deviate from the centreline of the tunnel in different relative spanwise directions and that

the maximum spanwise displacement of the diverging section was less than 15 cm as required. This choice also offered space for the support framework for the sidewalls to be supported directly by the plate structure itself without needing any additional support structure. A screenshot from a Pro/ENGINEER CAD model is provided in Figure 3-18 which illustrates the manner in which the completed sections are retrofitted to the outlet of the tunnel.

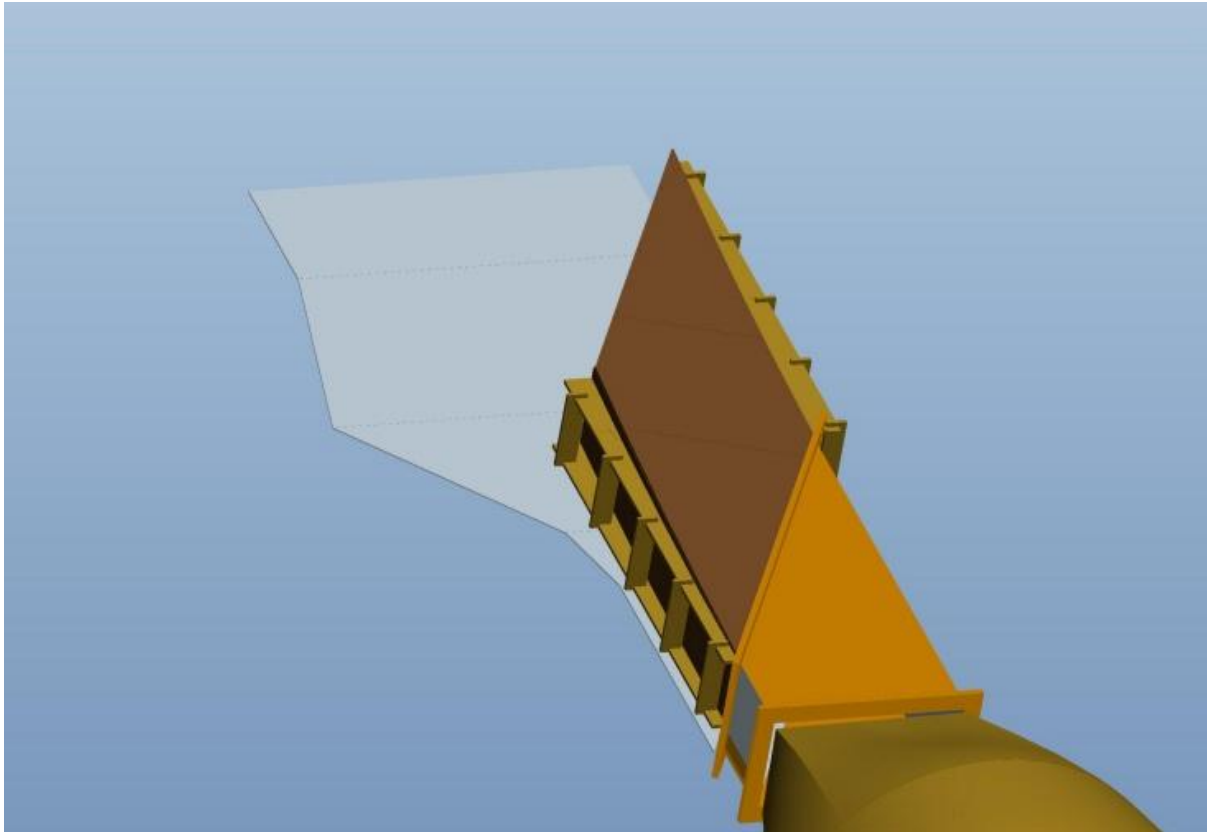


Figure 3-18 - Assembled CAD model of diverging section fitted to tunnel



Figure 3-19 - View of leading edge through Perspex side window

Figure 3-19 shows a view of the leading edge, static pressure tapings and the control flap for adjusting the relative diffusion on either side of the plate (see Figure 3-5) through the starboard sidewall upstream of the test sections which is made from transparent Perspex. This viewing facility offered by the Perspex sidewall was also used to determine the proximity of the probe to the plate through the use of a cathetometer (see section 3.6).

It would perhaps have been possible to narrow the entire working section of the wind tunnel with the use of foam curved into the respective profiles and place the roof on a hinge but this option was not explored owing to concerns regarding structural integrity and furthermore the impact regarding the loss of visibility of the traverse from outside the working section.

Table 3-1 summarises the experimental parameters with respect to a unique code where the deflection of the flap is measured on the portside of the tunnel and defined as being the plum line displacement between the underside of the plate and the corner of the steel trailing edge structural flap on the leading edge control flap. As an example the code G1N pertains to the case where the ‘square’ turbulence generating grid (nominally 1% turbulence intensity) was placed upstream of the leading edge, the converging negative pressure gradient (NPG) section was fitted on top of the plate, the trailing edge of control flap was displaced 91 mm from the bottom surface of the plate and no outlet grid was utilised.

Table 3-1 - Codes for test section combinations detailing experimental parameters

Code	Turbulent Grid	Pressure Gradient section	Flap Deflection [mm]	Outlet Grid
G0Z	no grid	ZPG	100	No
G1Z	square grid	ZPG	100	No
G3Z	vertical grid	ZPG	100	No
G0P	no grid	PPG	100	Yes
G1P	square grid	PPG	100	Yes
G3P	vertical grid	PPG	100	Yes
G0N	no grid	NPG	100	No
G1N	square grid	NPG	91	No
G3N	vertical grid	NPG	81.5	No

3.5 Inclined Manometer

As part of the experimental apparatus an inclined methylated spirit manometer with a pitot-static tube was utilised to calibrate the hot-wire probes used in conjunction with the CTA’s. The inclined manometer was, in effect, a conduit for the Validyne pressure transducer systems which were eventually used for measuring the airspeed within the working section. Prior to the use of the inclined manometer as, effectively, a calibration tool, a Baratron differential pressure transducer, available in the rheology laboratory at the University of Liverpool was utilised however, in practice, this approach suffered from two major drawbacks. Firstly, the smallest differential pressure available

(circa. 120 Pa) was too large with respect to those which would be measured in the actual wind tunnel experiments. Secondly, the act of transporting the Validyne pressure transducer from one laboratory to another seemed to be enough to result in a significant offset from the actual calibration. This was perhaps related to the fragility and sensitivity of the diaphragms utilised in measuring such small differential pressures in response to whatever forces were exerted on the equipment.

Owing to these difficulties experienced, an inclined manometer was used instead to effectively calibrate the Validyne pressure transducers utilised for recording the tunnel airspeed and measuring the streamwise static pressure distribution. This approach involved setting the tunnel for at least 30 different motor speed settings with the pitot-static tube tapped to the inclined manometer and then repeating for the same motor speed settings with the tappings swapped around to whichever Validyne transducer was being calibrated at the time. Furthermore, concurrent to this the hot-wire traverse itself would be placed in the calibration position and voltages recorded at each of the motor speed settings such that, firstly, any hysteresis in the motor speed settings could be observed and, secondly, to then use the recorded hot-wire voltages with respect to the measured freestream velocities as a perfectly valid calibration of the hot-wire itself. Please note however that the hot-wires were calibrated for each grid configuration, whereas the Validyne pressure transducers were only calibrated once per section, i.e. three times in total. Whilst this approach was certainly not perfect the calibration itself was achieved with differential pressures that were relevant, as in within the order of the highest tunnel speed settings, to those of the experiments and the AC transducer units were not physically interfered follow the calibrations made before each round of experiments.

3.6 Cathetometer

Hot-wire probes are notorious for their fragility; as a general rule if one touches the wire in just about any manner, then it's more than likely to be broken. They are very susceptible to failure, even with something as seemingly benign as dust and particle impacts. Hence in order to measure the initial height of the hot-wire probe to the plate in an effective manner where the probe was not susceptible to damage a cathetometer was utilised. This equipment (see Figure 3-20) takes advantage of the fact that the aluminium flat plate test surface is highly smooth, polished and therefore highly reflective. By aligning crosshairs on the travelling telescope of the cathetometer to both the incidence and reflective images of the hot-wire probe, and measuring the displacements thereof, one can determine the proximity to the plate by halving this distance. This was achieved externally from the working section of the wind tunnel on a standard flat workbench, owing to the advantage that the sidewalls of the working section upstream of the leading edge were made from transparent Perspex. This external approach ensured that the feet of the cathetometer would not cause any damage or scratching of the flat plate surface.



Figure 3-20 - Cathetometer (travelling microscope) used to measure hot-wire wall-normal proximity

3.7 Traverse Gear and Template

The traverse used for each hot-wire measurement possessed one degree of freedom (pitch) and the entire assembly consisted of a stepper motor driving a jack screw which would, in turn, pitch the probe assembly (holder, 55P15 probe and support) about the traverse spanwise axis. The majority of the traverse assembly and template, less the lines for the vacuum pump are rendered in Figure 3-21 (left), through the Computer Aided Design Pro/ENGINEER Wildfire 5.0 package where the convention for the bearing angles, with respect to the direction of the approach flow in the freestream are clearly highlighted. With the flow resolved using a minimum of three bearing angles the mean flow angles of the skewed flow could be determined by locating the maximum velocity in the profile. The resolved mean flow angles using this method have been presented and discussed in sub-section 4.2.3 for one specific case (G0Z). With the mean flow angle and velocity magnitude established it is possible, thereafter, to break this down into individual u and w components with simple trigonometry and the assumption that the v component of velocity is negligible. The

associated uncertainties in resolving the mean flow angles using this method are later discussed in 3.16.2.

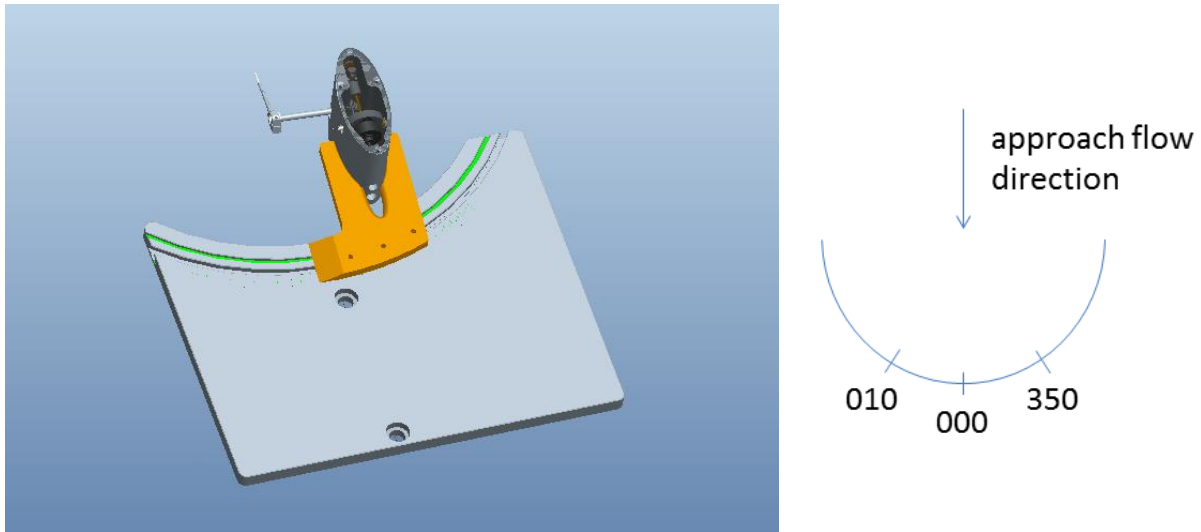


Figure 3-21 - Pro/ENGINEER model of traverse and positioning template (left) and bearing angle convention highlighted with respect to the approach flow direction (right)

All of the arms, yoke and stepper motor equipment were housed in an elliptical aluminium section, of 80 mm and 30 mm external semi-major and semi-minor axes, and then connected electrically to a stepper controller through one of the two outlet ports on the trailing edge of the elliptical housing, the other port being occupied by the cabling which powered the stepper motor. The traverse was fixed to the flat plate surface via a vacuum pump (tapped to the other outlet at the trailing edge) providing -0.85 bar of (suction) pressure with a single rubber compliant gasket ensuring an excellent, rigid seal and negligible gap between the mating surfaces of flat plate and traverse underbelly. This was equivalent of roughly 70kg of downward force (including the weight of the traverse). The vacuum pump was driven by compressed air supplied through one inlet valve for two outlet valves, one connected to the traverse and the other to the traverse template which was used to position the probe on the plate at appropriate streamwise and spanwise coordinates and station angles.

It should be noted that whilst the traverse was held as an asset unique to this project the design was inherited from that of recent 2-D boundary layer work (Zografakis (2013)), in the same suction

tunnel previously used by Abu-Ghannam and Shaw (1980). As such it presented some additional limitations in that the centreline of the probe was not concurrent with the centreline of the stepper motor housing, with an offset of 95 mm. Furthermore the use of an elliptical profile meant that the tunnel blockage would alter significantly when skewing the traverse around the normal axis in an attempt to resolve the mean flow angles in the tunnel. The length of the probe arm from the probe measuring volume to the axis of rotation was approximately 100 mm. Given that the axis of rotation was offset by 35 mm from the leading edge of the traverse gear, this resulted in the probe measuring volume being displaced by approximately 115 mm from the leading edge of the traverse gear.

The stepper motor was driven via a MSD415 microstepping drive housed in what is referred to as the stepper controller. The stepper controller was interfaced with digital outputs through a USB-6009 National Instruments data acquisition card which was programmed to send software-timed digital pulse trains in LabVIEW 8.5 along the 'step' line in order to pitch the probe in step increments, with respect to the direction (nose-up or nose-down) requested on the 'direction' line. These increments were determined to be the equivalent of 51.5 micron displacements along the normal axis, based on the average of 5 cathetometer measurements, each comprising 100 pulses. The MSD415 would cause the stepper motor to pulse by one step with each rising edge of the pulse train. The MSD415 required that the pulse width of each square wave in the pulse train be greater than 1.5 ms for reliable response (see MCP (2009)) but since absolute speed was not a particular concern in this case, given that the sampling time for each measurement was several orders of magnitude larger than overall pulse train length, the pulse width was kept constant at 10 ms. Furthermore it was also ensured that voltage signals would not be recorded from the CTA until the pulse train was completed.

The maximum consecutive number of pulses, in any direction, was measured to be just over 850 before either the wire would strike the plate or the jack screw would run out of range by fouling the

inside of the elliptical assembly and, hence, 850 pulses were used (43.775 mm total displacement) for each boundary layer and freestream traverse combined. It would have been possible to reduce the number of wall-normal measurement locations in each traverse towards the leading edge, where the boundary layers were thin and a sustained plateau in standard deviation outside the boundary layer is observed, but this shortcut wasn't taken as there could still be extra information discernible regarding the mean flow angles in the freestream, for example.

Each traverse, irrespective of streamwise, spanwise tunnel coordinates and station angle spanned the aforementioned 850 pulses, distributed through 100 wall-normal increments, which took the following form, where i = increment number (zero indexed). The pulses for each increment are stated explicitly in Equation 3-10 (and Table 3-2) and one can see that the algorithm both successfully maintains a high resolution in the near wall region and maximises the available displacement of the traverse by reaching a cumulative total of 850 pulses.

$$\frac{\text{pulses}}{\text{increment}} = \text{int}(0.49 \times e^{0.043547i}) \quad \text{Equation 3-10}$$

Table 3-2 - Number of pulses per increment

Iteration loop number	Stepper motor pulses
0	0
1 - 25	1
26 - 37	2
38 - 45	3
46 - 50	4
51 - 55	5
56 - 59	6
60 - 62	7
63 - 65	8
66 - 68	9
69 - 70	10
71 - 72	11
73 - 74	12
75 - 76	13
77	14
78 - 79	15

80	16
81 - 82	17
83	18
84	19
85	20
86	21
87	22
88	23
89	24
90	25
91	26
92	27
93	28
94	29
95	31
96	32
97	33
98	35
99	37

The template was designed such that the traverse could theoretically be set to any station angle either side of the centreline and it was always removed from the tunnel after the traverse was set at the desired combination of streamwise, spanwise coordinates and skew angle. The template was designed so that the sensing element of the probe was positioned at the centre of the arc swept by the traverse and as such the streamwise and spanwise probe coordinates would remain constant irrespective of the skew angle selected.

The mean flow angles generated by the sweep were resolved through adopting the following procedure with respect to the operation of the traverse and template, in similar accordance to the procedure used previously by Ramadan (2000). Firstly a minimum of three skew angles (with zero skew always included) were selected such that a velocity profile with respect to skew could be obtained. A unique profile was obtained at every wall normal coordinate by linearly interpolating the mean velocities to the zero skew measurement locations. These corrected velocity profiles were then fitted to a function of the following form as suggested by Bruun and Tropea (1985);

$$f(\lambda - \chi) = \cos^n(\lambda - \chi) \quad \text{Equation 3-11}$$

Where λ is the probe angular position and χ is the mean flow direction. Note as well that this cosine function reaches a maximum where the probe angular position (skew angle) and mean flow direction are coincident, i.e. $f(0) = 1$. Such that the values were scaled to their respective maxima the following function (Equation 3-12) was optimised using the Levenberg-Marquardt least squares fit algorithm in LabVIEW.

$$u(\chi) = u_{max} \cos^n(\lambda - \chi) \quad \text{Equation 3-12}$$

Where the following are equivalent; $a1 = u_{max}$; $a2 = \lambda$; $a3 = n$. Thereafter $a1$ and $a2$ approach the mean flow velocity and mean flow angle and the arbitrary constant $a3$ (n) for each profile is not of any physical concern and is determined for each profile independently. The success of this procedure is thoroughly analysed in chapter 4.

3.8 Pitot-Static Tube (Validyne)

Freestream velocities inside the working section of the tunnel were measured using a combination of pitot-static tube (visible in Figure 3-19), linearised analogue output voltages of a CD223 Validyne pressure transducer system and USB-6009 DAQ (interfaced with a PC). The Validyne system comprised DP15 AC transducers with the excitation being provided by the CD223 box. The 3-20 diaphragms used for these measurements were capable of measuring up to 0.125 psi (862 Pa) – see Validyne (2013) in full scale and were calibrated using a Baratron differential pressure system prior to each round of experiments, whereafter corrections for the zero flow voltage (largely due to drift in ambient conditions) were made in software, with the assumption that the gain remained unchanged.

These calibration measurements were also compared with the differential pressure across an inclined manometer, with the same pitot-static tube and shown to exhibit very similar Pa/V slopes.

The pitot-static tube was fed through a hole in the roof of the straight section settling chamber (700 mm straight section above the leading edge for all tests) and aligned with the streamwise axis of the tunnel at a wall-normal displacement of 250 mm, where the tube was fixed in place with a retort stand. The nose of the pitot-static tube was placed at an equivalent streamwise displacement of 100 mm along the measuring plane, only the tube was aligned with the centreline and therefore the streamwise static pressure tapings, rather than the measuring plane. Ultimately there should be minimal spanwise variations in the straight section settling chamber, particularly at wall-normal displacements around two orders of magnitude larger than the local boundary layer thickness.

3.9 Constant Temperature Hot-Wire Anemometry – CTA Boxes (54T30 & StreamlinePro)

All experiments for this thesis, in terms of the constant temperature anemometers and associated cabling etc., were supplied by Dantec. A different anemometer specification was used for one of the tunnel sections – ZPG from those of the non-zero pressure gradient sections. The ZPG tests, for each of the three grids, were conducted with a 54T30 miniature-CTA, whereas the NPG and PPG experiments utilised a Dantec StreamLine Pro system. The StreamLinePro CTA is considered to be a higher quality research-oriented device, relative to the 54T30 miniature CTA and, hence, when it became available it was utilised thereafter.

3.9.1 54T30 Miniature CTA Experimental Configuration

A Dantec 54T30 miniature CTA system was utilised for the experiments that were performed on the straight section, owing to the fact that it represented the only available choice at the time. These single-channel CTA systems are effectively interfaced by the user on a hardware level through the manipulation of jumpers, switches and pots for the selection of gain, offset and decade resistance and the output impedance is quoted as being 50 Ω (Dantec (1999)).

The feedback gain pot was maximised which did not result in any dynamic problems with the 55P15 wires and hence was left as such throughout all testing and the jumpers were left so that no hardware filtering, gains or offsets were triggered. As previously mentioned the CTA box contained two arrays of switches which act to set the decade resistances, termed SW1 and SW2, which are effectively the coarse (former) and fine (latter) adjust. These switches, in effect, denote a 4-bit decimal-binary conduit representing multipliers from 0-15. For 55P15 probes the coarse setting, SW1, should for all practical purposes be set to 0011, which corresponds to 3 x 20, i.e. 60 Ω . This will then be added in series to an in-line resistance of 80 Ω and the product of the fine adjust SW2 multiplier and 1.4 Ω . Hence if SW2 is set to 0100 then the total SW2 resistance will correspond to 5.6 Ω and the overall decade resistance to 80 + 60 + 5.6 = 145.6 Ω . One can then make fine adjustments using SW2 to achieve a target overheat ratio (0.8 for all experiments in this thesis) where the temperature-based overheat ratio is defined as follows;

$$a = \alpha_{20}(T_w - T_{amb}) \quad \text{Equation 3-13}$$

Given that the cold resistance of a 55P15 probe is around 3.5 Ω the wire temperature (through setting the decade resistance) would always be below 250°C for typical laboratory ambient temperatures. However the absolute temperature value was always checked to ensure that this was the case. Higher wire temperature settings (towards 300°C) can result in improved frequency

response but it will also accelerate the oxidation, and therefore degradation, of the wire.

Furthermore too high a wire temperature will simply burn out the wire and result in breakages.

These 54T30 CTA systems have 10kHz bandwidth (Dantec (1999)) which coincides with the very common selection of sampling frequency of 10kHz for hot-wire measurements and hence aliasing concerns regarding the folding/Nyquist frequency could be allayed. That said it was observed that there were some noise issues perhaps owing to the fact that Dantec issues the 54T30 miniature CTA's with 12V power supplies which utilise switch-mode voltage regulators. That is to say excess DC voltage downstream of the transformer, rectifier and smoothing is sloughed off through high frequency pulse switching, such that the target voltage of 12 V is obtained. Switch mode regulators are simpler and more efficient but the quality of the output relative to their linear counterparts is somewhat inferior. The noise generated by the power supply is graphically illustrated in Figure 3-22;

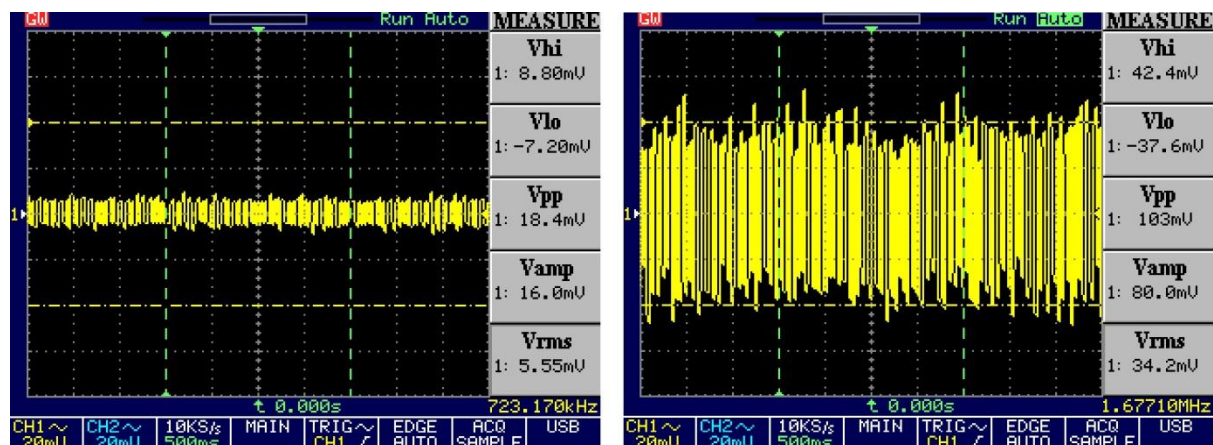


Figure 3-22 - AC coupling; battery (left) vs. mains (right)

Figure 3-22 was produced by capturing screenshots of an Instek GDS-820S 8-bit digital storage oscilloscope through its respective USB output interface combined with the FreeView software Instek (2009). The voltage probe of the oscilloscope was set to measure the potential difference of the top-bridge voltage for zero flow with the oscilloscope set to AC-coupling so as to offset the mean DC component and in effect quantify the noise content as a root mean square value. Here it was

observed that the noise content was substantially less when operating the 54T30 with a 12V battery as opposed to the factory 12V mains supply, 5.55mV (rms) vs. 34.2mV. Thereafter an A512 12V lead acid (6.5 Ah capacity) secondary (rechargeable) battery was used for all experiments conducted with the 54T30 miniature CTA.

Since the current drawn by the 54T30 CTA was typically less than 100mA it was possible to adopt a different recharging approach to optimise the battery life (by minimising discharge cycles and increasing the depth of discharge) given that with such current a full charge (6.5 Ah at 12 V) should last approximately 65 hours. However, this would involve keeping a meticulous record of battery usage where any errors could result in erroneous recordings or, worse still, damage through weak voltage. Hence the approach was adopted of the battery being recharged overnight after every day of testing using a variable bench power supply with the charging current hard-limited to approximately 1 A.

3.9.2 StreamLine Pro CTA Experimental Configuration

A Dantec StreamLine Pro CTA was utilised for both non-zero pressure gradient configurations – the negative and positive pressure gradient sections. The StreamLine Pro system is a generic anemometer which is capable of supporting multiple modules for multi-wire probes and works by supplying each module through linear regulation (Dantec (2011)), hence in contrast to the 54T30 miniature CTA, which by default is also a mains powered device, the electrical noise is considered to be much less of an issue, hence in part (and basis for) the claim to be a more research-oriented device (Dantec (2011)). The anemometer itself also works on the basis of the constant temperature/resistance principle and was run with a 1:20 bridge ratio. This principle is further discussed in section 3.12.

The StreamLine Pro system comes as a package with its own software, perhaps aimed at those who are performing the most common hot-wire routines and for those who have also purchased the adjoining Dantec calibration equipment for example. Given that the LabVIEW 8.5 programs were already written to process the incoming signals, in this particular laboratory environment, and control all the ancillaries, such as the stepper motor for the traverse, the Dantec software package was largely bypassed except that is for setting the decade resistance of the module and for reading the ambient temperatures measured by the temperature probe. The anemometer was claimed to have high precision decade resistance settings, which allowed the probe over temperature to be adjusted with a resolution of better than 0.1% (Dantec (2011)). Furthermore within the unit a high precision ohm-meter accurately measures the cold resistance which forms the basis for the decade setting, it is stated in Dantec (2011) that since the measuring current is so low (1 mA) that any heating of the wire as a result would be negligible. There is space for up to 6 CTA hot-wire modules with the StreamLine Pro systems although only one module was utilised for both of the hot-wire experimental configurations recorded with this CTA.

As with the miniature 54T30 CTA all of the hardware options for signal conditioning, these comprising offset, gain, filters etc. were not activated and, in effect, all signal conditioning (filtering) was achieved in software for the purposes of measuring the intermittency and generating spectral plots etc.

One of the major differences, relative to the 54T30 miniature CTA, was the availability of a thermistor temperature probe which, in combination with the Dantec Streamware pro software, offered a digital representation of the temperature. This probe was used to measure the ambient temperature of the laboratory outside of the working section rather than the flow in the working section itself but these temperatures were effectively equivalent given the isothermal environment and the effectiveness of the mixing with the tunnel operating. One can also use the temperature probe as the reference temperature when prescribing the decade resistance settings in Streamware

Pro but given that the experiments performed on the straight section were software-corrected using the Jørgensen (2001) procedure discussed in section 3.12.4 the same approach was utilised for both CTA systems for consistency.

3.10 Main Data Acquisition Card (USB 6210)

All hot-wire voltages (and through calibration) velocity time-history signals were recorded using a National Instruments USB-6210 data acquisition card interfacing with LabVIEW 8.5. The specifications, relevant to the application, are listed in Table 3-3 - National Instruments USB data acquisition devices. Furthermore the manner in which the USB-6210 fitted into the grand scheme of the experimental apparatus is highlighted in the flow chart of Figure 3-23. Therefore the USB-6210 records voltages from the 55P15 hot-wire probe through analogue input and the USB-6009 sends digital output pulses down its step line to drive the stepper motor inside the elliptical traverse body.

Table 3-3 - National Instruments USB data acquisition devices

Specification\Device	USB-6210	USB-6009
Analogue input bit resolution	16-bit	14-bit
No. channels (analogue input - differential)	8	4
Analogue input accuracy (minimum range)	0.088mV	1.53mV
Maximum sampling rate	250 kS/s	48 kS/s
Input impedance	> 10 GΩ	144 kΩ
Digital I/O logic levels	TTL	TTL
Single current drive	16 mA	8.5 mA
Digital timing	Software	Software
Physical dimensions (L x W x H)	16.9 x 9.4 x 3.1 cm	8.51 x 8.18 x 2.31 cm

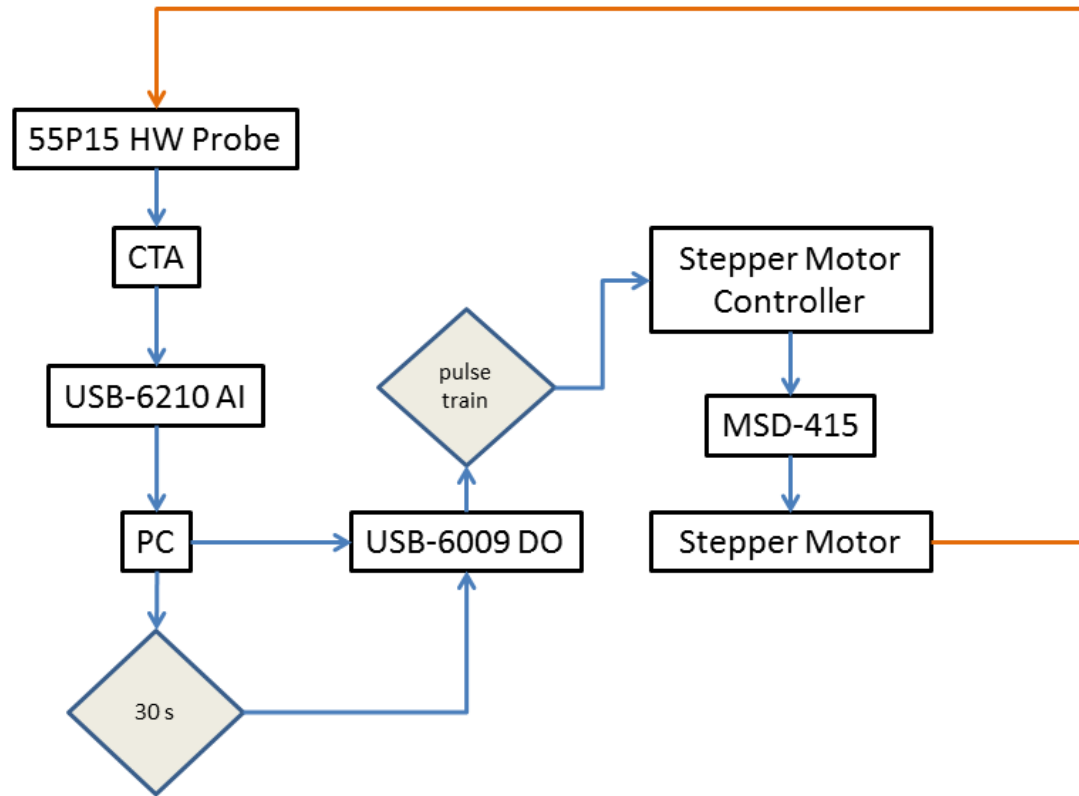


Figure 3-23 - Flow chart representing the main loop of the data acquisition and traversing process

Although the USB-6210 was capable of sampling at 250 kHz, a sampling frequency of 10 kHz was deemed to be suitable since the highest frequency content observed in the signal traces through performing FFT spectral plots, and observing that the drop-off in frequency content for turbulent boundary layers signals, typically occurred no higher than approximately 3 kHz. This is demonstrated in Figure 3-24 in a near wall profile where the intermittency was 100% for the positive pressure gradient with no grid (GOP) configuration.

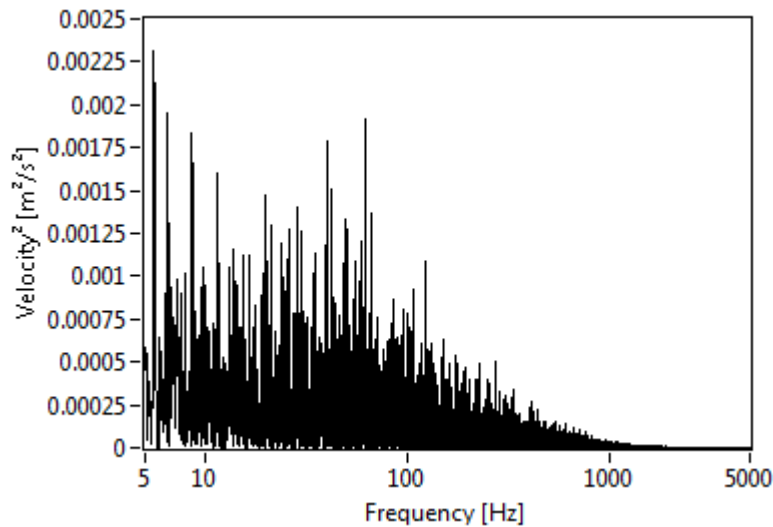


Figure 3-24 - Power spectrum of frequency content in turbulent boundary layer

3.11 Static Pressure Tappings

So as to measure the pressure distribution for each of the experimental boundary conditions (i.e. different sections, grids and tunnel speed combinations) static pressure tappings of 1 mm diameter, at 50 mm pitch along the centreline, were tapped to a 24-channel manually-torqued scanivalve system coupled with the second available channel of the CD223 Validyne system. Owing to the relatively complex geometry of the plate (see Figure 3-4) the centreline is defined as the mid-span of the straight section settling chamber (i.e. displaced 0.61 m from the spanwise datum) and forms a trajectory parallel to the straight sidewalls. The scanivalve was connected to each tapping through vinyl tubing of 0.086" OD and 0.054" ID from Scanivalve Corporation.

The manually-torqued scanivalve itself formed part of Tracker 220 series pressure transducer equipment Instruments (1999) but in this case the native pressure transducer of the Tracker 220 was bypassed and another Validyne AC transducer was used on the second channel of the CD223 box, as aforementioned. This time one of the ports on the Validyne was left open to the reference atmospheric pressure, such that the differential pressure transducer would therefore measure a gauge static pressure. There are a combined total of 139 static pressure tappings on the flat plate

sections all of which were drilled on a CNC miller, whereafter residual burrs were removed by hand (Ramadan (2000)). The sheer number of tapings is a result of previous research work carried out and only 24 of these tapings were utilised to measure the pressure distributions in the wind tunnel for each of the pressure gradient section, tunnel speed and grid combinations. Previously, multiple electronically controlled scanivalve systems have been used but only a single manually torqued option was available for this effort with a finite number of ports and as such it was not practical to make measurements from every tapping and a compromise was made in terms of the stations chosen for performing recordings. These 24 tapings, however, are detailed in Table 3-4 - Streamwise static pressure tapings in terms of their streamwise displacement from the leading edge, where one can observe that the density of recordings is greater towards the leading edge, owing to the relatively rapid changes of pressure expected in that region, and conversely more sparsely distributed towards the outlet of the test sections.

Table 3-4 - Streamwise static pressure tapings

Tapping Station	Streamwise Displacement [mm]
0	50
1	100
2	150
3	250
4	350
5	450
6	550
7	650
8	750
9	850
10	950
11	1050
12	1150
13	1250
14	1400
15	1550
16	1700
17	1850
18	2000
19	2150
20	2300

21	2450
22	2600
23	2750

Unfortunately the Validyne pressure transducer diaphragms utilised for these measurements, particularly where high turbulence intensity in the freestream resulted in low transition Reynolds numbers, were operating near the limits of their accuracy (± 0.1 % of full scale – 0.862 Pa) owing to the small static pressures involved. Nevertheless, even where the quantitative reliability of the results could perhaps be questioned, the qualitative trends still appear to be as expected, as will be discussed in Chapter 4.

3.12 Hot-Wire Systems, Calibration and Corrective Procedures

A hot-wire anemometer, in simple terms, is a thermal transducer Perry (1982), the principle of operation being as follows; an electric current is passed through a fine filament (wire) which is suspended between two prongs exposed to a cross flow. As the flow rate varies, the heat transfer from the filament varies, which in turn causes a variation in the heat balance of the filament. There are two modes of operation for hot-wire anemometer systems (Perry (1982)). One of which is the constant current mode; here the current in the wire is kept constant and variations in wire resistance caused by the flow are measured by monitoring the voltage variations across the filament. The second mode, and in fact the one utilised for this series of experiments, is constant temperature anemometry (CTA). Here the filament is placed in a feedback circuit which maintains the wire at constant resistance and hence constant temperature. This voltage required (to maintain constant resistance/temperature) is then recorded, usually at high-frequency, which in turn then provides data directly related to variations in flow velocity. The main advantage of using CTA's being that the wire has negligible thermal inertia, hence they possess excellent frequency response.

The electrical heat input into the wire is lost by conduction, convection and radiation Lekakis (1996). The relationship between the fluid velocity and the heat loss of a cylindrical wire is based on many assumptions. Under normal operation conditions, the radiation losses are much less than 0.1% of the electrical input and can be neglected, but would be important in low density flows (Lekakis (1996)).

3.12.1 Advantages and Disadvantages of Hot-Wire Anemometry Systems

Hot wire anemometry is likely to remain the principal research tool for most turbulent air/gas flow studies (Bruun (1996)). For measurements in low and moderate turbulence intensity flows (less than ~25%) the main advantages of conventional HWA are;

- Low cost when compared to the likes of Laser Doppler Anemometry (LDA) techniques, albeit this is only in relative terms.
- High frequency response, which provides hot-wires with the ability to respond rapidly to fluctuations in flow properties and combined with the continuous analogue output this can allow for excellent signal analysis.
- Size. The 55P15 boundary layer probe utilised for the hot-wire measurements in these investigations comprised a wire which was 5 μm in diameter and 1.25 mm in length. Such a small measuring volume ($6.25\text{E-}9\text{ m}^3$) provides high resolution in recordings of data.
- Multidimensional probes. Multiple probes can be constructed and arranged to collect numerous velocity components, potentially providing three-dimensional velocity profiles over a wide range of velocities, from very low velocities (approximately 0.2 m/s) to high-speed (compressible) flows (Bruun (1996)).
- Accuracy. Both HWA and LDA can provide similar and very accurate results (0.1 - 0.2%) in meticulously controlled experiments. However, in many practical applications, 1% accuracy is more likely for both systems (Bruun (1996)). This is also dependent upon the quality of

the hot-wire calibration and the drift thereof over time and with respect to external factors such as changes in ambient conditions.

In contrast the following list considers the main disadvantages on hot-wire anemometry systems;

- Conventional HWA is restricted to low and moderate turbulence intensity flows. At high turbulence intensities errors can occur from what is usually referred to as rectification. Due to rotational symmetry, the wire element is insensitive to a reversal of flow direction which may occur in highly turbulent flows
- Obtrusion. HWA, unlike LDA for example, is an obtrusive flow measurement technique; that is to say that the probe and the adjoining assembly used to hold the probe in place are placed within the flow which will, in turn, modify the local flow field. However, for a well-designed probe, the corresponding errors will often be small and the related flow disturbances are usually incorporated into probe calibration
- Probe breakage. Although a hot wire probe is a very delicate instrument, it can, if handled carefully, last for many months or years. The most common source of breakage is through mishandling of the probe, therefore maximum caution must be exercised at all times and procedures for locating the probe in the respective fixture (probe holder) must be clear and adhered to.
- Burn out can occur, due to over-energisation, if the probe is used at a high overheat ratios for long periods.
- Particle impact and contamination. The deposition of impurities in the flow on the sensor can dramatically alter the calibration characteristics and reduce frequency response. It was strongly recommended by Bruun (1996) that a flow filter be incorporated into an experimental flow facility where possible. The sensitivity of the probe to particle impact and contamination would exclude it from hostile environments where probe damage is likely to occur.

- Non-Linearity (Perry (1982)). Since a hot-wire anemometer is a thermal transducer, it's a rather complicated instrument. The wire has thermal inertia, with an associated time constant, furthermore the electric circuitry has its own time constants and there are complex interactions involved between the wire and circuitry. It is a non-linear device and this non-linearity causes considerable complications in calibration procedures (Perry (1982)).

There are other advantages, disadvantages and limitations which have not been listed within this section. This is largely because most of these are not relevant to the main focus of the study, particularly relating to fluid mediums other than air, such as water, where techniques such as LDA assume superiority. For information on the performance of hot-wire systems the reader is encouraged to study Bruun's book (Bruun (1996)) on the subject.

3.12.2 Hot-Wire Calibration

There are several methods for calibrating the voltages recorded from hot-wire anemometry systems with respect to 'known' velocities; polynomial fits, Kings Law - Equation 3-14 (King (1914)) and look-up tables – see Lueptow et al. (2004) for example.

$$E^2 = A^2 + BU^n \quad \text{Equation 3-14}$$

Each of the Dantec 55P15 boundary layer probes were calibrated prior to velocity signals being recorded and processed, with respect to tunnel freestream velocities estimated from dynamic pressure measured using the Validyne pressure transducer and USB-6009 configuration detailed in the Pitot-Static Tube (Validyne) section. First of all 55P15 miniature wire probes were used for all of the experiments, which are 5µm in diameter, 1.25 mm long platinum coated tungsten wires

suspended between two swan neck prongs with typical cold resistances of $3.45\ \Omega$. They are said to be optimised for use with 55H20 probe holders, 4 m BNC cables, all of which was adhered to with everything to Dantec specification.

Previous researchers have made use of calibration nozzles which are typically accurate down to 0.5m/s (Aydin and Leutheusser (1980)), towing carriages or utilising low velocity settling chambers of wind tunnels upstream of the working section for example but none of these options were readily available owing both to resources and the manner in which the traverse was held in place with suction and, hence, the associated tubing involved of finite length. Previously vortex shedding techniques have been employed (as per one of the two techniques described in Lee and Budwig (1991)) which exploit a Strouhal-Reynolds relationship with respect to the vortex shedding frequencies measured downstream of cylinders of known diameter. However, despite such a technique being relatively simple to implement, the original problem remains that one must be able to produce such velocities which weren't available and furthermore in a controlled isolated environment.

As such the minimum non-zero velocity from which the wire could be calibrated against was the idle speed of the tunnel which corresponded to just over 1m/s at the default calibration station for each of the pressure gradient sections tested. Thereafter Kings law curves were retrofitted to the calibration data (of typically 40 data points) using the 'solver' add-in in Microsoft Excel to optimise each of the three coefficients; A, B and n, such that the standard deviation between the data points and the curve were kept to a minimum. Solver in Microsoft excel makes use of the 'generalised reduced gradient algorithm' in order to optimise nonlinear problems (Microsoft (2011)), this is also known as the Frank-Wolfe algorithm, attributed to Frank and Wolfe (1956).

Typically minimum non-zero velocities of an order of magnitude less than those which were available (circa. 10 cm/s) would be sought owing to the low near wall velocities which are measured in low speed laminar boundary layer signals. Some such as Tsanis (1987) adopt the approach of

splicing King's law fits together over a wide range but such an approach would be without advantage in this research owing to the absence of data in the 0 – 1 m/s range and the relatively narrow span of measurements across all experiments; approximately 0 – 10 m/s, thanks largely to the size of the test section allowing for high Reynolds numbers at relatively low speeds. This also avoids the complication of discontinuities in the calibration by referring to one smooth continuous curve.

3.12.3 Wall-Proximity Effect and Initial Probe Height

The accuracy of hot-wire anemometry techniques can be compromised by the proximity of wall boundaries to the measuring volume of interest, where the effect of the boundary on the rate of heat loss is ignored (Wills (1962)). This effect, termed wall-proximity effect, is attributed to the asymmetry in thermal conductivities of the fluid and solid boundaries, hence it is reasonable for one to expect that given that there is a thermodynamic effect that corrections should account for the thermodynamic properties of the wall material (Gibbings et al. (1995)). Given that the solid boundary is usually at ambient temperature in a laboratory environment, additional heat is drawn from the fluid, an effect which amplifies as the heated wire approaches the boundary (Wills (1962)). This is a stand-alone effect, in that it doesn't accelerate the convection losses, merely it is a heat loss of its own and will be present regardless of whether or not flow is passing across the wire.

Hence, with the knowledge of the wall-proximity effect, the adoption of systematic methods, such as Wills (1962) – Wills proximity correct method, are often used for hot-wires to reinterpret the near-wall data such that the heat loss through the wire closely correlates to that of losses primarily through forced convection. Without such compensation the severity of error can be very high but this depends on how close to the solid boundary one is able to attain with their respective experimental apparatus and the magnitude of the local mean velocity vector. The effect will be

most pronounced as proximity tends towards 0 and for low freestream velocities with correspondingly low local velocities in the near-wall boundary layer region.

Wills' experiment for determining the proximity correction algorithm was based on the calibration method of Reichardt (1940) which utilised laminar and turbulent flow channels with known velocities. The resulting empirical correlation was of the form, allowing for the inclusion of an intermittency-weighted correction in Equation 3-15;

$$K_w \left(1 - \frac{\gamma_1}{2}\right) = Re_m - Re_c^n \quad \text{Equation 3-15}$$

where from Wills (1962);

$$K_w = e^{\left(1.678 - 1.229\left(\frac{\gamma}{r}\right)^{0.319}\right)} \quad \text{Equation 3-16}$$

and therefore the corrected velocity was equal to;

$$u_{corr} = \frac{\mu \left(Re_m - K_w \left(1 - \frac{\gamma_1}{2}\right)\right)^{\frac{1}{0.45}}}{\rho d} \quad \text{Equation 3-17}$$

Note that the inclusion of intermittency in the velocity correction equation was suggested by Wills (1962), albeit on limited available data.

The wall-proximity effect is illustrated in Figure 3-25 which plots zero flow voltage of a Dantec 55P15 boundary layer hot-wire probe against wall proximity in mm, it was found that the proximity effect was present to 2mm approximately. Furthermore this same figure contains a 2nd-order polynomial which is later used, with the tunnel and laboratory in its default zero flow configuration, to electronically determine the initial height of the probe in a systematic manner, bypassing further use

of the (less consistent or available) cathetometer. Only 5 data points were utilised for the polynomial fit and these correspond to those closest to the plate.

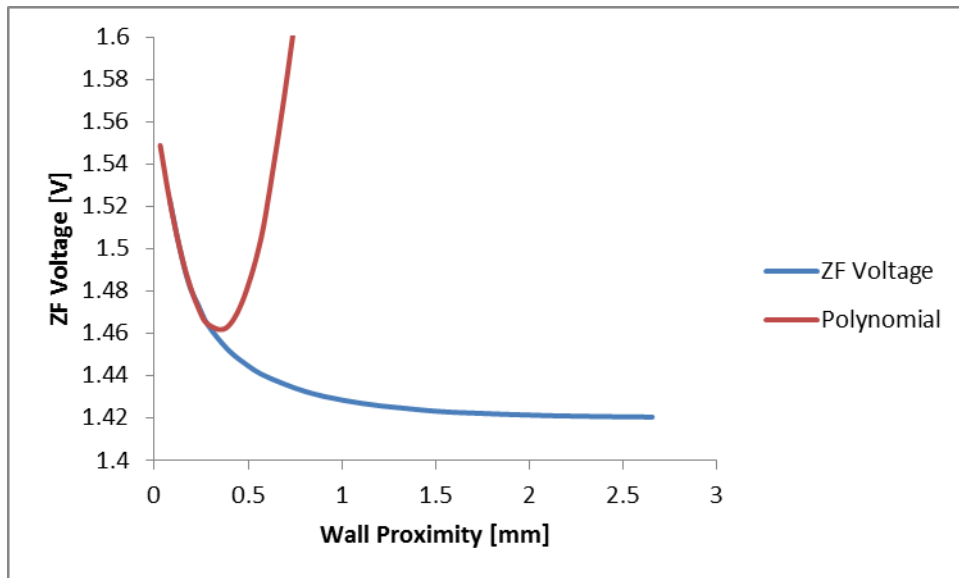


Figure 3-25 - Zero flow wall proximity effect with polynomial calibration in near wall region

The universality of Wills' correction method is challenged by some, such as Oka and Kostic (1972) and Krishnamoorthy et al. (1985), however they do concede that Wills' method is an industry standard of sorts and certainly applicable to laminar flat plate boundary layers on aluminium surfaces, such as within this thesis.

3.12.4 Corrective Procedures for Ambient Drift

In Perry (1982) it is stated that temperature correction is unnecessary if the ambient temperature is within $\pm 0.5^{\circ}\text{C}$ across the span of the calibration and experimental recordings. In Cimbala and Park (1990) it is stated that for a valid calibration performed at 30°C , a velocity measurement of 5 m/s will be in error by 16% (5.8m/s) as a result of a 2°C reduction in ambient temperature.

Once the probes were calibrated for their respective overheat ratio (see Equation 3-13) and ambient temperature the overheat settings were no longer adjusted whilst that calibration was in use. Note that the resistance based overheat ratio is also defined as per Equation 3-18;

$$a = \frac{R_w - R_{amb}}{R_{amb}} \quad \text{Equation 3-18}$$

This policy was initiated with the use of the 54T30 miniature CTA and then continued when the StreamlinePro CTA system was later adopted. As such to compensate for drift in the ambient temperature the Bearman (1971) equation (Equation 3-19) was followed as outlined in Jørgensen (2001) where the output voltages (E_a) are reassigned (to E_{corr}) with respect to the wire temperature setting and the ambient and reference (calibration) temperatures;

$$E_{corr} = E_a \left(\frac{T_w - T_{ref}}{T_w - T_{amb}} \right)^{0.5} \quad \text{Equation 3-19}$$

The ambient and reference temperatures were measured with the temperature probe for the StreamlinePro and from the thermometer in an adjacent laboratory in the case of the 54T30 which also includes the barometer used to measure ambient pressure. Note that there were no corrections made for changes in pressure other than its implied influence on parameters which include density as calculated through the ideal gas equation (Equation 3-20) with pressure as the subject of the equation;

$$p = \rho RT \quad \text{Equation 3-20}$$

Please note this temperature correction method was also incorporated into the ‘zero flow correlation’ algorithm for re-interpreting the zero flow voltages when measuring wall-normal proximity at different temperatures from those measured during the calibration. Furthermore prior to the acquisition of the StreamLine Pro CTA system, which had its own temperature probe, a

standard mercury thermometer assembled alongside the mercury barometer was utilised. That is to say the thermometer only method was used for the straight, nominally zero pressure gradient, section in terms of both measuring the ambient temperature conditions when calibrating the probe, for velocity and proximity, and for determining the offset from the calibration temperatures. This situation arose as the 54T30 miniature-CTA was being used at that time.

In order to prevent premature ageing of the wire the operating time for the wire was kept to a minimum. With the StreamLine Pro systems this could be achieved either by a mechanical button or through the dedicated Dantec software. The 54T30 miniature CTA system was run from a battery and whilst the battery had sufficient life to last for more than a full days worth of testing, the procedure of charging the battery at the end of each day of testing was always adopted. This charging process was achieved with a single variable bench power supply (Thurlby PL320) set to just over 12 volts and the charging current for the battery was limited to approximately 1A, although such high rates were never required.

Larsen and Busch (1980) and Schubauer (1935) investigated the effects of relative humidity on hot-wire measurements. Schubauer (1935) used a wind tunnel facility which was capable of varying the relative humidity (from 25% to 70%) whilst maintaining the temperature at a fixed 25°C, where variations of 6% were quantified in the measured hot-wire velocities due to the controlled variable of relative humidity. Whilst it can be shown that relative humidity has an influence on the heat transfer, and therefore the measured voltage, the effect is less significant compared to that of ambient temperature changes. Henceforth, it's not a parameter which was measured or actively controlled during the respective testing as it was deemed to have negligible influence on the results. In any case all of the tests were conducted over a relatively short period – approximately one week, relative to their calibration, where the humidity would effectively be included in the calibration.

3.13 Data Processing

All of the main data processing was carried out in LabVIEW 8.5, LabVIEW being a visual programming language enabling a system-design platform for code development. There were two flavours of LabVIEW which were available for the experimentation, these comprising LabVIEW 8.5 and 2010 Service Pack 1 (32-bit), the former being available through a stand-alone licence and the latter networked through the university's managed windows system to a licence server. As such LabVIEW 8.5 was utilised for recording experimental results and immediately processing them thereafter, owing to the reliability offered with a stand-alone licence. With LabVIEW it is possible to compile any program into a stand-alone executable, which can then be executed outside of the development environment provided the corresponding run-time engines are installed in the host operating system. This option was not used since there are occasions where one would wish to modify the code during exploratory testing operations for example.

This processing was executed during the period after the measurements had been recorded, whilst the tunnel was being reset to default, and the traverse being physically moved to the following station/skew angle. As a result of the processing a summary file with mean quantities, intermittencies and boundary layer integral parameters was also written to disk. These signals would then later be reprocessed, in the event of an incorrect prescription of proximity, by offsetting them accordingly so that each signal would intercept (0,0) – i.e. abide by the no slip condition near the wall.

Each signal file of 30 seconds worth of time-history (sampled at 10 kHz) was stored in a human-readable ASCII format which corresponded to each around 3.5 MB per file. Overall each completed test combination of grid and pressure gradient section consumed approximately 10 - 15 GB of storage. Hence roughly 100 GB's worth of storage space was required overall for all of the data files

which is a perfectly manageable volume with modern storage capacities. These files were also compressed in .zip format and backed up in alternative storage sources for safe-keeping.

3.14 Intermittency Algorithm

The algorithm, first employed by Shaw et al. (1985), for the discrimination between laminar and turbulent sections of the flow signal is described in detail in Fasihfar and Johnson (1992) for which the latter authors developed a criteria for setting the filter frequencies and residence time. This algorithm has since been implemented in LabVIEW 8.5 software such that flow signals can be analysed concurrently with measurements, as opposed to post-processing voltage signals non-natively in a compiled program at a later point. The relevant code is provided in Appendix B.

There are many different algorithms for determining the intermittency from continuous hot-wire signals, some of which involve differentiating the raw velocity signals, such as Kuan and Wang (1990), but the intermittency algorithm is executed by processing the Wills corrected signals as follows, with more details provided in the following sub-sections;

- Signal is high pass filtered at a frequency determined based on the thickness of the boundary layer and the magnitude of the freestream velocity, as per Ramadan (2000) -
$$f = \frac{U_{\infty}}{2\pi\delta}$$
- Signal is then rectified
- 'Window' placed around the signal of 10% of the local mean velocity but since the signal was previously rectified this was merely a Boolean operation with respect to the cut-off level.
- Everything outside of the window (larger than 10% of the local mean) is deemed turbulent, however not everything inside the window can be classified as laminar flow since turbulent bursts will bounce between the two criteria.

- Therefore a residence time criteria was enforced such that adjacent turbulent regions outwith the window were concatenated together should the number of laminar points be less than the residence time, $\Delta t = \frac{2\pi\delta}{U}$
- Thereafter the number of turbulent points in the flow signal are summated and compared with the total number of points in the flow signal – 300,000 for each of the measurements in each of these hot-wire signals. This is equivalent to the intermittency percentage as defined in Equation 2-7.

The graphical code for this program is illustrated in Figure 3-26 and the respective front panel in Figure 3-27 provides an excellent example of the overall procedure by focusing on a portion of the incoming signal where the overall intermittency is around 25%. It's clear from the incoming velocity signal where the turbulent bursts occur and it would appear that the algorithm works extremely well in identifying the turbulent regions of the flow field. It's also worth pointing out that, although the intermittency is defined with an arity of two parameters, the non-turbulent portion of the flow signal should strictly be broken down into laminar and calmed regions as identified by the modelling attempts of Ramesh and Hodson (1999) for example who tried to incorporate their stabilising effects and the influence on spot formation.

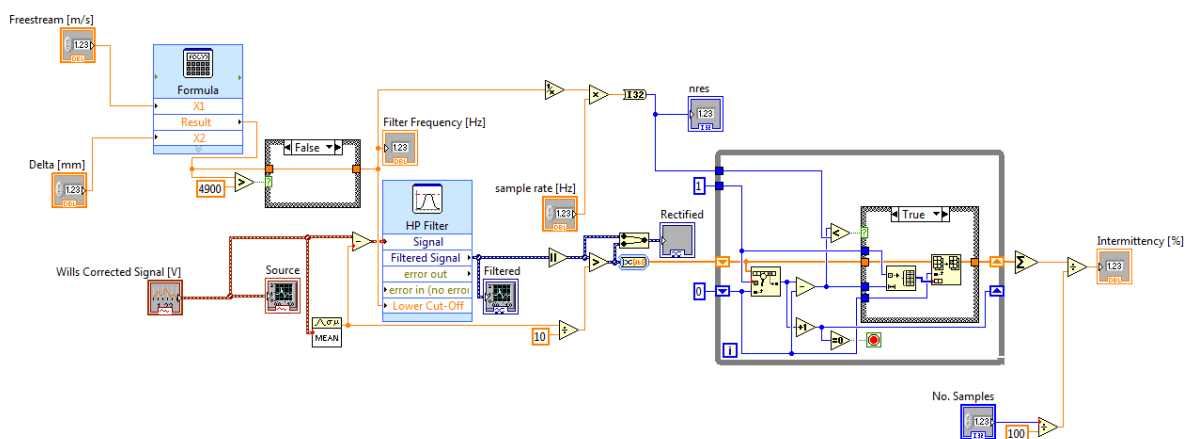


Figure 3-26 - LabVIEW intermittency algorithm

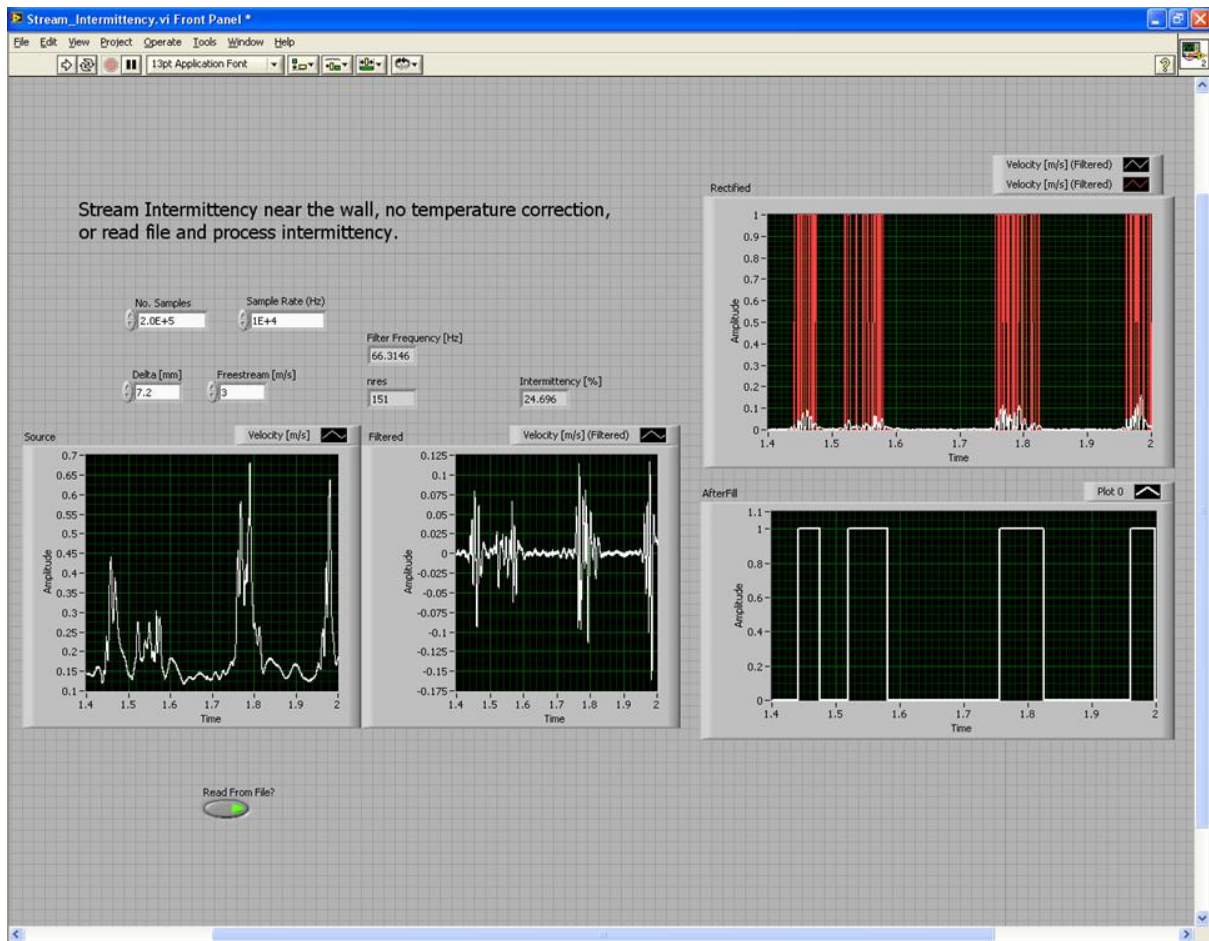


Figure 3-27 - Front panel of LabVIEW intermittency algorithm

3.14.1 High Pass Filter Setting for Intermittency Algorithm

It is a common approach in signal processing to remove unwanted frequencies, for example the 50-60 Hz range of common mains frequency noise. Again in wind tunnels it is common for low frequency fluctuations to be filtered out when stating the freestream turbulence intensity levels, as discussed in section 3-D Boundary Layers, particularly where attaining minimal turbulence intensities is one of the objective boundary conditions.

Likewise, in order to isolate the turbulent regions of the signal high pass filters are often utilised. In LabVIEW this is achieved with a 4th order infinite impulse response highpass Butterworth filter.

Previously it was common at the University of Liverpool to use 300 Hz to truncate the lower

frequencies, as per Madadnia (1989), owing to the then limited settings on analogue Dantec systems but more recently this has been updated with frequency settings based on local physical attributes of the boundary layer itself – namely the boundary layer thickness, δ , and the freestream velocity, U . This is defined as $\frac{U}{2\pi\delta}$ which corresponds to the minimum frequency of turbulence which could be locally accommodated in the boundary layer – see Figure 3-28.



Figure 3-28 - Largest vortices accommodated by a boundary layer

Usually frequency content in the signal below this cut off would be considered to be laminar instability waves, sound waves, low frequency noise and fluctuations convected from the freestream. A Tollmien-Schlichting stability diagram with a curve depicting the $\frac{U_\infty}{2\pi\delta}$ frequency criteria and the neutral stability curve for a zero pressure gradient is shown in Figure 3-29. This indicates that the high pass filter will successfully remove Tollmien-Schlichting activity.

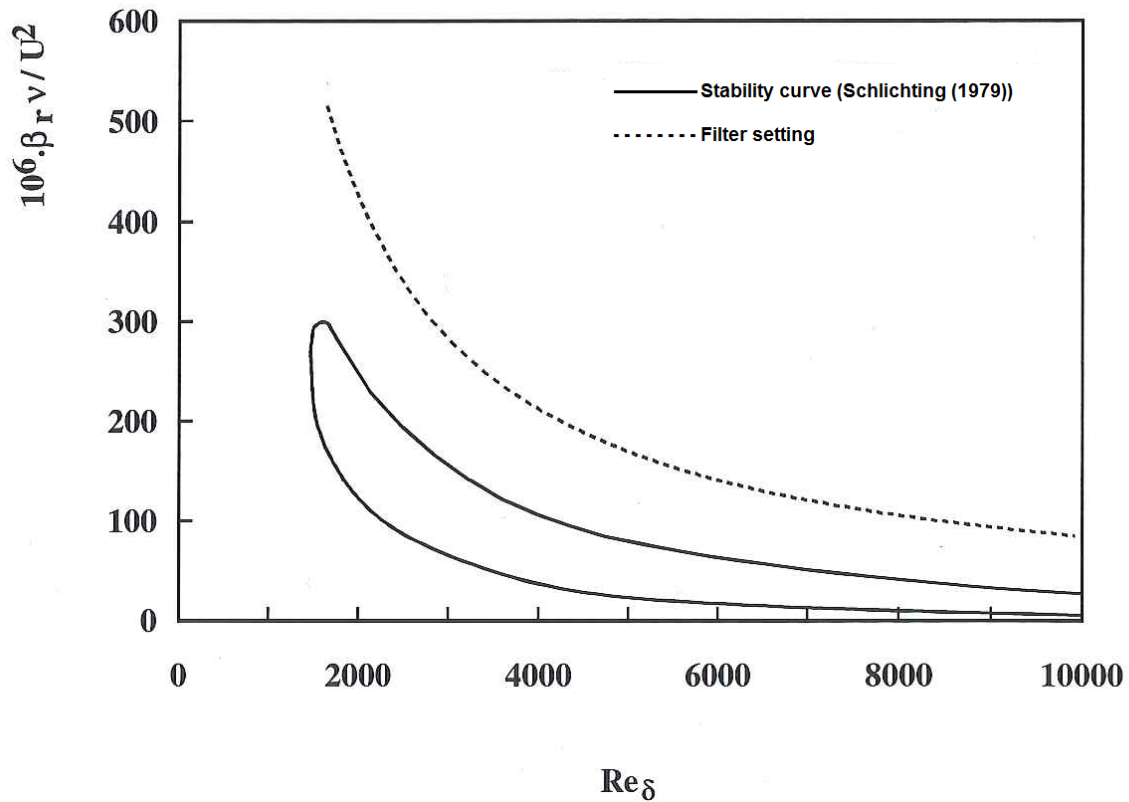


Figure 3-29 - Minimum turbulent frequency (dashed line) shown with neutral stability curve in zero pressure gradient laminar boundary layer (Ercan (1997))

3.14.2 Window Size for Intermittency Algorithm

The choice of 'window' size is important and can have a significant influence on what intermittency is determined by the algorithm overall. If the window size/threshold is too small then transition will be perceived to occur earlier than it in fact does. Likewise if the window setting is too large then transition onset will be detected too late. Therefore the window size fitted around the filtered signal was taken to be 10% of the local mean velocity, i.e. $\pm \frac{u}{10}$, which was considered to be a reasonable choice and has been used by previous researchers, e.g. Ercan (1997). In practice the negative polarity was unnecessary owing to the filtered time-histories being rectified and as such the criteria

of $\frac{u}{10}$ was all that was required for the initial discrimination between laminar and turbulent sections of the flow signal.

3.14.3 Residence Time for Intermittency Algorithm

Similar to the calculation of the filter frequency the residence time criteria for the intermittency algorithm was selected by appealing to the physical argument of the time that it would require for the largest vortex present within the boundary layer to complete one full circumference, namely $\frac{2\pi\delta}{U_\infty}$ which has the dimensions of seconds. Just to reiterate this in effect meant that any portions of the raw signal which were temporarily designated as non-turbulent would only retain that designation should the duration of non-turbulence be greater than the residence time. Should this fail to be the case then the interstitial non-turbulent regions would be classed as turbulent and filled to identify one coherent turbulent burst.

In terms of how this was coded into the LabVIEW intermittency routine first the residence time was converted into its equivalent number of points in the flow signal, with respect to the sampling frequency, e.g. a residence time of 0.01 seconds would correspond to 100 points for a sampling frequency of 10 kHz. Thereafter, and continuing with the example parameters, non-turbulent gaps spanning less than 100 points would be re-assigned with unity value – turbulent flow.

3.15 Experimental Procedure

When tests are ready to be executed, following calibration of all the measuring equipment and the boundary conditions of each experiment are in place, the following procedural experimental loop

was executed – see Appendix B for more detailed discussion of the LabVIEW codes which are alluded to;

- Tunnel motor off and allowed to settle
- Select streamwise probe coordinate and station angle
- Enter the tunnel and physically move the traverse to an appropriate station using the template
- Switch on the vacuum pump to fix traverse in place
- Remove template from tunnel
- In the case of the 2nd section (positive pressure gradient) replace the portside outlet grid after exiting the tunnel
- Set probe to 'operate'
- Run 'Home.vi' (see Appendix B) program to move the probe in close proximity to the plate, based on a target voltage under the conditions of zero flow
- Record temperature with Streamline Pro temperature probe and use this in conjunction with the 'ZF_Correlation.vi' (see Appendix B) routine to establish temperature corrected proximity
- Enter proximity/initial height yielded through 'ZF_Correlation.vi' into the 'Full.vi' main (see Appendix B) program along with all the other parameters; sampling time for each wall-normal increment, ambient temperature, ambient pressure, streamwise probe location, spanwise probe location, station angle and the filename of the test

Such that the filenames and probe coordinates follow a regular, decipherable pattern the naming convention of was utilised. The table lists what were considered to be the major stations but in fact the plate section was subdivided by three interstitial minor stations in 25 mm increments such that, for example, high resolution through a short transition region could be obtained in a systematic manner without having to resort to using arbitrary locations on the plate. The minor stations, when

used, were designated by the use of '+' characters relative to the parent major station. For example alpha+ corresponded to 125 mm streamwise displacement and, likewise, alpha+++ to 175 mm.

Thereafter three parameters are concatenated together; these comprising a NATO phonetic representation (FAA (2012)) of the streamwise leading edge displacement, an approximate (arbitrary) motor speed setting when matching Reynolds numbers between tests and a bearing representation of the station/skew angle.

Note also that the sampling time was maintained at 30 seconds for every experiment, other than those purely exploratory in nature, i.e. those which were executed to obtain rough profiles for a quick understanding of the nature of the flow field, without the absolute need for statistical steadiness in all parameters. The parameters relevant to the test being run were entered into the LabVIEW front panel of the main program (Full.vi), as depicted in Figure 3-30.

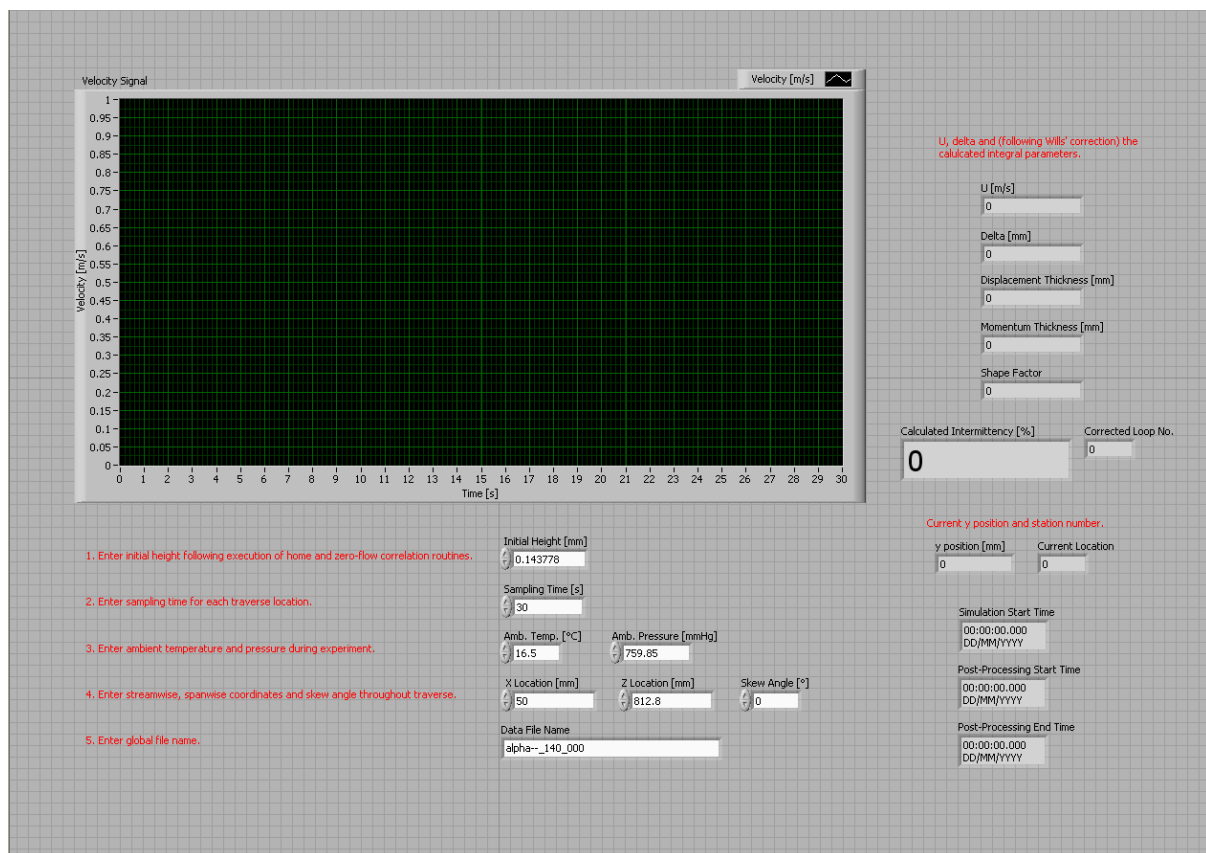


Figure 3-30 - LabVIEW front panel interface for main experimental program

Furthermore, it is important to note that the streamwise static pressure distributions (and therefore gradients) were not measured concurrently with each individual experiment but rather with the traverse equipment removed from the working section of the wind tunnel. It was observed that the traverse had a somewhat significant effect on the static pressure distribution, and likewise for different skew angles, as has been discussed later in section 4.1. Thus it was simpler have the traverse removed such as to uniquely define the pressure distribution for the tunnel speed and flap angle. Additionally, it was observed that whilst skewing the traverse mechanism that, depending on what angle was selected, it could effectively foul the static pressure tapings which would not only result in erroneous measurements but could also cause damage to the validyne diaphragms, given the large suction pressures associated with the traverse's suction pump. In actual fact, the suction pump was purposefully used in this manner in order to check and clear the individual static pressure tapings for blockages before the tapings themselves were retrospectively re-attached.

3.16 Measurement Uncertainties

During each experiment, and likewise for every calibration, there are associated uncertainties with the measurements recorded, such is the nature of experimental work. These uncertainties supplement the errors induced via drift in ambient conditions, as discussed in section 3.12. The current measurements, however, primarily focus on boundary layer fluctuations induced by freestream turbulence, and the receptivities thereof - see chapter 4 and the comparisons made with numerical computations in chapter 5. Fortunately these measurements of comparative velocity fluctuations incur less error, compared to the mean velocity measurements, as they (in effect) cancel each other out.

3.16.1 Calibration Uncertainty

Each calibration was performed with the combination of a pitot-static tube, inclined manometer – see sections 3.5 and 3.8 and, thereafter, a Validyne differential pressure transducer system. The assumption is made that the gradient of the Voltage output from the transducer remained constant, irrespective of any minor drift in the zero flow voltages, with the measured zero flow voltage offset in software – i.e. without any modifications to the transducer hardware settings. It is also assumed that the uncertainty from the Validyne measurements translates directly from the manometer uncertainty, owing to the fact that the 14-bit USB-6009 DAQ had sufficiently high resolution to produce excellent time-averaged pressure data, in addition to the strongly linear relationship between differential pressure and Voltage. It is estimated that the maximum uncertainty in velocity measurements, caused by an aggregate of the uncertainty in temperature (± 0.5 K), pressure (± 0.05 mmHg) and manometer length (± 0.25 mm) for a 10° inclination angle at the lowest tunnel speed used during the Validyne calibration (approximately 3 m/s) corresponded to approximately 2.50 %.

The dominant source of uncertainty, assuming that errors in the inclination angle and the density of the methylated spirits manometer fluid (measured using an Anton Paar DMA 35N portable density meter) are negligible, is the reading error in the manometer length. Fortunately this uncertainty decays with increasing tunnel speed (to approximately 0.20 % at the opposite end of the calibration) and is theoretically attenuated further by the aforementioned linear calibration fit for the differential pressure transducer.

3.16.2 Uncertainty in Alignment of Probe

For each streamwise location the first traverse was always performed with the probe positioned perpendicular to the measuring plane at $Z = 812.8$ mm. This alignment was accomplished in

conjunction with the crosshairs on the traverse template which was intended to keep alignment errors to a minimum. However, any offset angle in yaw (χ) will result in a different effective cooling velocity U_{eff} being sensed by the wire, as per Equation 2-20.

$$U_{eff} = U \cos \chi \quad \text{Equation 3-21}$$

Thus, according to Equation 3-21, an offset of 5° (for example) will result in an estimated error of approximately 0.38%. Given the manner in which the probe is positioned, with the use of the traverse template crosshairs, an error of 5° would perhaps be excessively conservative.

Furthermore, considering that the experimental procedure involved resolving the mean flow angles, significant deviations (greater than 5°) in the freestream approach flow would be clearly observable.

4 Chapter 4 – Swept Boundary Layer Transition Experimental Results

The experimental results from the main body of experimentation are presented with respect to the sequence in which the tests were executed, starting with the nominally zero pressure gradient section. Full details of all of the parameters for each case are presented in Table 3-1. In section 4.2 detailed results for the significant boundary layer parameters/profiles are presented for the G0Z case and thereafter less detailed results are presented on the basis of their specific relevance and salient features. Note that all wall normal profiles are presented in log form, owing to the high shear/gradients near the wall for most test conditions. Furthermore all plots represent traverses which have been resolved with the probe aligned with the measuring plane and therefore the approach flow. This corresponds to probe alignment with the G_x direction in Figure 3-15.

4.1 Streamwise Static Pressure Distributions

Prior to presenting the hot-wire results on a case by case basis the static pressure distributions for all 9 experimental cases (see Table 3-1) are provided in this section in Figure 4-1 and Figure 4-2. Figure 4-1 presents the data retrieved from the Validyne differential pressure transducer in terms of gauge static pressures (referenced to atmospheric pressure) and Figure 4-2 presents the same data, only it is normalised with respect to the freestream velocity measured at 100 mm displacement from the leading edge, which was coincidentally the station used for calibrating the probes and hence is a consistent reference across all profiles, as per Equation 4-1.

$$C_p = \frac{\Delta P}{\frac{1}{2}\rho U_\infty^2}$$

Equation 4-1

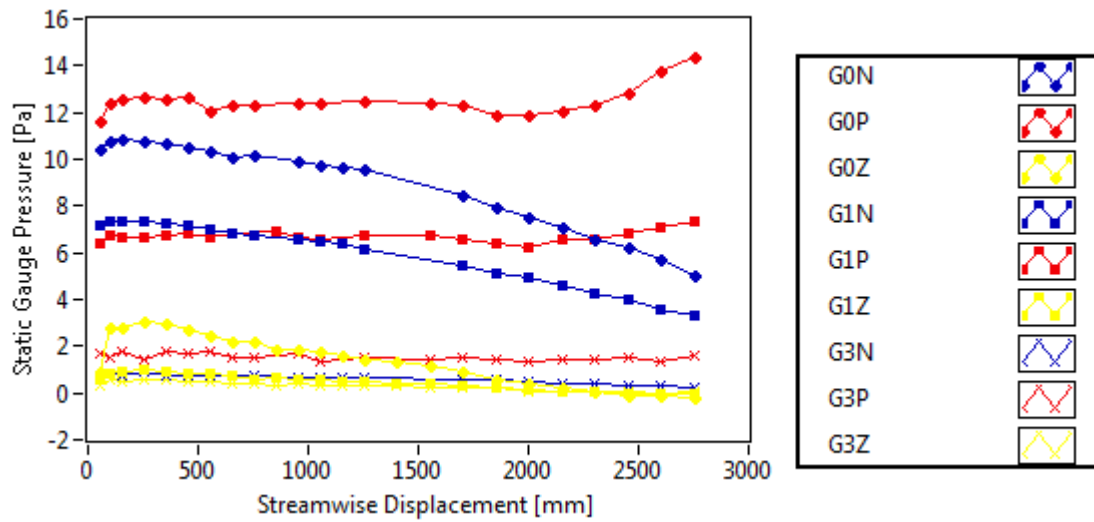


Figure 4-1 - Gauge pressure of pressure tapplings versus streamwise displacement from leading edge

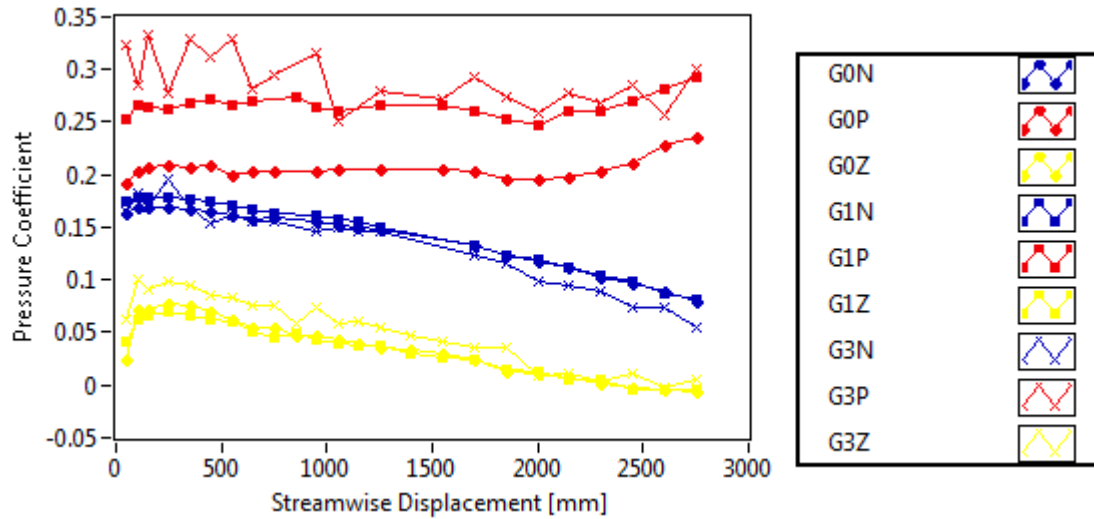


Figure 4-2 - Static pressure distributions normalised as pressure coefficient values against leading edge displacement

Figure 4-1 clearly indicates negative streamwise pressure gradients beyond the initial leading edge effects for all ZPG and NPG cases. This is as expected owing to the physical constriction of a decreasing free cross sectional area for the NPG cases and the displacement thickness of the boundary layers forming on all of the internal boundaries. The PPG cases on the other hand are somewhat different. They similarly exhibit pressure recovery effects towards the leading edge then something of a plateau in the initial straight section before entering the diverging section whereafter

the static pressure eventually increases. However, this doesn't appear to be the case for G3P which is likely due to the relatively low tunnel speeds associated with such a case and the correspondingly thicker boundary layers and displacement thicknesses causing increased blockage.

Figure 4-2 illustrates that the pressure coefficient profiles do appear to collapse to a single curve for all ZPG and NPG cases. However, this does not occur for the PPG cases and this can be attributed to the use of additional grids at the outlet to increase the level of blockage in order to retrieve the loss in flow quality instigated due to the apparent migration of the stagnation point to the underside of the plate, most likely resulting in a separation bubble on the top (measuring) surface – as discussed in section 3.2. As such the outlet grids have their own associated pressure drop which varies with tunnel speed, hence the absence of a collapse in the data. These profiles can be made to overlap should they be reallocated different reference pressures.

It should be noted that all static pressure distributions previously presented in Figure 4-1 and Figure 4-2 were resolved in the absence of the traverse equipment. Figure 4-3 and Figure 4-4 however are plotted with the hot wire probe mounted in the traverse and displaced 1050 mm from the leading edge on the measuring plane, where the fixed streamwise location for the hot-wire measuring volume is shown in green. The traverse was then skewed at 4 angles (denoted as bearing angles in the figure legends) where 000 is unskewed in order to first assess the additional blockage resulting from the traverse and secondly to determine the degree to which the pressure distributions vary significantly with skew angle which is likely to compromise the approach for resolving the mean flow angles, particularly given the lack of rotational symmetry offered by the traverse design, as previously discussed in section 3.7.

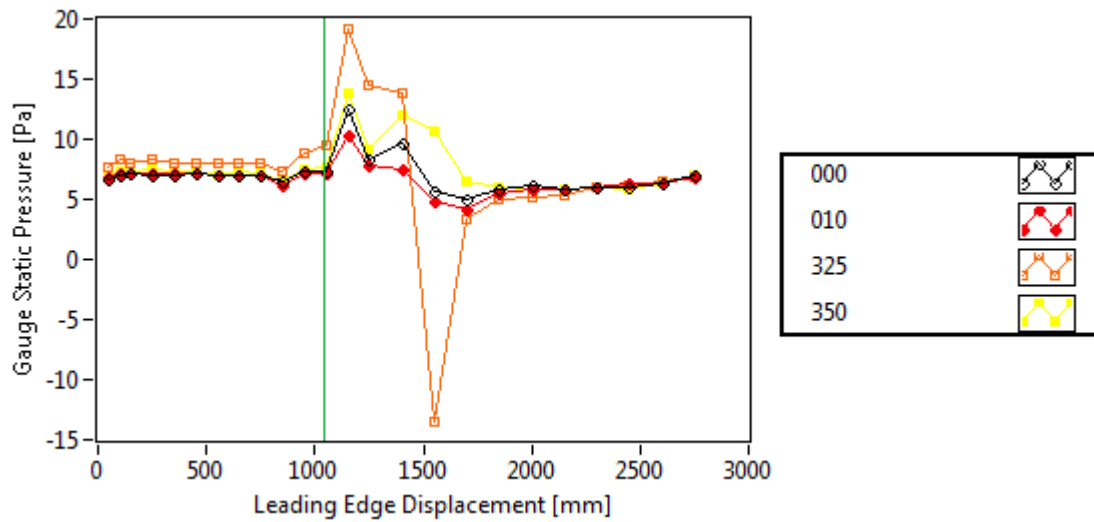


Figure 4-3 - Streamwise static pressure distribution with traverse skewed at different angles

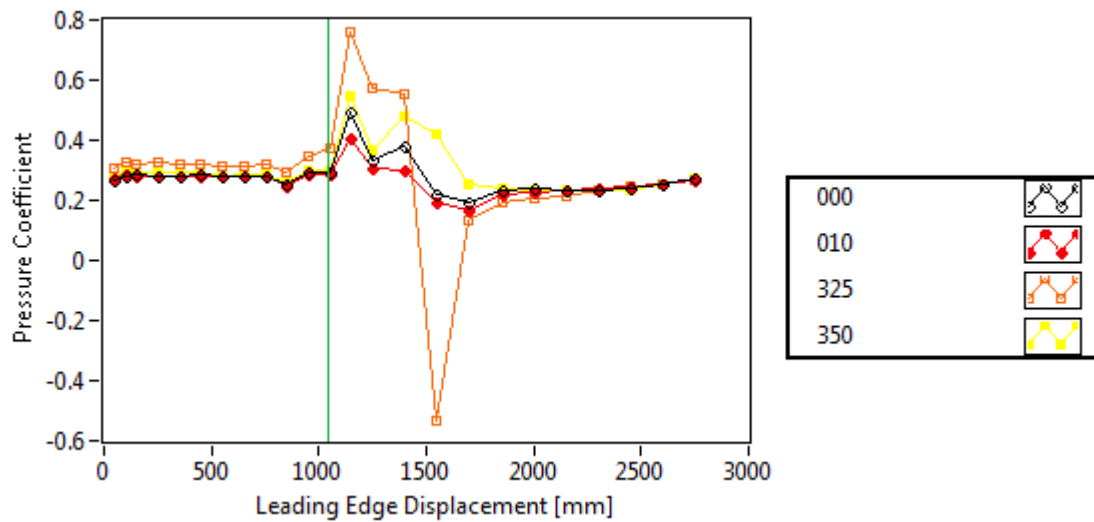


Figure 4-4 - Streamwise pressure coefficients with traverse skewed at different angles

In theory the freestream velocities recorded should correspond with the static pressure distribution, in accordance with Bernoulli's principle, but this was not the case as one can observe from Figure 4-5. This disparity is discussed further in relation to the following results in section 4.2 but can be primarily attributed to ambient drift, given that each combination of grid and section would span a weeks' worth of recording.

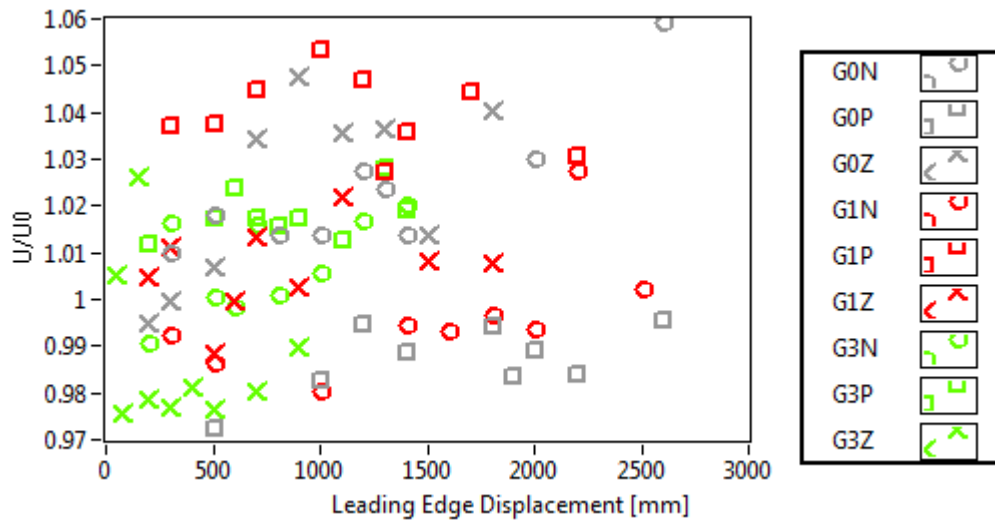


Figure 4-5 - Hot-wire U/U_0 profiles with respect to leading edge displacement for all grids and sections

4.2 Nominally Zero Pressure Gradient (GxZ)

Constant temperature hot-wire anemometry techniques were utilized for all experiments but some subtle differences in the equipment actually utilised are discussed in section 3.9. Two different CTAs were used in the experimental programme. For all of the nominally zero pressure gradient (ZPG) results presented in this section a 54T30 miniature CTA has been used. In contrast, for the non-zero pressure gradient sections a Dantec StreamLine Pro CTA was used.

4.2.1 Wall Normal Profiles under Zero Pressure Gradient (G0Z)

The first results presented are for the case where there is no grid and the tunnel was operated with its natural level of turbulence intensity (G0Z) - Figure 4-6 shows the velocities normalised by the local freestream velocity in Figure 4-7. One can observe from these figures that the mean velocities appear to assume relatively standard boundary layer profiles as seen with 2-D flows, as is to be expected for zero pressure gradient. This is to say that the profiles tend to start with relatively shallow near wall gradients which steepen with increasing streamwise Reynolds number, and hence

intermittency, as the prevalence of turbulence increases, owing to the increased transfer of momentum in the wall normal direction. These profiles also illustrate that there are always a significant number of points through the boundary layer thickness with the stepper motor algorithm implemented (as discussed in section 3.7). Additionally, the nearest point to the wall is always of the same order, circa. 0.075 – 0.125 mm, and as such when the boundary layer thickens with increasing Re_x , the respective y/δ values decrease and hence the thicker boundary layers are measured with higher resolution.

Furthermore at roughly half of the boundary layer thickness and, coincidentally, half way through transition there is a crossover in the profiles as they evolve from a laminar to a turbulent shape – note that hereafter the shape factor integral parameters are discussed at length in relation to the experimental profiles. Figure 4-8 also depicts the first two profiles (in normalised form) versus the Blasius solution (i.e. $m = 0$ for a Falkner-Skan-Cooke profile). The profiles are not observed to deviate significantly from the Blasius solution, as would be expected for zero pressure gradient laminar flows.

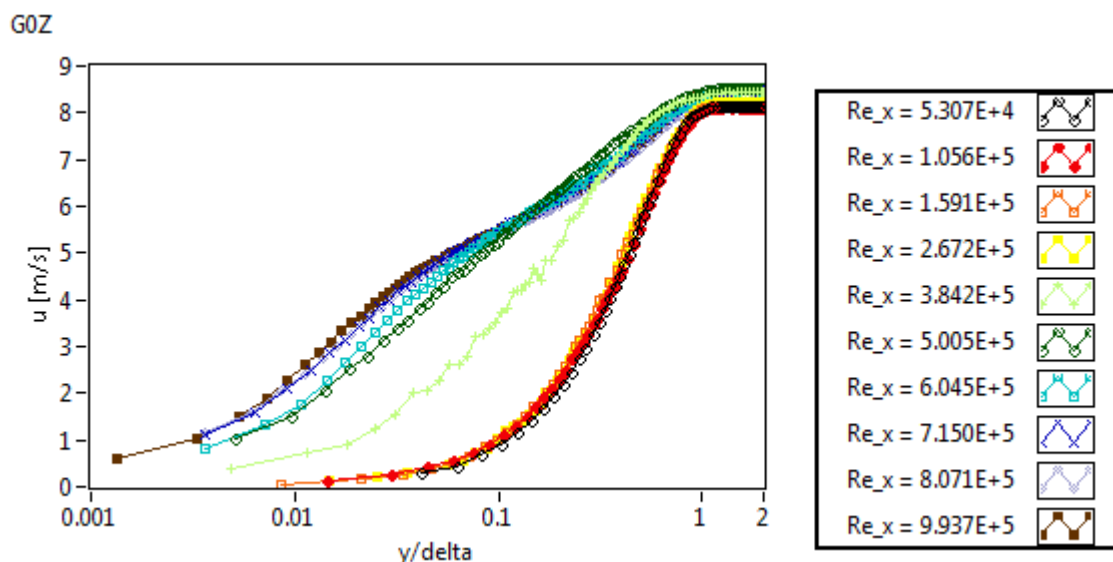


Figure 4-6 - G0Z wall normal velocities at various streamwise Reynolds numbers

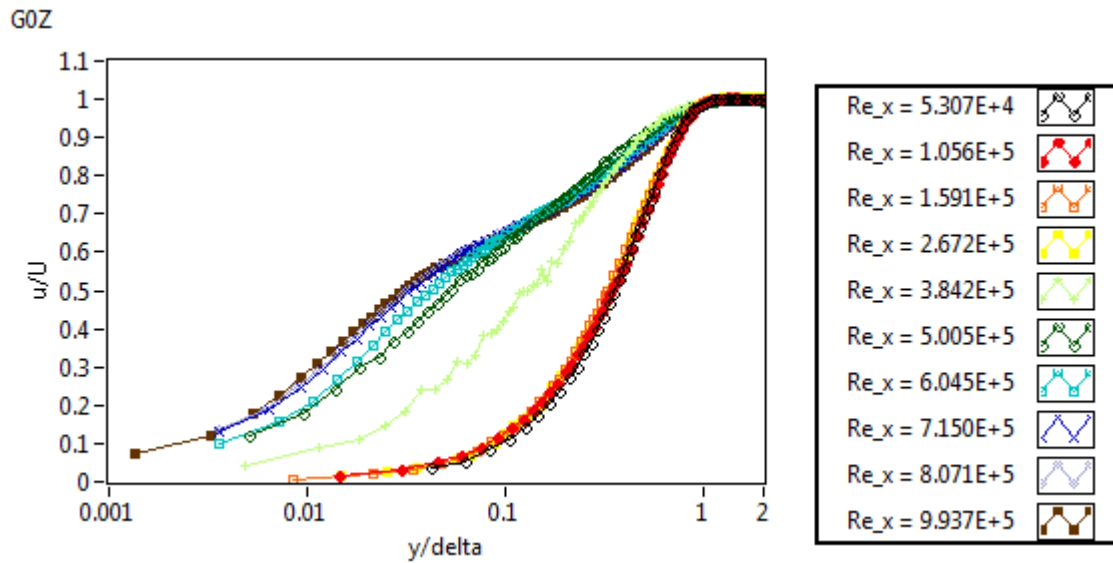


Figure 4-7 - G0Z normalised velocity profiles at various streamwise Reynolds numbers

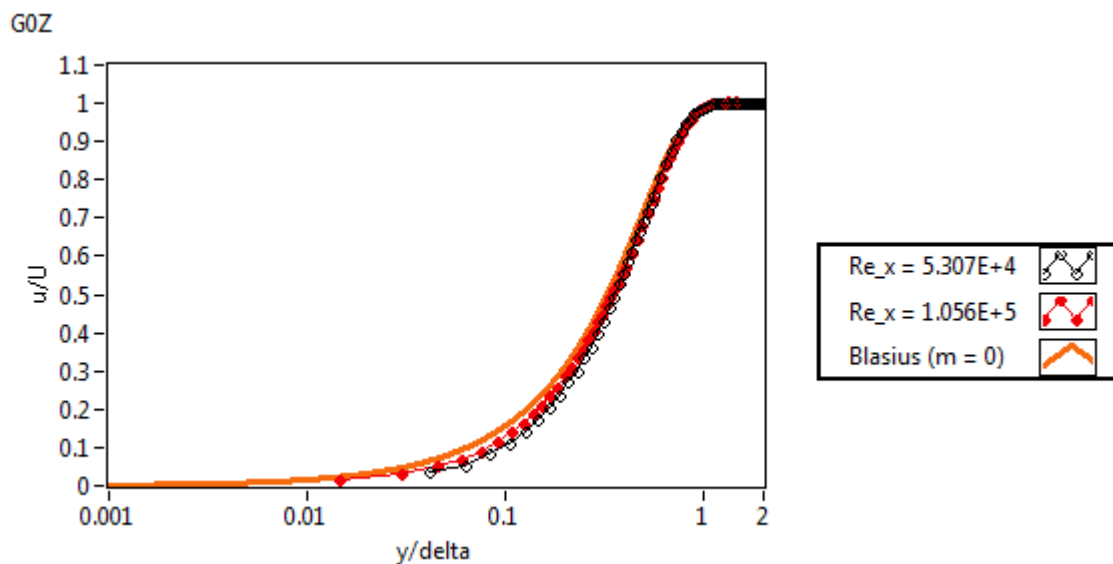


Figure 4-8 - First two profiles plotted against Blasius solution (G0Z)

Figure 4-9 illustrates the wall normal intermittency distributions with respect to y/δ and one can observe that there is something of a plateau in the near wall region (similar to those of Fasihfar and Johnson (1992) for example) up to approximately 30% of the boundary layer thickness, whereafter there is a drop off to the non-transitional freestream value of 0%. Furthermore one can observe that the intermittency near the wall increases from where transition starts until it saturates at the end of transition. In fact there is something of a collapse (universal y distribution for turbulent

boundary layers, Dhawan and Narasimha (1958)) of the saturated intermittency profiles above Re_x of approximately 700,000.

In this particular instance there is a reasonable spread of the streamwise locations for the transition map, albeit perhaps the intermittency for the fourth station would ideally be more dissimilar to the third. The stations resolved are chosen dynamically as the results are obtained and the transition region identified as this is unknown a priori.

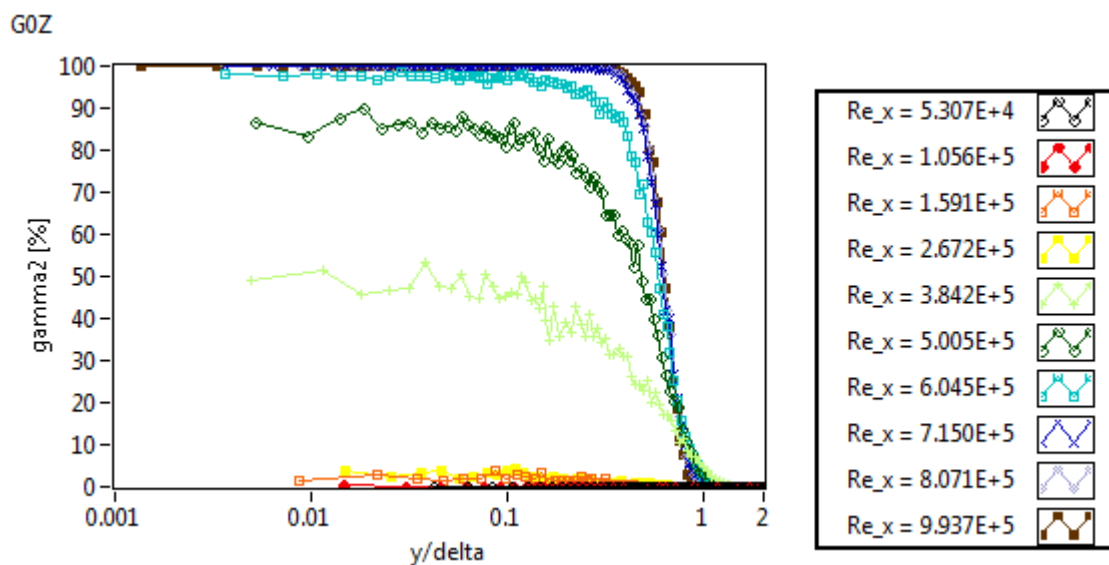


Figure 4-9 - G0Z Wall normal intermittency profiles at various streamwise Reynolds numbers

Figure 4-10 offers a three dimensional perspective on the manner in which intermittency evolves over the flat plate, note that the flow direction is marked in the direction of increasing streamwise Reynolds number. Whilst the intermittency may, in this case, plateau at 30% of the boundary layer thickness, given that the boundary layer thickness increases with Reynolds number so does the extent of the intermittent region.

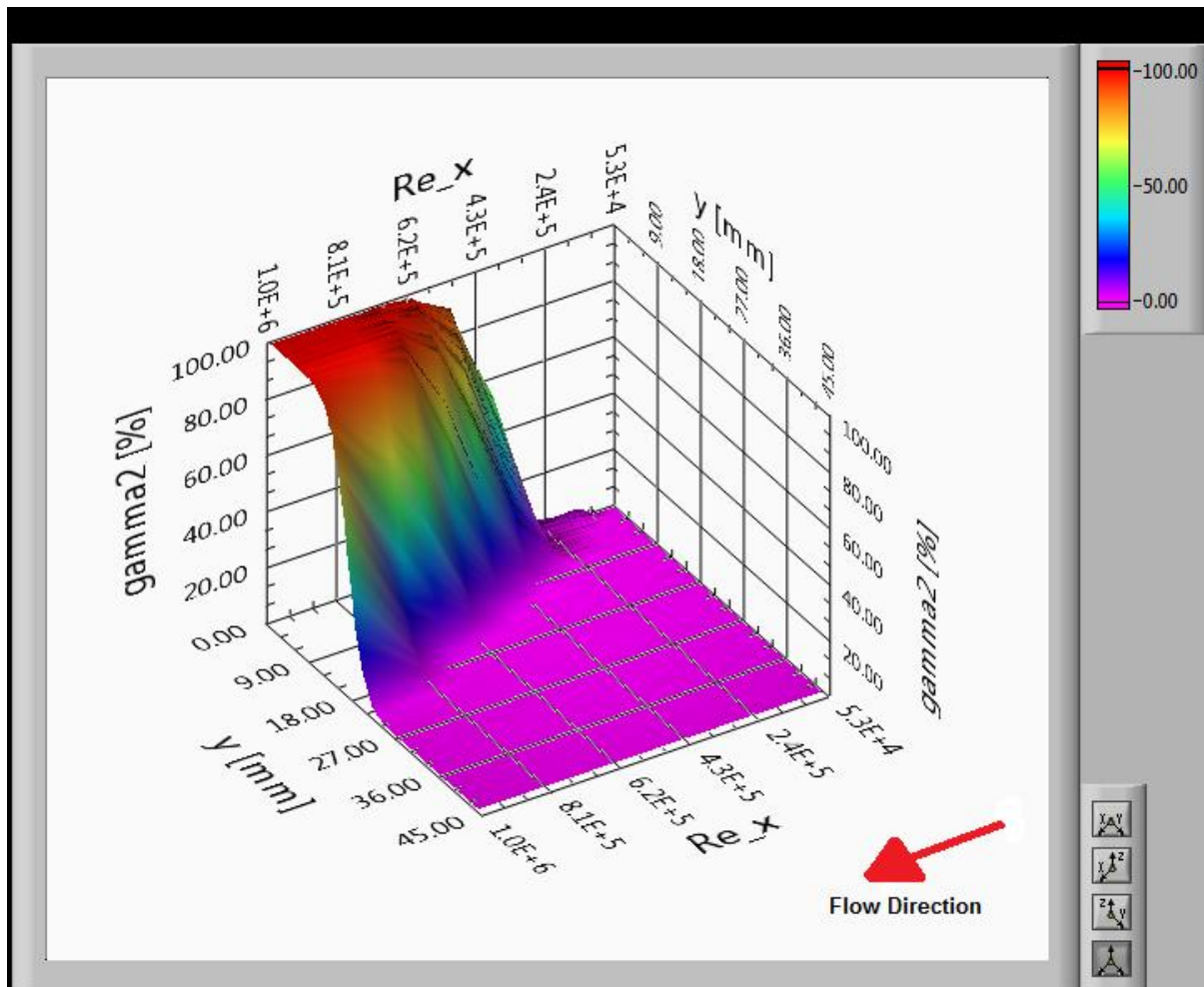


Figure 4-10 - 3-D plot of intermittency with respect to streamwise Reynolds number and wall normal displacement (G0Z)

Figure 4-11 is a plot of turbulence intensity against non-dimensional wall normal displacement where one can pick out the variations throughout the boundary layer thickness at different Re_x values and intermittencies. Transition is observed to initiate when the near wall magnitude of turbulence intensity approaches 23% (consistent with that of Johnson (2011b)) whereafter it peaks in intermittent signals and then drops down once transition is completed. This peak in the turbulence intensity occurs with intermittent signals (theoretically at $\gamma = 50\%$) because these are effectively a combination of a laminar signal and a turbulent one, resulting in extremely high standard deviations due to the large difference between the laminar and turbulent means. This is further explained in conjunction with Equation 4-2 from Fasihfar and Johnson (1992) where the total standard deviation (u'_{TOTAL}) is markedly increased when there is both significant intermittency and

disparities between conditionally sampled mean laminar (L) and turbulent (T) portions of an intermittent signal.

$$u'_{TOTAL} = \gamma \overline{u'_T{}^2} + (1 - \gamma) \overline{u'_L{}^2} + \gamma(1 - \gamma)(\overline{u_L} - \overline{u_T})^2 \quad \text{Equation 4-2}$$

The near wall turbulence intensity for fully developed turbulence flow is approximately 40% in this instance, which is significantly higher than the 26% figure obtained by Klebanoff (1954), although this value is decreasing with Re_x , hence the turbulent boundary layer hasn't reached its final equilibrium.

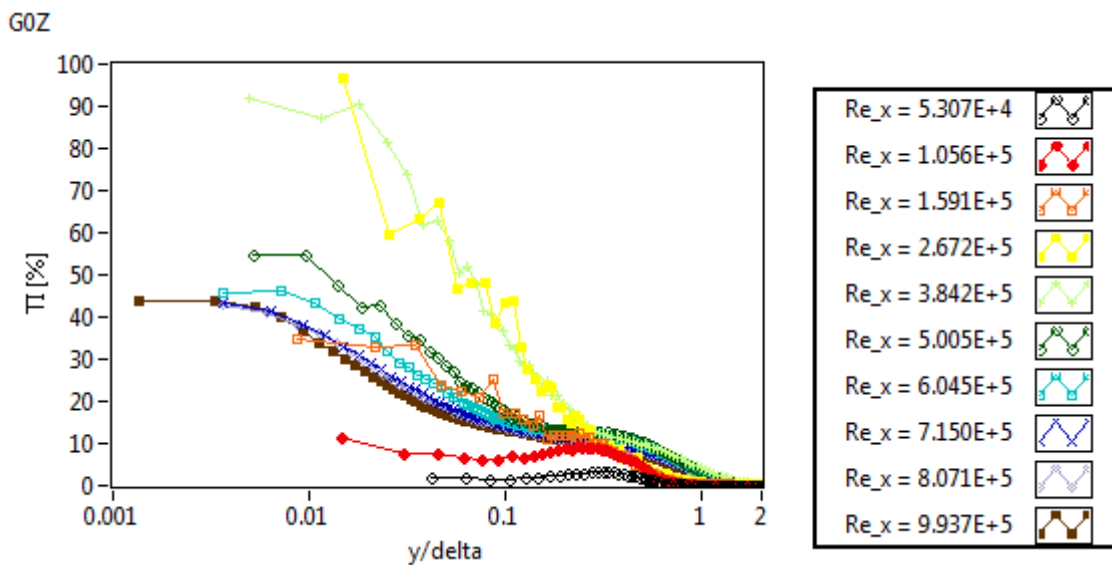


Figure 4-11 - Turbulence intensity distribution throughout different streamwise boundary layer profiles (G0Z)

The following two plots of Figure 4-12 and Figure 4-13 illustrate the u^+ versus y^+ profiles for the fully turbulent boundary layers identified from Figure 4-9. These two figures differ in that Figure 4-12 is a presentation of the original data fitted compared to both the viscous sublayer and law of the wall profiles, whereas in Figure 4-13 the profiles have been shifted by manually adjusting u_τ . This adjustment was only on the order of 10% but it allowed the log law to collapse within the y^+ values which would be expected and delayed the premature deviation from the viscous sublayer near the

wall. Qualitatively both profiles are similar and the effect of the change in u_τ is merely to translate the profiles in the positive u^+ direction.

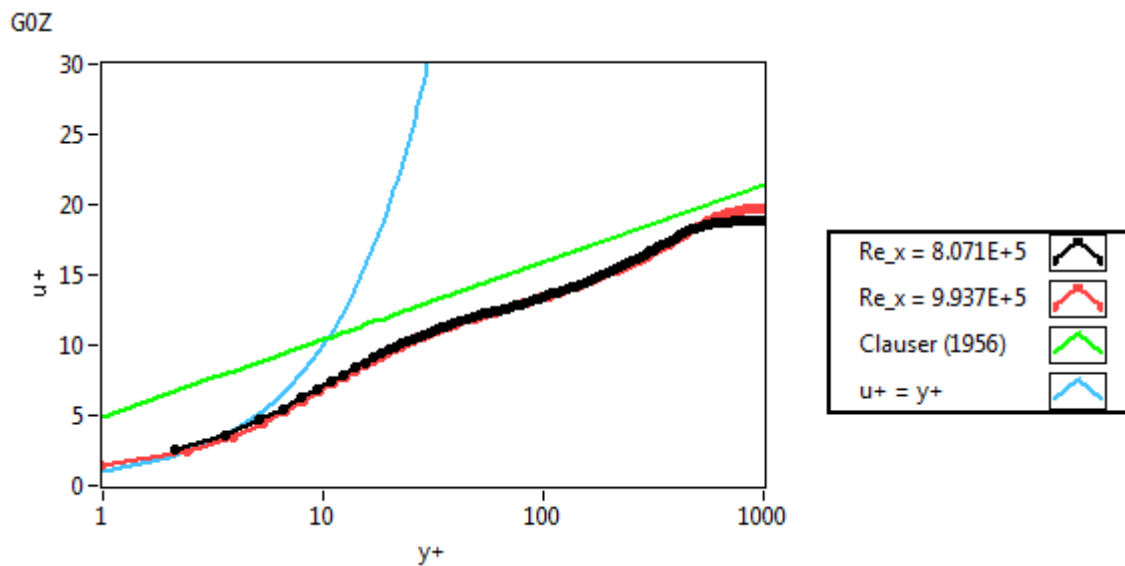


Figure 4-12 - Original $u^+ y^+$ plot for turbulent boundary layer profiles (G0Z)

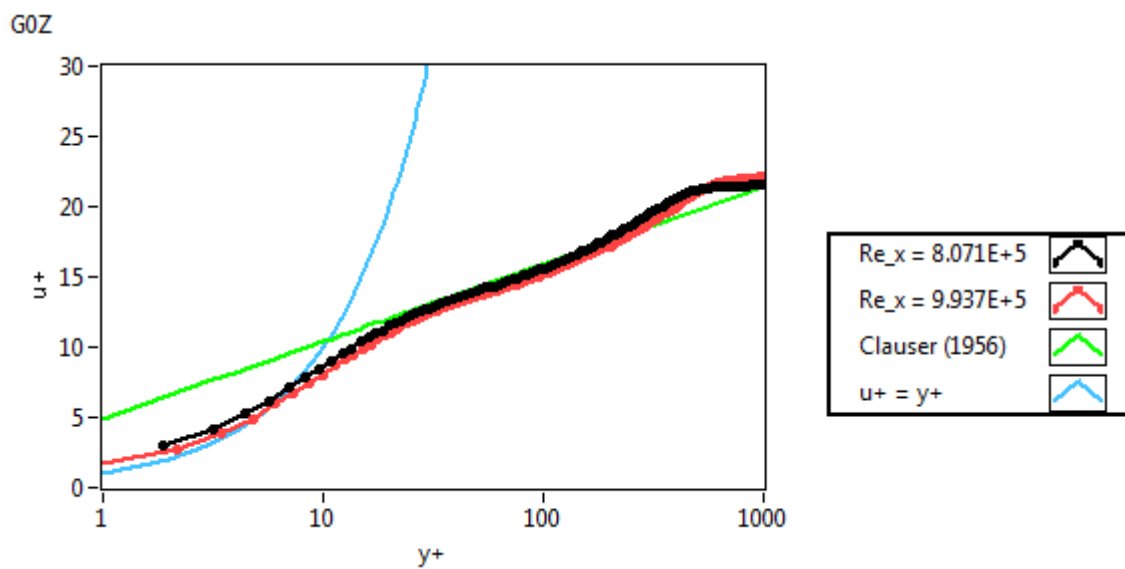


Figure 4-13 - Adjusted $u^+ y^+$ plot for turbulent boundary layer profiles (G0Z)

4.2.2 Streamwise Parameters under Zero Pressure Gradient (G0Z)

This sub section presents a comprehensive selection of parameters in the streamwise direction for the G0Z case, mainly the boundary layer integral parameters, where once more all plots are for unskewed traverses relative to the reference plane, i.e. a station bearing angle of 000°. First of all however a presentation is made of the near wall intermittency (as the mean of the first 10 points in the boundary layer – always within 30% of the boundary layer thickness) in Figure 4-14. This provides another graphic example of the non-linear evolution of the transition process. In regular unswept transition such profiles are often curve fitted to Narasimha profiles, as per Equation 2-19, so as to provide an accurate method of estimating the start and end of transition locations from the near wall intermittency measured at a sparse number of streamwise locations (in a manner similar to the procedure of Gostelow et al. (1994)) The relevant Narasimha fit has been included in Figure 4-14. However, the suitability of such an approximation is dependent upon the smoothness of the transition path and, as will be shown for later permutations, this is not always the case. Here the Narasimha fit deviates slightly from the observed intermittency path – particularly at $X = 500$ mm, perhaps owing to the absence of complete applicability in 3-D mean flows and also the distance over which the flow hovered at low, albeit non-zero, intermittencies in this G0Z case.

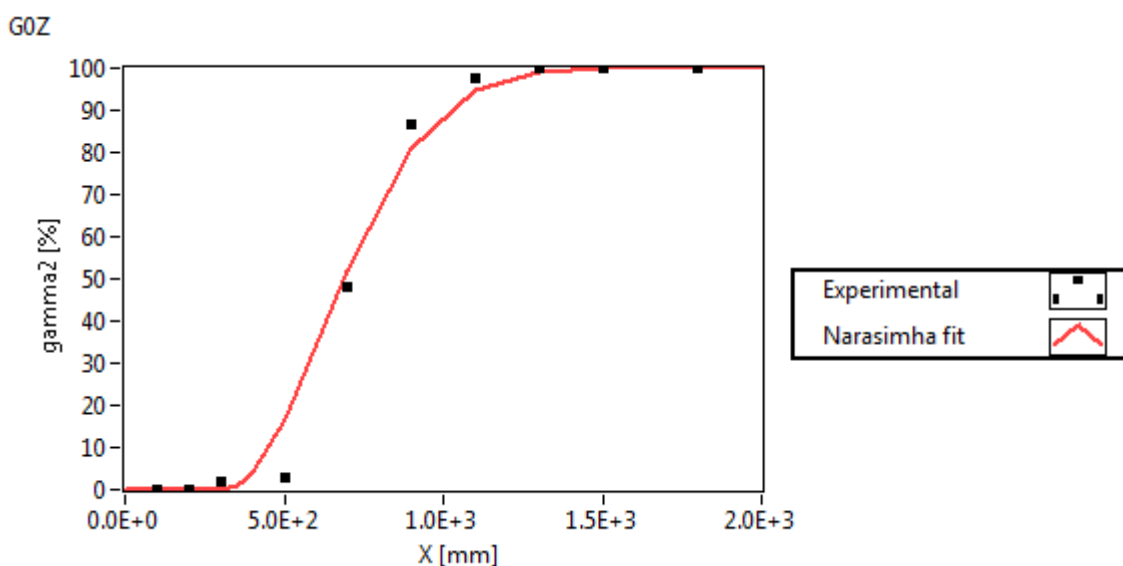


Figure 4-14 - Near wall intermittency versus streamwise displacement from leading edge with Narasimha (1957) fit (G0Z)

The boundary layer thickness and freestream velocities with respect to streamwise Reynolds number are illustrated for the G0Z case in Figure 4-15 and Figure 4-16. The freestream velocity, as a general trend, is seen to increase with Reynolds number, which is logical for a ZPG case owing to the displacement thickness of the boundary layer. However, whilst the magnitude the local freestream velocities plotted are similar – within approximately $\pm 2.5\%$ from the mean, the scatter is reasonably significant with respect to their differences and this can largely be attributed to variations in ambient conditions during the experimental tests having a significant influence on the recordings, despite notably the temperature correction procedures outlined in 3.12.4. The boundary layer thickness, regarded as being the first interpolated intercept to 99% of the freestream velocity, however doesn't suffer from a similar extent of scatter and for G0Z exhibits a relatively smooth increase with Re_x , albeit with a reasonable increased rate once transition is underway. This increase in growth rate is certainly in line with 2-D theoretical predictions of boundary layer growth, which on an unswept flat plate vary in proportion to $x^{0.5}$ for a laminar boundary layer and $x^{0.8}$ for a flat plate turbulent boundary layer obeying a $1/7^{\text{th}}$ power law in the range of $5 \times 10^5 < Re_x < 10^7$ White (1991). Note there are other power laws, e.g. a $1/9^{\text{th}}$ power law, which approximate the behaviour of turbulent boundary layers at higher Reynolds numbers than those experienced here, for example $10^6 < Re_x < 10^8$.

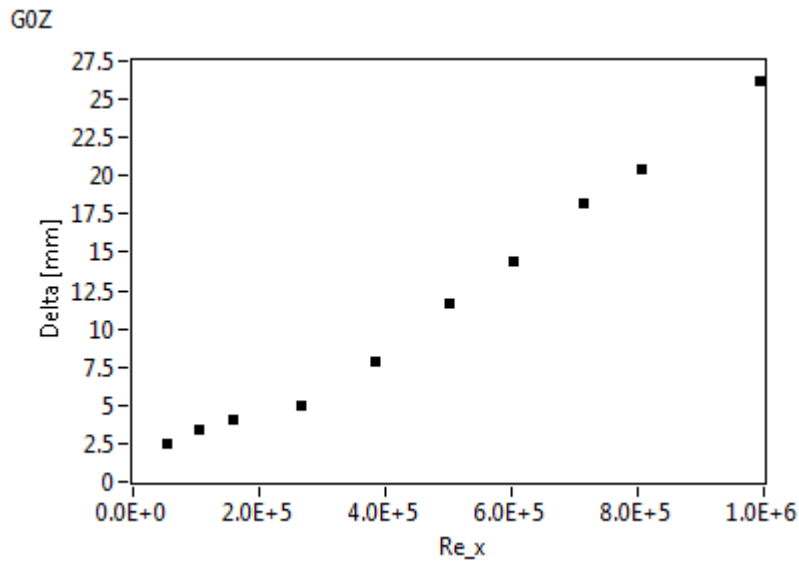


Figure 4-15 - Boundary layer thickness with streamwise Reynolds number (G0Z)

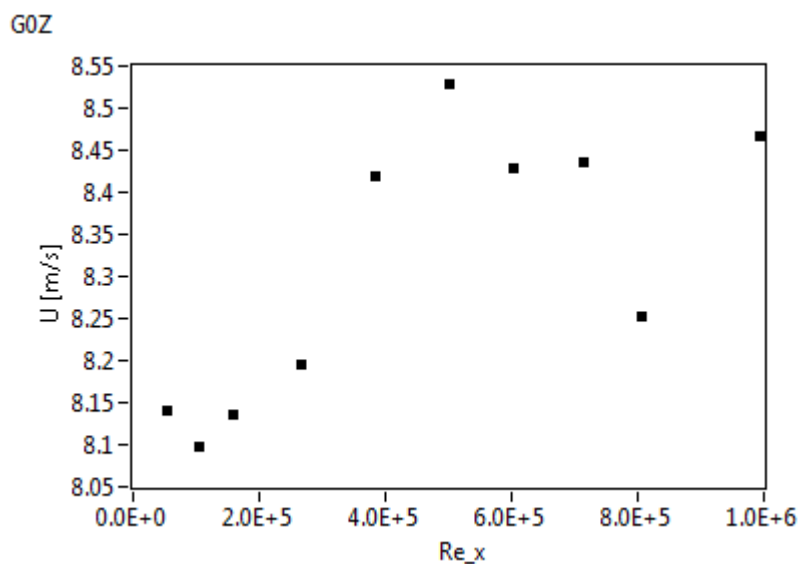


Figure 4-16 - Freestream velocity versus streamwise Reynolds number (G0Z)

Next consider the integral parameters of δ^* , θ , H and τ_w and C_f all for G0Z. Firstly the displacement thickness in Figure 4-17 shows a general increase with Re_x until just after transition commences where there is a drop in the displacement thickness before it begins a recovery and increases once more. This can be explained as during the initial phase of the transition θ remains relatively constant while the shape factor, H , is dropping hence by implication δ^* must decrease.

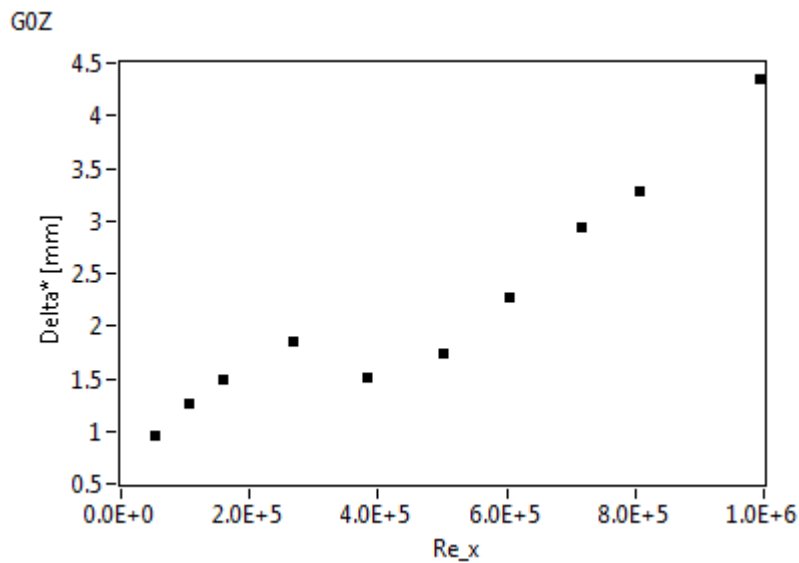


Figure 4-17 - Displacement thickness with streamwise Reynolds number (G0Z)

The momentum thickness, for G0Z, has similar characteristics to those of the displacement thickness – see Figure 4-18, only there is no observed reversal in its development and it progresses at a proportionally higher rate during transition where one observes a significant drop in the shape factor (see Figure 4-19) from their laminar values of approximately Blasius (2.6) to turbulent shape factors of approximately 1.4. The elevated laminar shape factors, relative to Blasius, can be attributed to the proximity of the initial profiles to the leading edge and the associated positive pressure gradient ubiquitous to all tests – see Figure 4-4. The turbulent shape factors appear to plateau to a stable value but it's also possible that with an increased order of magnitude in the Reynolds number that the shape factor would decrease further to approximately 1.3 but such an assumption is speculative. The main point, however, is that the shape factor does drop to a level typical of fully turbulent boundary layers.

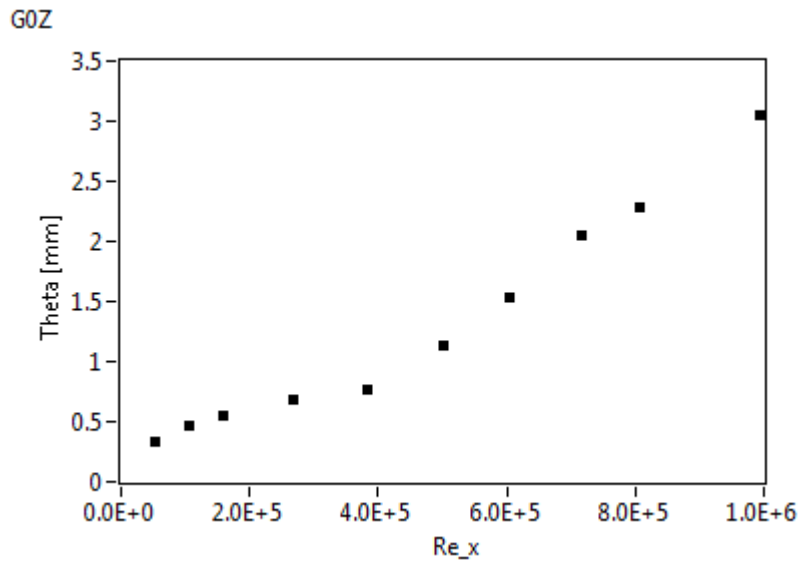


Figure 4-18 - Momentum thickness with streamwise Reynolds number (G0Z)

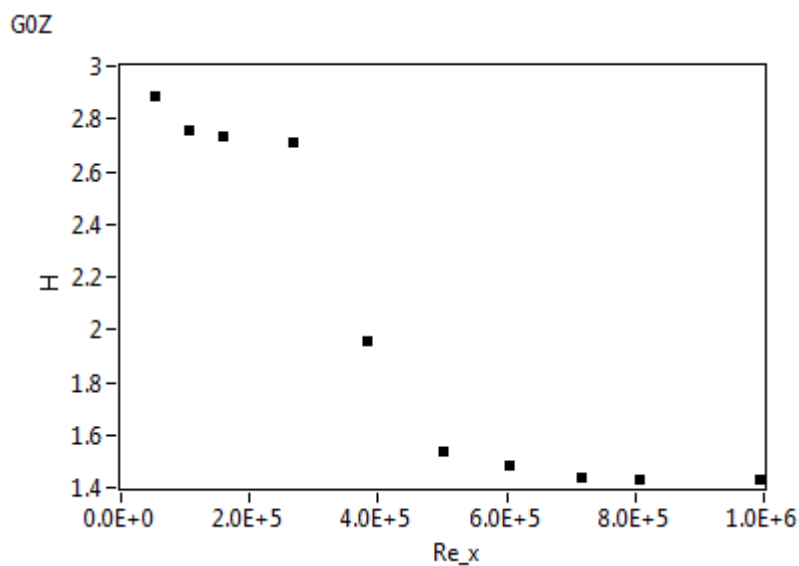


Figure 4-19 - Shape factor at various streamwise Reynolds numbers (G0Z)

The wall shear stress, τ_w , and skin friction coefficients, C_f , are displayed in the following two figures; Figure 4-20 and Figure 4-21. They adhere to qualitatively very similar trends where the skin friction drops in the laminar boundary layer before escalating dramatically in the transition region, both parameters drop thereafter once transition has been accomplished. As such the onset of transition is considered by some, for example Hallbäck (1996), to be marked by the minimum value of C_f . However, once more, the reliability of making such a determination is impeded by the inherent

uncertainties in measuring skin friction with a hot-wire probe, due to proximity errors, limited data near the wall, additional heat losses caused by the measuring surface on the wire and a reliance on serendipity for honing in on a parameter which changes so rapidly. This is in contrast to the integral parameters which are evaluated on the basis of a much larger number of points, even including those beyond the boundary layer thickness.

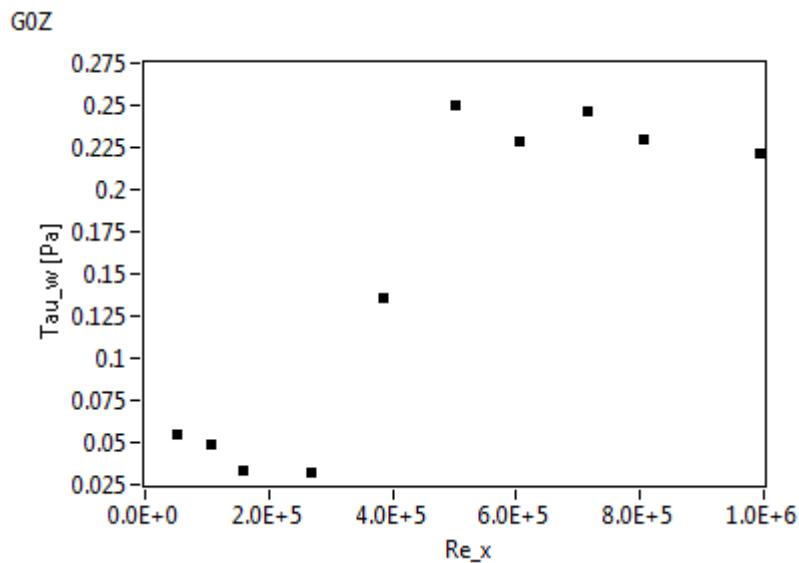


Figure 4-20 - Near wall shear stress versus streamwise Reynolds number (G0Z)

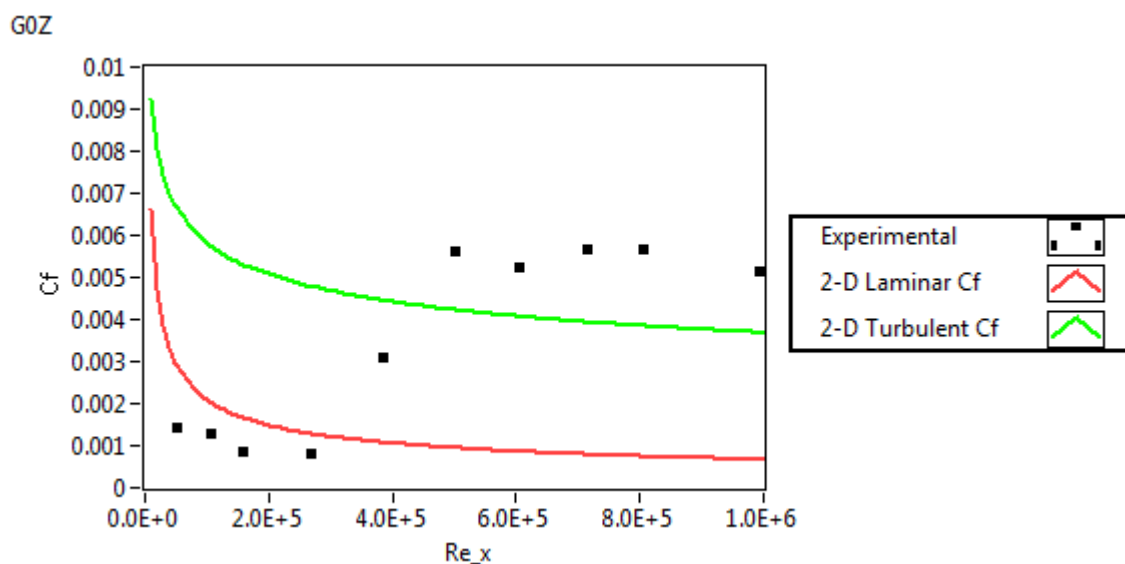


Figure 4-21 - Skin friction coefficient with streamwise Reynolds number (G0Z)

Comparisons between the theoretical skin friction coefficients in 2-D boundary layer flows and the experimental results for G0Z have been provided in Figure 4-21. The 2-D C_f values for comparison are as follows;

$$C_{f|lam} = 0.664Re_x^{-0.5} \quad \text{Equation 4-3}$$

$$C_{f|turb} = 0.0592Re_x^{-0.2} \quad \text{Equation 4-4}$$

The C_f values (Equation 4-3 and Equation 4-4) have been sourced from Schlichting (1979) where $C_{f|turb}$ is with respect to experimentally measured $1/7^{th}$ power law flat plate turbulent boundary layers in the range of $5 \times 10^5 < Re_x < 10^7$.

From Figure 4-21 one can observe that the qualitative similarities between the 2-D profiles and those of the 3-D experimental data (aligned with the flow). Quantitative differences are to be expected given the differences between the two base flows but the presentation does offer some assurances in that the data resolved is of similar order. It was interesting to note that the experimentally measured laminar profiles undercut Equation 4-3 whereas the opposite was observed between Equation 4-4 and the turbulent profiles.

4.2.3 Flow Angles (G0Z)

Significant effort was invested to resolve the mean flow angles, notably to determine the evolution of the crossflow in these three dimensional boundary layers. The method used in order to achieve this was outlined in section 3.7 and the following plot of Figure 4-22 represents those efforts for G0Z. There are several readings which appear to be in error which can perhaps be partially attributed to the algorithm outlined in section 3.7 but more significantly the traverse angles selected heavily influence the resolved mean flow angles which manifest themselves as significant changes in the intermittency and the local mean velocity therefore. It should be noted that other researchers (for example those at DLR) have used 'V' boundary layer probes to directly measure the leading edge

tangential and perpendicular components directly (L_x and L_z aligned in Figure 3-15) but even were these probe arrangements to be available the lack of a plurality in CTA modules wouldn't have permitted their use. The results presented for G0Z use the following traverse skew bearing angles; 000, 350 and 325. These choices, on the whole, appeared to result in the correct determination of the flow angle. The observations made can be summarised as follows. Firstly near the wall the mean flow angle tends to increase in magnitude in a somewhat linear fashion (see the non-log plot of Figure 4-23) which is consistent with the observations of Klinksiek and Pierce (1973) on three-dimensional turbulent boundary layers. Secondly the gradient in angle near the wall tends to be steeper for the laminar profiles and then mixes out with increased turbulence as the streamwise Reynolds number increases, the anachronism being the cases during early transition, which will either be a physical reality (in an undisturbed flow) or the result of the boundary layer being particularly sensitive to traverse skew with stability already reaching its natural limits, in other words inciting a super critical perturbation. Finally the mean flow angles beyond the boundary layer thickness tend towards the approach flow direction. The offset from 0° could be attributed to a very small misalignment of the traverse with respect to the measuring plane and/or a contributing influence of the elliptical traverse body, which may possess its own Reynolds number dependence with respect to a characteristic length of the shape.

Some of the points which were in error are clearly visible in Figure 4-22 where the algorithm used to resolve the mean flow angles can't locate a maximum within the range and merely returns the values attempted on the final iteration of the loop. A significant cluster of such points is observed at around 30° in Figure 4-22 near the wall for the early transitional Re_x values where the transition is likely to be most sensitive to perturbations, such as that which could be incited when skewing the traverse.

G0Z

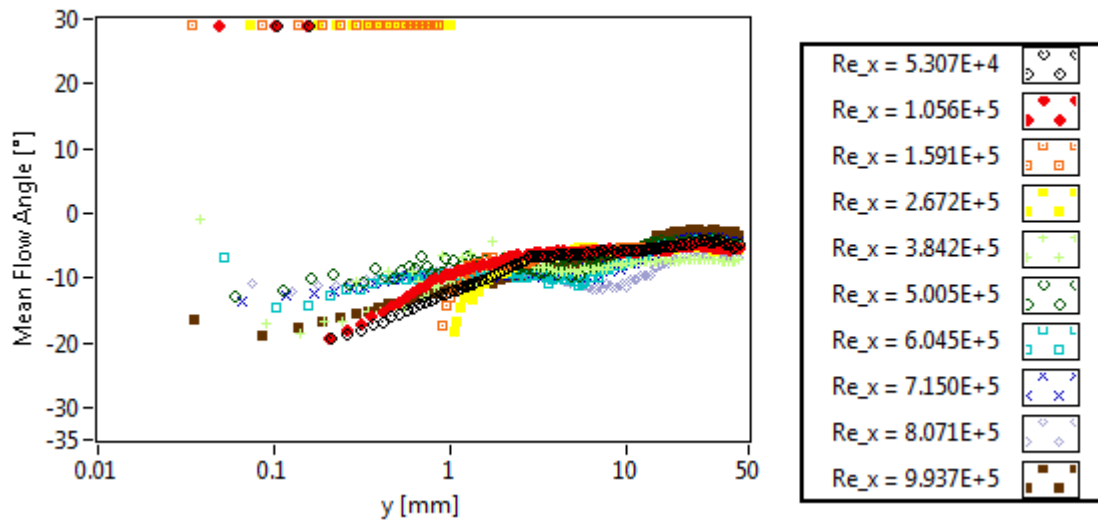


Figure 4-22 - Mean flow angles versus wall normal displacement (G0Z)

G0Z

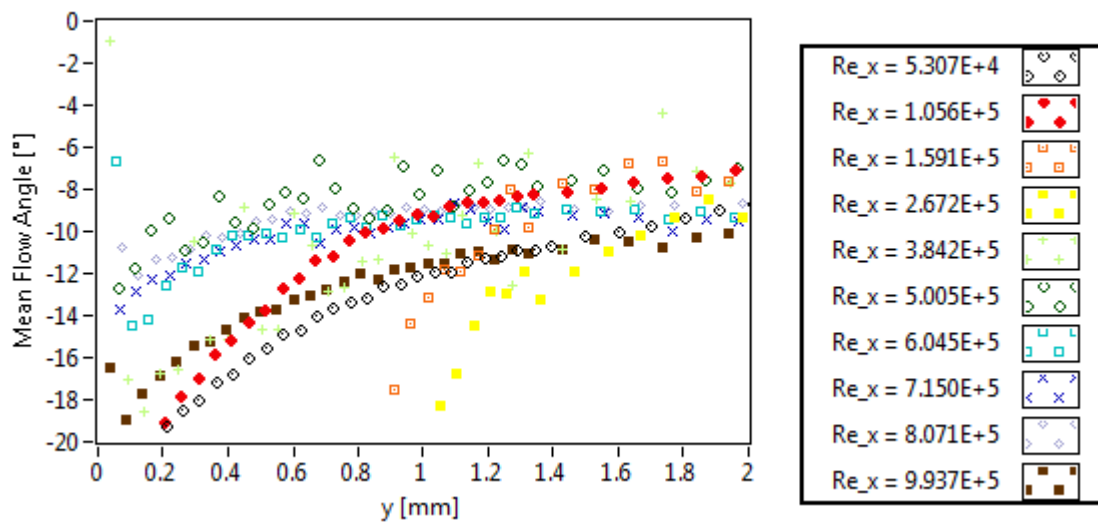


Figure 4-23 - Measured mean flow angles versus wall normal displacement non-log plot (G0Z)

Figure 4-24 and Figure 4-25 have been compiled to illustrate some of the general flow angle characteristics which were observed. This particular compilation does not conform to any of the standard test cases and was in fact merely a preliminary test performed outwith the main test program and executed using the vertical grid at a low tunnel speed, approximately mid-way through the transition process. Figure 4-24 represents the mean velocity distribution near the wall at various traverse skew angles whereas Figure 4-25 displays the same parameters, only further out towards

the boundary layer periphery/freestream as one can deduce from comparisons between the wall normal displacements listed in the two legends. Both near the wall and further out towards the freestream the profiles are seen to deviate from the theoretical cosine distribution. This is marked by a kink downwards in the unskewed traverse (0°). Furthermore higher velocities are omnipresent for the negative skew angles and hence one would therefore assume that the skewed flow is aligned in that direction. However, it is also possible that additional skew was instigated merely by the changing the angle of attack of the traverse which is perceived asymmetrically.

Two methods of testing this hypothesis were considered but neither were executed. One was to modify the traverse such that the probe was pitched on the opposite side of the elliptical body and then repeat the previous exploratory test. The other possibility was to repeat the test in a non-skewed facility – namely the suction tunnel at the University of Liverpool, where the mean spanwise flow should be zero and hence one would expect a cosine distribution which was symmetrical about zero degrees. However the latter option was not made available upon request and the former was discarded owing to the latency involved when requesting modifications, particularly those which may subsequently be reversed to the original specification, to equipment at the current level of throughput afforded and the time pressures accrued with substantial delays in getting to the position of executing experiments.

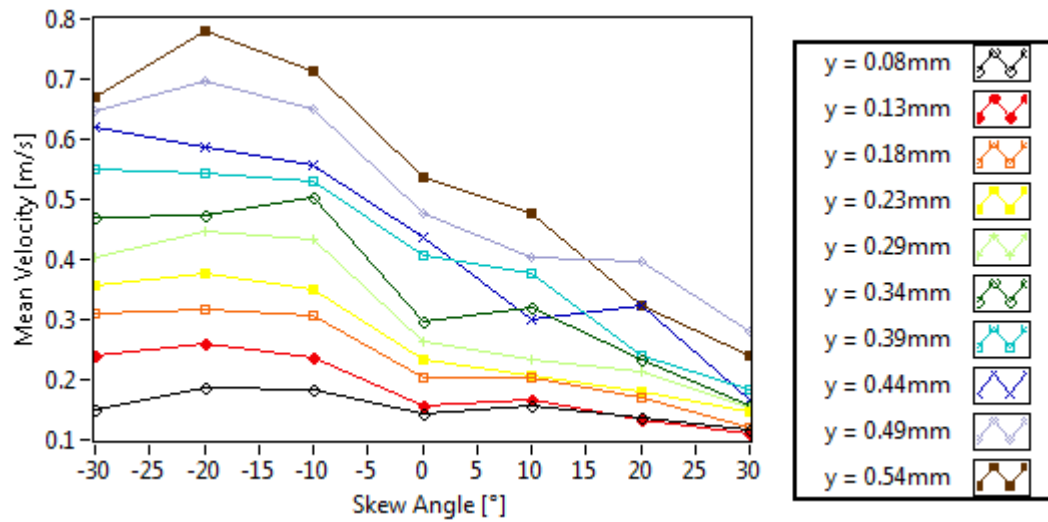


Figure 4-24 - Near wall velocity distribution across various skew angles (arbitrary test case)

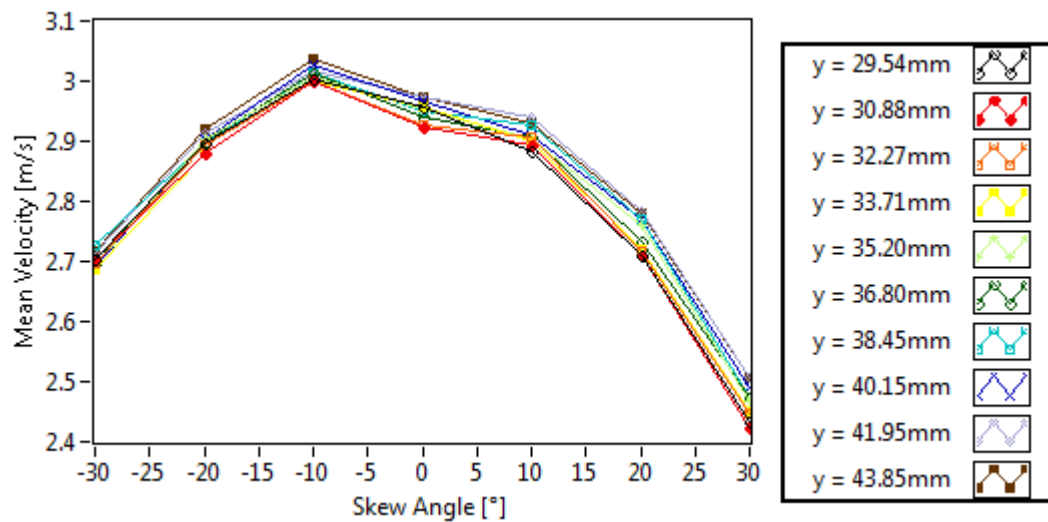


Figure 4-25 - Freestream velocity distribution across various skew angles (arbitrary test case)

4.2.4 Falkner-Skan-Cooke Comparisons (G0Z)

The Falkner-Skan-Cooke equations have been numerically solved using a shooting method implemented in a Fortran code. This particular Fortran code makes use of a predictor-corrector routine where the corrector phase is looped until satisfying a convergence criteria, which ultimately forces a solution down to numerical precision, with respect to the allocation of double memory for the 1-D arrays of $-f$, f' , f'' , g and g' . There are freely available (open source) alternatives for solving these equations, see for example the MATLAB code of Hoepffner (2006). The following figures are

presented to re-emphasise some of the salient features relevant to boundary layers with sweep and pressure gradient, where all data is presented for a sweep angle, θ of 60° . Firstly Figure 4-26 demonstrates the similarity profiles for f' and g , which represent an analogue of the normalised velocity profiles in the streamwise and spanwise direction, relative to the leading edge,. These are then resolved into components relative to the tunnel coordinate system (with unity velocity scaling) rather than the sweep angle, as per Figure 4-27. Note the inflection which is present in the spanwise velocity (w) for both positive and negative values of m , owing to the profiles returning back to 0 in the freestream.

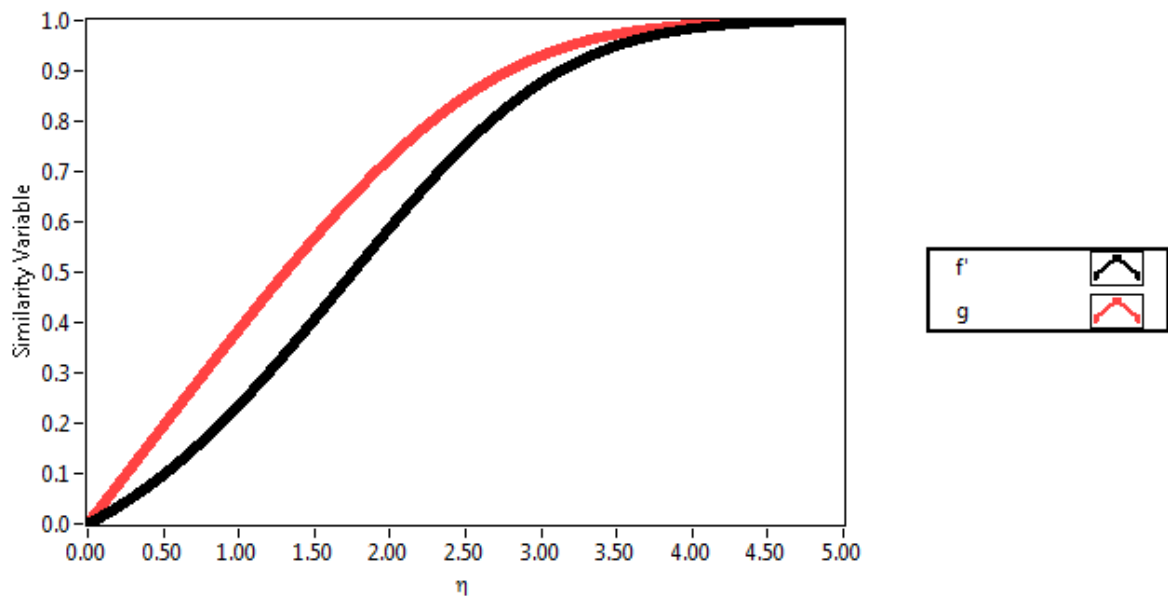


Figure 4-26 - Plot of similarity variables f' and g versus η ($m = -0.08$)

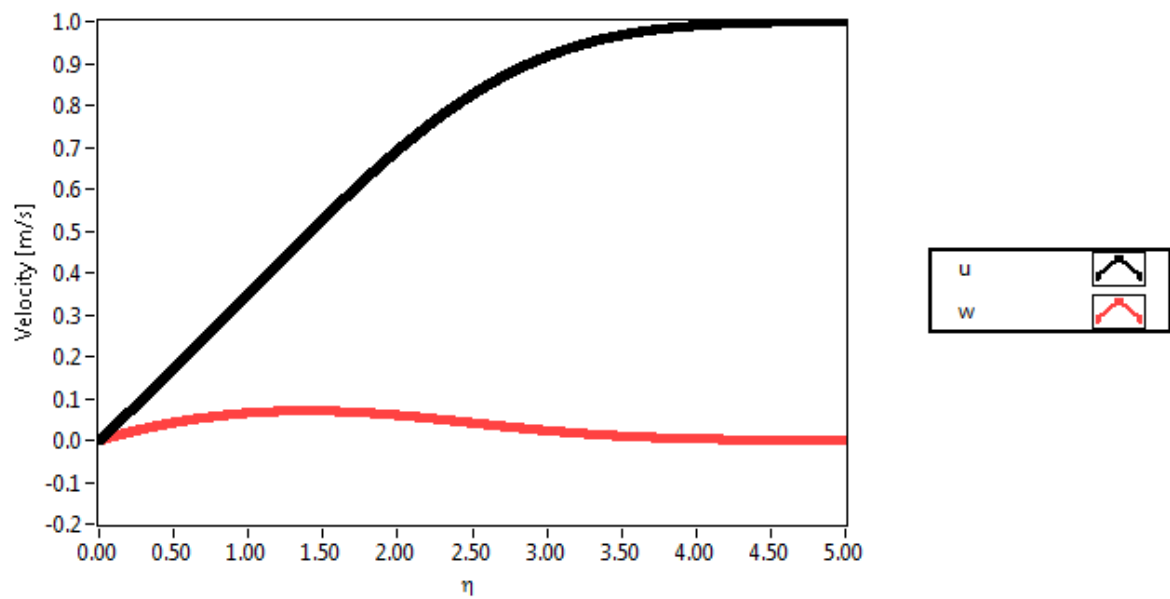


Figure 4-27 - Streamwise and spanwise velocities versus η ($m = -0.08$)

The same procedure has been executed for a positive m value of 1 to produce Figure 4-28 where the crossflow is observed to skew in the opposite direction. Furthermore the special case of Blasius flow ($m = 0$, Figure 4-29) is also provided which clearly demonstrates the absence of crossflow and therefore skew, as is to be expected.

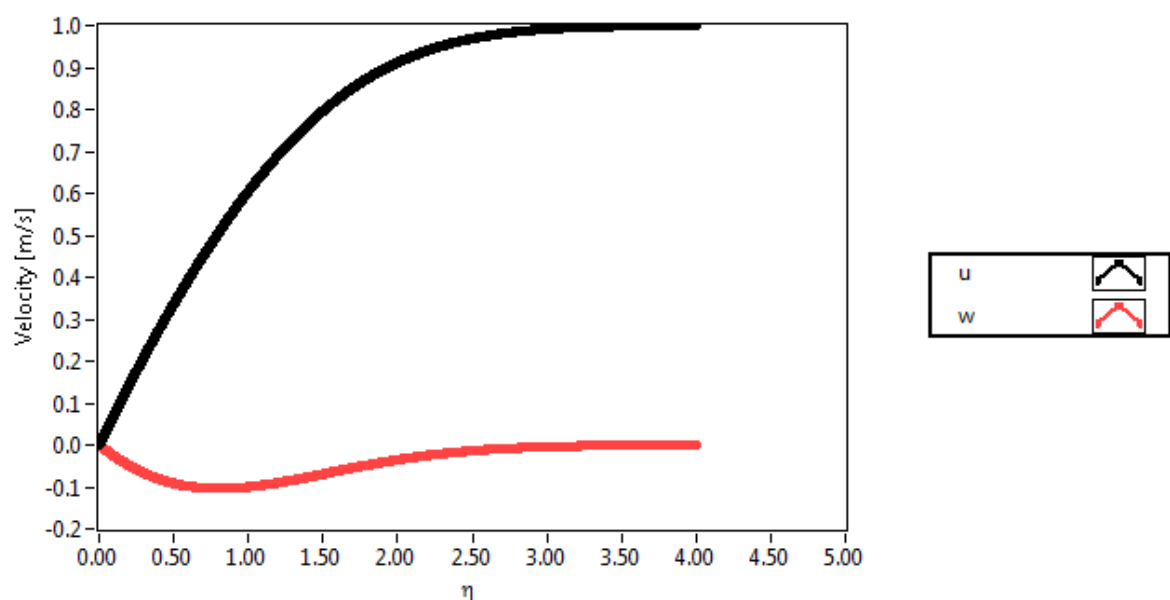


Figure 4-28 - Streamwise and spanwise velocities versus η ($m = 1$)

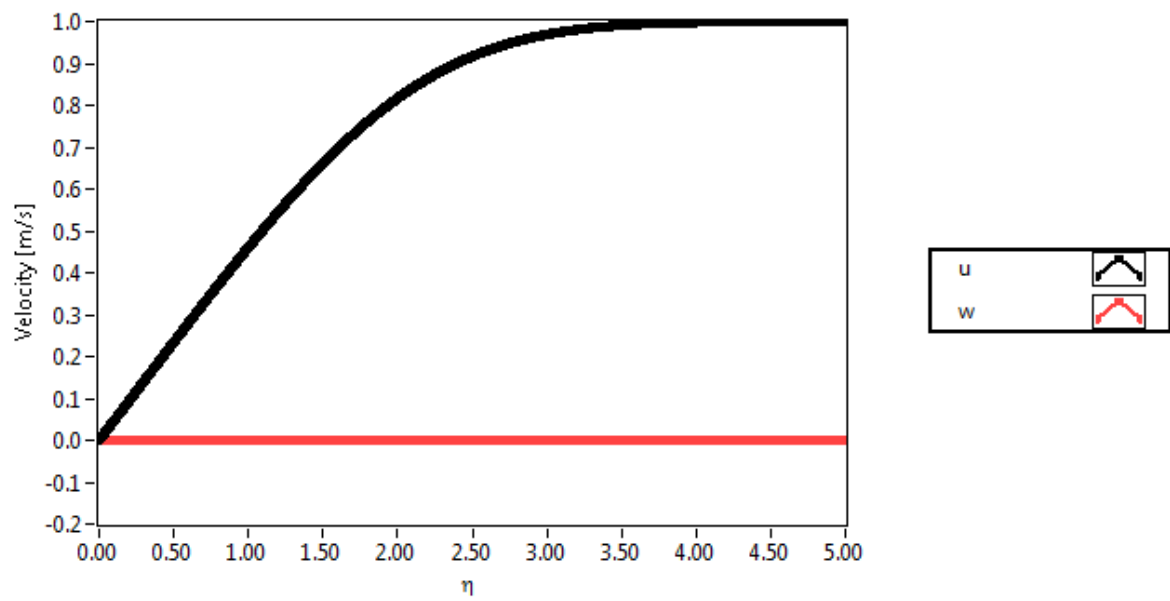


Figure 4-29 - Velocity magnitudes for the special case of Blasius flow ($m = 0$)

Figure 4-30 has been provided so as to demonstrate a match with the profiles offered by Stemmer (2010) – see Figure 2-9 in sub-section 2.5.1.

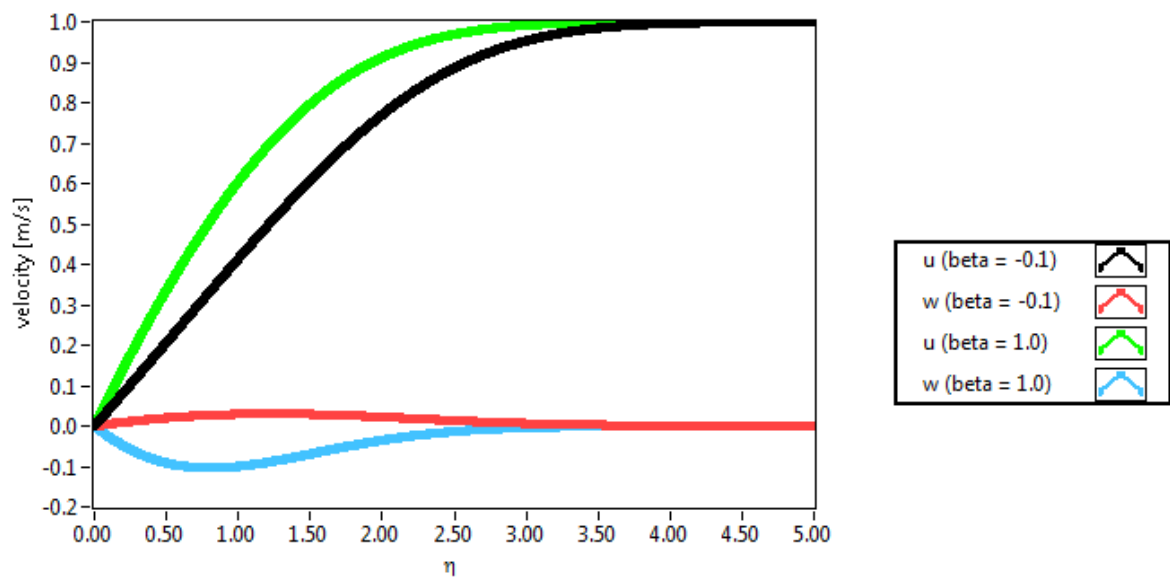


Figure 4-30 - Match with Stemmer (2010) for Falkner-Skan-Cooke profiles at β_H equals -0.1 and 1.0 and $\theta = 60^\circ$

Returning to the experimental measurements of G0Z, the deduced results from the mean flow angles are compared with the profiles which are obtained using the idealised Falkner-Skan-Cooke profiles in this sub-section. The aforementioned comparison is made for G0Z in Figure 4-31 where the m (Equation 2-30) and therefore β_H (Equation 2-31) - the Hartree parameter is varied so as to obtain a fit in the near wall region for mean flow angle versus wall normal displacement, y . Note for the Falkner-Skan-Cooke profile that y , scaled with respect to the G0Z freestream velocity, leading edge displacement and kinematic viscosity at the calibration station ($X = 100$ mm), was deduced from Equation 2-32;

and therefore;

$$y = \frac{\eta}{\sqrt{\frac{m+1}{2}} \sqrt{\frac{U}{\nu x}}} \quad \text{Equation 4-5}$$

$$MFA_{FSC}(y) = -\text{atan}\left(\frac{w(y)}{u(y)}\right) \quad \text{Equation 4-6}$$

The mean flow angles for the Falkner-Skan-Cooke profiles (denoted MFA_{FSC}) were resolved by first converting the $f'(y)$ and $g(y)$, into $u(y)$ and $w(y)$, with respect to Equation 2-36 and Equation 2-37 and then applying Equation 4-6. Equation 4-6 contains a negative term such as to make direct comparisons with the experimental results which were recorded with a reversed convention for the spanwise coordinates.

Falkner-Skan-Cooke profiles are fully constrained with the choice of two parameters only; these being the sweep angle and m . It was found, in this instance, that an m value of -0.087 provided a reasonable fit to the data in the near wall region, where of course the sweep angle is fixed at 60° so as to replicate the experimental configuration. Outwith the near wall region, however, the two profiles don't appear to collapse. G0Z deviates from its initial linear gradient trajectory which

becomes reduced and thereafter seems to plateau at -5° in the freestream. As $y \rightarrow \infty$ one would expect the mean flow angle to return to zero in the case of zero pressure gradient as there is no intended vectoring of the approach flow through the sidewall profiles.

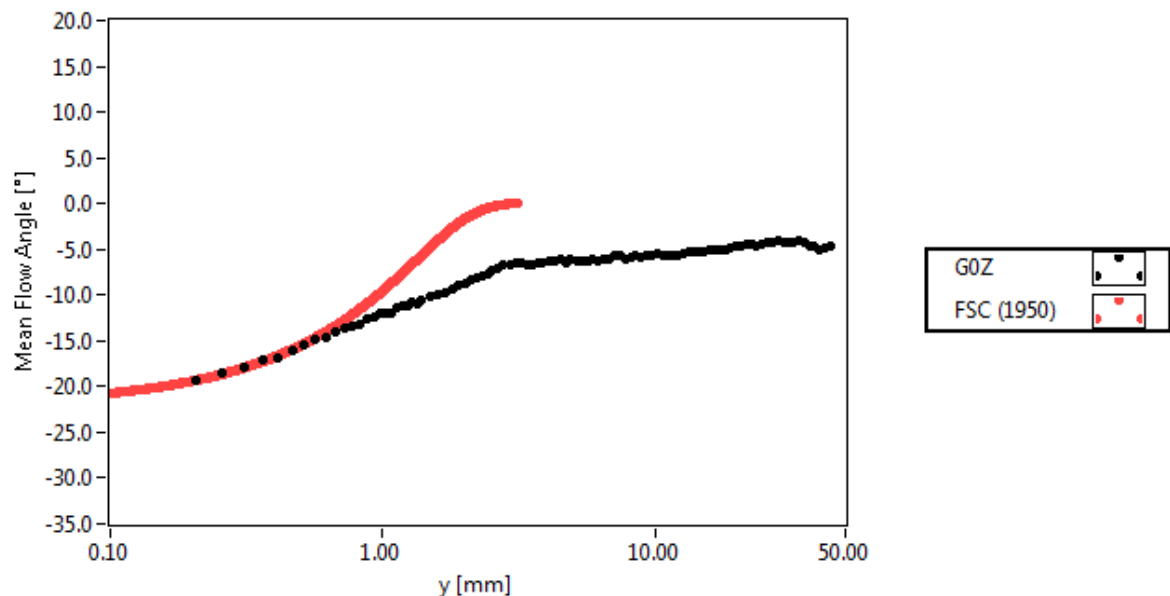


Figure 4-31 - Comparison between experimentally measured mean flow angles (G0Z) and Falkner-Skan-Cooke (1950) boundary layer profiles

Experiments never return exact replicas of their respective theoretical postulates but this would appear to be a significant deviation from the ideal profiles. The reasons for such a deviation have already been discussed in sections 3.7, 4.1 and 4.2.3, which highlighted the influence of skewing the traverse on the measured intermittency and static pressure distributions among other factors. Further to the already noted comments in section 4.6 some of the flow quality issues experienced across the span of the plate are also highlighted. An improved fit, however, which can be considered as being primitive compensation for the undesirable spanwise flow variations, is presented in Figure 4-32. Here the profile has been refitted with an arbitrary offset angle of 6° which approximately corresponds to the average flow angle measured in the freestream. On this occasion $m = -0.074$ provided a reasonable fit.

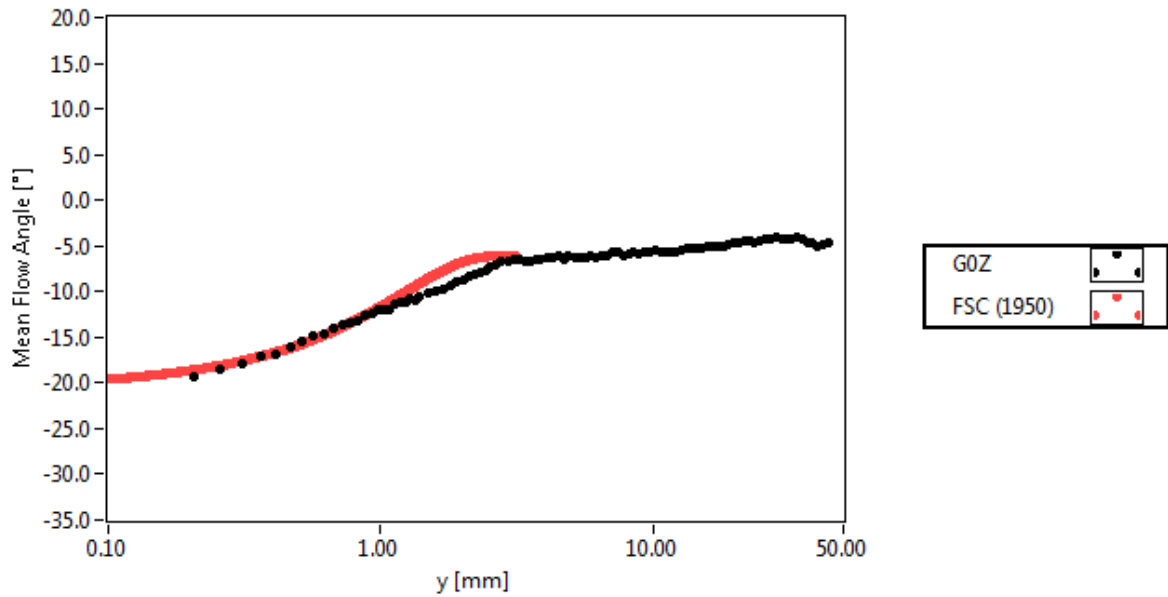


Figure 4-32 - Corrected Falkner-Skan-Cooke profiles with angle offset (G0Z)

4.2.5 G1Z

The normalised velocity profiles for the G1Z case are illustrated in Figure 4-33 where one can observe that there are minimal differences between these profiles and those of G0Z (Figure 4-7) on the peripheries of the overall transition process, other than there are more profiles in the transition region in G1Z and thus the overall process is better resolved. One slight anachronism is observed in Figure 4-34 in that the skin friction coefficient appears to be larger than for the upstream and downstream neighbours for the penultimate traverse ($Re_x = 4.725 \times 10^5$). There is no particular reason why this should physically be the case and it may be brought about by the first point in the boundary layer profile being displaced further from the plate surface than the following trace ($Re_x = 5.681 \times 10^5$).

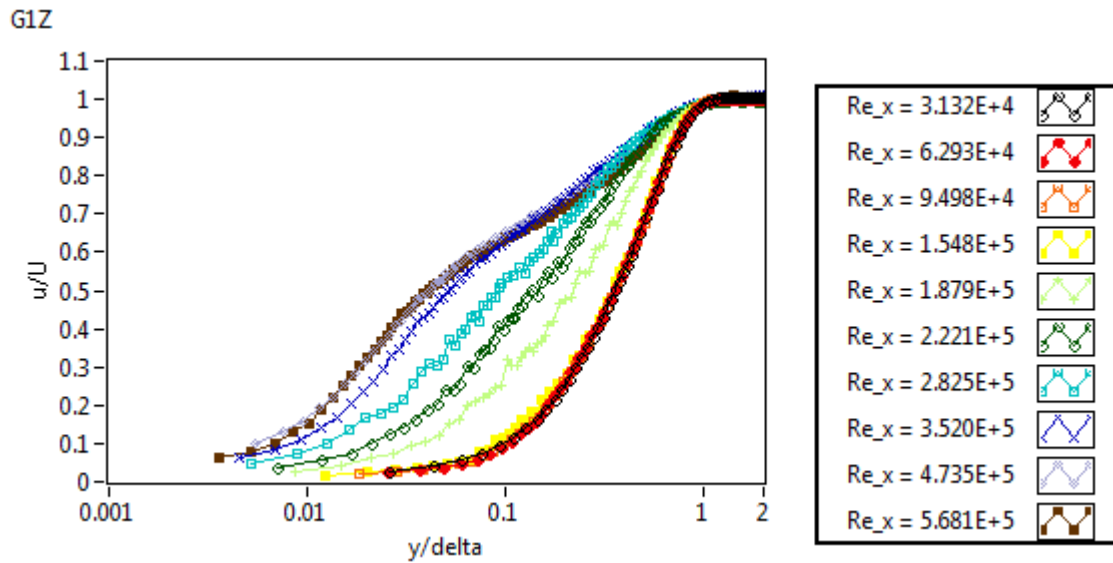


Figure 4-33 - Normalised velocity profiles (G1Z)

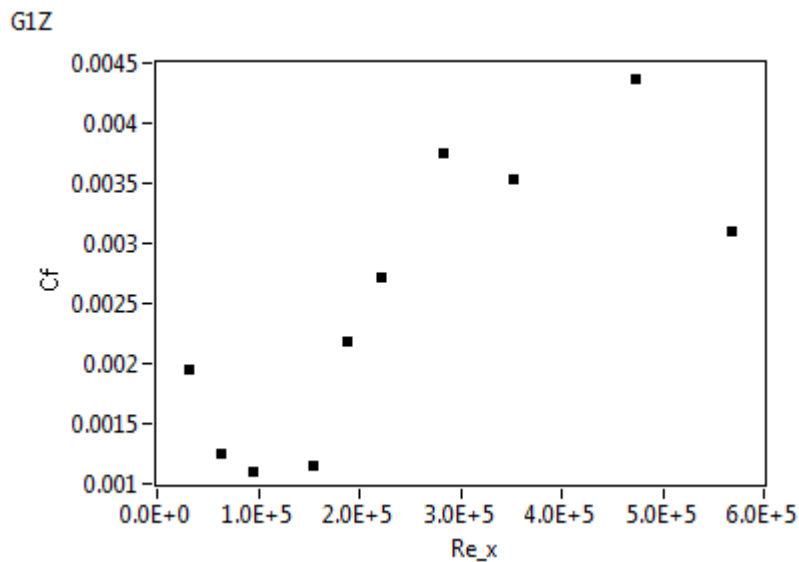


Figure 4-34 - Skin friction coefficient versus streamwise Reynolds number (G1Z)

For this G1Z case transition was observed to commence at $x_s = 138.2$ mm (where $Re_{x_s} = 4.34 \times 10^4$) until $x_e = 1420.8$ mm ($Re_{x_s} = 4.06 \times 10^5$) where transition was deemed to have been completed. The results for this case, and in fact all 9 cases, are summarised in Table 4-1 in section 4.5 where a collective analyses of all of the results are presented.

4.2.6 G3Z

The normalised velocity profiles for the G3Z case are represented in Figure 4-35 and the respective near wall intermittencies in Figure 4-36. From these two figures one can observe that only one laminar profile is present for this pressure gradient and turbulent grid combination – i.e. G3Z. This is certainly better than not having any laminar profiles to refer to but it's operating on the limits of acceptability given that it was resolved at the earliest station on the plate – 50 mm from the leading edge. In spite of this there are certainly sufficient points throughout the first ($Re_x = 1.009 \times 10^4$) and all subsequent boundary layer profiles for G3Z such that they are well resolved. That said it would appear from Figure 4-36 that the first station is right on the cusp of transition inception and as such significant uncertainty in reliably quantifying the point at which transition commences is expected.

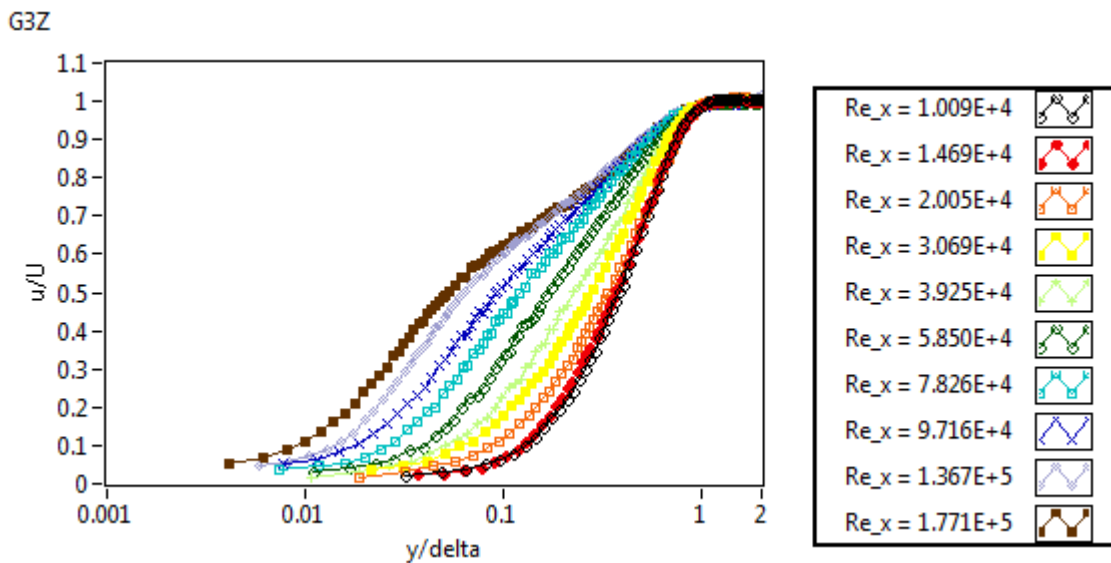


Figure 4-35 - Normalised velocity profiles (G3Z)

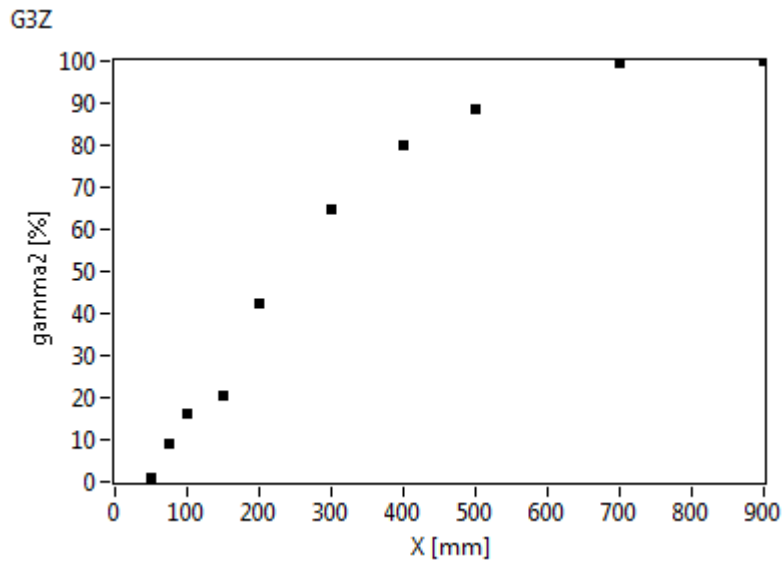


Figure 4-36 - Near wall intermittency versus leading edge streamwise displacement (G3Z)

Another issue with respect to the results gathered for G3Z concerned the skin friction coefficient profiles which at a glance appear to offer a confusing account of events but, whilst the evolution through the transition region isn't the smoothest, there is a general trend of increasing C_f until transition is complete. Once transition has been completed there is a further apparent increase in C_f but, once more, this is likely due to the difficulty in measuring C_f indirectly through hot-wire measurements.

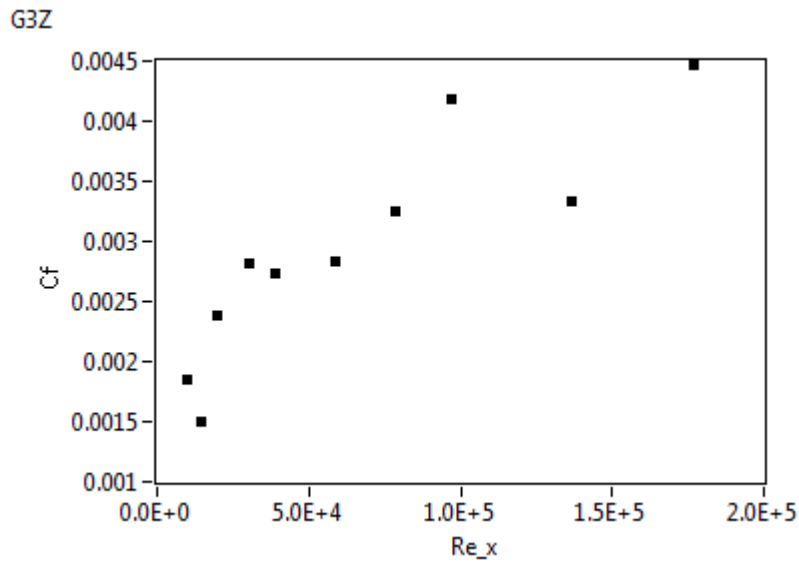


Figure 4-37 - Skin friction coefficient versus streamwise Reynolds number (G3Z)

4.3 Positive Pressure Gradient (GxP)

4.3.1 GOP

Naturally one would expect there to be significant differences between the zero pressure gradient cases and those of positive pressure gradients, and that certainly appears to be the case for GOP. For all of the non-zero pressure gradient cases, the non-zero pressure gradient starts at 700 mm from the leading edge, albeit physically it may start later due to the blockage caused by the boundary layers inside the test section – see Figure 4-2 where for the GOP case the pressure gradient become significantly positive after 1.5 m. Firstly one can observe from Figure 4-38 that the second and third traverses, corresponding to $Re_x = 3.097$ and 6.314×10^5 , inflect below the first traverse taken at $Re_x = 6.567 \times 10^4$. This represents an inflection in the boundary layer profiles, an effect which is more visible in non-logarithmic, albeit still non-dimensionalised format, as per Figure 4-39.

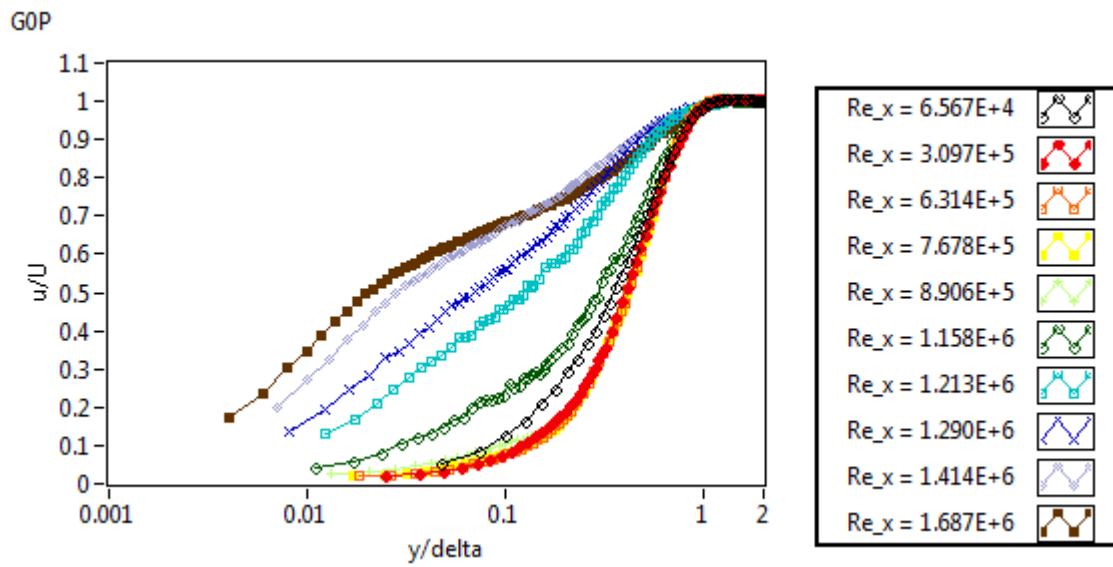


Figure 4-38 - Normalised velocity profiles – log plot (GOP)

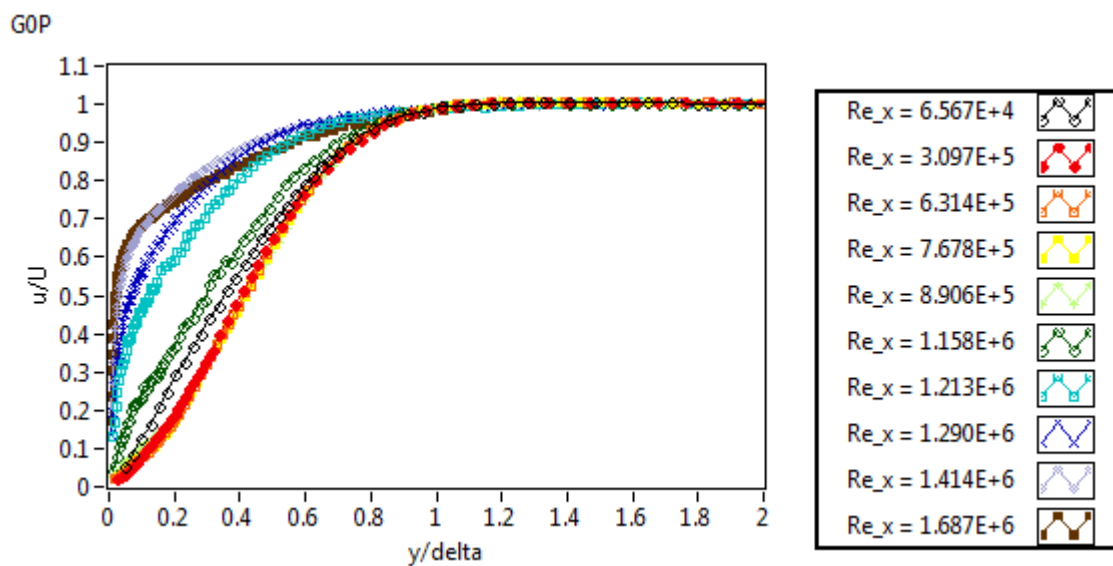


Figure 4-39 - Normalised velocity profiles (GOP)

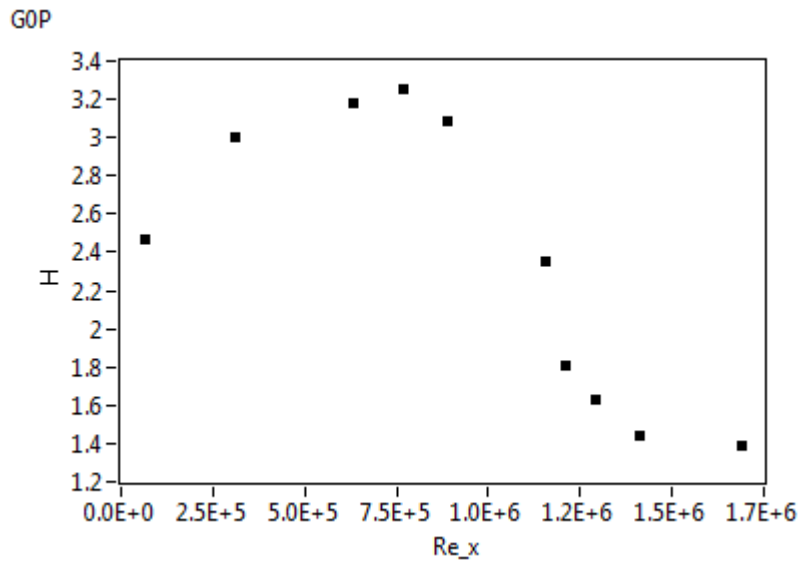


Figure 4-40 - Shape factor versus streamwise Reynolds number (GOP)

The aforementioned dip in the boundary layer profiles is clearly observed in the shape factor plot of Figure 4-40 where the shape factor is seen to increase until transition is observed to commence with the advent of non-zero intermittency – see Figure 4-41. One may postulate that this behaviour of apparent stabilisation can be attributed to the corresponding ZPG case (G0Z) having its transition initiated by crossflow instabilities which are suppressed through the action of positive pressure gradients and thereafter the transition develops once the streamwise instabilities (TS waves) have reached sufficient amplitude such that turbulent spots are produced.

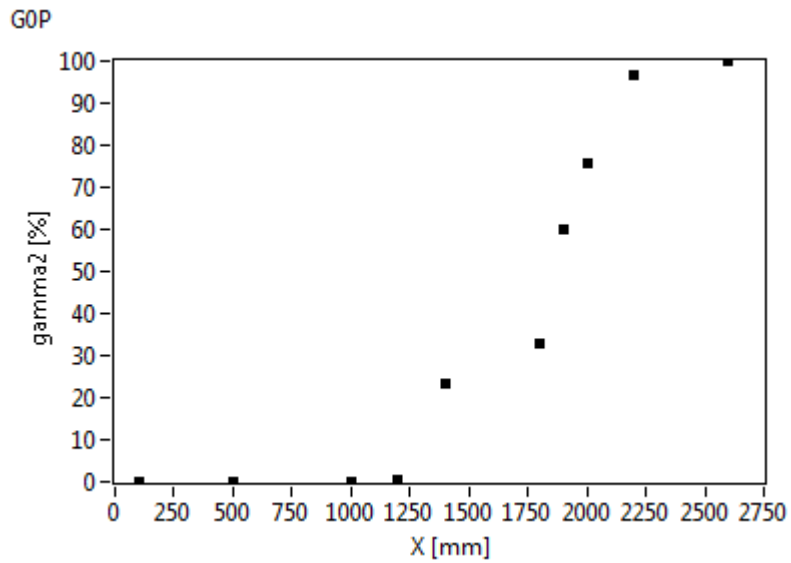


Figure 4-41 - Near wall intermittency versus leading edge streamwise displacement (GOP)

Figure 4-42 illustrates the displacement thickness distribution with respect to streamwise Reynolds number for GOP and from this plot one can observe a somewhat unconventional profile with a sustained dip in displacement thickness following the onset of transition. Whilst the peak shape factors observed in Figure 4-40 are below those expected for separation of the bulk flow to occur there could perhaps be a small but nevertheless significant local separation bubble, followed by a local acceleration.

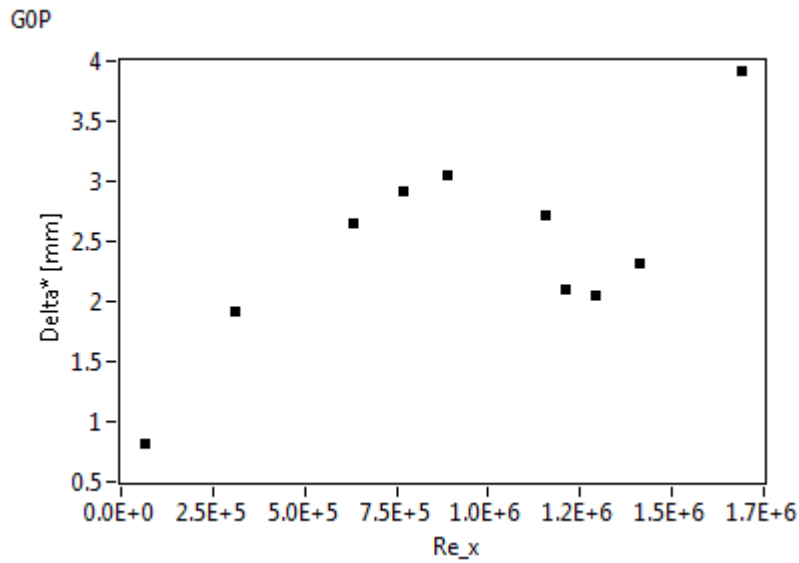


Figure 4-42 - Displacement thickness against streamwise Reynolds number (G0P)

Another interesting observation is present in Figure 4-43 which depicts the evolution of the boundary layer thickness with Re_x . Here it is seen that the boundary layer undergoes fairly typical growth in the laminar region (e.g. $x^{0.5}$) but thereafter near linear growth with the onset of transition, which one would generally consider to be fairly rapid.

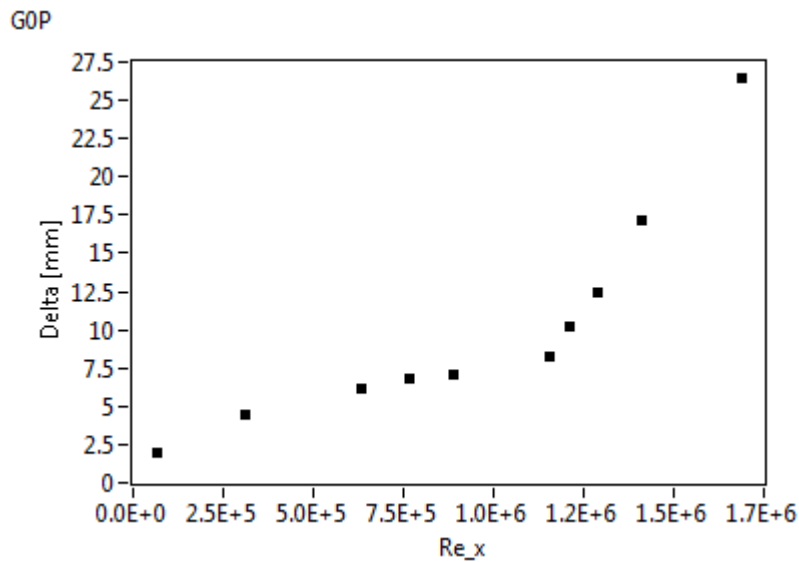


Figure 4-43 - Boundary layer thickness versus streamwise Reynolds number (G0P)

4.3.2 G1P

The normalised velocity profiles across various streamwise Reynolds numbers in the G1P case are displayed in Figure 4-44. Here, similar to Figure 4-38 for the GOP case, one can observe the near wall inflection present in the boundary layer profiles towards the leading edge which would appear to be particularly pronounced in the approximate $2 \times 10^5 < Re_x < 3 \times 10^5$ range. Additionally, similar to the GOP case, the peak turbulence intensities top 100% when the streamwise Reynolds number is approximately 5×10^5 , as demonstrated in Figure 4-45.

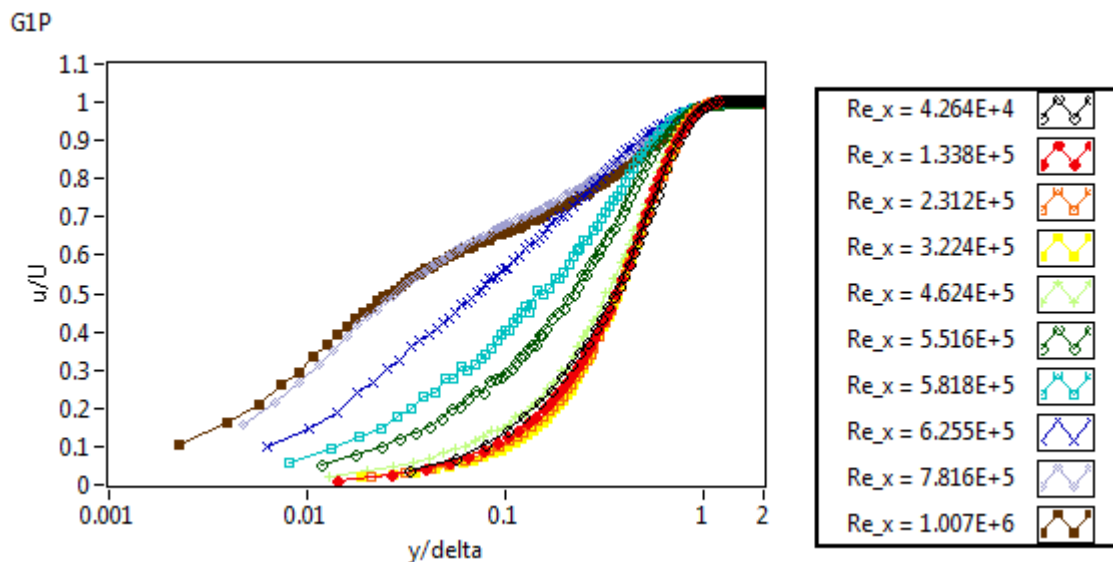


Figure 4-44 - Normalised velocity profiles (G1P)

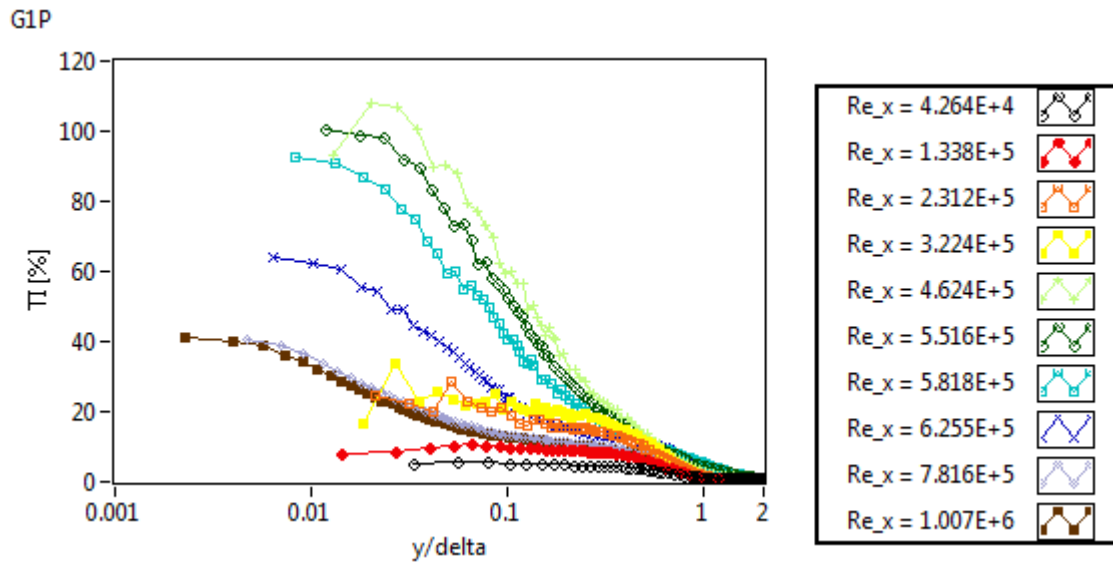


Figure 4-45 - Turbulence intensity versus y/δ (G1P)

The turbulence intensities in Figure 4-45 appear to be well resolved apart from perhaps the third and fourth profiles which exhibit some scatter near the wall. Hot-wire readings in the near wall region should always be interpreted with caution but perhaps in this case a physical explanation is plausible. This physical explanation is best understood by cross-examining in conjunction with Figure 4-46 where one can observe that the third and fourth profiles, 2.312×10^5 and 3.224×10^5 , exhibit very low but, as significantly, non-zero near wall intermittencies. Note that even with the scatter one can see that the near wall turbulence intensity coinciding with the onset of transition is approximately 23%, as suggested by Johnson (2011b). The most likely reason for this noticeable increase in the scatter is because on the threshold of transition the probability of turbulent spots being produced is still relatively low and as such the frequency and number of turbulent bursts, across the signal duration, will also be low. It's likely therefore that with increased sampling time (for the same sampling frequency) that better statistical steadiness would be realised for these profiles.

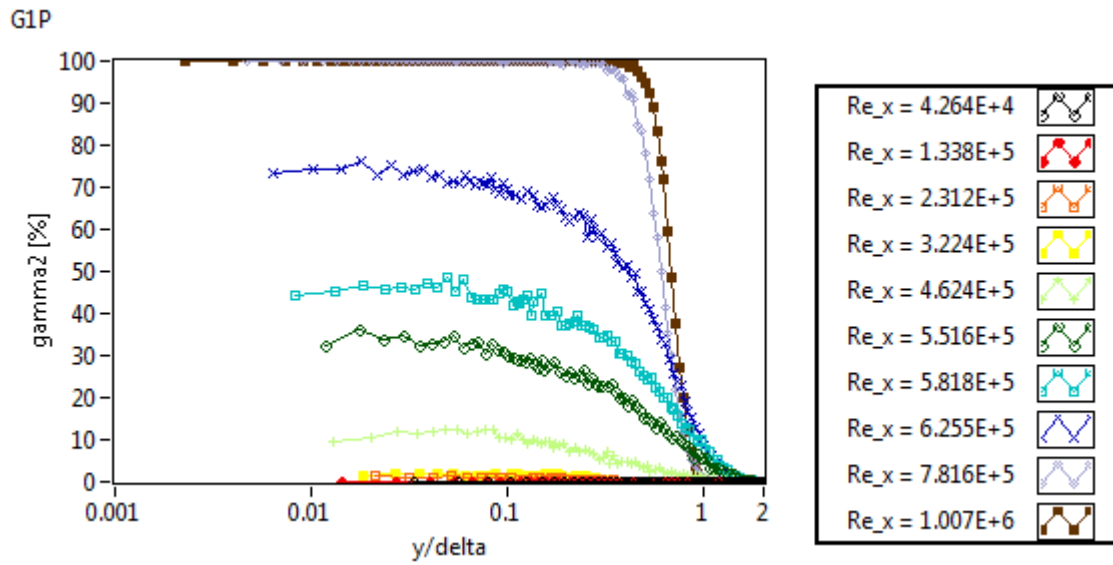


Figure 4-46 - Intermittency versus y/δ at various streamwise Reynolds numbers (G1P)

Similar displacement thickness profiles to the GOP case were obtained for G1P, as illustrated with the dip in δ^* in Figure 4-47, although for G1P the dip is less severe and the corresponding peak in shape factor, prior to transition onset, lower in magnitude at approximately 3.

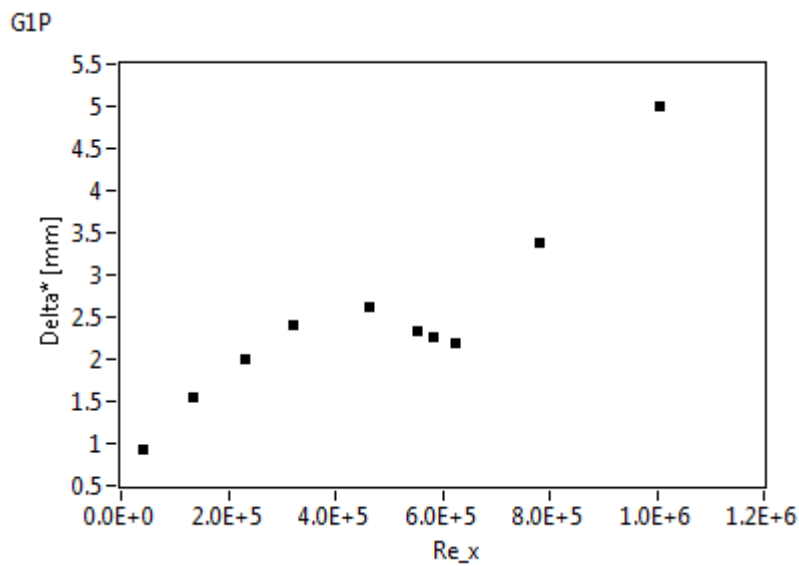


Figure 4-47 - Displacement thickness against streamwise Reynolds number (G1P)

4.3.3 G3P

The presentation of the positive pressure gradient results is concluded with consideration of the G3P case where, firstly, the normalised velocity profiles of Figure 4-48 are reviewed. The immediately discernible difference when compared to the GOP and G1P profiles is that there are no profile inflections considerably below the initial profile, albeit the traverse streamwise locations are essentially arbitrary so there is no direct correlation with respect to the sequencing. The most likely reason for the absence of the inflection, relative to GOP and G1P is perhaps best understood with consideration of the pressure gradients in Figure 4-1 and Figure 4-2. The absence of inflection may indicate that, unlike GOP and G1P, no appreciable positive pressure gradient was achieved for G3P and hence the typical inflection of a PPG was not observed.

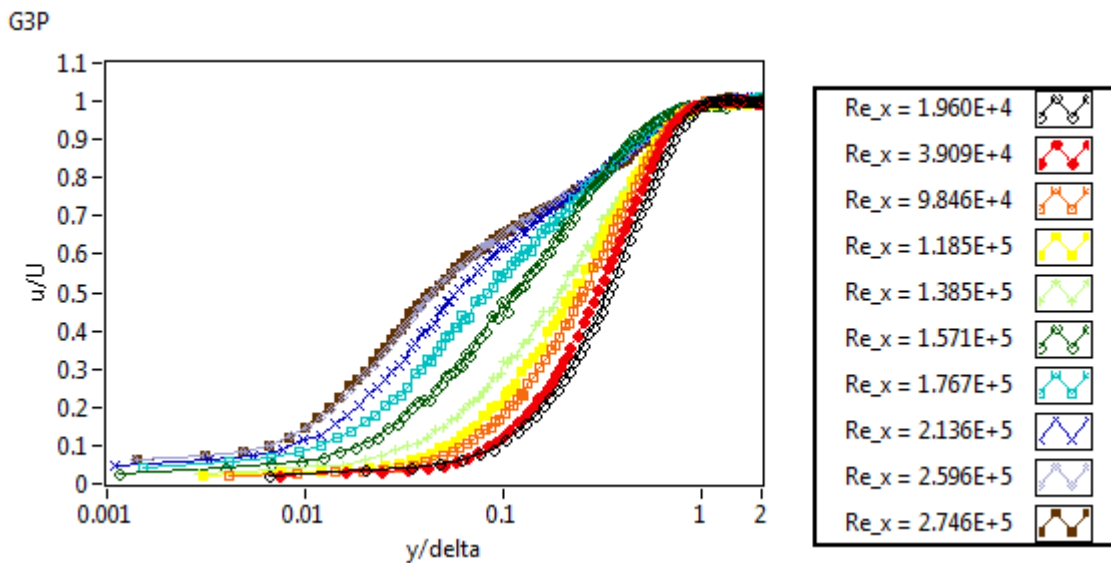


Figure 4-48 - Normalised velocity profiles (G3P)

The following 3-D plot of intermittency with respect to Re_x and y , Figure 4-49, is presented once more to graphically illustrate the penetration of intermittency from the plate towards the freestream with increasing streamwise Reynolds number and, likewise, the increase in the near wall intermittency values. The G3P 3-D plot shows how the intermittency surface is well resolved with 2 laminar, 6 transitional and 2 fully turbulent boundary layer profiles.

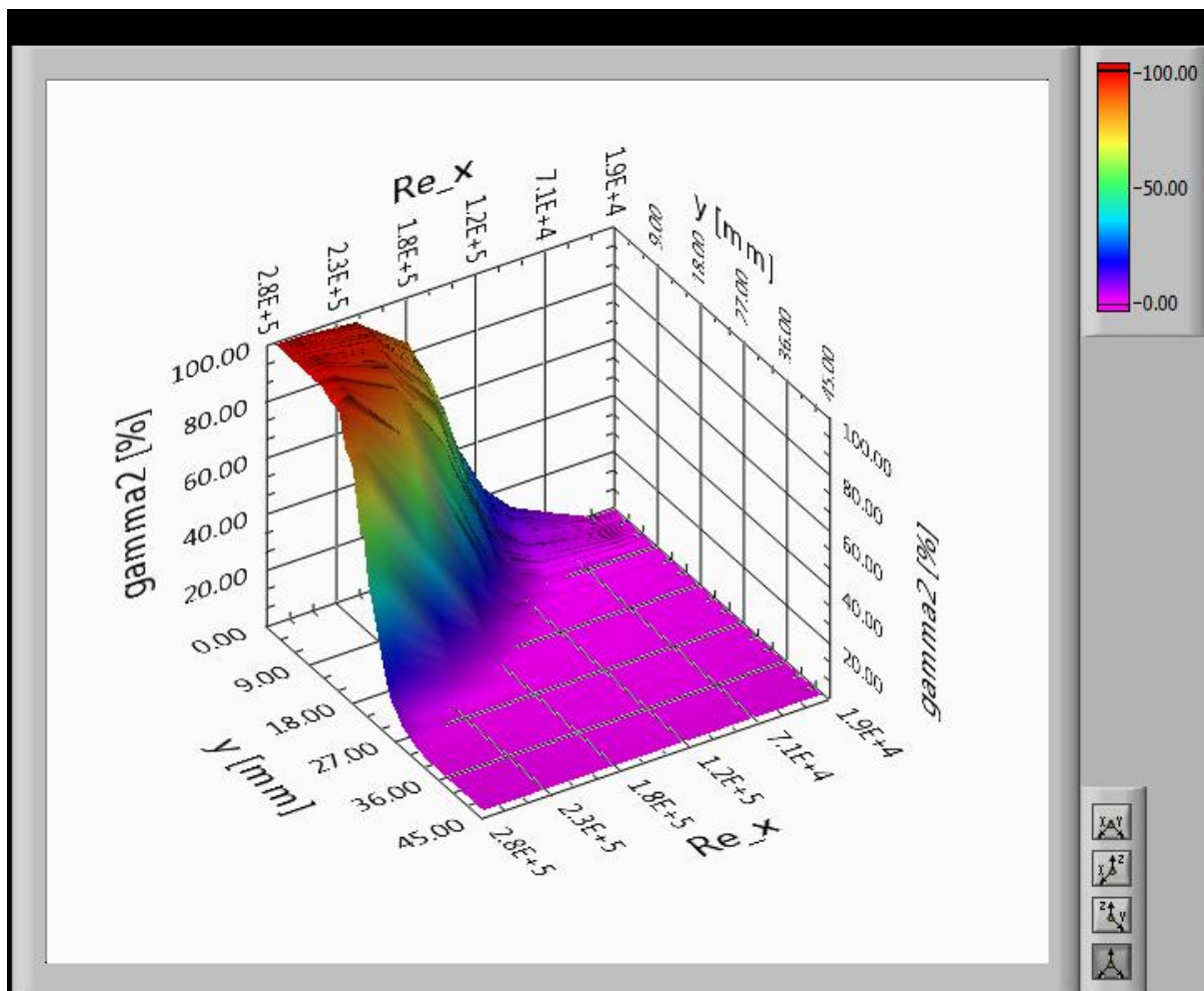


Figure 4-49 - 3-D transition map (G3P)

The intermittency distributions are also displayed in 2-D format with respect to y/δ and Re_x in Figure 4-50. This figure highlights the 2, 6, 2 profile formation but more importantly, from a physical perspective, significant drops in the intermittency are observed in close proximity to the wall ($y/\delta < 0.03$). This near wall drop off is something which has been observed previously by the likes of Gostelow and Walker (1990) and Kuan and Wang (1990) and in fact some take the approach of using the peak intermittency in a boundary layer profile, rather an average of the expected near wall plateau in intermittency, as the de facto intermittency with respect to the characteristic Reynolds number. Strictly speaking however one must be careful when making direct comparisons due to the multitude of intermittency algorithms which are available, each having their own respective

strengths and weaknesses where some, albeit not the implemented algorithm, have been reviewed by Hedley and Keffer (1974). Some of these intermittency algorithms make use of higher order statistical manipulations of the signal to discriminate between turbulent and non-turbulent regions of the flow. This is usually confined to the velocity time-history but there are also algorithms which identify turbulent regions by discriminating on the basis of temperature signals and assuming that the ‘hot’ regions are coincident with the turbulent flow if, that is, the momentum and thermal diffusivity are comparable – i.e. Prandtl numbers approaching unity, see Murlis et al. (1982). The latter not being an option in an isothermal environment.

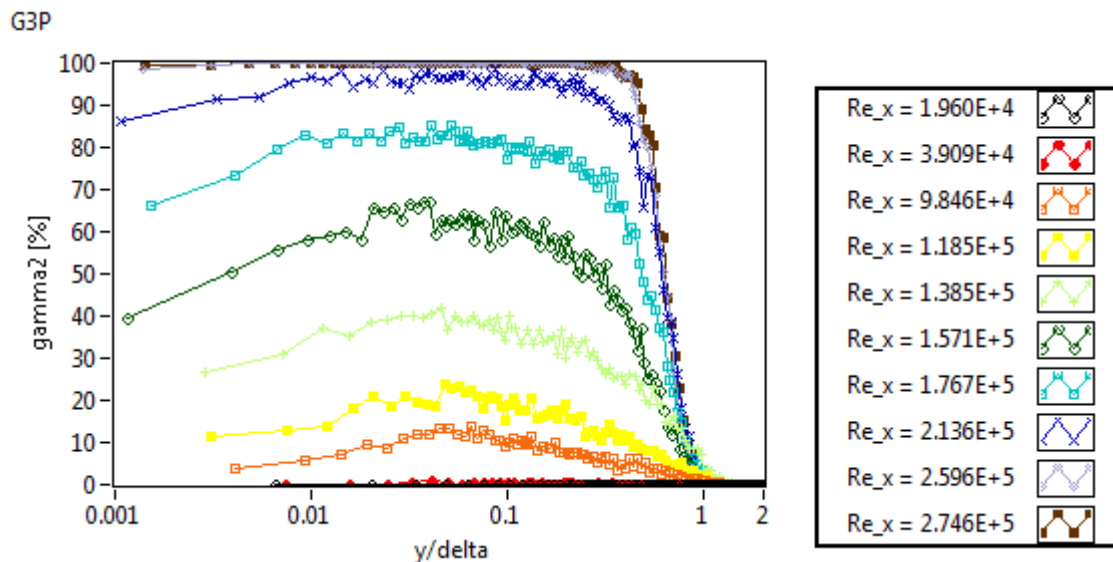


Figure 4-50 - Intermittency versus y/δ (G3P)

4.4 Negative Pressure Gradient (GxN)

4.4.1 G0N

Firstly for the G0N case the near wall intermittencies of Figure 4-51 are discussed. Figure 4-51 shows that only one laminar profile was present for G0N and thereafter a somewhat scattered

transition profile is observed which is perhaps instigated by the amplification of the crossflow instabilities due to the action of the negative pressure gradient. The non-dimensional velocity profiles of the second and third traverses (Figure 4-52) appear to mildly undercut the initial station which is backed up by considering the shape factor profiles of Figure 4-53 which show an increasing shape factor across the first three profiles before there is a drop while transition is underway.

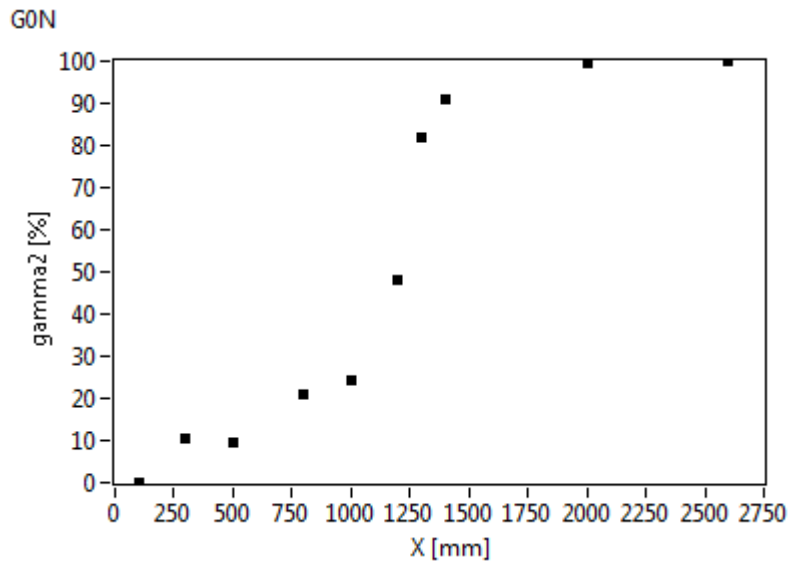


Figure 4-51 - Near wall intermittency versus leading edge streamwise displacement (G0N)

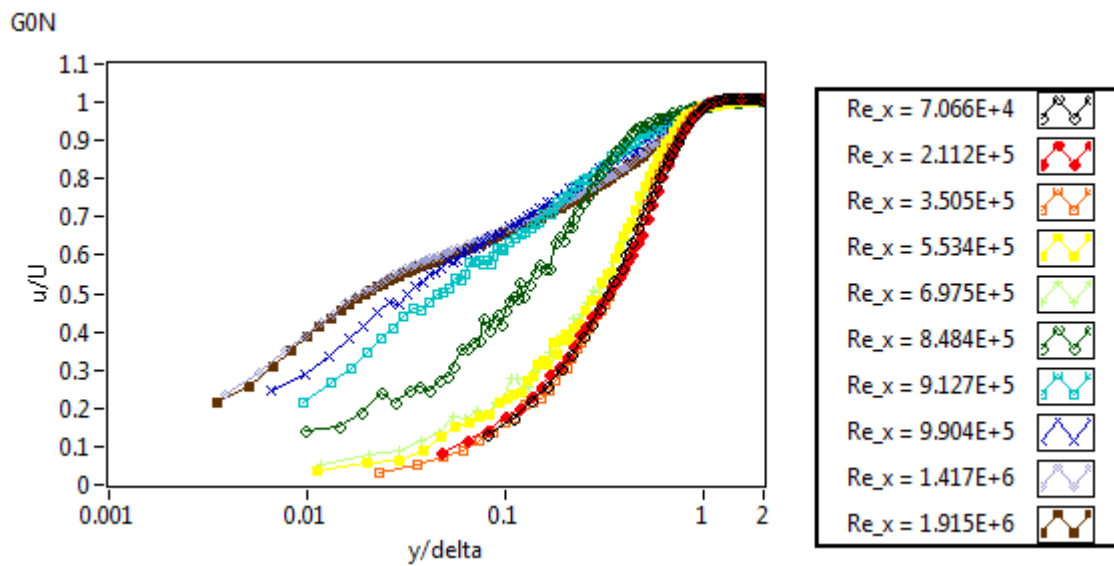


Figure 4-52 - Normalised velocity profiles (G0N)

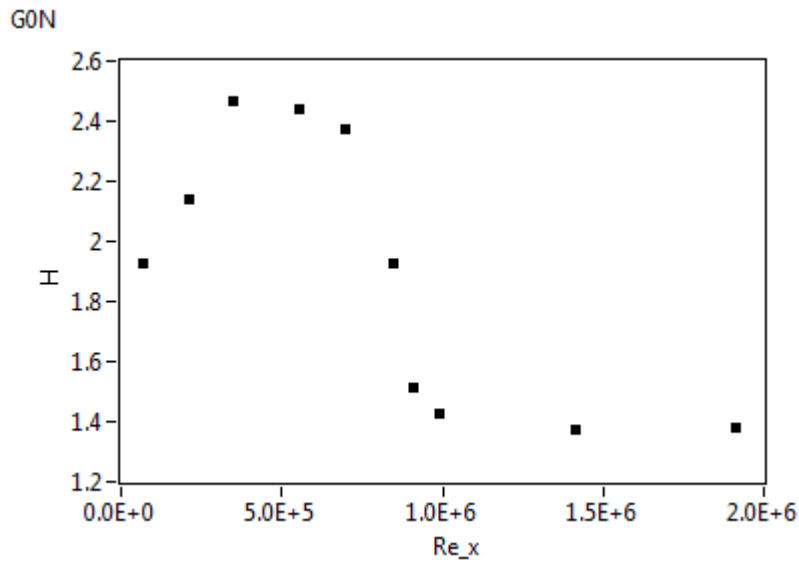


Figure 4-53 - Shape factor versus streamwise Reynolds number (G0N)

In contrast to the PPG cases the displacement thickness (Figure 4-54) does not appear to dip for G0N and exhibits an accelerated growth approximately half way through transition ($y_2 = 50\%$) meanwhile the shape factor drops abruptly.

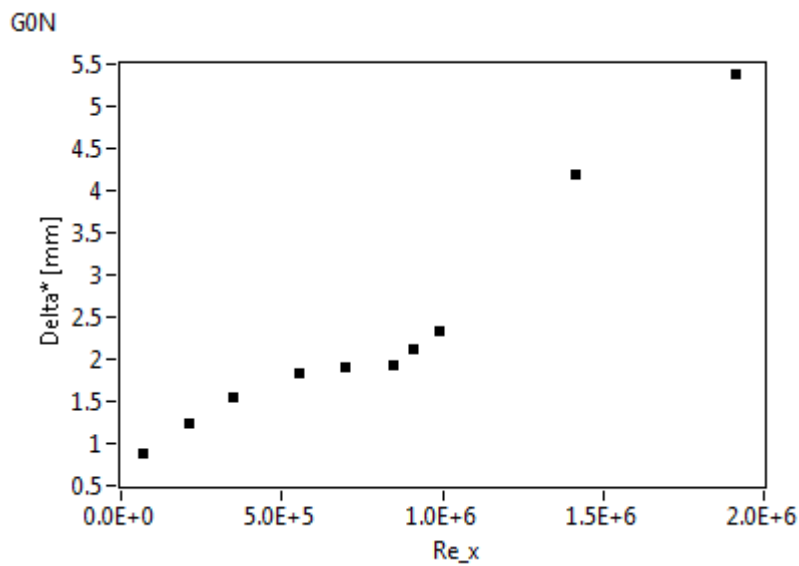


Figure 4-54 - Displacement thickness versus streamwise Reynolds number (G0N)

4.4.2 G1N

The G1N normalised velocity profiles Figure 4-55 appear to exhibit similar behaviour to those of G0N. However, the displacement thickness distribution, as per Figure 4-56, does portray a minor dip again coinciding with the approximate midway point in the transition process. The second and third velocity profiles ($Re_x = 1.625 \times 10^5$ and 2.727×10^5) are observed to undercut the profile closest to the leading edge (5.510×10^4) which is backed up by an increase in shape factor from the leading edge until transitional activity has become substantial.

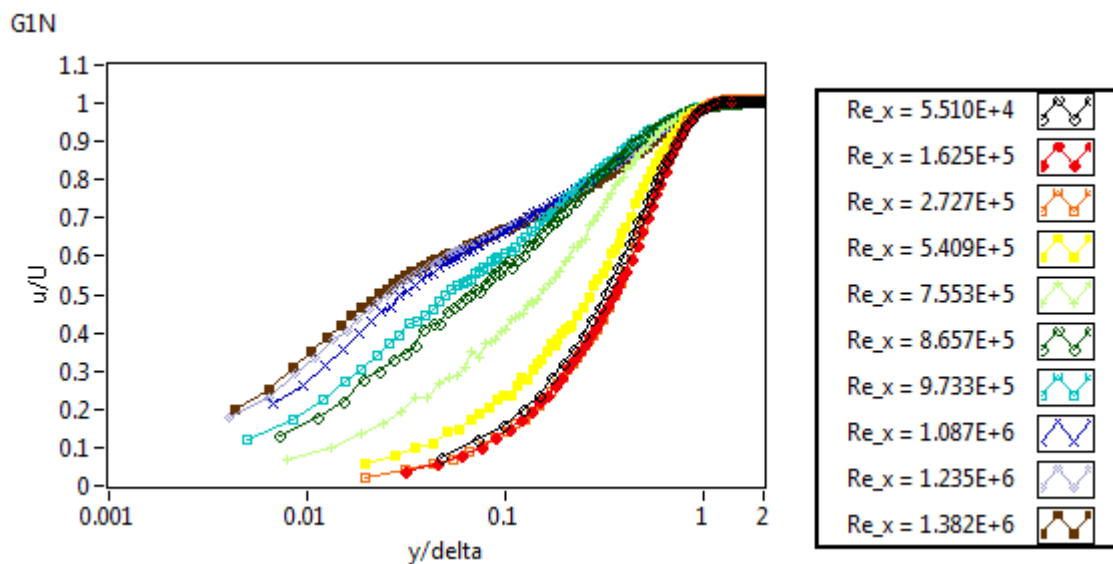


Figure 4-55 - Normalised velocity profiles (G1N)

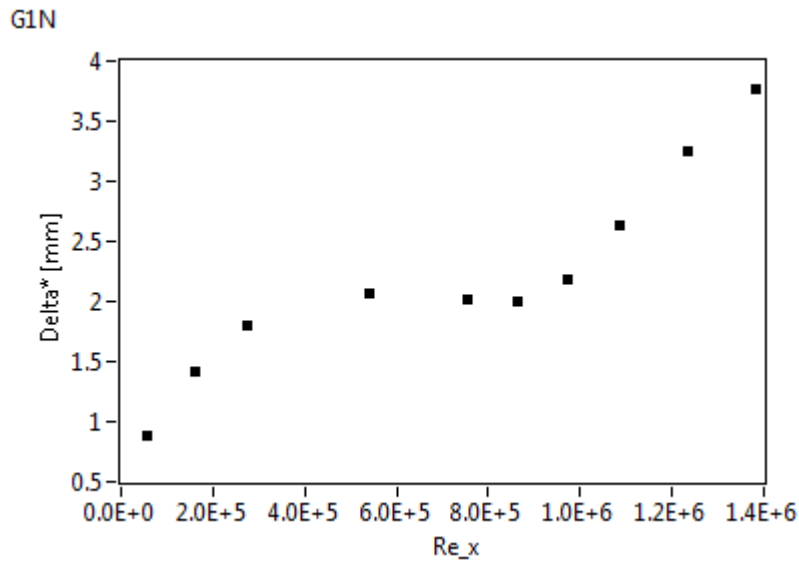


Figure 4-56 - Displacement thickness versus streamwise Reynolds number (G1N)

4.4.3 G3N

G3N represents the final permutation of all the main tunnel parameters considered and the normalised velocity distributions are plotted in Figure 4-57. In contrast to the earlier NPG cases there is no apparent undercut of the primary profile which could perhaps be explained with reference to the pressure distributions in Figure 4-1 where the physical pressure gradients, in addition to the actual static pressures, are seen to be close to zero. Of course in incompressible flow the actual static pressures are theoretically irrelevant, it is the pressure gradients which matter, but unfortunately the measured pressures were operating at the limit of the Validyne differential pressure transducer systems. Hence it is difficult to reliably interpret the pressure gradients for the grid producing the highest turbulence level, i.e. G3, owing to the correspondingly low tunnel speeds and therefore gauge static pressures.

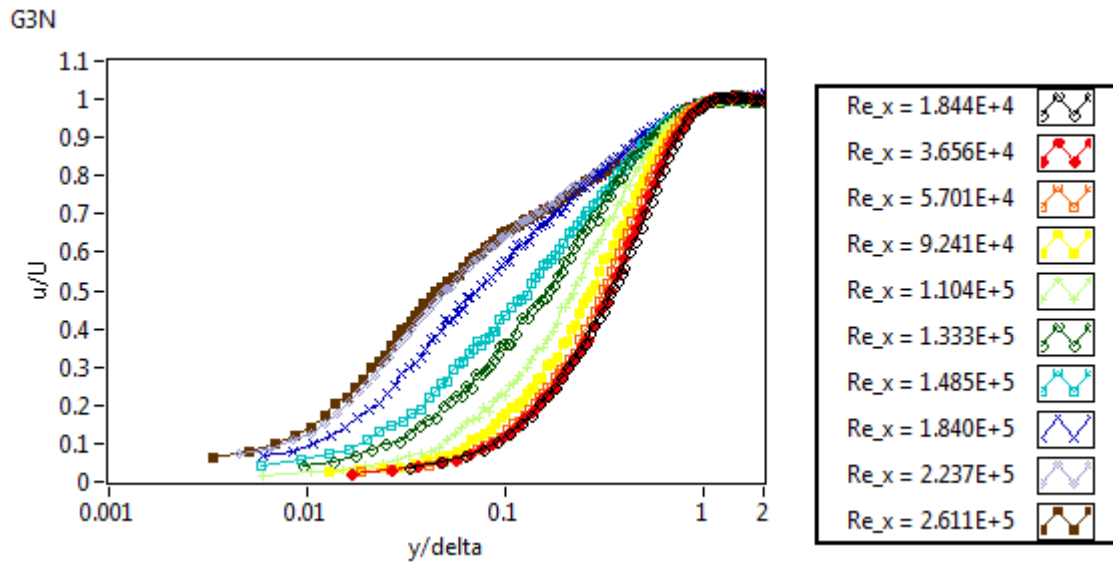


Figure 4-57 - Normalised velocity profiles (G3N)

There are perhaps two other noteworthy observations with respect to G3N. These are that the skin friction coefficient (Figure 4-58) isn't characterised by a drop off once fully turbulent flow is attained – see Figure 4-59. Of course, again, skin friction is measured indirectly and is therefore subject to significant uncertainty but the intermittencies aren't fully saturated at the penultimate profile so perhaps an additional profile resolved in excess of $Re_x = 2.611 \times 10^5$ would demonstrate a noticeable drop in skin friction in line with those observed elsewhere. Once more the near wall intermittencies in Figure 4-59 are seen to dip near the wall, as was the case with G3P (and in fact G3Z) which perhaps suggests that the shape of the near wall intermittency distributions are a function of the freestream turbulence – in terms of either the intensity, integral length scale or a combination of both. Note that the integral length scale of the G3 grid would be on the order of 15 mm, whereas for G1 it was 5 mm.

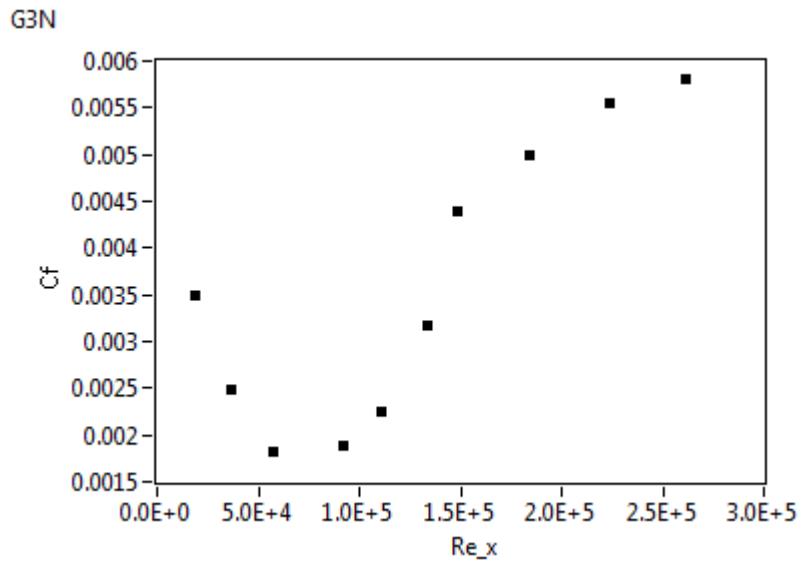


Figure 4-58 - Skin friction coefficient against streamwise Reynolds number (G3N)

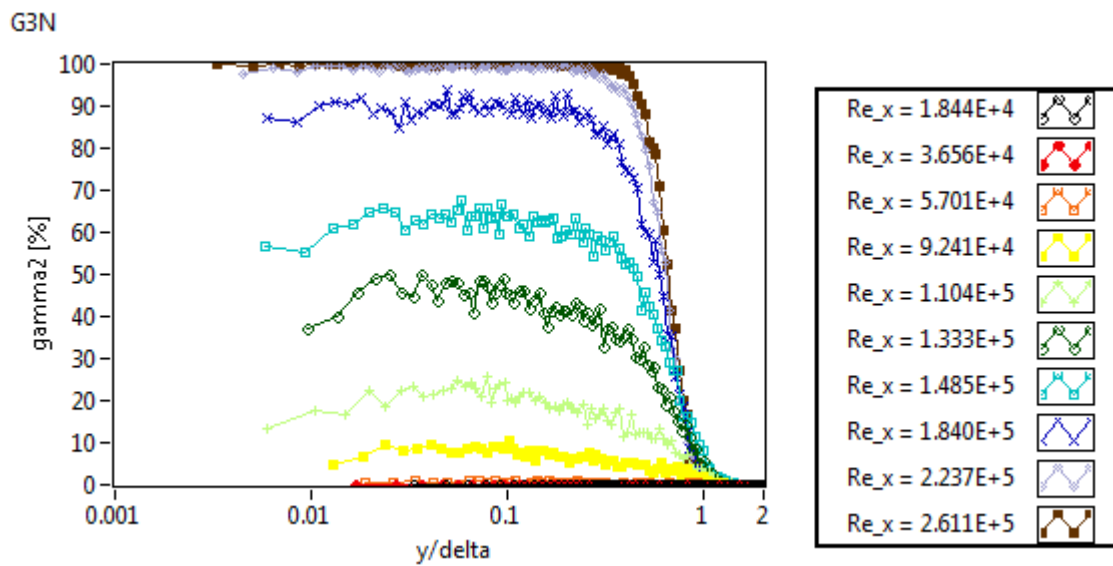


Figure 4-59 - Intermittency versus y/δ (G3N)

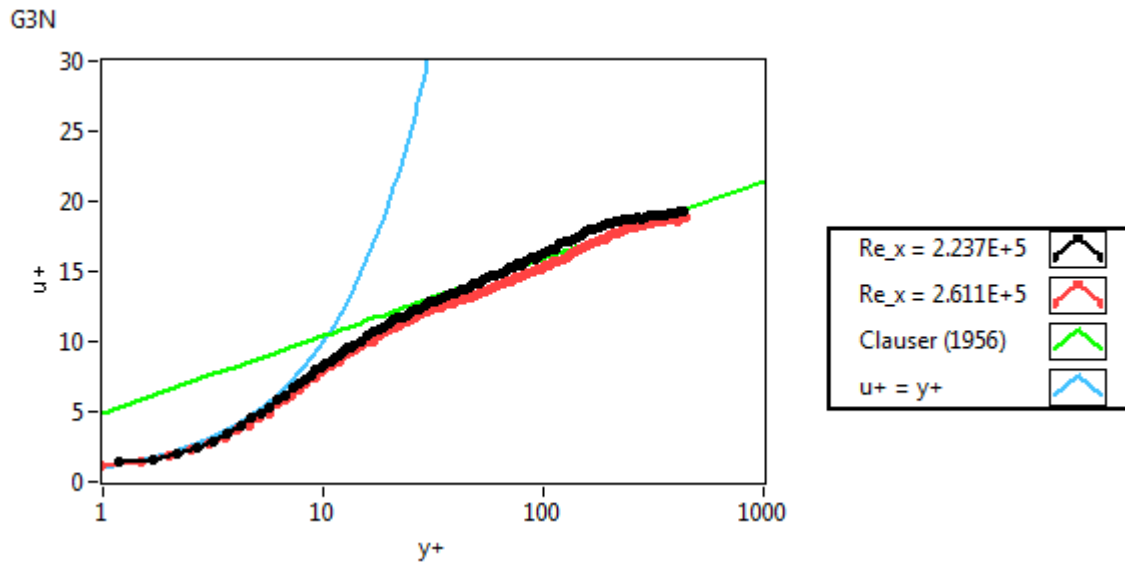


Figure 4-60 - u^+ versus y^+ plot for turbulent profiles (G3N)

Figure 4-60 represents the relationship between u^+ and y^+ for the G3N case. Unlike the profiles which were presented in Figure 4-13 for G0Z these profiles have not been adjusted. The profiles appear to match very well with both the law of the wall and the viscous sublayer relationships. However, the profiles (at their respective Re_x values) haven't collapsed on top of each other which can perhaps be attributed to the fact that the $Re_x = 2.237 \times 10^5$ profile hasn't fully reached saturated intermittency in the near wall region as one can observe from Figure 4-59. Furthermore, upon the threshold of the end of transition, the fully turbulent profiles are still somewhat transitional as a fraction of the turbulent spots will have been formed in the upstream transition region and as such some skewness in the statistics for spot lifespan and region of origin will initially be present for some distance downstream.

4.5 Collective Analysis of Results

So far the results from the main experimental programme have been predominantly evaluated on a case by case basis. In this section the results are compiled into a format that allows ease of comparison – these are namely the plots of Figure 4-61 and Figure 4-62 which compare the start and

end of transition in terms of the streamwise Reynolds numbers and Figure 4-63 and Figure 4-64 which use momentum thickness Reynolds numbers instead. The momentum thickness Reynolds number plots are also compared directly with the famous empirical transition correlations of Abu-Ghannam and Shaw (1980) for unswept zero pressure gradient boundary layers. These are then summarised in Table 4-1 and Table 4-2 with transition length parameters added.

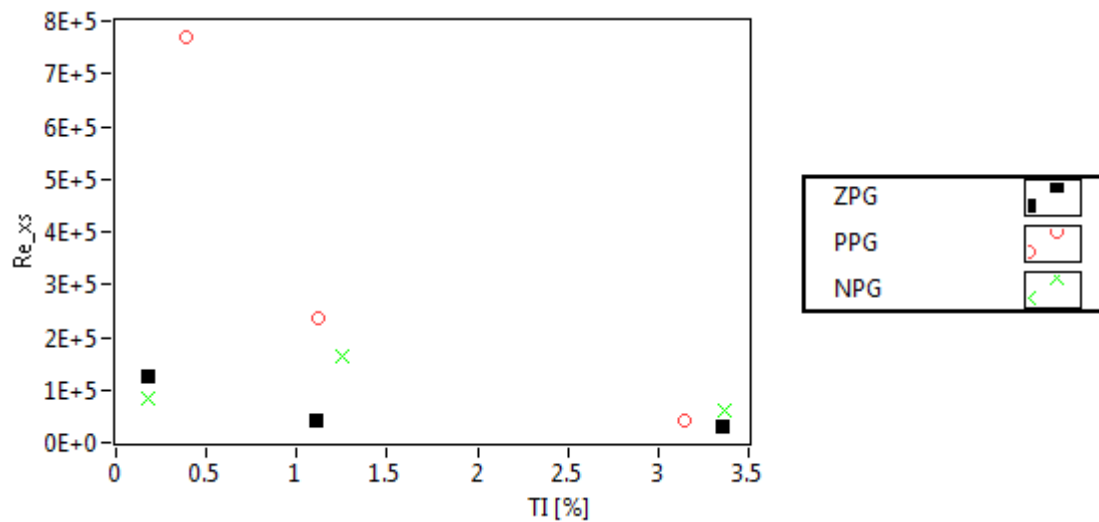


Figure 4-61 - Streamwise start of transition Reynolds number versus turbulence intensity for all pressure gradients

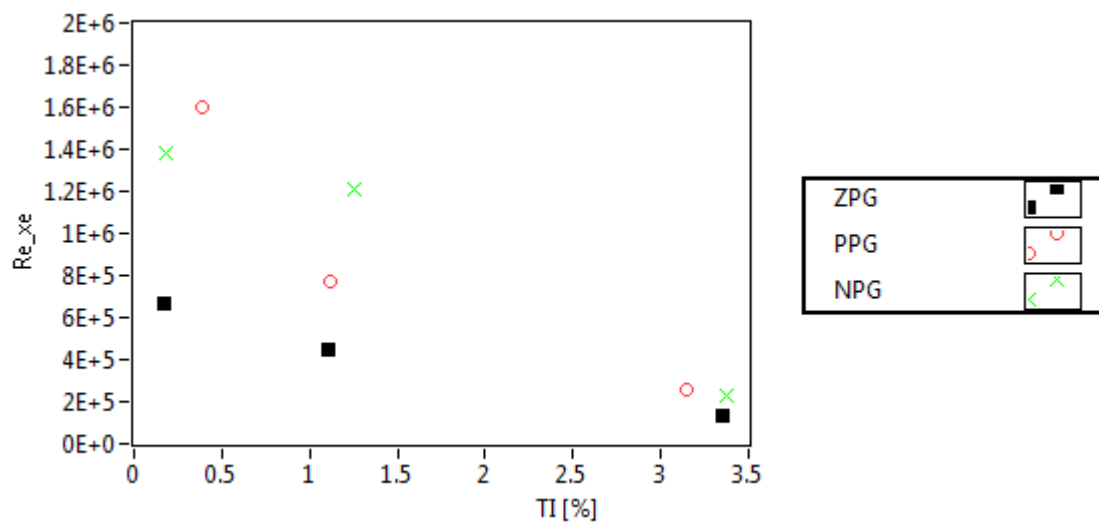


Figure 4-62 Streamwise end of transition Reynolds number versus turbulence intensity for all pressure gradients

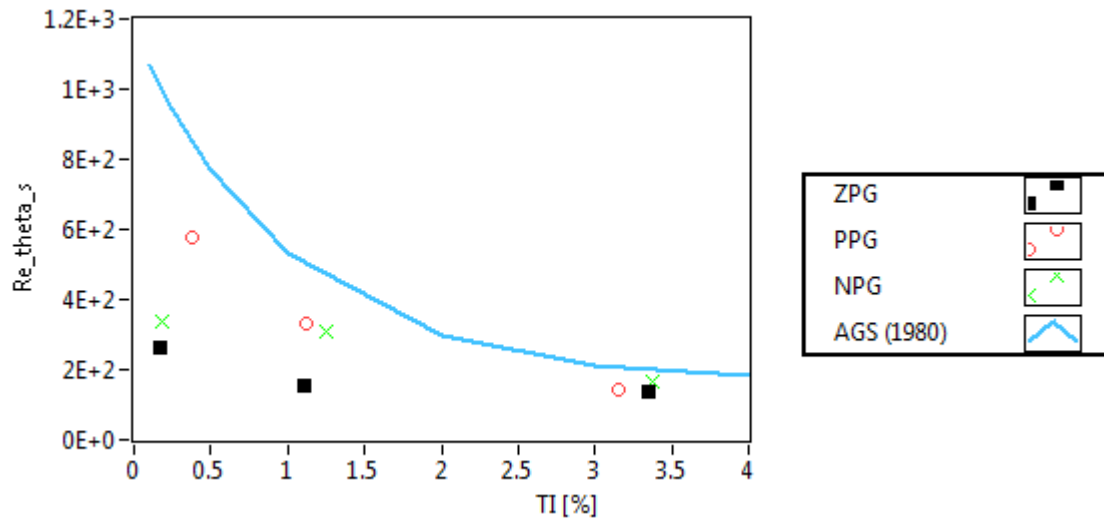


Figure 4-63 - Momentum thickness Reynolds number at the start of transition for all pressure gradients versus turbulence intensity with Abu-Ghannam and Shaw (1980) comparison

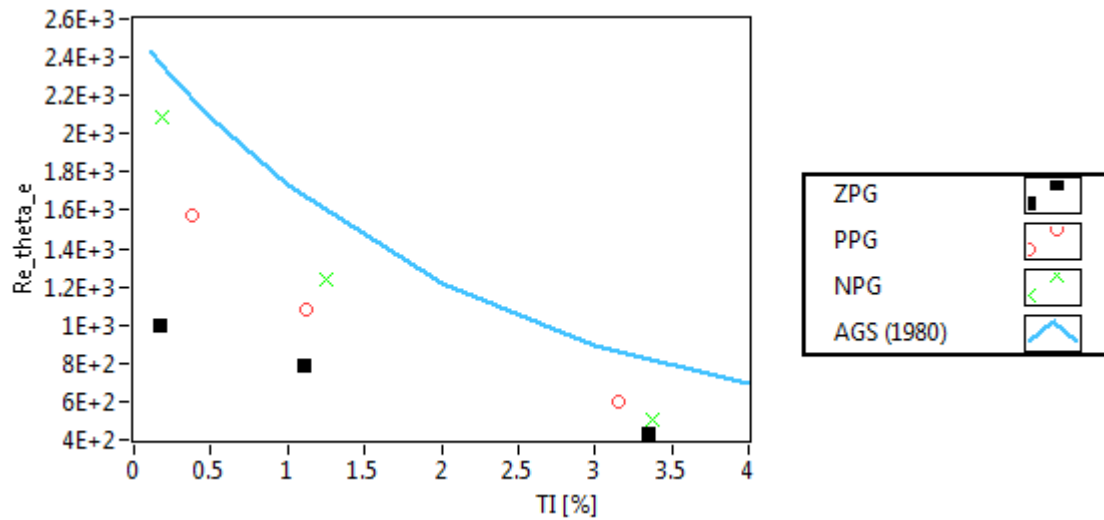


Figure 4-64 - Momentum thickness Reynolds number at the end of transition for all pressure gradients versus turbulence intensity with Abu-Ghannam and Shaw (1980) comparison

Perhaps the first observation is that the transition starts and ends earlier than the empirical correlations set by Abu-Ghannam and Shaw (1980), Equation 4-7 (repetition of Equation 2-21) and Equation 4-8, for all levels of freestream turbulence intensity across all pressure gradients.

$$Re_{\theta_s} = 163 + \exp(6.91 - \tau) \quad \text{Equation 4-7}$$

$$Re_{\theta_e} = 2.667 \times Re_{\theta_s} \quad \text{Equation 4-8}$$

This is a result which would appear to back up the observations of Gray (1952) for swept transition in that, because transition is initiated earlier when substantial sweep is present, a higher percentage of the chord will therefore experience non-zero intermittency. From a stability perspective this is owing to the crossflow instabilities which are present due to the crossflow incited by the 60° swept leading edge.

Table 4-1 - Narasimha table for start and end of transition for all cases (streamwise leading edge displacement)

Grid & Section	FS TI [%]	Re_{x_s}	Re_{x_e}	Re_{x_t}	x_s [mm]	x_e [mm]	x_t [mm]
G0Z	0.172	1.27E+05	6.67E+05	5.40E+05	239.4	1212.4	973.0
G1Z	1.111	4.34E+04	4.49E+05	4.06E+05	138.2	1420.8	1282.6
G3Z	3.351	3.07E+04	1.34E+05	1.04E+05	150.0	687.2	537.2
G0P	0.384	7.70E+05	1.60E+06	8.30E+05	1203.6	2472.1	1268.5
G1P	1.114	2.35E+05	7.76E+05	5.41E+05	507.8	1688.8	1181.0
G3P	3.149	4.34E+04	2.53E+05	2.10E+05	221.8	1271.4	1049.6
G0N	0.178	8.43E+04	1.38E+06	1.30E+06	119.5	1954.4	1834.9
G1N	1.251	1.63E+05	1.21E+06	1.04E+06	301.2	2161.4	1860.2
G3N	3.369	5.93E+04	2.29E+05	1.70E+05	312.8	1230.3	917.5

Table 4-2 - Narasimha table for start and end of transition for all cases (momentum thickness)

Grid & Section	FS TI [%]	Re_{θ_s}	Re_{θ_e}	$Re_{\theta_e}/Re_{\theta_s}$	θ_s [mm]	θ_e [mm]	θ_t [mm]
G0Z	0.172	2.61E+02	1.00E+03	3.836	0.493	1.821	1.328
G1Z	1.111	1.56E+02	7.92E+02	5.083	0.496	2.502	2.006
G3Z	3.351	1.35E+02	4.27E+02	3.171	0.658	2.185	1.527
G0P	0.384	5.75E+02	1.57E+03	2.739	0.898	2.430	1.532
G1P	1.114	3.30E+02	1.08E+03	3.278	0.714	2.353	1.640
G3P	3.149	1.42E+02	6.03E+02	4.244	0.727	3.030	2.304
G0N	0.178	3.35E+02	2.09E+03	6.230	0.474	2.947	2.472
G1N	1.251	3.10E+02	1.24E+03	3.996	0.573	2.221	1.648
G3N	3.369	1.63E+02	5.07E+02	3.108	0.861	2.720	1.859

One would assume that the PPG and NPG results would straddle the ZPG results but this proves not to be the case. The reasons for this are considered and discussed in more detail in section 4.6 but for now the focus is directed towards interpreting the non-zero pressure gradients. Firstly Re_{θ_s} and Re_{x_s} appear (individually) to be approximately of the same order for G1 and G3 but markedly different for G0 where the GOP is very significantly higher than G0N, particularly in terms of Re_{x_s} –

see Table 4-1 where Re_{x_s} is almost an order of magnitude higher. Table 4-1 includes the streamwise transition Reynolds numbers, Re_{x_t} , which is merely the difference between the start and end of transition Re_x values and Table 4-2 offers the ratio $Re_{\theta_e}/Re_{\theta_s}$ which in the empirical correlation again of Abu-Ghannam and Shaw (1980) is given as a fixed value of 2.667 - see Equation 4-8. From Table 4-2 it's fairly obvious that this relationship doesn't hold for zero pressure gradient and, indeed, the ratio between the two would appear to be governed by relationships with both the turbulence intensity and the pressure gradient, i.e. a complicated, non-linear relationship.

4.6 Spanwise Flow Quality Issues

Whilst in section 4.5 the crossflow instabilities have been identified as the source of rapidity of transition onset, relative to unswept transition, it must also be reiterated that, as with many other wind tunnel facilities, there were flow quality issues present which are likely to influence the results.

The spanwise flow quality was examined for both the NPG and ZPG cases but due to time constraints this was not executed for the PPG configuration. In chapter 3 the measuring plane, along which all measurements from the main experimental programme were executed, was defined as 812.8 mm from the spanwise datum, where the spanwise datum was taken to be the portside (from the perspective of the approach flow) sidewall of the straight section settling chamber upstream of where the ZPG, PPG and NPG sections were retrofitted to the wind tunnel. Therefore all measurements for the main experimental programme were parallel to this surface, displaced by the constant offset of 812.8 mm (equivalent of 32"). Either sidewall of the straight section settling chamber represent valid choices but the sidewalls of the non-zero pressure gradient test sections vary in the spanwise direction and are therefore inconvenient datum choices.

Additionally the spanwise profiles were performed for the ZPG section when an, until then, unidentified problem with the blower tunnel speed controller system was present resulting in

arbitrary, undamped oscillations in the freestream velocities. This problem was traced to a dislodged and snapped V-belt, the function of which was to provide feedback to the motor controller through a tachometer. As such the tunnel was unknowingly operating in an open loop configuration until the problem was rectified.

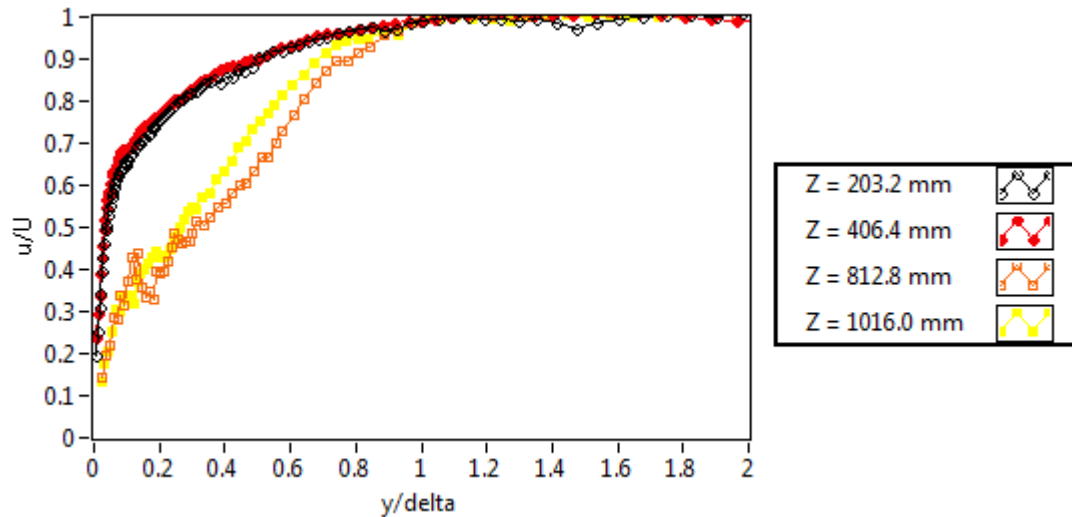


Figure 4-65 - Normalised velocity profiles at different spanwise positions – no grid, ZPG

The resulting scatter owing to the broken tachometer belt can be observed from Figure 4-65 but nevertheless one can still make out the considerable variations in the profiles across the span of the plate. Note that all of the profiles were resolved at a fixed displacement of $X = 15''$ (381 mm) from the leading edge and that the respective figure hasn't been assigned a case code, i.e. G0Z, owing to the manner in which these results were unknowingly compromised.

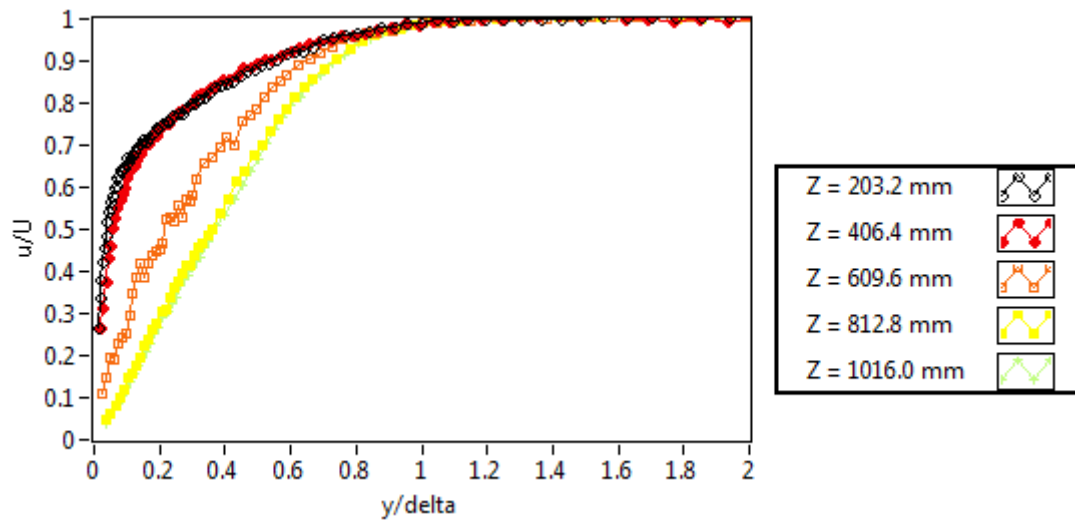


Figure 4-66 - Normalised velocity profiles at different spanwise positions (G1N)

A similar test was also performed for the NPG section, this time with the square grid and a fully functioning tachometer belt in place on the wind tunnel, with the tunnel operating at the G1N test speed and the flap maintained at the G1N flap angle (91 mm deflection) – hence an all-round more valid test. Once more these profiles were resolved 15" (381 mm) from the leading edge. The scatter in this case was far reduced but reasonably significant for $Z = 24"$ (609.6 mm) which is perhaps caused by this station coinciding with the centreline of the (1.22 m wide) tunnel where the streamwise static pressure tappings are situated.

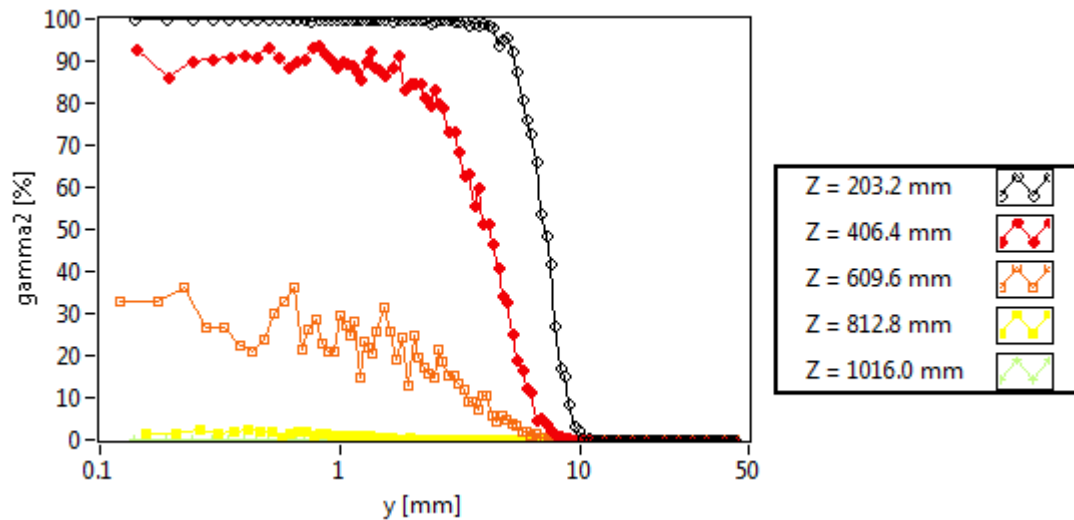


Figure 4-67 - Spanwise intermittency distribution at X = 381 mm (G1N)

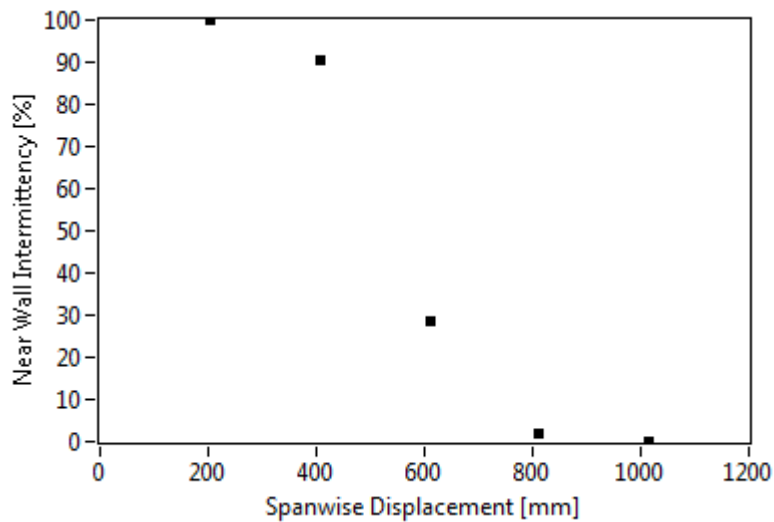


Figure 4-68 - Near wall intermittency across leading edge span at X = 381 mm (G1N)

From both Figure 4-67 and Figure 4-68 it was observed that the distribution in intermittency was not homogeneous tangential to the swept leading edge. There are several reasons as to why this would be the case but first it should be pointed out that the freestream turbulence intensity decays in the direction of the approach flow, which is not perpendicular to the leading edge, and as such an inverse relationship will exist between the turbulence intensity and the spanwise displacement, with respect to the manner in which Z has been defined.

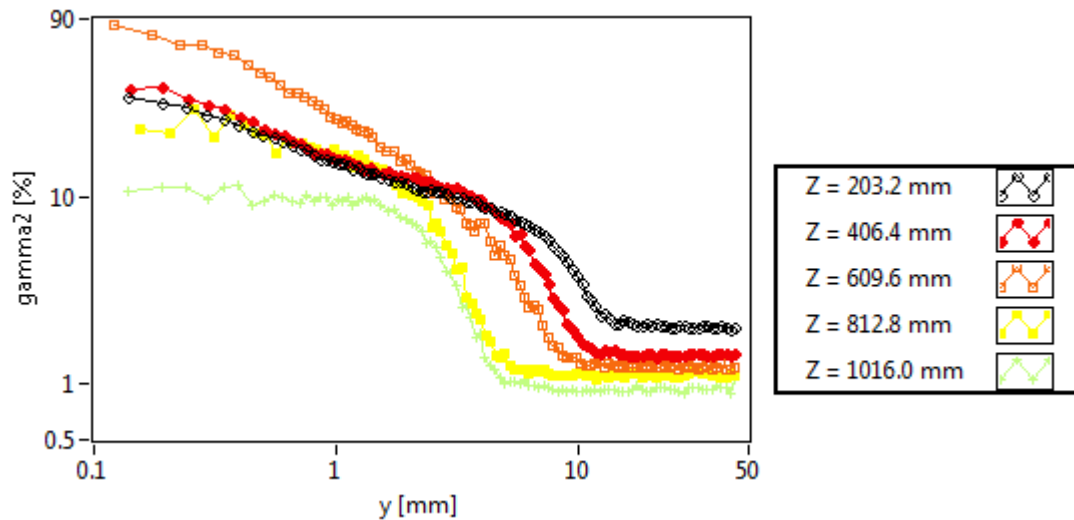


Figure 4-69 - Spanwise variation in turbulence intensity at X = 381 mm (G1N)

This variation in turbulence intensity across the span at a fixed leading edge displacement ($X = 381$ mm) is clearly demonstrated in the log-log plot of Figure 4-69 where the turbulence intensity is seen to be around 2% at the first station ($Z = 203.2$ mm) and around 1% on the actual measuring plane itself ($Z = 812.8$ mm). These observations are not to be interpreted as suggesting that the freestream turbulence decays along the leading edge but rather they hopefully demonstrate variance which is always going to occur when, unlike the leading edge, the grids are aligned perpendicular to the approach flow. Nevertheless similar observations of transitional/fully turbulent boundary layer profiles close to the datum were obtained in the absence of a turbulence generating grid (Figure 4-65) where the freestream turbulence intensity experiences negligible decay in the approach flow direction, given that the tunnel is effectively operating at its natural intensity of freestream turbulence.

If the inhomogeneity of turbulence intensity across the span is not responsible for these observations then other possibilities must be considered. It is possible that a localised distribution of angle of attack across the span of the leading edge exists which could cause a separation bubble on the top surface of the plate close to the spanwise datum (portside sidewall). The leading edge of

the plate does deflect reasonably significantly under load (circa 5 mm for a 200 kN load at the corner) given the absence of proximal support structure in the region but under operating conditions the leading edge bears no load and this is not thought to be the reason for the inhomogeneity in flow quality across the span. However, the aerodynamic loads are considerably lower and if this was to prove to be an issue then the repeatability between experiments would be an issue and the smoothness of transition profiles (such as with G3P - Figure 4-49) are likely to have been unattainable.

The most likely reasons for the spanwise flow quality issues are contamination and, secondly, inadequate flow control provided by the bleed flap underneath the plate. In Reed and Saric (1989) it is stated, albeit in reference to swept wings, that disturbances which are produced in corners, such as those in wind tunnel working sections, may propagate along the leading edge and affect stability elsewhere, instigating leading edge contamination. From the near wall intermittency distributions across the span (Figure 4-68) one would expect this contamination to emanate from the region upstream of the leading edge where $Z = 0$. That said however, one would expect it to be possible to bleed any dirty approach flow away through the use of a carefully designed flap. It was observed, however, that by modifying the flap angle one was only able to exert an influence on the flow quality on the side of the plate beyond the centreline pressure tapings where the measurements were in fact recorded. An increase in flap angle was only observed to spread, but not migrate/transfer, the leading edge contamination from the spanwise datum.

Given that there would appear to be an absence of consistent flow across the span of the plate, this would in turn compromise the presence of the idealised Falkner-Skan-Cooke boundary layer profiles, which may, in turn, give reason for some of the problems experienced when attempting to resolve the flow angles. This theory goes some way to explaining the differences between the idealised Falkner-Skan-Cooke profiles and the experimentally derived measurements - see Figure 4-31.

4.7 Receptivities of Pre-Transitional Boundary Layers (Experiments)

Analysing the receptivity of boundary layers with respect to frequency content in the freestream approach flow is important to determine the manner in which the transition will evolve, as has been discussed previously in the literature review of chapter 2 and specifically sub-section 2.5.3.

Therefore the receptivities along the swept flat plate for all pre-transitional boundary layer profiles ($\gamma_{2|NW} < 1\%$) have been presented in this section for both the G1 and G3 grids across all pressure gradient sections. The receptivities for the cases with no grid – G0 are to some extent non-physical because, in that case, the transition evolves through a ‘natural’ process where the frequency or frequencies at which the boundary layer resonates possibly have negligible power in the freestream and hence the equivalent freestream frequencies are not responsible for initiating the process, as in the frequencies for which the boundary layer expresses instability.

Likewise non pre-transitional receptivity profiles – i.e. where significant turbulence content is present are also open to non-physical interpretations, in terms of receptivity, because by such a point significant non-linearities are present. Any equivalent high frequency content, associated with turbulent flow, would decay rapidly in the freestream, and therefore the apparent receptivities would tend towards infinity as the majority of high frequency content in the freestream signals would largely be constituted of low amplitude noise.

The receptivities for every case were determined by first calculating an FFT power spectrum (using a Hanning window) for the entire signal length at the first point greater than $\frac{y}{\delta} = 0.1$ and, likewise the first point greater than $\frac{y}{\delta} = 2$, and then determining the ratios between the two for each frequency, as per Equation 4-9.

$$R = \frac{\left(\frac{u'_{BL}}{\bar{U}_{BL}}\right)}{\left(\frac{u'_{FS}}{\bar{U}_{FS}}\right)} \quad \text{Equation 4-9}$$

Given a constant sampling frequency of 10 kHz, and sampling time of 30 seconds, this procedure produced spectra for every $\frac{1}{30}$ Hz up to 5 kHz. In order to reduce scatter and, in effect, smooth the plots the approach of grouping individual frequencies into frequency bins was adopted. The number of bins chosen was 256 and the width of each bin (from 200 to 1285) was determined through Equation 4-10;

$$W(i) = Ae^{Bi} \quad \text{Equation 4-10}$$

where W was the bin width, A the smallest bin size - 200, i the index of the loop from 0 to 255 and B an arbitrary coefficient (0.00726906) which implied the rate of exponential growth. Thereafter the receptivities were determined by summing the spectral power in each frequency bin where each bin was then graphically represented as being the midspan of each frequency range. Later, in section 5.3, the frequencies have been non-dimensionalised in order to provide comparisons across different tests under varying conditions. In the following sub-sections the receptivities are provided for the first three boundary layer profiles with respect to increasing streamwise displacement in each case. All of these boundary layer profiles for G1 and G3 have correspondingly low near wall intermittencies of less than 5% for each of the three profiles presented apart from the G3Z case where only one profile satisfies this criteria.

4.7.1 ZPG Receptivities

First the experimental results from the zero pressure gradient cases are presented in log frequency form for every case; G0Z, G1Z and G3Z. Figure 4-70 provides the receptivity spectral plots for G0Z where one can observe extremely high receptivities, with respect to the manner in which the parameter has been defined and then determined. However, as previously stated, the natural level of turbulence in the wind tunnel (G0) was sufficiently low to allow for natural transition to take

place. As such the receptivities are high as the primary instability fluctuations in the boundary layer develop exponentially with x by low levels in the freestream. Similar ‘receptivity’ observations were made for the other grid free cases, i.e. G0P and G0N.

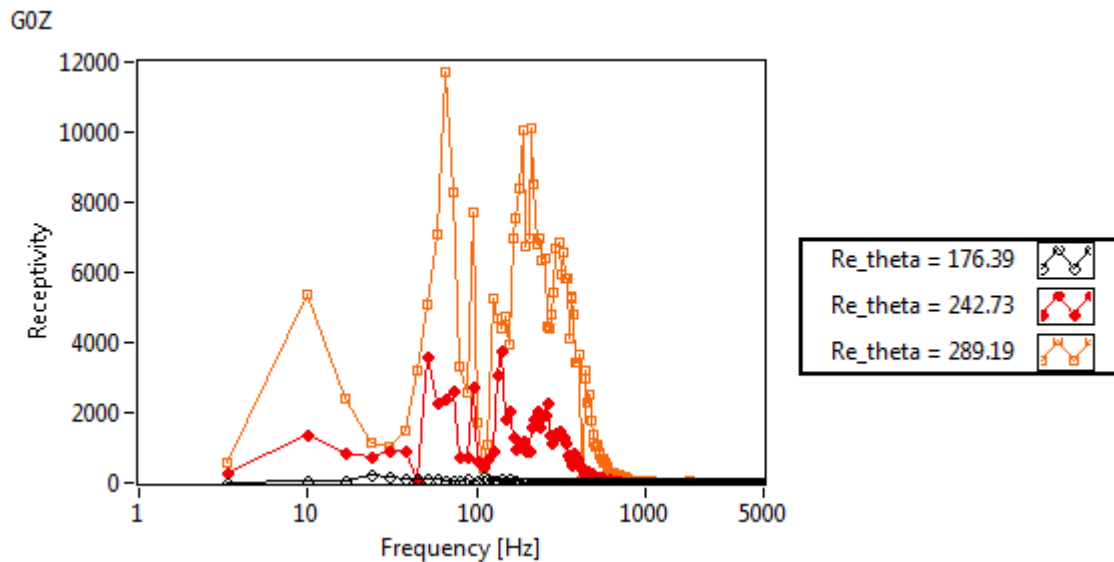


Figure 4-70 - Pre-transitional boundary layer receptivity (G0Z)

Figure 4-71 and Figure 4-72 offer the receptivities which were determined for the G1Z and G3Z cases, this time in log-log form. One can observe that the receptivities are markedly different from that of Figure 4-70. For both G1Z and G3Z it is observed that the receptivities are greatest at low frequencies and increase in the direction of increasing Re_{θ} . The Re_{θ} values for G3Z are all lower than those for G1Z and as such one would expect the largest receptivities at low frequencies for that case at $Re_{\theta} = 117.52$ to reside below that of the lowest G1Z of $Re_{\theta} = 141.22$ where the low frequency receptivity of the former is seen to be approximately twice as large as the latter. Perhaps the main reason for a non-proportional increase in low frequency receptivity can be explained with reference to Figure 4-36 where the near wall intermittencies are seen to be significantly non-zero (> 10%) for the second and third profiles and, as such, the signals pre-transitional status could be disputed. Significant non-zero intermittencies may increase the low frequency receptivity as the switching between transitional states is likely to have its own respective low temporal frequency

until higher intermittencies are attained. In contrast to G0Z the ZPG cases with grids were observed to progress through a bypass transition mechanism.

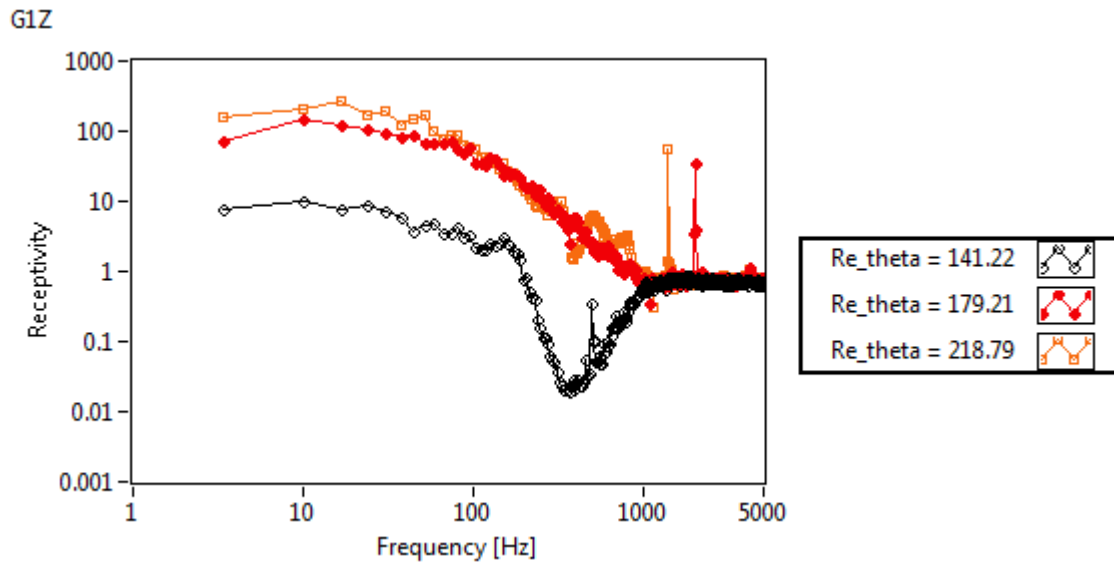


Figure 4-71 - Pre-transitional boundary layer receptivity (G1Z)

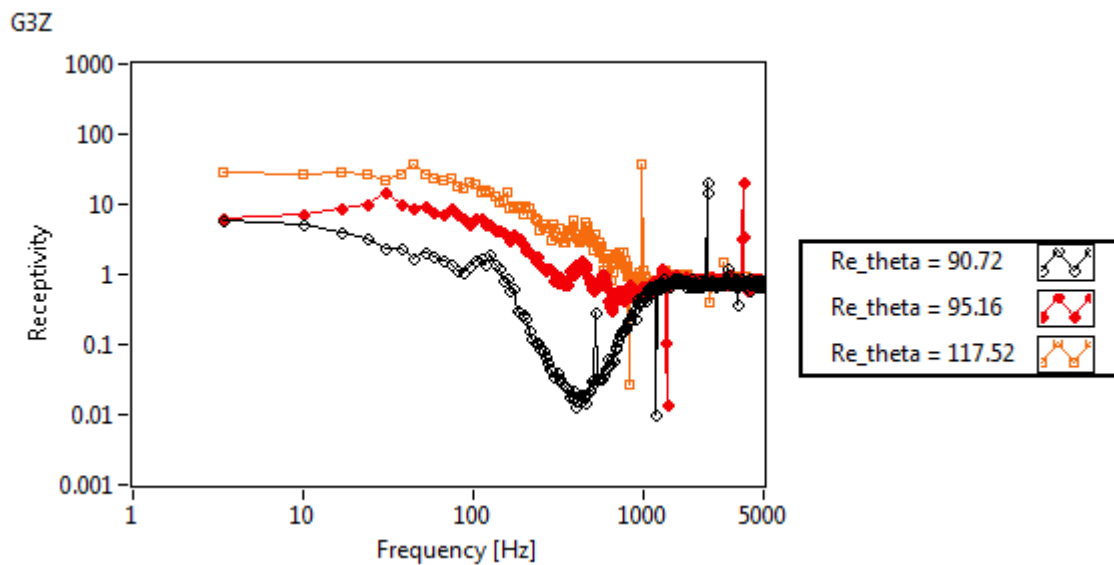


Figure 4-72 - Pre-transitional boundary layer receptivity (G3Z)

4.7.2 PPG Receptivities

Here the receptivities for the experimental positive pressure gradient cases are presented. Firstly G1P (Figure 4-73) is considered. Here it was observed once more that the highest receptivities were seen for low temporal frequencies. Similar to the ZPG cases there is a significant drop in the receptivity at frequencies above 200 Hz, even though these frequencies were clearly present in the freestream, until the final profile at $Re_\theta = 328.07$ where the drop off is less substantial, albeit the receptivities above 200 Hz are not substantial relative to those for the lower frequencies.

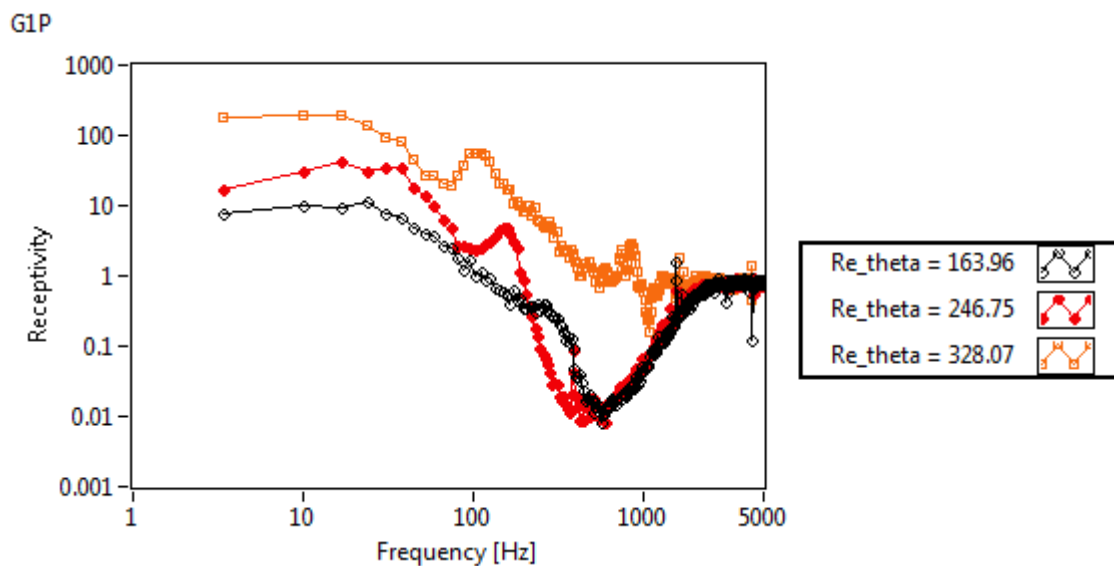


Figure 4-73 - Pre-transitional boundary layer receptivity (G1P)

Very similar trends were observed for the G3P case of Figure 4-74 where the low frequencies are dominant for driving receptivity and the drop off in receptivity after 200 Hz is only observed for the lowest two Re_θ values. Notice that the receptivities above approximately 1 kHz collapse to unity, this is owing to the fact that little or no frequency content is physically present in the flow and, hence, the majority of frequencies above 1 kHz are merely noise which theoretically should be monotonically distributed throughout the measurements. There are occasional peaks observed in the receptivities above 1 kHz but these are understandable given both the effectively random nature

of the signal noise and the negligible magnitudes which were returned, making them sensitive to a dominating influence from any part of the frequency bin.

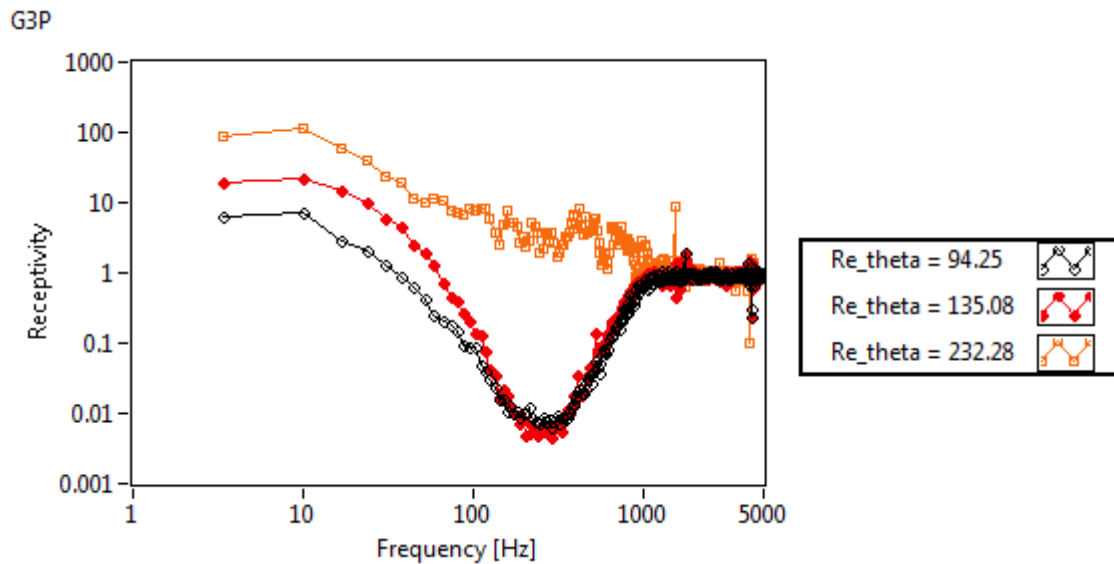


Figure 4-74 - Pre-transitional boundary layer receptivity (G3P)

4.7.3 NPG Receptivities

In this sub-section the receptivities of the negative pressure gradient bypass cases are discussed, i.e. G1N and G3N, and these are plotted in Figure 4-75 and Figure 4-76. These figures differ substantially from each other with respect to the range over which the frequencies content was receptive in the boundary layer. In Figure 4-75 the receptivity is seen to remain at a substantial level until a few hundred Hz, whereas for G3N (Figure 4-76) the drop off is observed at significantly lower frequencies – approximately an order of magnitude lower.

Another interesting observation contained in Figure 4-75 is the presence of a plateau and or a spike in the receptivity in the approximate range of 100 – 200 Hz before the eventual drop off, perhaps

indicating the significant influence of instability wave activity, albeit at a freestream turbulence intensity where the expectation was to observe domination from the bypass transition mechanism.

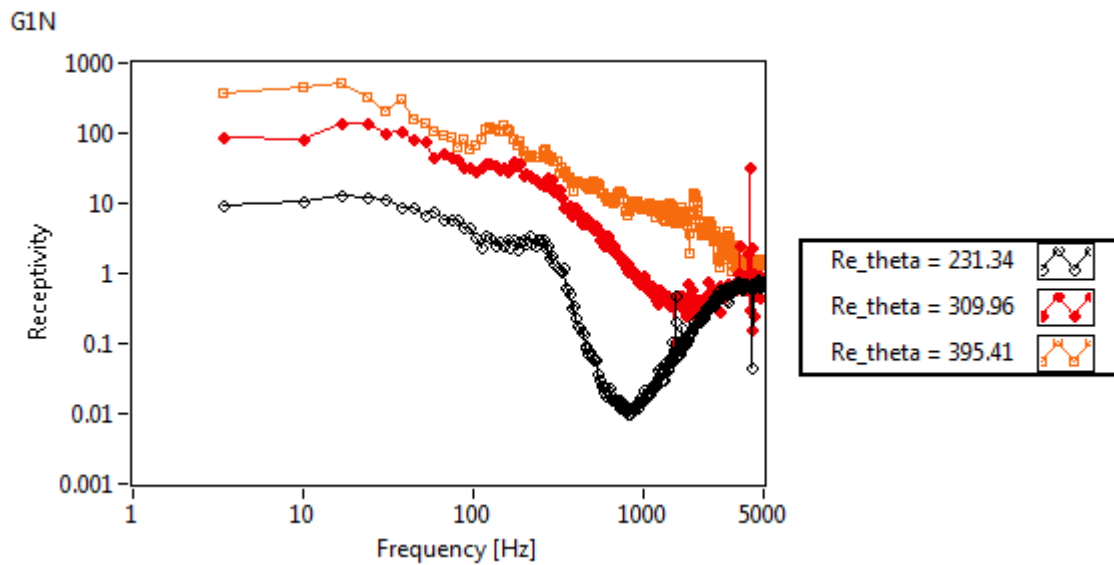


Figure 4-75 - Pre-transitional boundary layer receptivity (G_{1N})

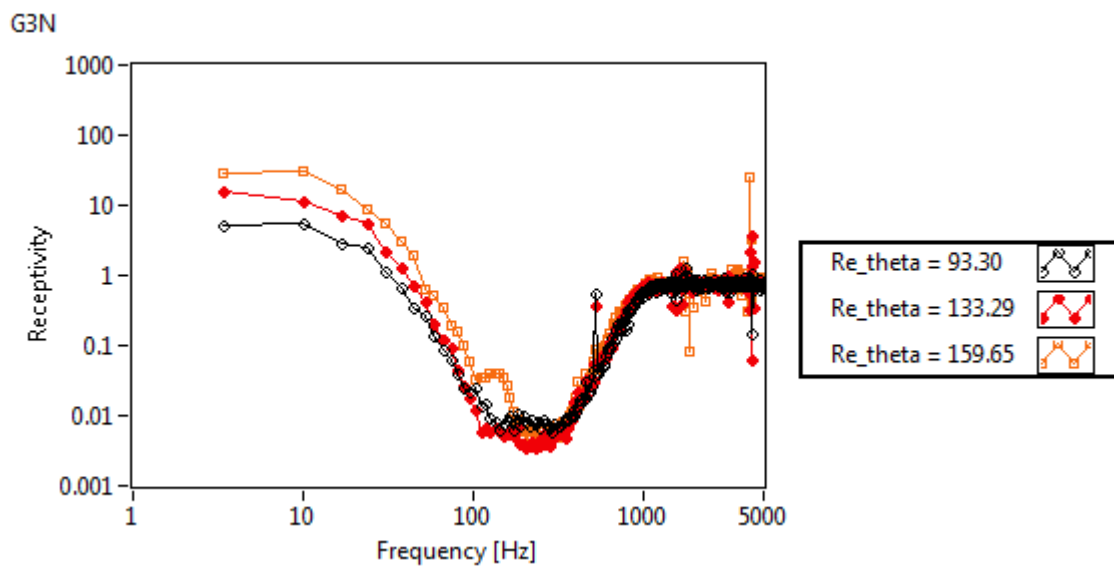


Figure 4-76 - Pre-transitional boundary layer receptivity (G_{3N})

5 Chapter 5 – Crossflow Boundary Layer Receptivity Code

The purpose of the numerical receptivity calculations performed and presented in this chapter are to contribute towards the understanding of the response of laminar boundary layers (with crossflow) to general three-dimensional disturbances in the freestream. A multitude of disturbances, of varying frequency combinations and orientations have been individually and collectively analysed in order to ascertain which frequencies are responsible for initiating the transition process under three different pressure gradients, ZPG, PPG and NPG where the pressure gradients are applied normal to the swept leading edge and the 2-D mesh is situated along this plane. Thereafter the trends which were observed are compared directly with the experimental results with the objective of improving the theoretical understanding of bypass transition in flat plate boundary layers with crossflow. The basis for such work is that in the absence of a complete knowledge of environmental disturbances a priori, it is useful to focus on the worst case scenarios instead by searching for the initial states which maximise disturbance amplitude at given downstream positions. Such analyses are useful for identifying the upper bounds on growth rates, which in turn is useful for predicting transition (Bottaro (2010)).

5.1 3-D Steady Code

The governing equations of the flow solved in the steady code are the Navier-Stokes equations in their steady, incompressible form, where these equations are provided in section 2.4.1. The code stores all of the flow variables at the cell centres of each rectangular mesh element and uses the pressure correction solution method, as part of a fourth order (unbounded central differencing) approximation for the values on the cell faces. Non-zero pressure gradients were imposed across a section of the plate – between 58 mm and 442 mm by linearly interpolating for each cell centre

between two target velocities (inflow and outflow velocities) and then effectively applying Bernoulli's equation, Equation 5-4, to designate the resulting pressure boundary condition.

The approach inflow was broken down into two components, dependent upon the sweep angle of the leading edge, and the outflow velocities were treated in the following manner;

$$u_{\infty|in} = U_{\infty|in} \cos \varphi \quad \text{Equation 5-1}$$

$$w_{\infty|in} = w_{\infty|out} = U_{\infty|in} \sin \varphi \quad \text{Equation 5-2}$$

$$u_{\infty|out} = U_{\infty|out} \cos \varphi \quad \text{Equation 5-3}$$

$$\frac{p_{\infty|in}}{\rho} + \frac{U_{\infty|in}^2}{2} = \frac{p_{\infty|out}}{\rho} + \frac{U_{\infty|out}^2}{2} \quad \text{Equation 5-4}$$

The boundary conditions applied for the base flows are summarised in Table 5-1 for each of the three steady solution files upon which the disturbances were superimposed and their unsteady behaviour analysed using the solution code detailed in section 5.2. The outlet velocities correspond to inviscid flows of the experimental analogues conducted in chapter 4 – i.e. they are the product of the inlet approach flow (always 10 m/s) and the area ratio between the outlet and inlet of the experimental test sections.

Table 5-1 - Boundary conditions for steady base flows

Case	Sweep Angle [°]	$U_{\infty in}$ [m/s]	U_{out} [m/s]
ZPG	60	10	10
PPG	60	10	9.792
NPG	60	10	10.386

Both the steady and unsteady codes were resolved on a 550 x 400 two dimensional grid with the dimensions as per Figure 5-1 and the grid oriented normal to the swept leading edge. In Figure 5-1 flow approaches from left to right and forms a boundary layer on an infinitesimally thin flat plate which is displaced 25 mm from the flow inlet. The physical extent of the domain is 550 mm in the streamwise direction and 20 mm in the normal direction, where the plate is centred in the normal extent at 10 mm. The magnitude of the approach flow is 10 m/s which results in a Reynolds number based on the chord length of 525 mm and (kinematic viscosity $\nu = 0.00001 \text{ m}^2/\text{s}$) of 5.25×10^5 which is typical of many boundary layer transition problems.

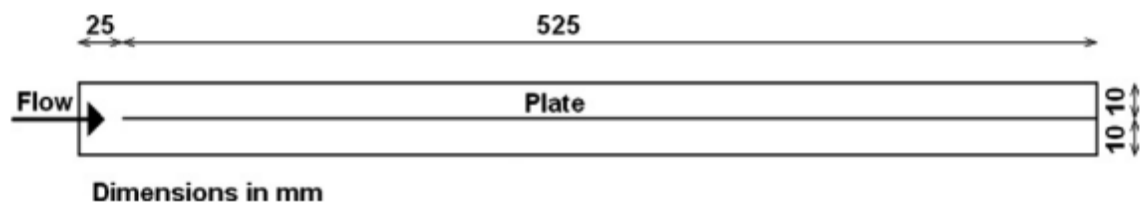


Figure 5-1 - Grid dimensions (in mm) for numerical receptivity calculations - Johnson (2011a)

5.1.1 3-D Steady Code Results

The output of the steady code for zero pressure gradient, in terms of the velocity magnitude, is indicated in the contour plot of Figure 5-2. The boundary layer on the flat plate is more clearly visible in Figure 5-3 where the normal coordinates, have been stretched 10-fold for demonstrative purposes. Here one can observe that the domain is sufficiently large such that the full boundary layer is captured throughout.

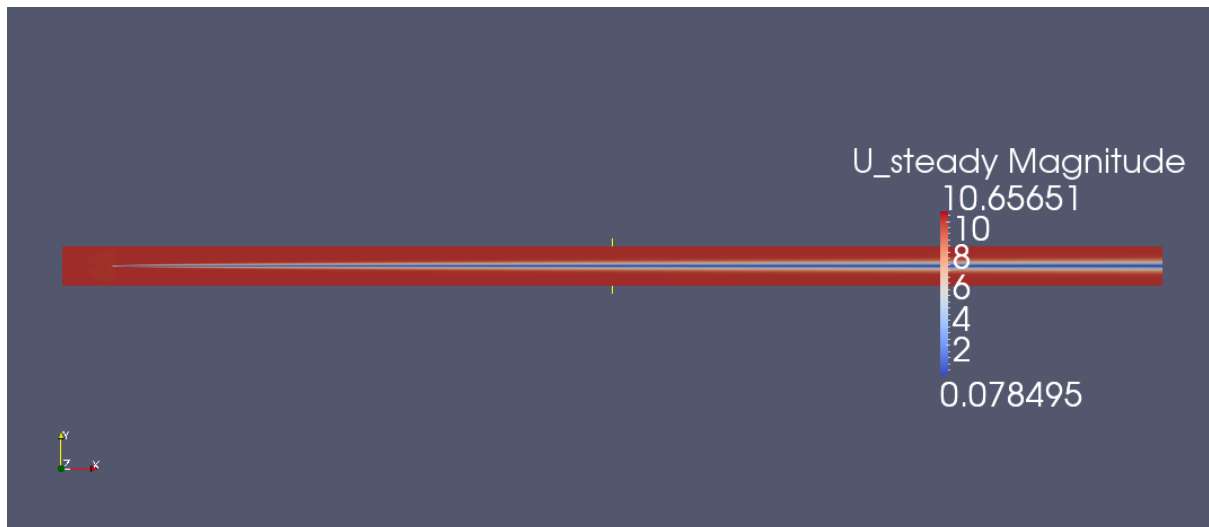


Figure 5-2 - Contour plot of velocity magnitude for steady ZPG flow [m/s]



Figure 5-3 - Contour plot of velocity magnitude for steady ZPG flow (stretched in normal direction) [m/s]

Unlike the previous contour plots the line plots of Figure 5-4, Figure 5-5 and Figure 5-6 are for a positive pressure gradient (PPG) case. Firstly it should be noted that the lines are plotted for either side of the plate and hence they are effectively symmetric (for steady flow only) about $y = 10\text{mm}$. These figures clearly indicate that the pressure gradient is only exerting an influence on the u velocity component, as desired, and whilst the w velocity does develop normal to the plate the w velocity in the freestream remains constant. Furthermore from the wall normal pressure distributions of Figure 5-6 it can be observed that the wall normal pressure gradient, $\frac{dp}{dy}$, approximately equals 0 near the wall once the transient effects from the leading edge are overcome.

Such an approximation, however, wasn't set as a boundary condition and the pressure on the plate was effectively computed directly, with the resulting wall normal gradient thereafter implied.

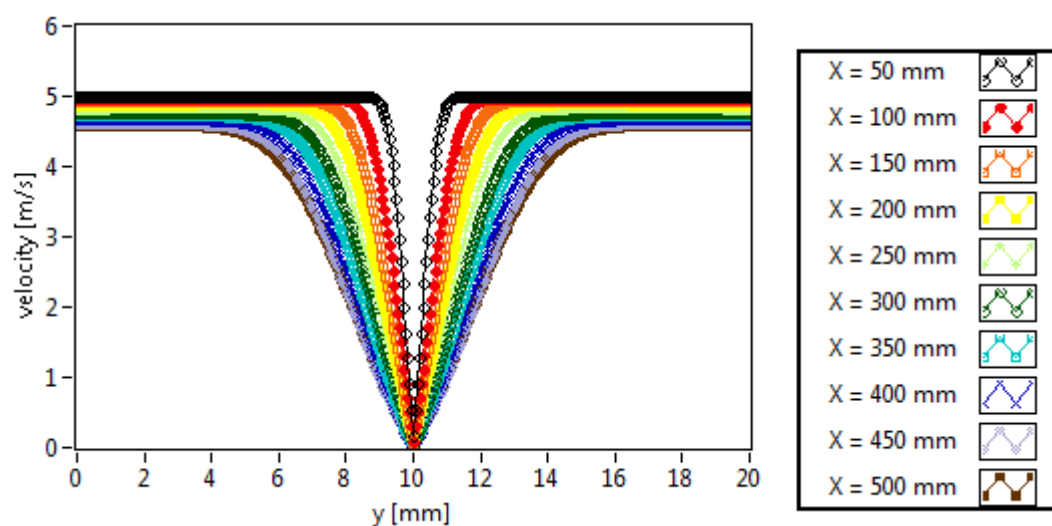


Figure 5-4 - u velocities for PPG with respect to normal coordinate at various streamwise displacements

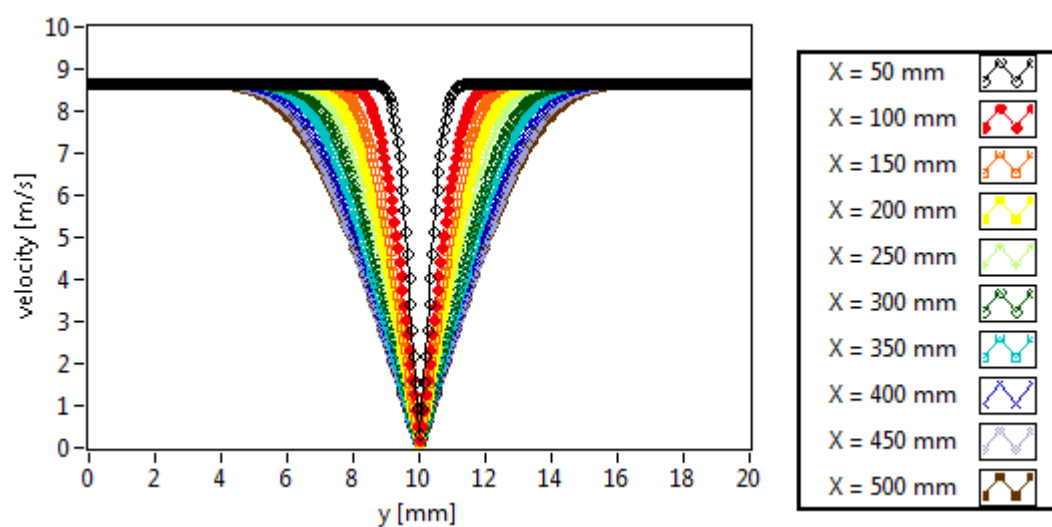


Figure 5-5 - w velocities for PPG with respect to normal coordinate at various streamwise displacements

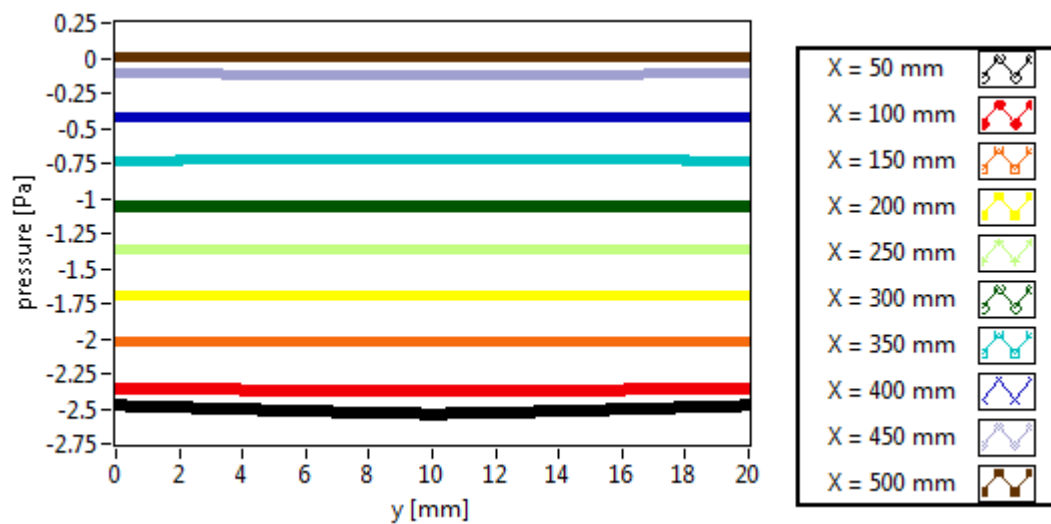


Figure 5-6 - Static pressure normal distributions at various streamwise locations for PPG

Numerical artefacts of the steady code solutions did exist upstream of the leading edge and these have been highlighted in Figure 5-7. These artefacts can be accounted for as being due to the combination of an infinitesimally thin leading edge and the use of unbounded central differencing momentum discretisation schemes. It's likely that with the implementation of alternative bounded momentum discretisation, such as upwind schemes, that such numerical artefacts would dissipate. Unfortunately, however, such schemes are known to be more dissipative and would enhance the decay of the freestream solutions, thus compromising efforts to resolve receptivity with respect to those oscillations. Nevertheless, these artefact oscillations are not observed beyond the leading edge and should therefore not affect receptivity.

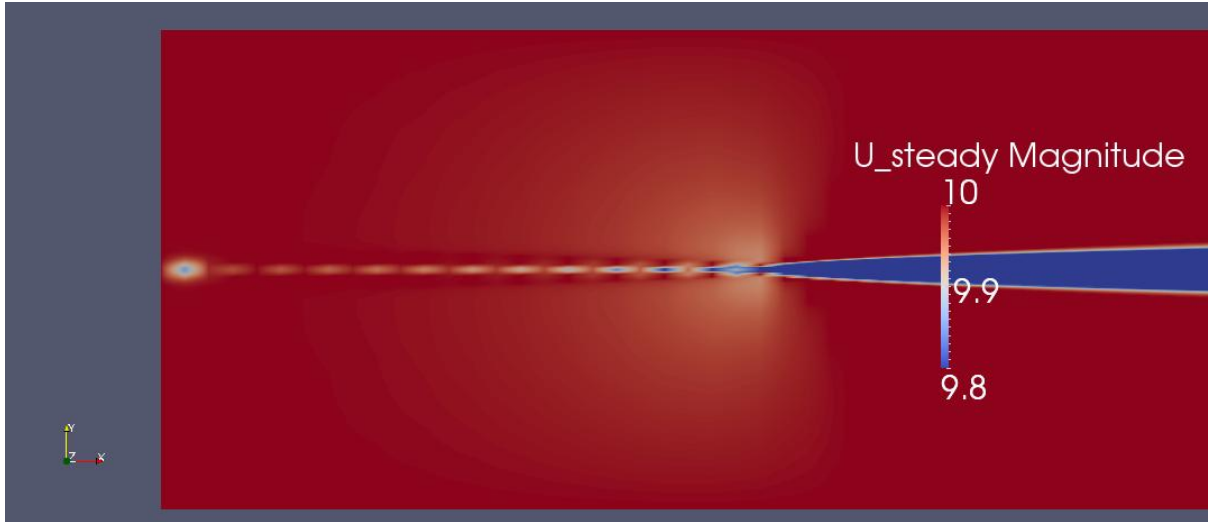


Figure 5-7 - Velocity contour plot upstream of leading edge highlighting numerical artefacts

5.2 3-D Unsteady Code

The steady code converges to a steady solution of the Navier-Stokes equations in three dimensions, as discussed in section 5.1. This steady solution was then used as the base flow on top of which an unsteady flow was superimposed, where the unsteady code operated using very similar numerical approaches – i.e. 4th order central differencing was used etc. This unsteady flow comprised linear waves in the complex form of

Equation 5-5 which could be considered as periodic in time and invariant in the spanwise direction as the flow is effectively infinite in this extent. These wave solutions would then be used as inputs in the form of $u'v'$ or $v'w'$ orientations, which correspond to oscillations in the spanwise-planar and streamwise-planar directions.

$$u' = u_f(x, y)e^{i(\omega_z z + \omega t)}$$

Equation 5-5

If each flow quantity is thought of as the sum of the base flow and the unsteady perturbation then the resulting two continuity equations - Equation 5-6 and Equation 5-7 and six momentum equations from Equation 5-8 through to Equation 5-15 govern the unsteady flow, where the subscript c is indicative of a cosine wave solution and, similarly, s denotes a sine wave solution. X_c in Equation 5-8, for example, is merely an indication that the proceeding balance relates to the momentum equation in the streamwise direction for a cosine solution.

Continuity Equations

$$C_c : \quad \frac{\delta u_c}{\delta x} + \frac{\delta v_c}{\delta y} + i\omega_z w_s = 0 \quad \text{Equation 5-6}$$

$$C_s : \quad \frac{\delta u_s}{\delta x} + \frac{\delta v_s}{\delta y} - i\omega_z w_c = 0 \quad \text{Equation 5-7}$$

Momentum Equations

$$\begin{aligned} X_c : \quad i\omega u_c + \frac{\delta}{\delta x} \left(\frac{p_c}{\rho} + 2Uu_c \right) + \frac{\delta}{\delta y} (vu_c + uv_c) - \nu \nabla^2 u_c \\ + \nu \omega_z^2 u_c + wu_s \omega_z + uw_s \omega_z = 0 \end{aligned} \quad \text{Equation 5-8}$$

$$\begin{aligned} X_s : \quad i\omega u_s + \frac{\delta}{\delta x} \left(\frac{p_s}{\rho} + 2Uu_s \right) + \frac{\delta}{\delta y} (vu_s + uv_s) - \nu \nabla^2 u_s + \nu \omega_z^2 u_s \\ - wu_c \omega_z - uw_c \omega_z = 0 \end{aligned} \quad \text{Equation 5-9}$$

$$Y_c : \quad i\omega v_c + \frac{\delta}{\delta x}(Uv_c + vu_c) + \frac{\delta}{\delta y}\left(\frac{p_c}{\rho}\right) - \nu \nabla^2 v_c + \nu \omega_z^2 v_c \\ + wv_s\omega_z + vw_s\omega_z = 0$$

Equation 5-10

$$Y_s : \quad i\omega v_s + \frac{\delta}{\delta x}(Uv_s + vu_s) + \frac{\delta}{\delta y}\left(\frac{p_s}{\rho}\right) - \nu \nabla^2 v_s + \nu \omega_z^2 v_s \\ - wv_c\omega_z - vw_c\omega_z = 0$$

Equation 5-11

$$Z_c : \quad i\omega w_c + \frac{\delta}{\delta x}(Uw_c + wu_c) + \frac{\delta}{\delta y}(vw_c + wv_c) - \omega_z \frac{p_s}{\rho} - \nu \nabla^2 w_c \\ + \nu \omega_z^2 w_c + 2ww_s\omega_z + ww_s\omega_z = 0$$

Equation 5-12

$$Z_s : \quad i\omega w_s + \frac{\delta}{\delta x}(Uw_s + wu_s) + \frac{\delta}{\delta y}(vw_s + wv_s) + \omega_z \frac{p_c}{\rho} - \nu \nabla^2 w_s \\ + \nu \omega_z^2 w_s - 2ww_c\omega_z - ww_c\omega_z = 0$$

Equation 5-13

Both sine and cosine solutions were produced for $u'v'$ and $v'w'$ orientations (spanwise planar and streamwise planar waves) in order to check that they produced equivalent outputs for debugging purposes which, once realised and thereafter, only cosine solutions were executed. However, owing to the fact that several graphical output codes for processing the resulting output files were written for use in LabVIEW and ParaView, the output statements were maintained so as to continue to write out all unsteady components, even though the output files were effectively sparse, with 50% of the outputs as zeros. This, however, is not meant to imply that only 50% of the governing equations were active during the solution procedure as all equations, both for mass and momentum

conservation, possessed ‘cross-talk’ terms. That is to say Equation 5-6, the cosine continuity equation for example, contains the sine component $i\omega_z w_s$ and similarly Equation 5-7, the sine continuity equation contains $i\omega_z w_c$.

Furthermore, contrary to the 2-D genesis of this approach by Johnson (2011a), given that the steady solution contains non-zero spanwise velocities there are more terms which would reduce back to those given in Johnson (2011a) where $w = 0$ for either the cosine or sine governing equations.

The freestream fluctuations for each solution collectively represent a large number of waves with differing spatial, temporal frequencies and velocity orientations. In Johnson (2011a) the decay of any such waveforms exhibit decay (β) in the streamwise direction in the form of Equation 5-14.

$$\beta = -\frac{U}{2\nu} + \left(\left(\frac{U}{2\nu} \right)^2 + \omega_x^2 + \omega_y^2 + \omega_z^2 \right)^{0.5} \quad \text{Equation 5-14}$$

The following is a flowchart presentation for the main execution sequence in the unsteady Fortran code routine;

- Read in boundary_layer_3d.res converged steady solution file (ZPG, PPG or NPG steady solution file)
- Read lastfile.dat which contains the discrete spatial frequencies in an extended hexadecimal format concatenated to information concerning the frequency orientation
- Set main solution parameters such as time step increment, number of time steps and solution over-relaxation
- Determine whether the unsteady flow solution was of $u'v'$ or $v'w'$ type, as specified in lastfile.dat
- Start calculation with the initial condition for the linear perturbation in each of cell, set to the analytical solution value for a freestream
- Read in previous solution, if present

- Allocate memory for residuals of each of the governing equations and initialise them all as zero
- Begin time-marching loop
- Compute the fluxes through each of the faces
- Compute viscous terms
- Update the velocities in the momentum equations
- Calculate the continuity errors on each of the faces
- Execute pressure-correction (see Patankar and Spalding (1972)) over-relaxation iterative loops (separately) for cosine and sine pressure terms
- Update velocities for the pressure change and exit the loop if the minimum solution time is reached and convergence criteria are satisfied or return for another pass through the time-marching loop until convergence is achieved or the maximum number of time steps is reached

These unsteady solution procedures were executed for 2106 frequency and solution orientation combinations; $2(u'v' \text{ and } v'w') \times 13(a_x) \times 9(a_y) \times 9(a_z)$ for three different pressure gradients, hence a total of 6318 unsteady solution files and 3 steady files – one for each pressure gradient were produced. Each frequency configuration would consume approximately three days in solution time to reach what were considered to be converged solutions. However the exact quantity of processing time would vary significantly from one case to another depending on how many time steps were required to achieve convergence and, furthermore, the number of iterations required per time step for each pass through the pressure-correction loop. Given the large number of solution files which required processing the University of Liverpool HTCondor (version 7.8.6) high-throughput computing cluster was utilised. This facility makes use of unoccupied computer resources (dead-cycles) within the available university pools. Many of these machines, if not the majority, were to multi-core

specifications and hence jobs could, in theory, be executed on a single machine up to the maximum arity of cores/threads available, depending upon what is the limiting factor.

Whilst the availability of such a facility offered the opportunity to execute a large array of frequency combinations simultaneously, the environment in which the programs are executed can be erratic in the sense that the facility is shared, both with other HTCondor users, and often directly by the physical occupier of the computer in the HTCondor pool. Furthermore, in line with university policy, the computers in the pool are reset at midnight every night and given that each solution would take more than 24 hours it was essential to make use of ‘checkpointing’ as it is known in the HTCondor ‘vanilla universe’ when using a single submission approach – i.e. as opposed to an approach where intermediary jobs are routinely re-submitted. Unfortunately this is not as simple as enabling checkpointing and demanding that the HTCondor facility continues from the hang point from where the job was vacated, as it requires the implementation of robust coding practice in the unsteady Fortran codes themselves. In practical terms this mainly involved writing the solution files for every 10 time steps and reading the solution time from the last saved solution file, such that target solution times were reached accurately, as opposed to entering an infinite loop, given that the overall processing time was larger than each individual computer/nodes maximum consecutive uptime. Another important consideration was that once a job had completed sufficient time steps, such as to be commanded to write a solution file, if it were to then overwrite the existing solution file but not finish writing the file then the program would be left with a partially written solution file, which then result in a crash when read into the unsteady program once the job was resubmitted. Hence, the approach of writing the file under an alias and then renaming it with respect to the convention of a filename hierarchy understood by the unsteady program, was utilised. This approach was far more robust given that renaming a file is an operation which takes a fraction of a second for a modern computer, whereas writing an approximately 40MB ASCII file takes many orders of magnitude longer.

5.2.1 3-D Unsteady Code Results

Both Figure 5-8 and Figure 5-9 denote screenshots from Paraview 3.98.1 of contour plots of turbulence intensity for a typical (individual) receptive and a typical non-receptive frequency case – both examples are $v'w'$ cases. Additionally, wall normal profiles at a fixed streamwise displacement of 400 mm from the inlet (375 mm from the leading edge) have also been included where the grey markers indicate the extremities of the line plots.

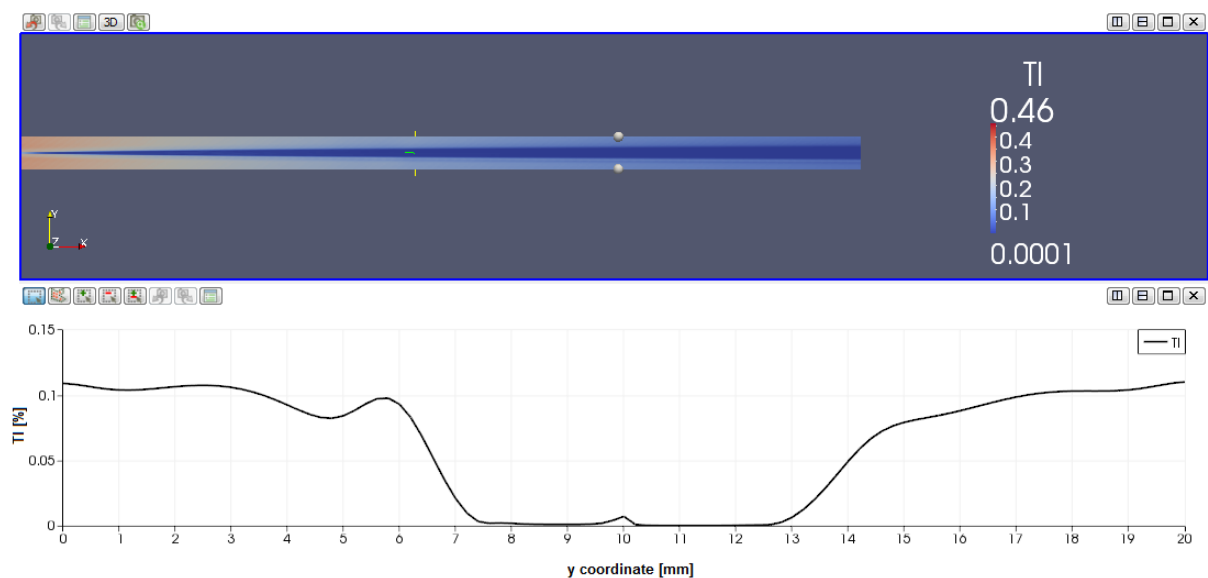


Figure 5-8 - Paraview screenshot of typical non-receptive turbulence intensity contours with additional line plot normal to the plate

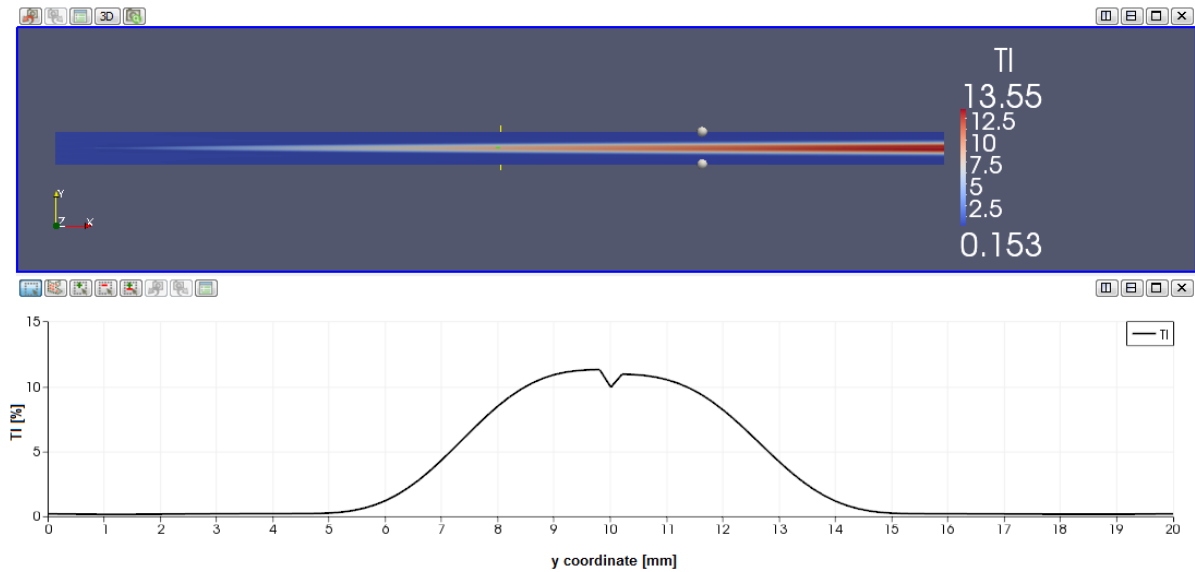


Figure 5-9 - Paraview screenshot of receptive turbulence intensity contours with additional line plot normal to the plate

A major drawback of many numerical simulations is the absence of capturing the leading edge, meaning that the complicated receptivity of the leading edge is omitted. This is true even when the leading edge is modelled as part of the mesh in DNS with a symmetry condition, where they have been shown to damp the vertical Reynolds stress by a factor of 6 (Ovchinnikov et al. (2008)). Hence, since a symmetry boundary condition was not desired or in fact used, flow is present on either side of the plate and as such the plate intersects the wall normal profiles at a y coordinate of 10 mm in the domain.

There are several important observations to be made at this stage, firstly the profiles exhibit approximately reversed qualitative behaviour, which is to say where the turbulence intensity is high near the wall (relative to the freestream) in Figure 5-8, it is by contrast low in Figure 5-9. Similarly the opposite is true outside of the boundary layers where the freestream turbulence intensity is high in Figure 5-8 and low in Figure 5-9, relative to their near wall values. It should be noted with this linear approach that the turbulence intensities at the inlet are essentially arbitrary which has no influence on the determined receptivities as the near wall turbulence intensities essentially scale linearly with those of the freestream. As such the boundary layer is receptive to

the frequency combination of Figure 5-9 but not so in Figure 5-8. This is due to the respective frequency combinations of the two different cases exhibiting dissimilar response in the boundary layer. In Figure 5-8 all of the spatial frequencies are higher which is interesting in itself because one can observe from the contour plot that the amplitude of the incoming waves decays fairly rapidly in the streamwise direction.

Every permutation of the following frequency codes of Table 5-2 and

Table 5-3 for all the spatial frequency components were computed where the corresponding frequency magnitudes are listed. For example the $u'v'$ case of G08000 contained spatial frequencies of 0.1 (G0), 0.3 (80) and 0.03 (00) in the streamwise, wall normal and spanwise direction. This choice of 13 streamwise, 9 wall normal and 9 spanwise frequencies resulted in a total of 1053 frequency permutations for each wavetype – $u'v'$ and $v'w'$. Hence there were 2106 resulting output files in total for each pressure gradient, along with the steady base flow for each pressure gradient, from which the unsteady solutions were computed.

Table 5-2 - Frequency magnitude with corresponding extended hexadecimal code (x frequencies)

Frequency Code	Frequency Magnitude [radians/mm]
00	0.001
20	0.001778
40	0.003162
60	0.005623
80	0.01
A0	0.017783
C0	0.031623
E0	0.056235
G0	0.100001
I0	0.17783
K0	0.316232
M0	0.562349
O0	1.00001

Table 5-3 - Frequency magnitude with corresponding extended hexadecimal code (y and z frequencies)

Frequency Code	Frequency Magnitude [radians/mm]
00	0.03
20	0.053348
40	0.094869
60	0.168703
80	0.300001
A0	0.533487
C0	0.94869
E0	1.68704
G0	3.00003

Some of the individual receptivities are plotted in the following figures in order to highlight some of the typical trends which were observed. For simplicity the following figures of individual receptivities are presented for the ZPG case only but very similar receptivity trends were observed across all pressure gradients and the effect of the pressure gradient was predominantly to amplify or attenuate comparative receptivities.

Firstly Figure 5-10 illustrates an example where one frequency combination (200060 – $u'v'$) is receptive on one side of the plate (above) but not the other, albeit the receptivities above the plate aren't increasing at a particularly high rate with respect to Re_θ . Figure 5-11 on the other hand, while asymmetry exists between each side of the plate, demonstrates a case (20A0C0 – $u'v'$) where the boundary layer isn't receptive in either case. This asymmetry in receptivity on either side of the plate is very typical for the $u'v'$ waveforms. One can observe from the two aforementioned figures that reasonably checker board oscillations are present in the data towards the leading edge where the boundary layer is comparatively thin and leading edge receptivity caused with respect to the infinitely sharp leading edge profile is present. This may be attributed to the use of central differencing and could, perhaps, be reduced with consideration of the cell face values rather than the cell centre. Nevertheless these oscillations were not considered to be too severe so can be

accepted, particularly given that they appear to have negligible influence on the receptivity which is being ascertained.

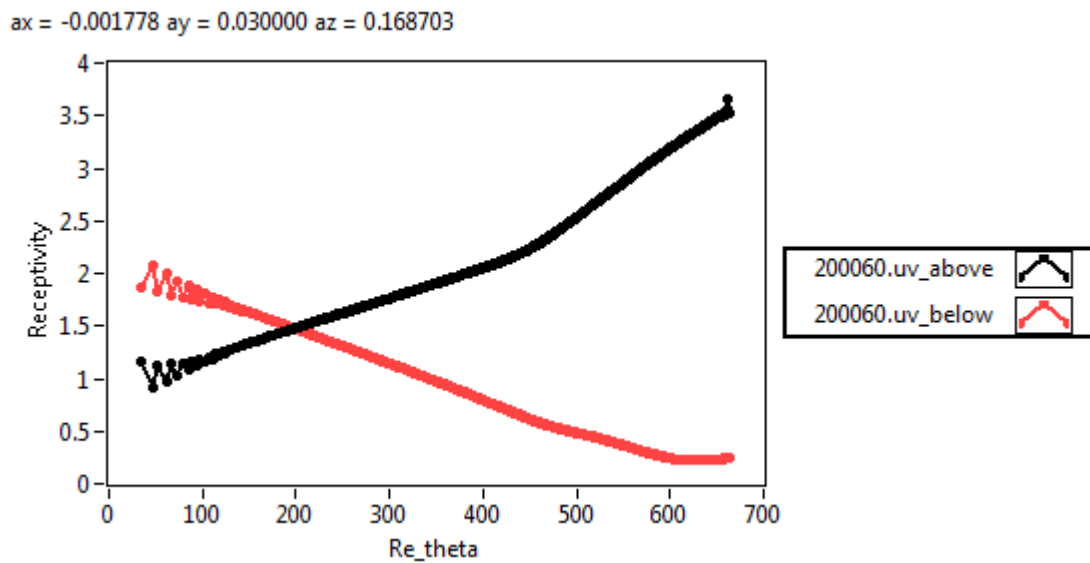


Figure 5-10 - Receptivity versus Re_θ for 200060 u'v' case (ZPG)

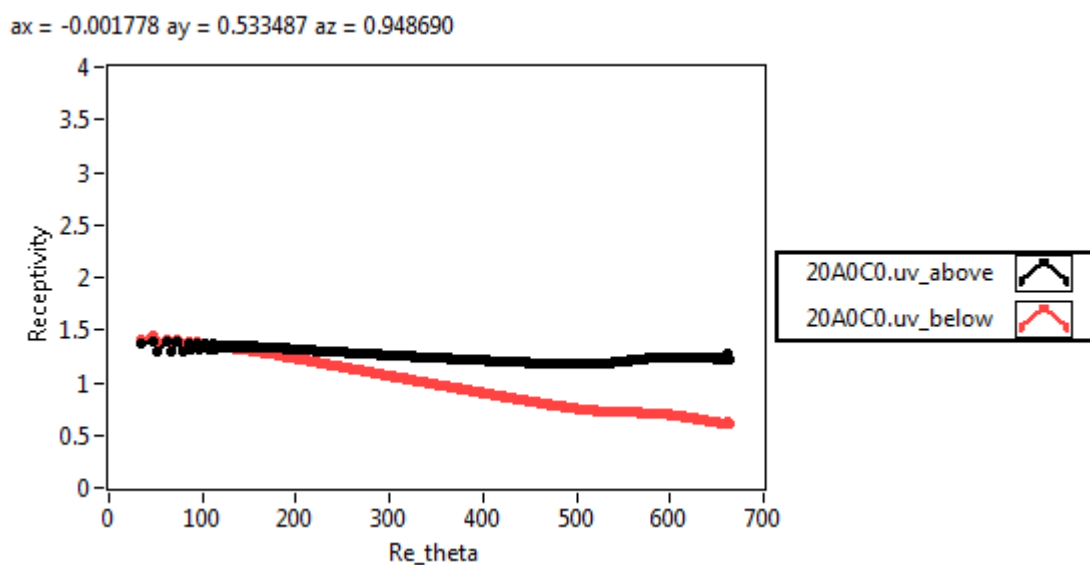


Figure 5-11 - Receptivity versus Re_θ for 20A0C0 u'v' case (ZPG)

A receptive $v'w'$ case (00A060) is given in Figure 5-12. Here one can observe that, in addition to this being a receptive combination of frequencies and orientation, that there are negligible differences with respect to the receptivity outputs observed. This was typically, but not always, the case for $v'w'$

waveforms as can be understood from Figure 5-13 where the receptivity below the plate maintains its steady increase with Re_θ after a Re_θ of around 750, where, in contrast, the receptivity accelerates above the plate. On the whole the differences on either side of the plate were predominantly negligible for $v'w'$ (i.e. the streamwise-planar) waveforms.

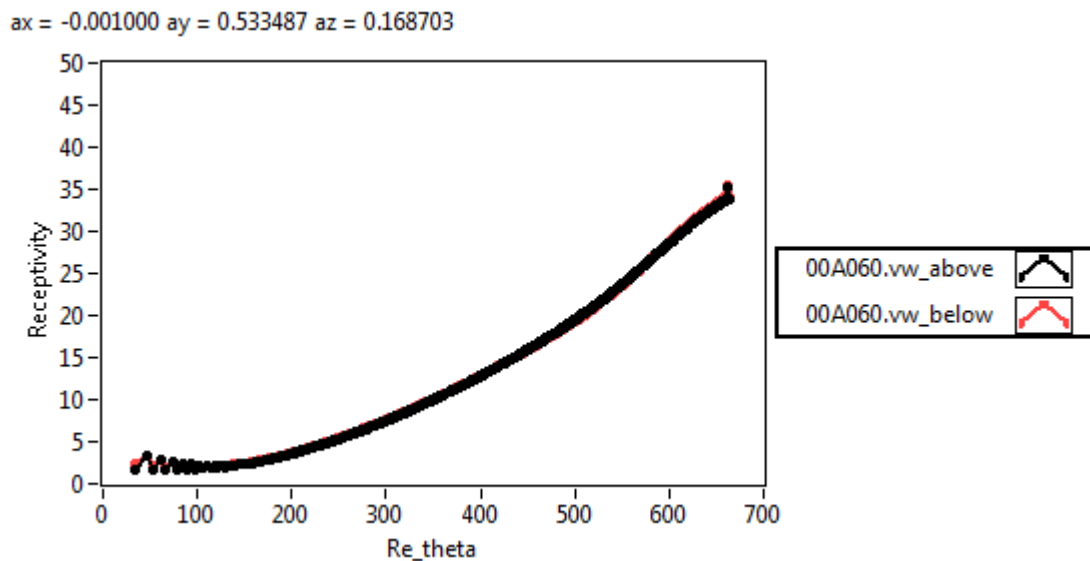


Figure 5-12 - Receptivity versus Re_θ for 00A060 $v'w'$ case (ZPG)

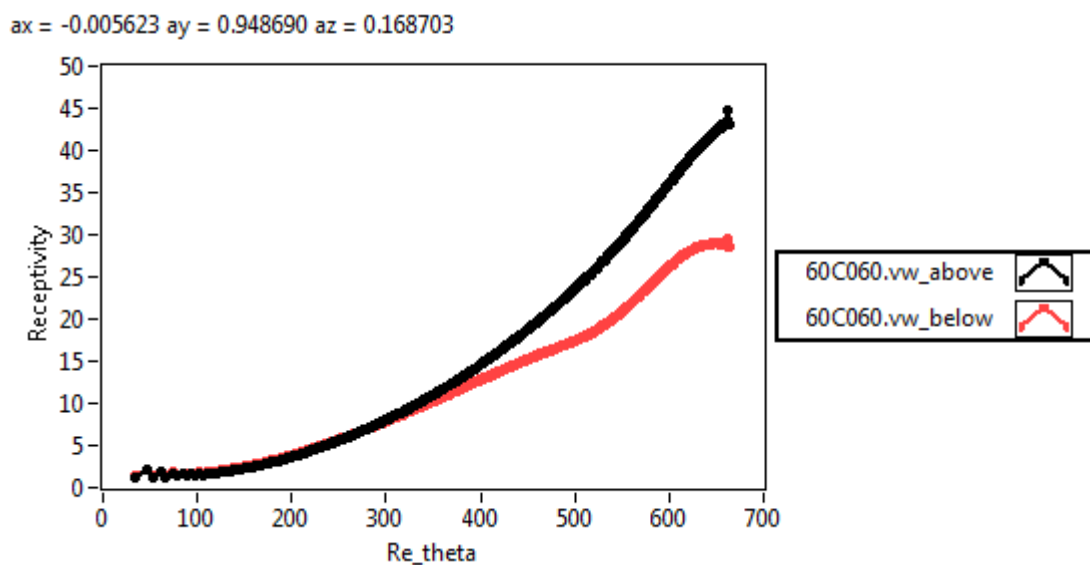


Figure 5-13 - Receptivity versus Re_θ for 60C060 $v'w'$ case (ZPG)

Once all of the resulting individual unsteady output files converged they were then processed for receptivity for the entire plate (both above and below) and then written out to ASCII data files with an arbitrary .rpy extension and a unique file string name consisting of concatenated frequency codes and the solution orientation, i.e. $u'v'$ or $v'w'$. Thereafter 5 points on the plate have been selected, which roughly correspond to the range of observed momentum thickness Reynolds numbers, for the start of transition in the experiments, for a more comprehensive analysis of the spectrum of frequencies considered. This is achieved by performing double integrals of the receptivities across the limits of the y and z spatial frequencies (for fixed values of a_x) which were evaluated as in Equation 5-15.

$$\overline{R_{yz}}(a_x) = \frac{1}{\Delta a_y a_z} \int_{a_{zmin}}^{a_{zmax}} \int_{a_{ymin}}^{a_{ymax}} R da_y da_z \quad \text{Equation 5-15}$$

Then once all of the integrals had been evaluated the resulting receptivities, unique to an individual a_x and Re_θ , were plotted on a graph such as Figure 5-14 which is the receptivities for the ZPG case for $u'v'$ waves above the plate. Figure 5-15 is an almost identical case, only on this occasion the receptivities are resolved below the plate. One can already observe that although the qualitative trends are similar the receptivities are seen to be higher below the plate.

ZPG uv above

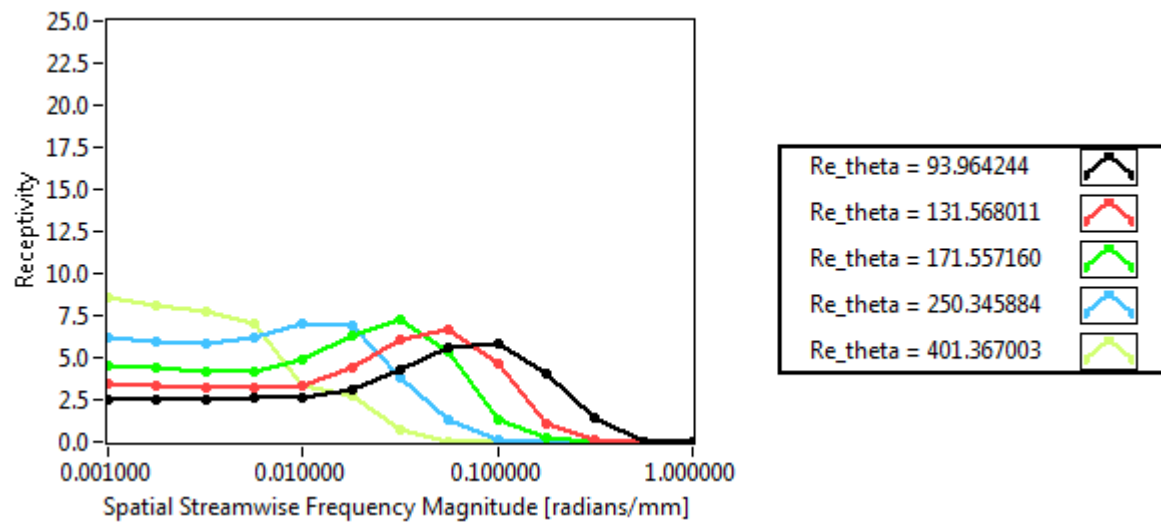


Figure 5-14 - Receptivity versus spatial streamwise frequency magnitude for uv waves under nominally zero pressure gradient at various momentum thickness Reynolds numbers (above plate)

ZPG uv below

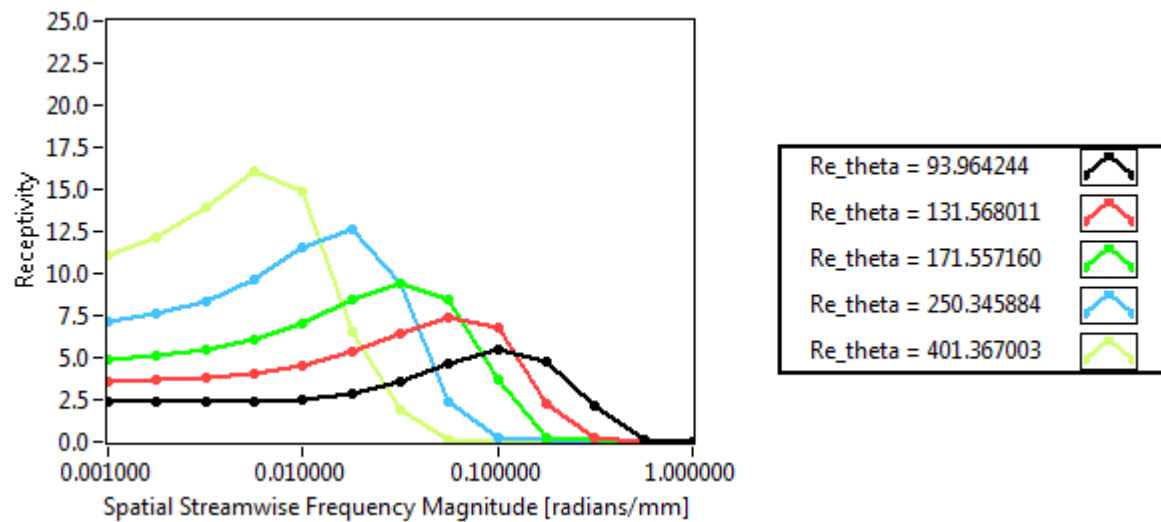


Figure 5-15 - Receptivity versus spatial streamwise frequency magnitude for uv waves under nominally zero pressure gradient at various momentum thickness Reynolds numbers (below plate)

Other immediate observations in both Figure 5-14 and Figure 5-15 are that the receptivities are greatest for the lowest values of a_x and, furthermore, that the receptivity increases with increasing Re_{θ} . It is well known that laminar boundary layers are most responsive to low frequency fluctuations, see for example Blair (1992), and these results already appear to confirm such observations. The same trends are observed in Figure 5-16 and Figure 5-17.

ZPG vw above

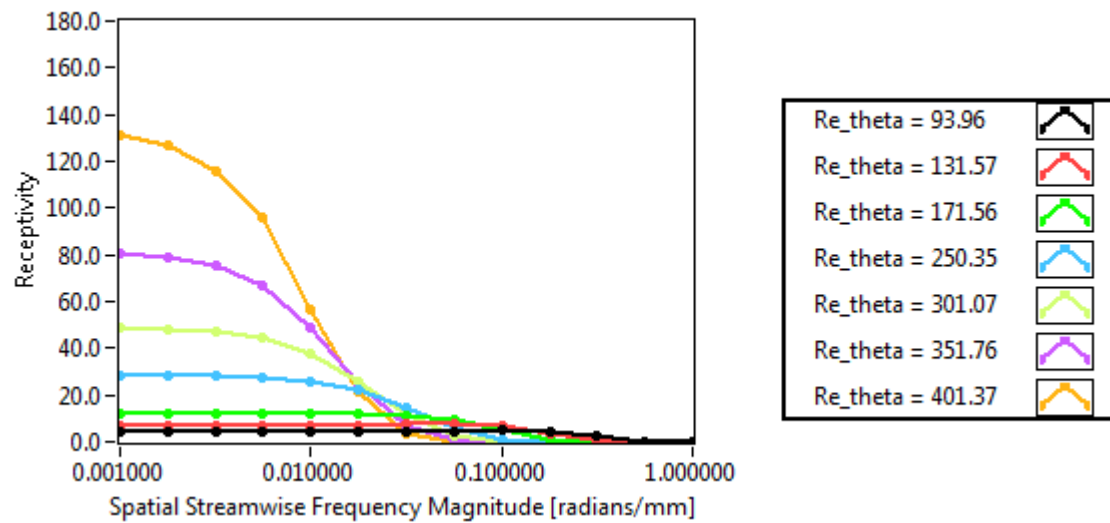


Figure 5-16 - Receptivity versus spatial streamwise frequency magnitude for $v'w'$ waves under nominally zero pressure gradient at various momentum thickness Reynolds numbers (above plate)

ZPG vw below

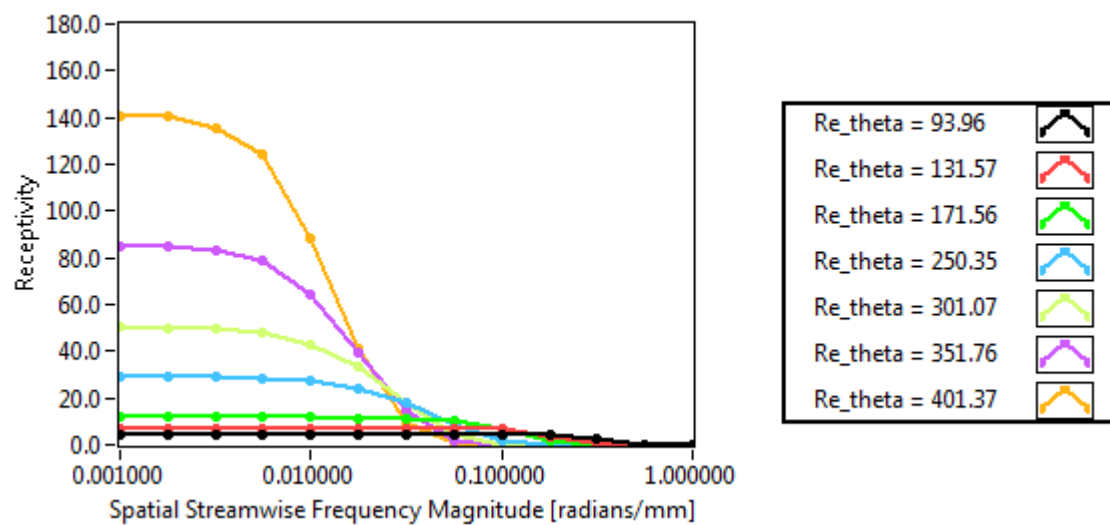


Figure 5-17 - Receptivity versus spatial streamwise frequency magnitude for $v'w'$ waves under nominally zero pressure gradient at various momentum thickness Reynolds numbers (below plate)

5.3 Comparisons between Numerical and Experimental Results

In this section the receptivity outputs from the numerical codes are compared directly with the experimental results. In order to make direct comparisons between the two one must firstly non-

dimensionalise the frequencies, owing to the differing kinematic viscosities and freestream velocities. The non-dimensionalisation is achieved for each frequency in the form of Equation 5-16.

$$\Omega_x = \frac{\nu a_x}{U_0} \quad \text{Equation 5-16}$$

The other frequencies from the numerical work are non-dimensionalised in a similar manner;

$$\Omega_y = \frac{\nu a_y}{U_0} \quad \text{Equation 5-17}$$

$$\Omega_z = \frac{\nu a_z}{U_0} \quad \text{Equation 5-18}$$

In the experimental work the frequency orientations are unknown, as such it's impossible to break them down into their component frequencies, therefore a bulk frequency non-dimensionalisation is used, as per Equation 5-19.

$$\Omega = \frac{fL}{U_0} \quad \text{Equation 5-19}$$

Note that the freestream velocities, from which the frequencies are normalised, are taken to be at the calibration station ($X = 100$ mm) in the experimental work and the inlet velocity upstream of the leading edge in the numerical calculations and the characteristic length is taken as the length of the flat plate in the numerical work for both cases, i.e. 525 mm.

5.3.1 Non-Dimensional Numerical Receptivities

In this sub-section the receptivities are presented in non-dimensional frequency form for the numerical calculations through executing the procedures described in section 5.2. These are first presented with respect to unique $u'v'$ and $v'w'$ wave orientations from Figure 5-18 to Figure 5-23. Thereafter the $u'v'$ and $v'w'$ receptivities are combined in the manner of Equation 5-20 to form the unique receptivity plots (below the plate) from Figure 5-24 to Figure 5-26.

$$R_{combined} = \sqrt{R_{uv}^2 + R_{vw}^2} \quad \text{Equation 5-20}$$

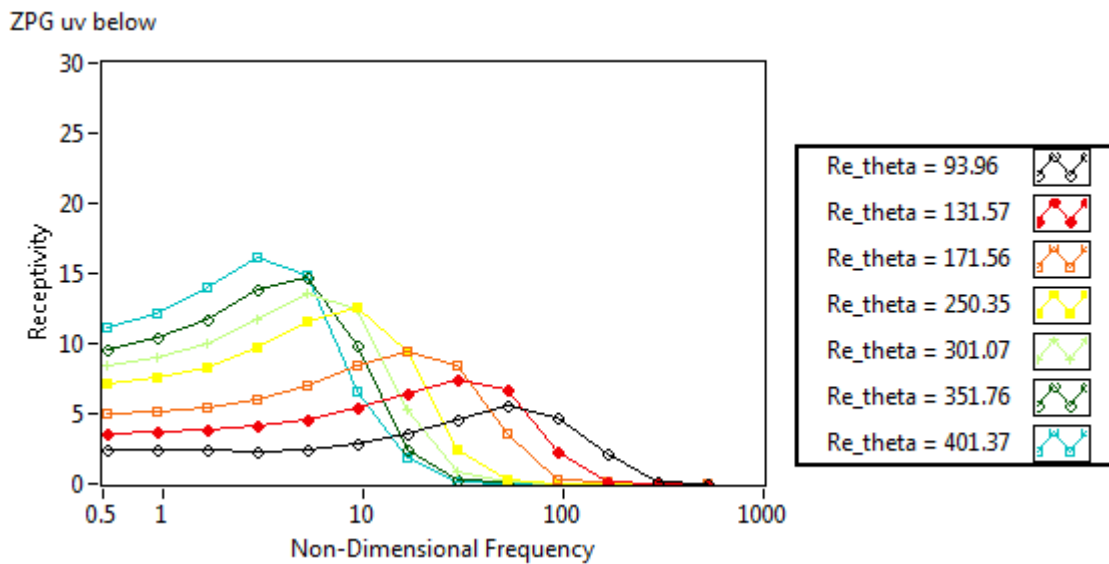


Figure 5-18 - Numerical $u'v'$ receptivity versus non-dimensional frequency at various momentum thickness Reynolds numbers below the plate (ZPG)

ZPG vw below

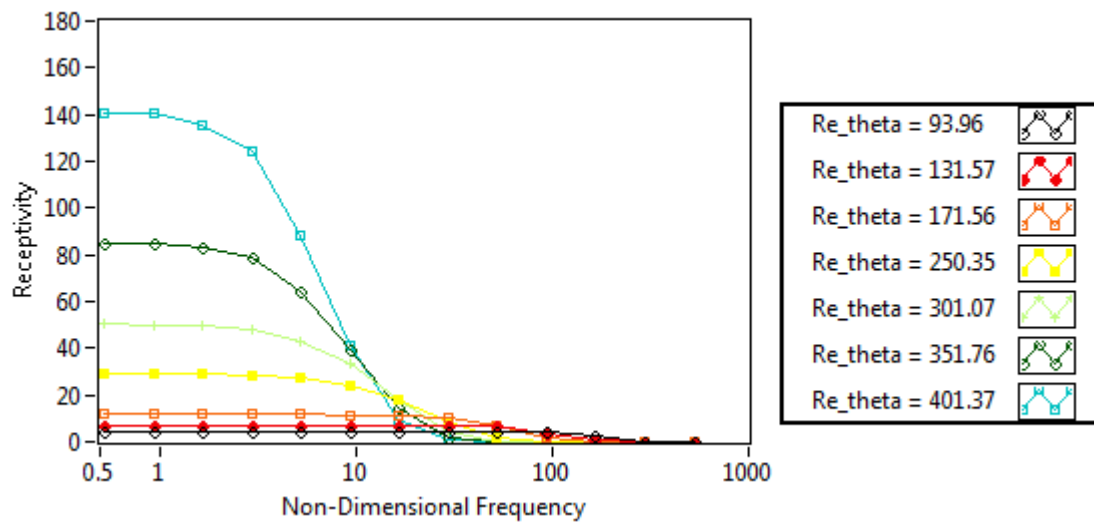


Figure 5-19 - Numerical $v'w'$ receptivity versus non-dimensional frequency at various momentum thickness Reynolds numbers below the plate (ZPG)

PPG uv below

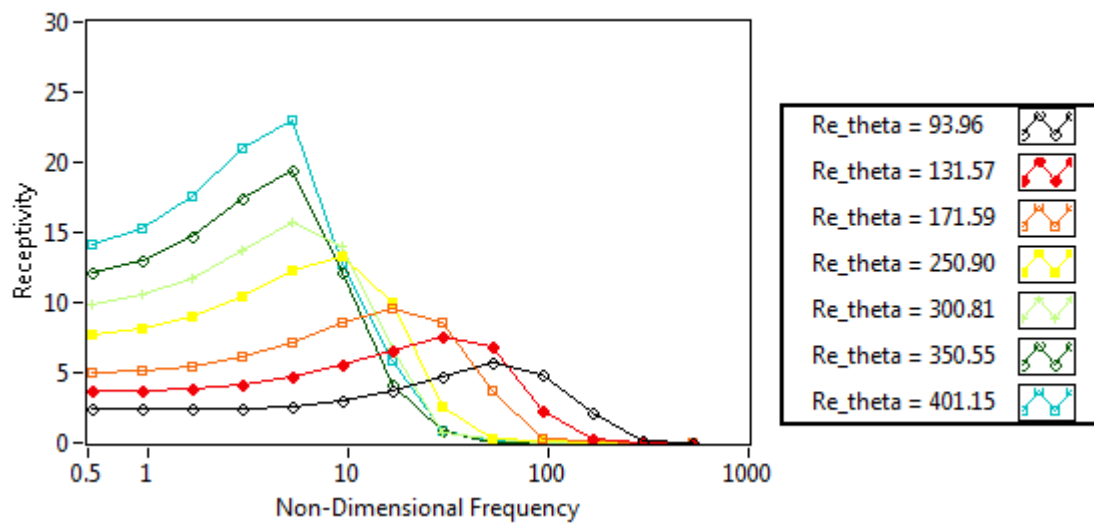


Figure 5-20 - Numerical $u'v'$ receptivity versus non-dimensional frequency at various momentum thickness Reynolds numbers below the plate (PPG)

PPG vw below

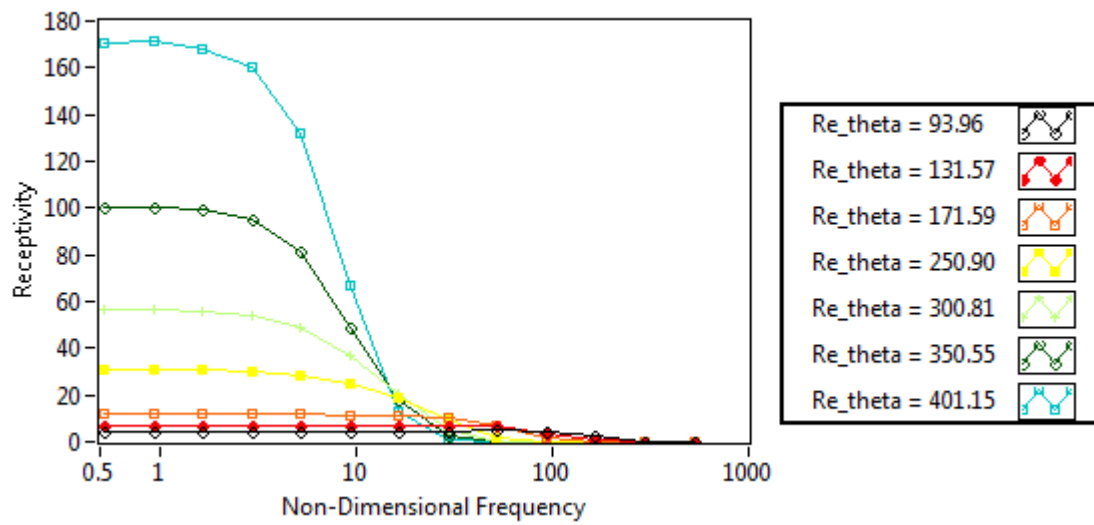


Figure 5-21 - Numerical $v'w'$ receptivity versus non-dimensional frequency at various momentum thickness Reynolds numbers below the plate (PPG)

NPG uv below

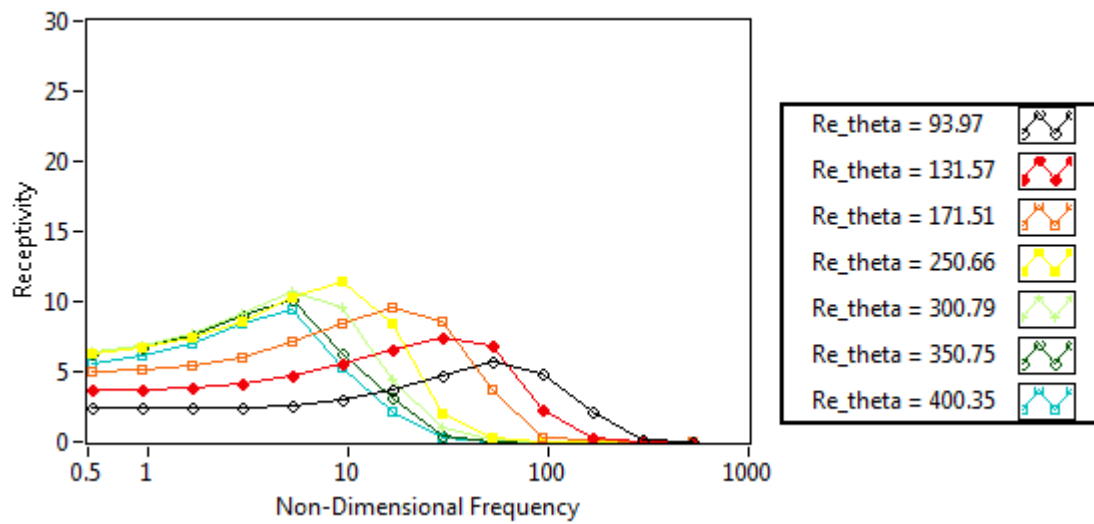


Figure 5-22 - Numerical $u'v'$ receptivity versus non-dimensional frequency at various momentum thickness Reynolds numbers below the plate (NPG)

NPG vw below

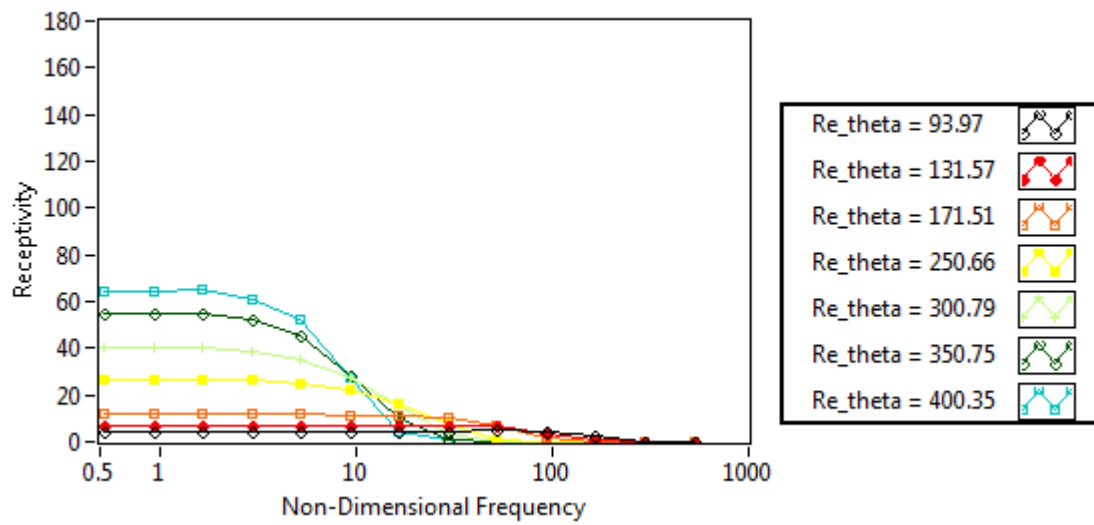


Figure 5-23 - Numerical $v'w'$ receptivity versus non-dimensional frequency at various momentum thickness Reynolds numbers below the plate (NPG)

ZPG

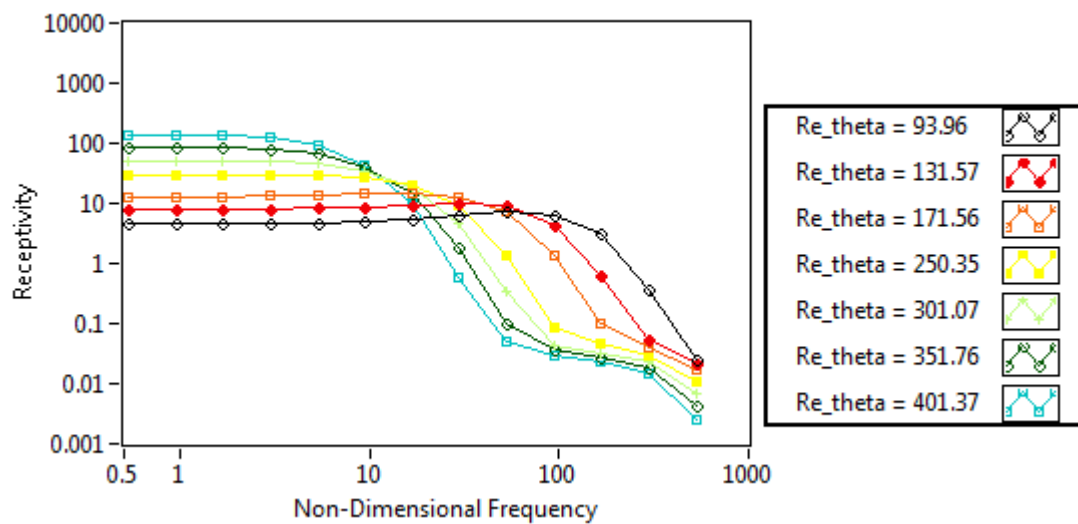


Figure 5-24 - Numerical combined receptivity versus non-dimensional frequency at various momentum thickness Reynolds numbers below the plate (ZPG)

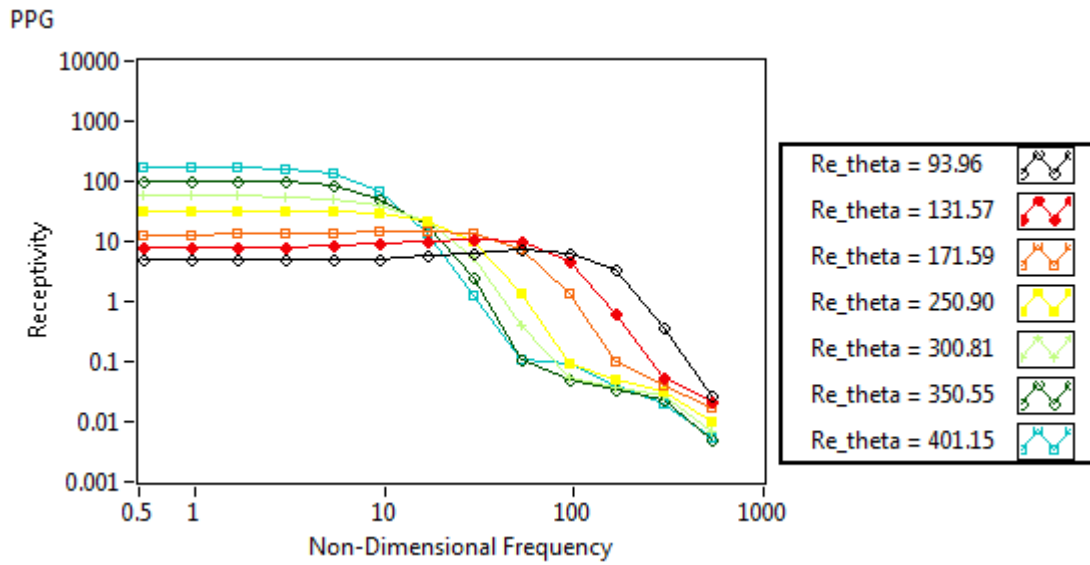


Figure 5-25 - Numerical combined receptivity versus non-dimensional frequency at various momentum thickness Reynolds numbers below the plate (PPG)

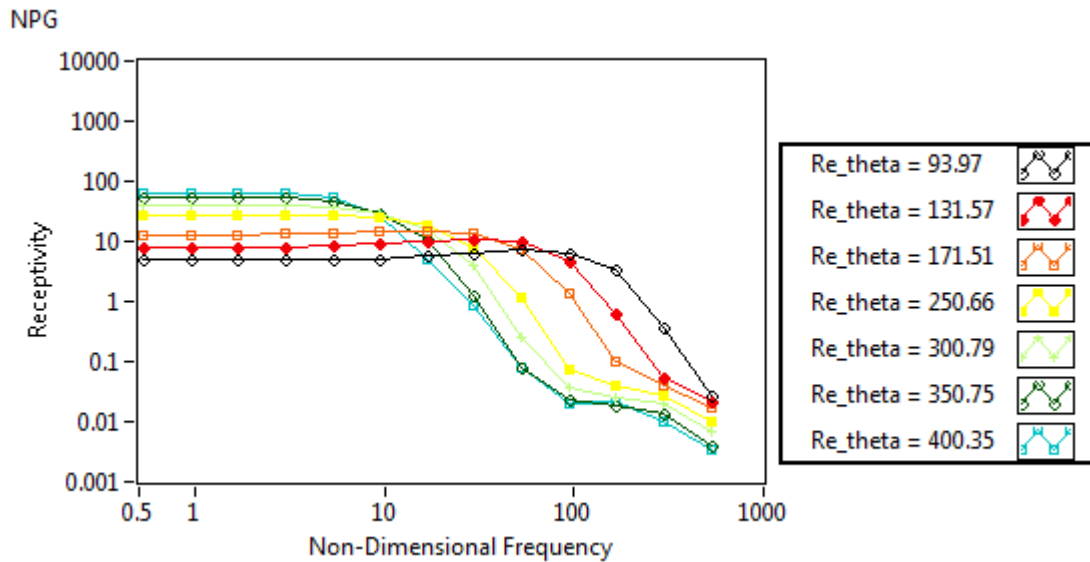


Figure 5-26 - Numerical combined receptivity versus non-dimensional frequency at various momentum thickness Reynolds numbers below the plate (NPG)

Before even comparing these results to the equivalent experimental cases one can first observe that the receptivities (in their combined form) are largest for the PPG and, in contrast, smallest for the NPG case, with the ZPG results somewhere in between. The first few profiles in each case are very similar and this can be accounted for by the fact that these occur in a nominally zero pressure gradient region for all cases. Outwith this region the receptivity, particularly at low frequencies,

grow at different rates, with respect to Re_θ , with the PPG case seeing the largest acceleration in the non-zero pressure gradient region.

It's also clear that the $v'w'$ wave orientations dominate the receptivity, relative to their $u'v'$ counterparts, and the $v'w'$ fluctuations can be thought of as analogous to the streamwise oriented streaks which are often observed in transition, including in swept transition, as previously discussed in section 2.5. The $u'v'$ oscillations, on the other hand, don't offer similar magnitudes of receptivity, which is attributed to the span over which they can exert their influence relative to the $v'w'$ waves. The $u'v'$ waves are stacked in the normal direction to the plate and can only exert their influence over the order of the boundary layer thickness, whereas the $v'w'$ waves can exert their influence in the streamwise direction and typically in a boundary layer flow $L \gg \delta$.

5.3.2 Non-Dimensional Experimental Receptivities

Similar to the numerical work the existing receptivity plots for the experimental results (in the bypass regime) have been modified for presentation in the form of non-dimensional frequencies. The frequencies were non-dimensionalised using Equation 5-19 where the characteristic length was chosen as being 525 mm, i.e. equivalent to that of the numerical receptivity calculations, and U_0 as the freestream velocity resolved at $X = 100$ mm, i.e. the calibration station used across all cases.

The presentation of the results are made first with respect to the pressure gradient and for each turbulence grid thereof in the bypass regime, i.e. only for G1 and G3. The results are presented first for ZPG in Figure 5-27 and Figure 5-28, for the PPG cases in Figure 5-29 and Figure 5-30 and for NPG in Figure 5-31 and Figure 5-32.

Firstly it should be noted that, unlike the numerical calculations, there exists only a small number of stations available for processing which range from $90 < Re_\theta < 400$ and each of these reside in the straight section settling chamber prior to the advent of the intended non-zero pressure gradients.

In every case the highest receptivities occur for the lowest non-dimensional frequencies but both the manner in which the receptivities then drop off and how they scale with Re_θ varies significantly between cases.

Starting with the ZPG cases it is observed for the lowest Re_θ values on offer that a qualitatively different trend exists in the receptivity. Towards the leading edge the boundary layer would appear not to be receptive in the 10 - 100 non-dimensional frequency range but further downstream (at higher Re_θ values) the receptivities exhibit a less pronounced drop off where all frequencies are seen to be receptive until approximately $\Omega = 100$. Similar observations were made for every case, less that of G3N (Figure 5-32) where the dip remains across all Re_θ values indicated.

A physical interpretation of these observations could perhaps be attributed to the advent of non-zero (albeit small) intermittency and the associated high frequency content that emerges in the boundary layer during this phase, hence driving up the receptivities at higher frequencies. The opposite trend, however, is observed when making comparisons with the ZPG numerical results in Figure 5-24 where the drop off in receptivity, with respect to Ω , is seen to be sustained less for increasing Re_θ .

Theoretically, the receptivity of the pre-transitional boundary layers should be open transitioning through the bypass mode should scale linearly with the freestream turbulence intensity, and as such the receptivity should only be a function of Re_θ – or indeed any other suitable scaling parameter, Re_{δ^*} for example. As such, given that the Re_θ values of G3Z in Figure 5-28 are all less than those of G1Z in Figure 5-27, one would expect the G3Z receptivities to reside within the lowest Re_θ value of G1Z. This is observed to be approximately the case for all but the final Re_θ value (117.52) in G3Z where, as previously discussed, there is a significant contribution of non-zero intermittency, which compromises the comparison slightly.

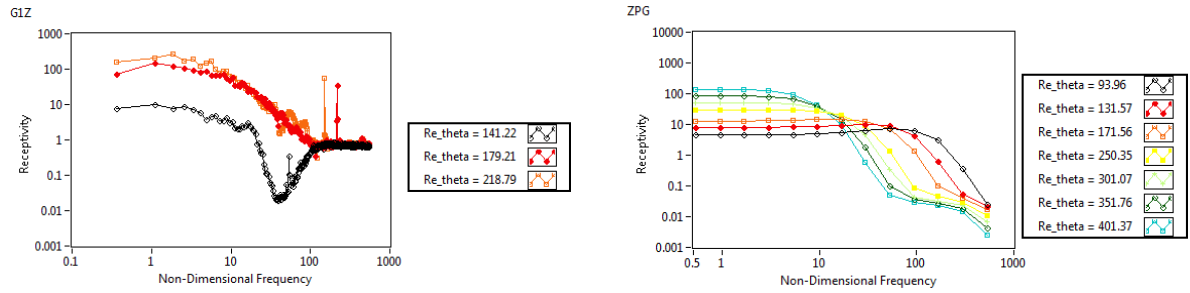


Figure 5-27 - Experimental receptivity (left) versus non-dimensional frequency at various pre-transitional momentum thickness Reynolds numbers (G1Z) – ZPG numerical results provided for comparison (right)

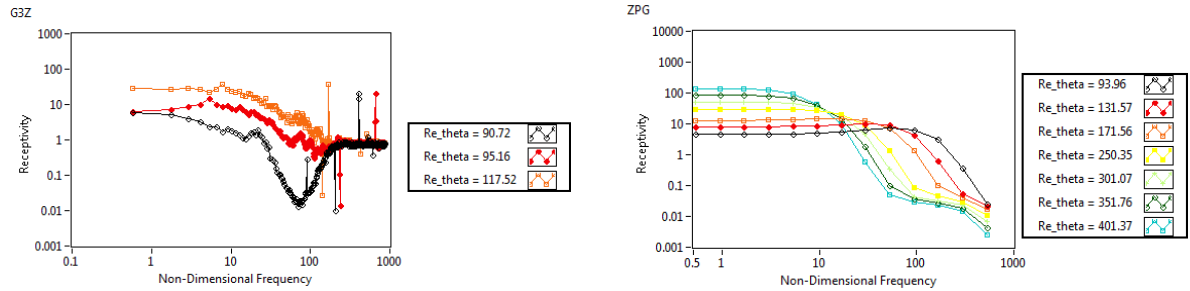


Figure 5-28 - Experimental receptivity (left) versus non-dimensional frequency at various pre-transitional momentum thickness Reynolds numbers (G3Z) - ZPG numerical results provided for comparison (right)

Here the PPG results are analysed and compared with their numerical counterpart of Figure 5-25.

Once more, as was observed previously, significant drop off in receptivity appears to occur in the 10 – 100 region until the boundary layer profiles become significantly transitional. It's interesting to note that in Figure 5-25, as with all of the numerical receptivity plots, there is no 'recovery' in the receptivity back to unity above $\Omega = 100$ but this is to be expected because, unlike in the numerical code where these high frequencies are artificially generated in the freestream, they barely register any physical presence in the real flow, partly owing to the manner in which they rapidly decay. In either case, for frequency content to be considered as being receptive, the receptivity should be considerably greater than 1, which is rarely the case in these regions.

Once more there is some overlap in the receptivity profiles, in that they don't exactly scale linearly across all Re_{θ} values for both the G1P and G3P cases. For example the low frequency receptivity in G3P at $Re_{\theta} = 135.08$ is approximately 20, whereas for $Re_{\theta} = 163.96$ in G1P it is approximately 10.

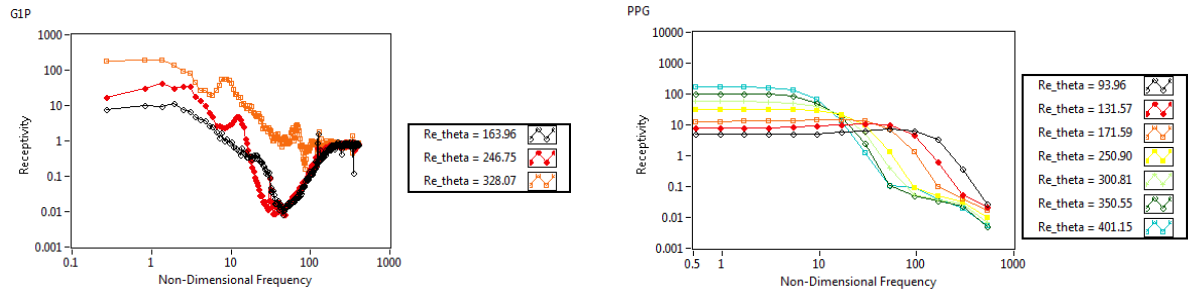


Figure 5-29 - Experimental receptivity (left) versus non-dimensional frequency at various pre-transitional momentum thickness Reynolds numbers (G1P) - PPG numerical results provided for comparison (right)

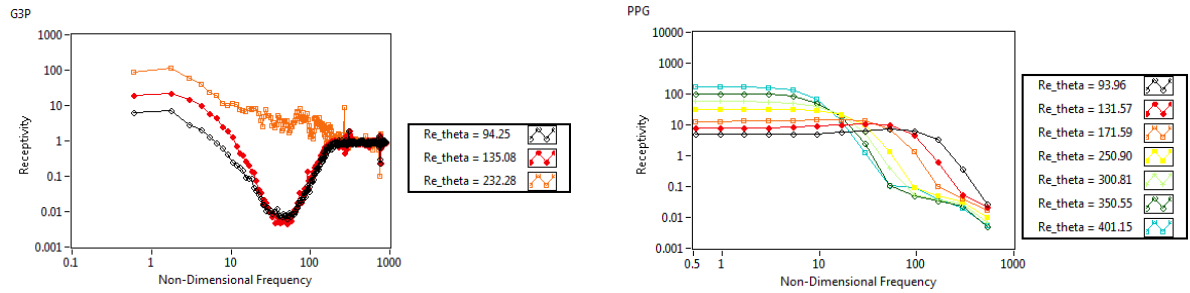


Figure 5-30 - Experimental receptivity (left) versus non-dimensional frequency at various pre-transitional momentum thickness Reynolds numbers (G3P) - PPG numerical results provided for comparison (right)

Finally the NPG cases of Figure 5-31 and Figure 5-32 are compared with reference to the numerical NPG case of Figure 5-26. Once more similar trends for receptivity versus Ω are observed. The final profile for the G3N case ($Re_{\theta} = 159.65$) exhibits higher receptivities than the lowest Re_{θ} value for G1n (231.34) but not thereafter.

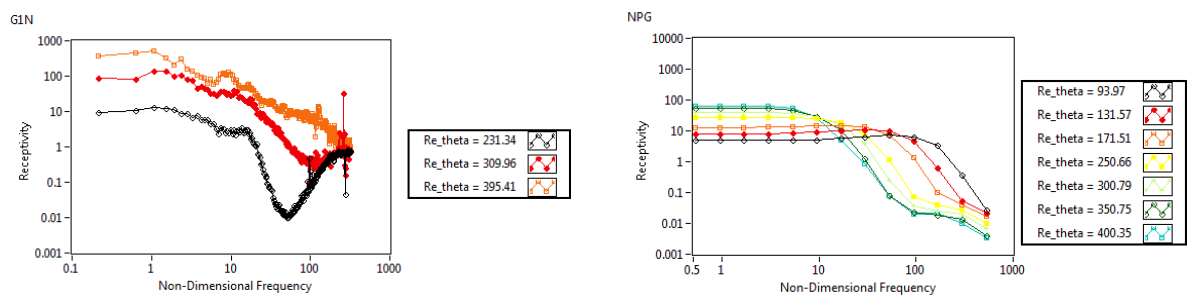


Figure 5-31 - Experimental receptivity versus non-dimensional frequency at various pre-transitional momentum thickness Reynolds numbers (G1N)

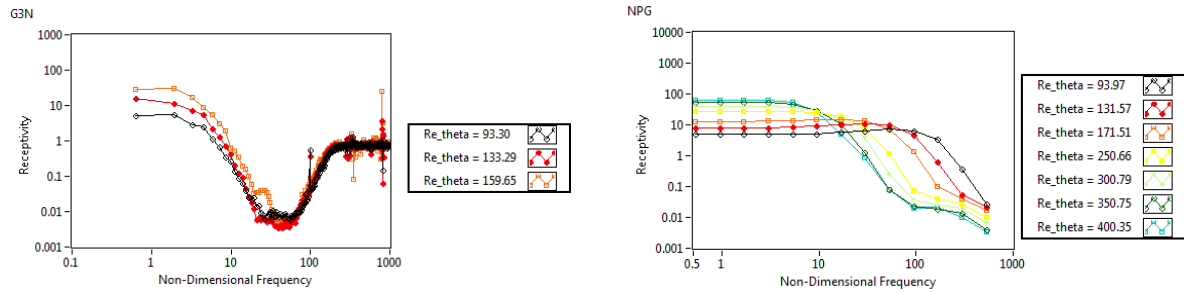


Figure 5-32 - Experimental receptivity versus non-dimensional frequency at various pre-transitional momentum thickness Reynolds numbers (G3N)

Although comparisons have been made between the numerical and experimental results, with respect to the pressure gradient section fitted to the tunnel at the time of the test, it is worth remembering that some of the plots from the numerical calculations and all of the experimental results relate to the nominally zero pressure gradients regions within the vicinity of the leading edge. They are therefore not concurrently pre-transitional signals and exposed to the intended non-zero pressure gradients. In order to achieve this the tunnel would have to be run at significantly lower velocities whereupon the entire transition map would not be available with the equipment available as the boundary layers would be too thick to measure with the traverse limited to a maximum of 50 mm displacement.

Given that the results plotted in this sub-section relate to the same area of the test facility (straight section settling chamber) the receptivities between tests (in theory) should match for equivalent Re_θ values. This proves to be less often the case than not. What is interesting, however, is that the receptivity for calibration station ($X = 100$ mm) used across all tests is approximately 10 at low frequency for all pressure gradients and freestream turbulence intensities. This would suggest that there is significant influence on the receptivity from the leading edge which is not something which was desired and, in contrast, was considered to be negligible with respect to the numerical calculations.

5.4 Comparisons with 2-D Results

In this section some comparisons are made between the 3-D receptivity results and those of similar 2-D analyses, as conducted in Johnson and Ercan (1999) and Johnson (2011a). Figure 5-33 has been compiled for direct (equivalently scaled) comparisons with Figure 5-34 (present 3-D work) which represents the $v'w'$ receptivity for 2-D numerical calculations under zero pressure gradient performed through a similar approach by Johnson (2011a).

Comparisons between the two figures appears to demonstrate that the low frequency receptivities between 2-D and 3-D transition are of similar magnitude for low Re_θ but thereafter the two deviate significantly as Re_θ increases beyond 300 where the low frequency 3-D receptivity accelerates rapidly. This observation is backed up with reference to Figure 4-63 and the experimental results where the start of transition momentum thickness Reynolds numbers are seen to deviate more significantly from the 2-D correlations of Abu-Ghannam and Shaw (1980) at lower freestream turbulence intensity values where Re_θ is required to be larger to incite transition.

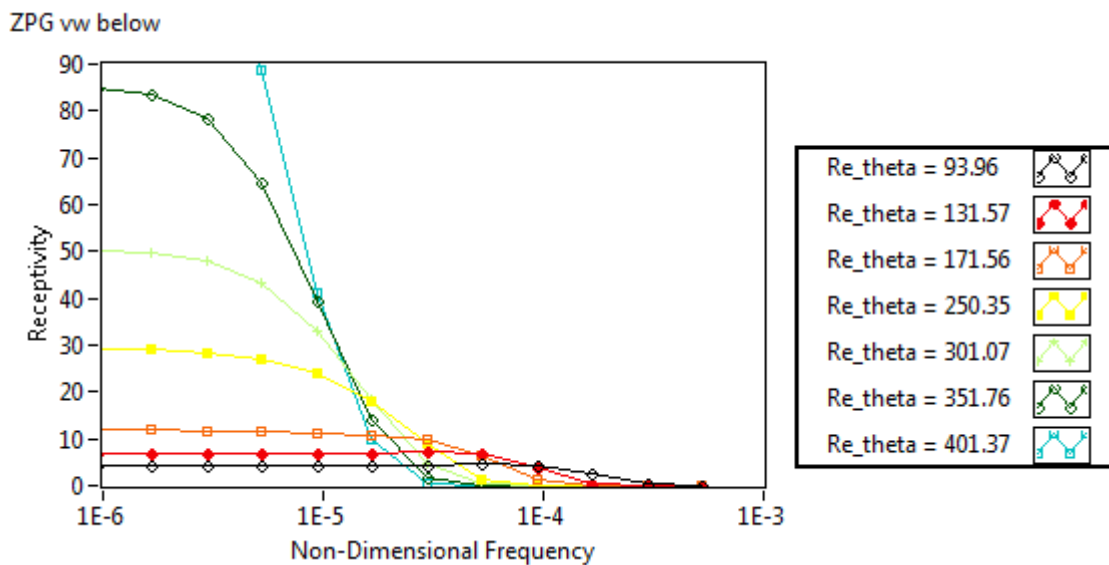


Figure 5-33 - 3-D $v'w'$ receptivity scaled for direct comparisons with 2-D results

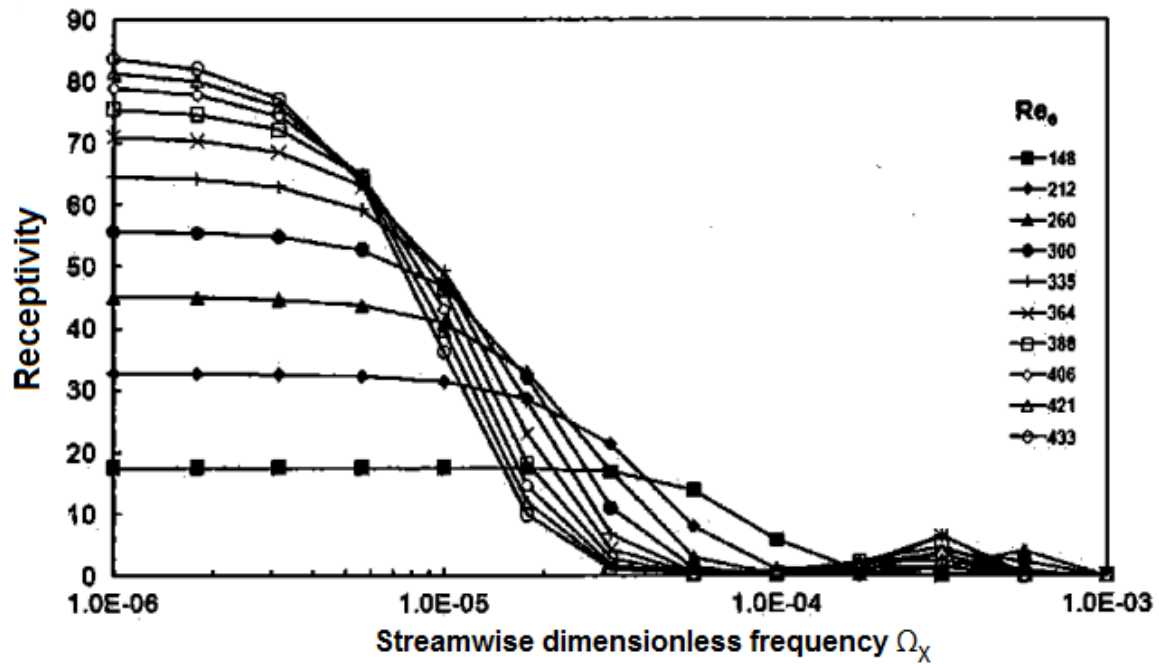


Figure 5-34 - 2-D receptivity of $v'w'$ disturbances versus streamwise dimensionless frequency, Johnson (2011a)

Physically the observed differences in receptivity must be caused by the 3-D mean flow and therefore the sweep which is responsible for the non-zero mean spanwise velocity profiles which then act to aid in the transport of the fluctuating velocities as per the continuity and momentum equations specified in section 5.2 from Equation 5-6 through to Equation 5-13. Once the sweep angle returns towards 0 degrees the receptivity will collapse back to the 2-D results where one would assume that the increased receptivity behaviour observed at higher Re_θ values would gradually fall back to the 2-D observations. Now that this procedure has been established and extended to 3-D it would certainly be interesting to perform a multitude of tests across various sweep angles and pressure gradients in order to determine, for example, the angle of sweep which offers peak receptivity for a given topology.

6 Chapter 6 – Conclusions and Suggestions for Future Work

6.1 Conclusions

The approach adopted for this study on swept boundary layer transition has yielded interesting results which contribute towards an improved understanding of the transition process for swept flows. This has been made possible thanks to the development of suitable experimental techniques to obtain detailed boundary layer profile data.

Firstly it has been demonstrated that transition begins and ends at lower momentum thickness Reynolds numbers, relative to unswept transition, consistent with the observations of Gray (1952) on swept wings. Direct comparisons have been made with the empirical transition correlations of Abu-Ghannam and Shaw (1980) in Chapter 4, which represents something of an industry standard for 2-D transitional flows.

For the three turbulence levels examined the level of freestream turbulence intensity with no grid (G0) exhibited transition characteristics consistent with those of natural transition where a combination of primary instability crossflow modes and Tollmien Schlichting instabilities were responsible for driving transition. In contrast transition for the other two cases with grids (G1 and G3) progressed through a bypass mode.

These experimental cases of bypass transition compare favourably with numerical CFD work which was conducted in parallel, particularly in terms of their qualitative behaviour. The numerical work indicated that transition, through a bypass mode, would largely be driven by low frequency content in the freestream and this concurred with the receptivities ascertained from the experiments.

Furthermore it was deduced that the boundary layers would become more receptive with increasing momentum thickness Reynolds number, relative to their unswept counterparts, a trend qualitatively matched between experiment and simulation.

Reasonably significant quantitative differences (albeit less than an order of magnitude) between experiment and simulation were present in the results, which can most likely be attributed to the influence of leading edge receptivity in the pre-transitional boundary layers in the experiments, as well as possible contamination of the flow from the sidewalls across the span of the flat plate.

Furthermore it was concluded from the numerical calculations that the receptivities to freestream turbulence were highest for the positive pressure gradient and, in contrast, lowest for the negative pressure gradient – a similar finding to those reported in unswept boundary layers, as in Johnson (2013). Unfortunately transition was seen to start prior to the non-zero pressure gradients in the experiments and thus direct comparisons with the simulations were not available. This fact can be attributed to committing to resolving the full transition map with the available traverse which was limited to approximately 45 mm of range and, hence, the tunnel was typically operated at higher Reynolds numbers than desired such that the thick turbulent boundary layers at the end of transition could be fully resolved.

6.2 Recommendations and Suggestions for Future Work

Whilst, on the whole, the systematic experimental procedure proved to be sufficient, and optimised with respect to the available equipment, there are of course several avenues available for pursuing improvements. The main source of unwanted compromise, from the perspective of time required and errors incited, was the single wire approach in combination with skewing the probe. As has been previously discussed, skewing the traverse (in certain cases) inflicts significant physical changes in the observed signals for the same wire measuring volume. As such it would be better practice to use two probes (with two CTA modules) in a v-arrangement in order to resolve the leading edge perpendicular and tangential components directly, as per the likes of Zurigat and Malik (1995), where the influence of the traverse for such an arrangement would effectively be the same at each location.

Furthermore, a modified flap with the primary intention of enhancing the potential diffusion underneath the plate was actually designed but never built, owing to time constraints. This design merely consisted of a flat plate, approximately 275 mm in width, running across the span of the working section underneath the plate (again parallel to the leading edge) supported by the surrounding structure itself. The justification for requesting this re-design was based on the fact that the existing flap does not mate continuously with the trailing edge of the bottom surface of the working section and there is, in effect, a small backward facing step prior to the flow re-attaching with the existing flap. A new flap, or perhaps even a more comprehensive re-design, would improve the diffusion capabilities beneath the plate, thus offering improved flow quality control so as to, in effect, replicate a symmetry boundary condition in the mean flow. Additionally, with improvements in the flow quality that is bled underneath the plate, one would hope that the spanwise flow quality issues, i.e. the contaminated flow, would be corrected on the measured side of the plate, such that a closer representation of idealised Falkner-Skan-Cooke profiles is achievable.

The traverse utilised was designed for a different tunnel which operates at higher speeds (when analysing transition) on a shorter plate and therefore has thinner boundary layers. 50 mm worth of traverse displacement by design (in practice ~ 45 mm) proved to be borderline for the current work with its much larger plate. In effect, this made it difficult to perform a Reynolds collapse for the entire transition map at significantly different Reynolds numbers.

It would also be possible, particularly with respect to the comparisons made to the numerical work, just to bypass producing an entire transition map and run the tunnel at significantly lower speeds with a focus solely on the pre-transitional boundary layers and their receptivity to turbulence in the freestream. Such an approach would also shift the start of transition further away from the leading edge and, as such, the influence of leading edge receptivity should be more significantly suppressed and, furthermore, transition inception could be staged in non-zero pressure gradient regions. It

would certainly be interesting to see if such a move would improve the quantitative matching between the numerical and experimental receptivities.

One of the stated future ambitions has always been to advance the numerical receptivity calculations to more complex topologies. In terms of progressing to the next stage, the results presented in Appendix A provide further insight into the potential problems which would have to be overcome. The main issue which has been highlighted is the apparent tendency for the wider stagnation region, proximal to the leading edge, associated with shapes of finite thickness and curvature to suppress the incoming fluctuations.

7 List of Tables

Table 3-1 - Codes for test section combinations detailing experimental parameters	67
Table 3-2 - Number of pulses per increment	73
Table 3-3 - National Instruments USB data acquisition devices	81
Table 3-4 - Streamwise static pressure tapings	84
Table 4-1 - Narasimha table for start and end of transition for all cases (streamwise leading edge displacement)	158
Table 4-2 - Narasimha table for start and end of transition for all cases (momentum thickness).....	158
Table 5-1 - Boundary conditions for steady base flows	173
Table 5-2 - Frequency magnitude with corresponding extended hexadecimal code (x frequencies) 186	
Table 5-3 - Frequency magnitude with corresponding extended hexadecimal code (y and z frequencies).....	187
Table 10-1 - SI base units	240

8 List of Figures

Figure 2-1 - Two dimensional flat plate boundary layer flow depicting freestream velocity, local velocity components, boundary layer thickness, freestream approach flow and typical coordinate system, from Andersson (1999).....	6
Figure 2-2 - Transition paths following receptivity (Saric et al. (2002))	10
Figure 2-3 - Natural transition process in a flat plate boundary layer Schlichting (1979).....	10
Figure 2-4 - Turbulent spot generated by spark (Schubauer and Klebanoff (1955))	15
Figure 2-5 - Unfiltered hot-wire velocity signals demonstrating intermittency effect (offset for clarity)	16
Figure 2-6 - Unfiltered hot-wire signal traces Fasihfar and Johnson (1992)	17
Figure 2-7 - Filtered hot-wire velocity signals demonstrating intermittency effect (positive pressure gradient, square grid)	17
Figure 2-8 - Filtered velocity for intermittent signal (Fasihfar and Johnson (1992)).....	18
Figure 2-9 - Falkner-Skan-Cooke velocity profiles for two β_H values - Stemmer (2010)	36
Figure 2-10 - Possible instability mechanisms acting on a swept wing and their prevalent locations (Bippes (1999))	37
Figure 2-11 - Crossflow and Tollmien Schlichting instability waves on a swept wing - Oertel (2010) .	40
Figure 3-1 - Isometric CAD drawing of tunnel and plate with no section fitted above plate.....	45
Figure 3-2 - Panoramic view of the tunnel, measuring and ancillary equipment with the positive pressure gradient section fitted	45
Figure 3-3 - Third angle projection of University of Liverpool large blower tunnel with significant dimensions only (no test section fitted at outlet) [mm]	46
Figure 3-4 - Dimensioned CAD drawing of flat plate section in third angle projection [mm]	48
Figure 3-5 - Schematic of wind tunnel flat plate and control flap for bleeding air under the leading edge	48
Figure 3-6 - 55P15 miniature boundary layer hot-wire probe	49
Figure 3-7 - Velocity contours for stagnation migration example [m/s]	52
Figure 3-8 - Pressure contours for stagnation migration example [Pa - gauge]	53
Figure 3-9 - Schematic highlighting the main features, reference and measurement locations for the swept flat plate.....	54
Figure 3-10 - Grid assembly for housing meshes [mm]	55
Figure 3-11 - Square mesh dimensions inside grid framework [mm]	56
Figure 3-12 - Vertical mesh dimensions inside grid framework [mm]	57
Figure 3-13 - Straight section framework with roof and sidewalls	59
Figure 3-14 - Curved sidewall framework for diverging (positive) section with roof sub-sections	60
Figure 3-15 - Tunnel roof profile (left) with freestream and tunnel Cartesian coordinate systems (right).....	61
Figure 3-16 - Free cross section height profile.....	64
Figure 3-17 - Spanwise profile for meanline of sections.....	64
Figure 3-18 - Assembled CAD model of diverging section fitted to tunnel.....	65
Figure 3-19 - View of leading edge through Perspex side window	66
Figure 3-20 - Cathetometer (travelling microscope) used to measure hot-wire wall-normal proximity	70

Figure 3-21 - Pro/ENGINEER model of traverse and positioning template (left) and bearing angle convention highlighted with respect to the approach flow direction (right).....	71
Figure 3-22 - AC coupling; battery (left) vs. mains (right)	78
Figure 3-23 - Flow chart representing the main loop of the data acquisition and traversing process	82
Figure 3-24 - Power spectrum of frequency content in turbulent boundary layer.....	83
Figure 3-25 - Zero flow wall proximity effect with polynomial calibration in near wall region	92
Figure 3-26 - LabVIEW intermittency algorithm	97
Figure 3-27 - Front panel of LabVIEW intermittency algorithm.....	98
Figure 3-28 - Largest vortices accommodated by a boundary layer	99
Figure 3-29 - Minimum turbulent frequency (dashed line) shown with neutral stability curve in zero pressure gradient laminar boundary layer (Ercan (1997)).....	100
Figure 3-30 - LabVIEW front panel interface for main experimental program	103
Figure 4-1 - Gauge pressure of pressure tapings versus streamwise displacement from leading edge	108
Figure 4-2 - Static pressure distributions normalised as pressure coefficient values against leading edge displacement	108
Figure 4-3 - Streamwise static pressure distribution with traverse skewed at different angles.....	110
Figure 4-4 - Streamwise pressure coefficients with traverse skewed at different angles	110
Figure 4-5 - Hot-wire U/U ₀ profiles with respect to leading edge displacement for all grids and sections.....	111
Figure 4-6 - G0Z wall normal velocities at various streamwise Reynolds numbers	112
Figure 4-7 - G0Z normalised velocity profiles at various streamwise Reynolds numbers.....	113
Figure 4-8 - First two profiles plotted against Blasius solution (G0Z)	113
Figure 4-9 - G0Z Wall normal intermittency profiles at various streamwise Reynolds numbers.....	114
Figure 4-10 - 3-D plot of intermittency with respect to streamwise Reynolds number and wall normal displacement (G0Z).....	115
Figure 4-11 - Turbulence intensity distribution throughout different streamwise boundary layer profiles (G0Z)	116
Figure 4-12 - Original $u^+ y^+$ plot for turbulent boundary layer profiles (G0Z)	117
Figure 4-13 - Adjusted $u^+ y^+$ plot for turbulent boundary layer profiles (G0Z).....	117
Figure 4-14 - Near wall intermittency versus streamwise displacement from leading edge with Narasimha (1957) fit (G0Z)	118
Figure 4-15 - Boundary layer thickness with streamwise Reynolds number (G0Z).....	120
Figure 4-16 - Freestream velocity versus streamwise Reynolds number (G0Z)	120
Figure 4-17 - Displacement thickness with streamwise Reynolds number (G0Z)	121
Figure 4-18 - Momentum thickness with streamwise Reynolds number (G0Z).....	122
Figure 4-19 - Shape factor at various streamwise Reynolds numbers (G0Z)	122
Figure 4-20 - Near wall shear stress versus streamwise Reynolds number (G0Z)	123
Figure 4-21 - Skin friction coefficient with streamwise Reynolds number (G0Z).....	123
Figure 4-22 - Mean flow angles versus wall normal displacement (G0Z)	126
Figure 4-23 - Measured mean flow angles versus wall normal displacement non-log plot (G0Z)	126
Figure 4-24 - Near wall velocity distribution across various skew angles (arbitrary test case).....	128
Figure 4-25 - Freestream velocity distribution across various skew angles (arbitrary test case).....	128
Figure 4-26 - Plot of similarity variables f' and g versus η ($m = -0.08$)	129
Figure 4-27 - Streamwise and spanwise velocities versus η ($m = -0.08$).....	130

Figure 4-28 - Streamwise and spanwise velocities versus η ($m = 1$)	130
Figure 4-29 - Velocity magnitudes for the special case of Blasius flow ($m = 0$)	131
Figure 4-30 - Match with Stemmer (2010) for Falkner-Skan-Cooke profiles at β_H equals -0.1 and 1.0 and $\theta = 60^\circ$	131
Figure 4-31 - Comparison between experimentally measured mean flow angles (G0Z) and Falkner- Skan-Cooke Cooke (1950) boundary layer profiles.....	133
Figure 4-32 - Corrected Falkner-Skan-Cooke profiles with angle offset (G0Z).....	134
Figure 4-33 - Normalised velocity profiles (G1Z)	135
Figure 4-34 - Skin friction coefficient versus streamwise Reynolds number (G1Z).....	135
Figure 4-35 - Normalised velocity profiles (G3Z)	136
Figure 4-36 - Near wall intermittency versus leading edge streamwise displacement (G3Z)	137
Figure 4-37 - Skin friction coefficient versus streamwise Reynolds number (G3Z).....	138
Figure 4-38 - Normalised velocity profiles – log plot (G0P)	139
Figure 4-39 - Normalised velocity profiles (G0P)	139
Figure 4-40 - Shape factor versus streamwise Reynolds number (G0P)	140
Figure 4-41 - Near wall intermittency versus leading edge streamwise displacement (G0P).....	141
Figure 4-42 - Displacement thickness against streamwise Reynolds number (G0P)	142
Figure 4-43 - Boundary layer thickness versus streamwise Reynolds number (G0P)	142
Figure 4-44 - Normalised velocity profiles (G1P)	143
Figure 4-45 - Turbulence intensity versus y/δ (G1P).....	144
Figure 4-46 - Intermittency versus y/δ at various streamwise Reynolds numbers (G1P)	145
Figure 4-47 - Displacement thickness against streamwise Reynolds number (G1P)	145
Figure 4-48 - Normalised velocity profiles (G3P)	146
Figure 4-49 - 3-D transition map (G3P).....	147
Figure 4-50 - Intermittency versus y/δ (G3P).....	148
Figure 4-51 - Near wall intermittency versus leading edge streamwise displacement (G0N)	149
Figure 4-52 - Normalised velocity profiles (G0N).....	149
Figure 4-53 - Shape factor versus streamwise Reynolds number (G0N).....	150
Figure 4-54 - Displacement thickness versus streamwise Reynolds number (G0N)	150
Figure 4-55 - Normalised velocity profiles (G1N).....	151
Figure 4-56 - Displacement thickness versus streamwise Reynolds number (G1N)	152
Figure 4-57 - Normalised velocity profiles (G3N).....	153
Figure 4-58 - Skin friction coefficient against streamwise Reynolds number (G3N).....	154
Figure 4-59 - Intermittency versus y/δ (G3N)	154
Figure 4-60 - u^+ versus y^+ plot for turbulent profiles (G3N)	155
Figure 4-61 - Streamwise start of transition Reynolds number versus turbulence intensity for all pressure gradients	156
Figure 4-62 Streamwise end of transition Reynolds number versus turbulence intensity for all pressure gradients	156
Figure 4-63 - Momentum thickness Reynolds number at the start of transition for all pressure gradients versus turbulence intensity with Abu-Ghannam and Shaw (1980) comparison.....	157
Figure 4-64 - Momentum thickness Reynolds number at the end of transition for all pressure gradients versus turbulence intensity with Abu-Ghannam and Shaw (1980) comparison.....	157
Figure 4-65 - Normalised velocity profiles at different spanwise positions – no grid, ZPG.....	160
Figure 4-66 - Normalised velocity profiles at different spanwise positions (G1N).....	161

Figure 4-67 - Spanwise intermittency distribution at $X = 381$ mm (G1N)	162
Figure 4-68 - Near wall intermittency across leading edge span at $X = 381$ mm (G1N).....	162
Figure 4-69 - Spanwise variation in turbulence intensity at $X = 381$ mm (G1N)	163
Figure 4-70 - Pre-transitional boundary layer receptivity (G0Z)	167
Figure 4-71 - Pre-transitional boundary layer receptivity (G1Z)	168
Figure 4-72 - Pre-transitional boundary layer receptivity (G3Z)	168
Figure 4-73 - Pre-transitional boundary layer receptivity (G1P).....	169
Figure 4-74 - Pre-transitional boundary layer receptivity (G3P).....	170
Figure 4-75 - Pre-transitional boundary layer receptivity (G1N)	171
Figure 4-76 - Pre-transitional boundary layer receptivity (G3N)	171
Figure 5-1 - Grid dimensions (in mm) for numerical receptivity calculations - Johnson (2011a).....	174
Figure 5-2 - Contour plot of velocity magnitude for steady ZPG flow [m/s]	175
Figure 5-3 - Contour plot of velocity magnitude for steady ZPG flow (stretched in normal direction) [m/s]	175
Figure 5-4 - u velocities for PPG with respect to normal coordinate at various streamwise displacements.....	176
Figure 5-5 - w velocities for PPG with respect to normal coordinate at various streamwise displacements.....	176
Figure 5-6 - Static pressure normal distributions at various streamwise locations for PPG	177
Figure 5-7 - Velocity contour plot upstream of leading edge highlighting numerical artefacts.....	178
Figure 5-8 - Paraview screenshot of typical non-receptive turbulence intensity contours with additional line plot normal to the plate.....	184
Figure 5-9 - Paraview screenshot of receptive turbulence intensity contours with additional line plot normal to the plate.....	185
Figure 5-10 - Receptivity versus Re_θ for 200060 $u'v'$ case (ZPG).....	188
Figure 5-11 - Receptivity versus Re_θ for 20A0C0 $u'v'$ case (ZPG)	188
Figure 5-12 - Receptivity versus Re_θ for 00A060 $v'w'$ case (ZPG)	189
Figure 5-13 - Receptivity versus Re_θ for 60C060 $v'w'$ case (ZPG)	189
Figure 5-14 - Receptivity versus spatial streamwise frequency magnitude for uv waves under nominally zero pressure gradient at various momentum thickness Reynolds numbers (above plate)	191
Figure 5-15 - Receptivity versus spatial streamwise frequency magnitude for uv waves under nominally zero pressure gradient at various momentum thickness Reynolds numbers (below plate)	191
Figure 5-16 - Receptivity versus spatial streamwise frequency magnitude for $v'w'$ waves under nominally zero pressure gradient at various momentum thickness Reynolds numbers (above plate)	192
Figure 5-17 - Receptivity versus spatial streamwise frequency magnitude for $v'w'$ waves under nominally zero pressure gradient at various momentum thickness Reynolds numbers (below plate)	192
Figure 5-18 - Numerical $u'v'$ receptivity versus non-dimensional frequency at various momentum thickness Reynolds numbers below the plate (ZPG).....	194
Figure 5-19 - Numerical $v'w'$ receptivity versus non-dimensional frequency at various momentum thickness Reynolds numbers below the plate (ZPG).....	195

Figure 5-20 - Numerical $u'v'$ receptivity versus non-dimensional frequency at various momentum thickness Reynolds numbers below the plate (PPG)	195
Figure 5-21 - Numerical $v'w'$ receptivity versus non-dimensional frequency at various momentum thickness Reynolds numbers below the plate (PPG)	196
Figure 5-22 - Numerical $u'v'$ receptivity versus non-dimensional frequency at various momentum thickness Reynolds numbers below the plate (NPG).....	196
Figure 5-23 - Numerical $v'w'$ receptivity versus non-dimensional frequency at various momentum thickness Reynolds numbers below the plate (NPG).....	197
Figure 5-24 - Numerical combined receptivity versus non-dimensional frequency at various momentum thickness Reynolds numbers below the plate (ZPG).....	197
Figure 5-25 - Numerical combined receptivity versus non-dimensional frequency at various momentum thickness Reynolds numbers below the plate (PPG).....	198
Figure 5-26 - Numerical combined receptivity versus non-dimensional frequency at various momentum thickness Reynolds numbers below the plate (NPG)	198
Figure 5-27 - Experimental receptivity (left) versus non-dimensional frequency at various pre-transitional momentum thickness Reynolds numbers (G1Z) – ZPG numerical results provided for comparison (right)	201
Figure 5-28 - Experimental receptivity (left) versus non-dimensional frequency at various pre-transitional momentum thickness Reynolds numbers (G3Z) - ZPG numerical results provided for comparison (right)	201
Figure 5-29 - Experimental receptivity (left) versus non-dimensional frequency at various pre-transitional momentum thickness Reynolds numbers (G1P) - PPG numerical results provided for comparison (right)	202
Figure 5-30 - Experimental receptivity (left) versus non-dimensional frequency at various pre-transitional momentum thickness Reynolds numbers (G3P) - PPG numerical results provided for comparison (right)	202
Figure 5-31 - Experimental receptivity versus non-dimensional frequency at various pre-transitional momentum thickness Reynolds numbers (G1N)	202
Figure 5-32 - Experimental receptivity versus non-dimensional frequency at various pre-transitional momentum thickness Reynolds numbers (G3N)	203
Figure 5-33 - 3-D $v'w'$ receptivity scaled for direct comparisons with 2-D results.....	204
Figure 5-34 - 2-D receptivity of $v'w'$ disturbances versus streamwise dimensionless frequency, Johnson (2011a)	205
Figure 10-1 - OpenFOAM multi-block structured grid with colour co-ordinated boundary conditions	230
Figure 10-2 - OpenFOAM $u'v'$ receptivity example of instantaneous velocity magnitude contour plot after 980 ms of solution time	248
Figure 10-3 - Turbulence intensity contours time-averaged over one wave period for OpenFOAM $u'v'$ receptivity example	249
Figure 10-4 - Schematic of NACA 0002 2-D mesh.....	251
Figure 10-5 - NACA 0002 2-D Gambit mesh.....	252
Figure 10-6 - NACA 0002 mesh detail at leading edge.....	252
Figure 10-7 - Cropped average velocity magnitude contours (NACA 0002)	253
Figure 10-8 - Cropped average velocity magnitude contours for infinitesimally thin flat plate	253
Figure 10-9 - NACA 0002 turbulence intensity contours	254

Figure 10-10 - Turbulence intensity line plot from inlet to leading edge (NACA 0002)	255
Figure 11-1 - LabVIEW graphical sub-vi code for recording wire velocities with King's law coefficients and relevant wire temperatures written to comment string	257
Figure 11-2 - LabVIEW graphical code for Kings law (with Jørgensen (2001) temperature correction) sub-vi	258
Figure 11-3 - LabVIEW sub-vi graphical code for seeking freestream velocity and boundary layer thickness from y and u arrays	259
Figure 11-4 - LabVIEW graphical code for gamma1 sub-vi - intermittency processing.....	260
Figure 11-5 - LabVIEW graphical code for gamma2 sub-vi - intermittency processing plus Wills correction Wills (1962)	260
Figure 11-6 - LabVIEW integral parameters graphical code for sub-vi.....	261
Figure 11-7 - LabVIEW graphical code sub-vi for summary output file.....	262
Figure 11-8 - LabVIEW zero flow correlation graphical code (ZF_Correlation.vi)	263
Figure 11-9 - LabVIEW home seek graphical code (Home.vi)	265
Figure 11-10 - LabVIEW graphical code for main experimental program (Full.vi)	266

9 References

- ABU-GHANNAM, B. J. & SHAW, R. 1980. Natural transition of boundary layers—the effects of turbulence, pressure gradient, and flow history. *Journal of Mechanical Engineering Science*, 22, 213-228.
- ANDERSON, J. 2010. *Fundamentals of Aerodynamics*, McGraw-Hill Education.
- ANDERSSON, P. 1999. *Modelling of boundary layer stability*, Citeseer.
- ARNAL, D. Boundary layer transition: predictions based on linear theory. In AGARD, Special Course on Progress in Transition Modelling 63 p (SEE N94-33884 10-34), 1994.
- AYDIN, M. & LEUTHEUSSER, H. J. 1980. Very low velocity calibration and application of hot-wire probes. *DISA Information*, 1, 17.
- BEARMAN, P. W. 1971. Corrections for the effect of ambient temperature drift on hot-wire measurements in incompressible flows. *DISA Information No. 11*.
- BIPPES, H. 1990. Instability features appearing on swept wing configurations. *Laminar-Turbulent Transition*. Springer.
- BIPPES, H. 1999. Basic experiments on transition in three-dimensional boundary layers dominated by crossflow instability. *Progress in Aerospace Sciences*, 35, 363-412.
- BLAIR, M. F. 1992. Boundary-layer transition in accelerating flows with intense freestream turbulence. I-Disturbances upstream of transition onset. II-The zone of intermittent turbulence. *ASME Transactions Journal of Fluids Engineering*, 114, 313-332.
- BLASIUS, H. 1907. *Grenzschichten in Flüssigkeiten mit kleiner Reibung. Inaugural-Dissertation...* von H. Blasius, Druck von BG Teubner.
- BLASIUS, H. 1950. The Boundary Layers in Fluids with Little Friction.
- BOIKO, A. V. 2012. *Physics of Transitional Shear Flows: Instability and Laminar-Turbulent Transition in Incompressible Near-Wall Shear Layers*, Springer Science+ Business Media.
- BOTTARO, A. 2010. A 'receptive' boundary layer. *Journal of Fluid Mechanics*, 646, 1-4.
- BRADSHAW, P. & PANKHURST, R. C. 1964. The design of low-speed wind tunnels. *Progress in Aerospace Sciences*, 5, 1-69.
- BRANDT, L. 2001. *Study of generation, growth and breakdown of streamwise streaks in a Blasius boundary layer*. Karlstad University.
- BRANDT, L. 2003. *Numerical studies of bypass transition in the Blasius boundary layer*. KTH.
- BRUUN, H. H. 1996. Hot-wire anemometry: principles and signal analysis. *Measurement Science and Technology*, 7.

- BRUUN, H. H. & TROPEA, C. 1985. The calibration of inclined hot-wire probes. *Journal of Physics E: Scientific Instruments*, 18, 405.
- CANT, S. 2002. High-performance computing in computational fluid dynamics: progress and challenges. *Philosophical Transactions of the Royal Society of London. Series A: Mathematical, Physical and Engineering Sciences*, 360, 1211-1225.
- CANTWELL, B. J. 1981. Organized motion in turbulent flow. *Annual Review of Fluid Mechanics*, 13, 457-515.
- CHEVALIER, M., HÖPPFNER, J., AKERVIK, E. & HENNINGSON, D. S. 2007. Linear feedback control and estimation applied to instabilities in spatially developing boundary layers. *Journal of Fluid Mechanics*, 588, 163.
- CIMBALA, J. M. & PARK, W. J. 1990. A direct hot-wire calibration technique to account for ambient temperature drift in incompressible flow. *Experiments in Fluids*, 8, 299-300.
- CLAUSER, F. H. 1956. The turbulent boundary layer. *Advances in applied mechanics*, 4, 1-51.
- COOKE, J. C. The boundary layer of a class of infinite yawed cylinders. Proc. Camb. Phil. Soc, 1950. Cambridge Univ Press, 645-648.
- COURANT, R., FRIEDRICHS, K. & LEWY, H. 1967. On the partial difference equations of mathematical physics. *IBM journal of Research and Development*, 11, 215-234.
- CROUCH, J. D., GAPONENKO, V. R., IVANOV, A. V. & KACHANOV, Y. S. Theoretical and experimental comparisons of the stability and receptivity of swept-wing boundary layers. APS Division of Fluid Dynamics Meeting Abstracts, 1997.
- DAGENHART, J. R. & SARIC, W. S. 1999. *Crossflow stability and transition experiments in swept-wing flow*, Citeseer.
- DANTEC 1999. Miniature CTA 54T30 - Installation & User's Guide. 1.2 ed.
- DANTEC 2011. Dantec Dynamics: StreamWare Pro Software v5.00 Installation and User's Guide.
- DHAWAN, S. & NARASIMHA, R. 1958. Some properties of boundary layer flow during the transition from laminar to turbulent motion. *Journal of Fluid Mechanics*, 3, 418-436.
- ECKARDT, D. Flow field analysis of radial and backswept centrifugal compressor impellers. I-Flow measurements using a laser velocimeter. Performance prediction of centrifugal pumps and compressors, 1979. 77-86.
- EMMONS, H. W. 1951. The laminar-turbulent transition in a boundary layer. Part I. *J. Aero. Sci*, 18, 490-498.
- ERCAN, A. H. 1997. *Experimental Analysis and Modelling of Boundary Layer Transition*. PhD Thesis.

- ESCUDIER, M. P., RAMADAN, A. & JOHNSON, M. W. 2001. Response of a skewed turbulent boundary layer to favourable pressure gradient. *Experiments in Fluids*, 30, 657-671.
- FAA. 2012. *Radio and Interphone Communications* [Online]. Available: http://www.faa.gov/air_traffic/publications/atpubs/ATC/atc0204.html#atc0204.html.5.
- FALKNER, V. M. & SKAN, S. W. 1931. LXXXV. Solutions of the boundary-layer equations. *The London, Edinburgh, and Dublin Philosophical Magazine and Journal of Science*, 12, 865-896.
- FASIHFAR, A. & JOHNSON, M. W. 1992. An improved boundary layer transition correlation. *ASME paper*, 245.
- FRANK, M. & WOLFE, P. 1956. An algorithm for quadratic programming. *Naval research logistics quarterly*, 3, 95-110.
- FRANSSON, J. H. M., BRANDT, L., TALAMELLI, A. & COSSU, C. 2004. Experimental and theoretical investigation of the nonmodal growth of steady streaks in a flat plate boundary layer. *Physics of Fluids*, 16, 3627.
- FYODOROV, A. V. 1988. Excitation of cross-flow instability waves in boundary layer on a swept-wing. *Zhurn. Prikl. Mekhan. Tekhn. Fiz*, 5, 46-52.
- GAD-EL-HAK, M. & TSAI, H. M. 2005. *Transition and Turbulence Control. University of Singapore Institute For Mathematical Sciences Lecture Notes Series*, World Scientific.
- MASTER, M. 1967. On the flow along swept leading edges (Flow turbulence on leading edge of attachment line of swept wing studied in wind tunnel). *Aeronautical Quarterly*, 18, 165-184.
- GEORGE, W. K. 2007. Is there a universal log law for turbulent wall-bounded flows? *Philosophical Transactions of the Royal Society A: Mathematical, Physical and Engineering Sciences*, 365, 789-806.
- GIBBINGS, J. C., MADADNIA, J. & YOUSIF, A. H. 1995. The wall correction of the hot-wire anemometer. *Flow Measurement and Instrumentation*, 6, 127-136.
- GIBSON, M. M. 1960. *The Design of a Wind Tunnel for Boundary Layer Research*. PhD, University of Liverpool.
- GOLDSTEIN, M. E. 1983. The evolution of Tollmien-Schlichting waves near a leading edge. *Journal of Fluid Mechanics*, 127, 59-81.
- GOSTELOW, J., BLUNDEN, A. & WALKER, G. 1994. Effects of free-stream turbulence and adverse pressure gradients on boundary layer transition. *Journal of turbomachinery*, 116, 392-404.
- GOSTELOW, J. P. & WALKER, G. J. Similarity behavior in transitional boundary layers over a range of adverse pressure gradients and

- turbulence levels. ASME, 35th International Gas Turbine and Aeroengine Congress and Exposition, 1990.
- GOSTELOW, J. P., WALKER, G. J., SOLOMON, W. J., HONG, G. & MELWANI, N. Investigation of the calmed region behind a turbulent spot. International Gas Turbine and Aeroengine Congress & Exhibition, ASME TURBO EXPO 96, 1996. 1-9.
- GRAY, W. E. 1952. *The effect of wing sweep on laminar flow*, Royal Aircraft Establishment.
- GREGORY, N., STUART, J. T. & WALKER, W. S. 1955. On the stability of three-dimensional boundary layers with application to the flow due to a rotating disk. *Philosophical Transactions of the Royal Society of London. Series A, Mathematical and Physical Sciences*, 155-199.
- HALL, D. J. & GIBBINGS, J. C. 1972. Influence of stream turbulence and pressure gradient upon boundary layer transition. *Journal of Mechanical Engineering Science*, 14, 134-146.
- HALLBÄCK, M. 1996. *Turbulence and Transition Modelling: Lecture Notes from the ERCOFTAC/IUTAM Summerschool Held in Stockholm, 12-20 June, 1995*, Springer.
- HAN, J.-C., DUTTA, S. & EKKAD, S. 2012. *Gas turbine heat transfer and cooling technology*, Taylor & Francis.
- HARTREE, D. R. On an equation occurring in Falkner and Skan's approximate treatment of the equations of the boundary layer. *Proc. Camb. Phil. Soc*, 1937. Cambridge Univ Press, 223-239.
- HEDLEY, T. B. & KEFFER, J. F. 1974. Turbulent/non-turbulent decisions in an intermittent flow. *Journal of Fluid Mechanics*, 64, 645-678.
- HERBERT, T. 1997. Parabolized stability equations. *Annual Review of Fluid Mechanics*, 29, 245-283.
- HOEPFFNER, J. 2006. *Falkner-Skan-Cooke boundary layer MATLAB code* [Online]. Available: <http://www.lmm.jussieu.fr/~hoepffner/codes.php>.
- HUGHES, J. D. & WALKER, G. J. 2001. Natural transition phenomena on an axial compressor blade. *Journal of Turbomachinery*, 123, 392-401.
- INSTEK. 2009. *GW Instek GDS-800 250/150/100/60MHz Digital Storage Oscilloscope* [Online]. Available: <http://www.gwinstek.com/en/product/productdetail.aspx?pid=3&mid=7&id=51>.
- INSTRUMENTS, D. T. P. 1999. Tracker 220 Series.
- IVANOV, A. V. & KACHANOV, Y. S. A method of study of the stability of 3D boundary layers using a new disturbance generator. International Conference on the Methods of Aerophysical Research. Proceedings. Part I, 1994. 125-130.

- JAHANMIRI, M. 2011. Boundary Layer Receptivity: A Retrospect. Chalmers University of Technology.
- JARRIN, N., BENHAMADOUCHE, S., LAURENCE, D. & PROSSER, R. 2006. A synthetic-eddy-method for generating inflow conditions for large-eddy simulations. *International Journal of Heat and Fluid Flow*, 27, 585-593.
- JOHANSSON, A. A low speed wind-tunnel with extreme flow quality- Design and tests. ICAS, Congress, 18 th, Beijing, China, 1992. 1603-1611.
- JOHNSON, M. W. 2001. On the flow structure within a turbulent spot. *International Journal of Heat and Fluid Flow*, 22, 409-416.
- JOHNSON, M. W. 2002. Predicting transition without empiricism or DNS. *Transactions of the ASME-T-Journal of Turbomachinery*, 124, 665-669.
- JOHNSON, M. W. 2011a. Bypass transition receptivity modes. *International Journal of Heat and Fluid Flow*, 32, 392-401.
- JOHNSON, M. W. 2011b. Munich ERCOFTAC Lecture Notes.
- JOHNSON, M. W. & ERCAN, A. H. Boundary layer transition model. 1996.
- JOHNSON, M. W. & ERCAN, A. H. 1999. A physical model for bypass transition. *International Journal of Heat and Fluid Flow*, 20, 95-104.
- JOHNSON, M. W. & FASHIFAR, A. 1994. Statistical properties of turbulent bursts in transitional boundary layers. *International Journal of Heat and Fluid Flow*, 15, 283-290.
- JOHNSON, M. W. P., A. 2013. The effect of pressure gradient on boundary layer receptivity.
- JONÁŠ, P., MAZUR, O. & URUBA, V. 2000. On the receptivity of the by-pass transition to the length scale of the outer stream turbulence. *European Journal of Mechanics, B/Fluids*, 19, 707-722.
- JØRGENSEN, F. E. 2001. *How to Measure Turbulence with Hot-Wire Anemometers: A Practical Guide*, Dantec Dynamics.
- KACHANOV, Y. S. 1994. Physical mechanisms of laminar-boundary-layer transition. *Annual Review of Fluid Mechanics*, 26, 411-482.
- KACHANOV, Y. S. 2000a. Three-dimensional receptivity of boundary layers. *European Journal of Mechanics-B/Fluids*, 19, 723-744.
- KACHANOV, Y. S. 2000b. Three-Dimensional Receptivity of Boundary Layers to External Perturbations. *Laminar-Turbulent Transition*. Springer.
- KENDALL, J. M. Experimental study of disturbances produced in a pre-transitional laminar boundary layer by weak freestream turbulence. AIAA, 18th Fluid Dynamics and Plasmadynamics and Lasers Conference, 1985.
- KERSCHEN, E. J. 1993. Boundary Layer Receptivity Theory. DTIC Document.

- KING, L. V. 1914. On the convection of heat from small cylinders in a stream of fluid: determination of the convection constants of small platinum wires, with applications to hot-wire anemometry. *Proceedings of the Royal Society of London. Series A*, 90, 563-570.
- KLEBANOFF, P. S. 1954. Characteristics of turbulence in a boundary layer with zero pressure gradient. NACA Report 1247, NASA-Langley Research Center, Hampton, VA, 1955. See also NACA Technical Note 3178.
- KLEBANOFF, P. S., TIDSTROM, K. D. & SARGENT, L. M. 1962. The three-dimensional nature of boundary-layer instability. *J. Fluid Mech*, 12, 1-34.
- KLINE, S. J., REYNOLDS, W. C., SCHRAUB, F. A. & RUNSTADLER, P. W. 1967. The structure of turbulent boundary layers. *Journal of Fluid Mechanics*, 30, 741-773.
- KLINKSIEK, W. F. & PIERCE, F. J. 1973. A finite difference solution of the two and three-dimensional incompressible turbulent boundary layer equations. *Journal of Fluids Engineering*, 95, 445.
- KOBAYASHI, R., KOHAMA, Y. & KUROSAWA, M. 1983. Boundary-layer transition on a rotating cone in axial flow. *Journal of Fluid Mechanics*, 127, 341-352.
- KOHAMA, Y. 1987. Some expectation on the mechanism of cross-flow instability in a swept wing flow. *Acta Mechanica*, 66, 21-38.
- KRISHNAMOORTHY, L. V., WOOD, D. H., ANTONIA, R. A. & CHAMBERS, A. J. 1985. Effect of wire diameter and overheat ratio near a conducting wall. *Experiments in Fluids*, 3, 121-127.
- KUAN, C. L. & WANG, T. 1990. Investigation of the intermittent behavior of transitional boundary layer using a conditional averaging technique. *Experimental Thermal and Fluid Science*, 3, 157-173.
- KUDAR, K., CARPENTER, P. & DAVIES, C. 2006. Klebanoff Modes In Swept Boundary Layers. In: GOVINDARAJAN, R. (ed.) *IUTAM Symposium on Laminar-Turbulent Transition*. Springer Netherlands.
- KURIAN, T., FRANSSON, J. H. M. & ALFREDSSON, P. H. 2011. Boundary layer receptivity to free-stream turbulence and surface roughness over a swept flat plate. *Physics of Fluids*, 23, 034107.
- LARSEN, S. E. & BUSCH, N. E. 1980. On the humidity sensitivity of hot-wire measurements. *DISA Information*, 1, 4.
- LASSEIGNE, D. G., CRIMINALE, W. O., JOSLIN, R. D. & JACKSON, T. L. 1999. Receptivity and Bypass Dynamics. NASA Langley Technical Report Server.
- LAUNDER, B. E. 1963. *The turbulent boundary layer in a strongly negative pressure gradient*. Massachusetts Institute of Technology, Department of Mechanical Engineering.

- LEE, T. & BUDWIG, R. 1991. Two improved methods for low-speed hot-wire calibration. *Measurement Science and Technology*, 2, 643.
- LEKAKIS, I. 1996. Calibration and signal interpretation for single and multiple hot-wire/hot-film probes. *Measurement Science and Technology*, 7, 1313-1333.
- LINDGREN, B. & JOHANSSON, A. V. 2002a. Design and evaluation of a low-speed wind-tunnel with expanding corners. *Flow Facility Design and Experimental Studies of Wall-Bounded Turbulent Shear-Flows*, 63.
- LINDGREN, B. & JOHANSSON, A. V. 2002b. Evaluation of the flow quality in the mtl wind-tunnel. *Flow Facility Design and Experimental Studies of Wall-Bounded Turbulent Shear-Flows*, 109.
- LUEPTOW, R. M., BREUER, K. S. & HARITONIDIS, J. H. 2004. Computer-aided calibration of X-probes using a look-up table. *Experiments in Fluids*, 6, 115-118.
- MADADNIA, J. 1989. *Experimental Study of Stability and Transition of Boundary Layer Flow*. PhD Thesis, University of Liverpool.
- MARUSIC, I., MCKEON, B., MONKEWITZ, P., NAGIB, H., SMITS, A. & SREENIVASAN, K. 2010. Wall-bounded turbulent flows at high Reynolds numbers: Recent advances and key issues. *Physics of Fluids*, 22, 065103.
- MAYLE, R. E. Role of laminar-turbulent transition in gas turbine engines. 1991.
- MCP. 2009. *MSD415 Microstepping Drive* [Online]. Available: <http://www.motioncontrolproducts.com/pdfs/msd415-microstepping-driver.pdf>.
- MCP 2012. Motion Control Products: 35NCLA-B01 Engineering Drawing.
- MICROSOFT. 2011. *Microsoft Support: Solver Uses Generalized Reduced Gradient Algorithm* [Online]. Available: <http://support.microsoft.com/kb/82890>.
- MORKOVIN, M. V. 1969. Critical evaluation of transition from laminar to turbulent shear layers with emphasis on hypersonically traveling bodies. DTIC Document.
- MURLIS, J., TSAI, H. M. & BRADSHAW, P. 1982. The structure of turbulent boundary layers at low Reynolds numbers. *Journal of Fluid Mechanics*, 122, 13-56.
- NARASIMHA, R. 1957. On the distribution of intermittency in the transition region of a boundary layer. *J. Aero. Sci*, 24, 711-712.
- OERTEL, H. 2010. *Crossflow and Tollmien Schlichting instability waves figure* [Online]. Available: By Herbert.Oertel / www.prof-oertel.de (Own work) [CC-BY-SA-3.0 (<http://creativecommons.org/licenses/by-sa/3.0>) or GFDL (<http://www.gnu.org/copyleft/fdl.html>)], via Wikimedia Commons.

- OKA, S. & KOSTIC, Z. 1972. Influence of wall proximity on hot-wire velocity measurements. *DISA Information*, 29-33.
- ORR, W. M. F. The stability or instability of the steady motions of a perfect liquid and of a viscous liquid. Part I: A perfect liquid. Proceedings of the Royal Irish Academy. Section A: Mathematical and Physical Sciences, 1907. JSTOR, 9-68.
- OVCHINNIKOV, V., CHOUDHARI, M. M. & PIOMELLI, U. 2008. Numerical simulations of boundary-layer bypass transition due to high-amplitude free-stream turbulence. *Journal of Fluid Mechanics*, 613, 135.
- PATANKAR, S. V. & SPALDING, D. B. 1972. A calculation procedure for heat, mass and momentum transfer in three-dimensional parabolic flows. *International Journal of Heat and Mass Transfer*, 15, 1787-1806.
- PEARCEY, H. H. 1962. The aerodynamic design of section shapes for swept wings. *Advances in Aeronautical Sciences*, 3, 277-322.
- PERRY, A. E. 1982. *Hot-wire anemometry*, Clarendon Press.
- POHLHAUSEN, K. 1921. Zur näherungsweise Integration der Differentialgleichung der laminaren Grenzschicht. *ZAMM-Journal of Applied Mathematics and Mechanics/Zeitschrift für Angewandte Mathematik und Mechanik*, 1, 252-290.
- POLL, D. I. A. 1985. Some observations of the transition process on the windward face of a long yawed cylinder. *J. Fluid Mech*, 150, 329-356.
- PRANDTL, L. 1904. Über Flüssigkeitsbewegung bei sehr kleiner Reibung. *Int. Math. Kongr Heidelberg. Leipzig*.
- PRANDTL, L. 1914. Der luftwiderstand von Kugeln. *Nachr. Ges. Wiss. Göttingen, Math.-phys. Kl*, 177-190.
- RAMADAN, A. 2000. *Simulation of Flows over the Leading Edge of a Swept Wing*. PhD Thesis, University of Liverpool.
- RAMESH, O. N. & HODSON, H. P. 1999. A new intermittency model incorporating the calming effect. *ROLLS ROYCE PLC-REPORT-PNR*.
- RAYLEIGH, L. 1880. On the stability, or instability, of certain fluid motions. *Proc. Loiss. Math. Sot*, 11, 57-70.
- REED, H. L. 1987. Wave interactions in swept-wing flows. *Physics of Fluids*, 30, 3419.
- REED, H. L. & SARIC, W. S. 1989. Stability of three-dimensional boundary layers. *Annual Review of Fluid Mechanics*, 21, 235-284.
- REICHARDT, H. 1940. Die Wärmeübertragung in turbulenten Reibungsschichten. *ZAMM-Journal of Applied Mathematics and Mechanics/Zeitschrift für Angewandte Mathematik und Mechanik*, 20, 297-328.
- REYNOLDS, O. 1883. An experimental investigation of the circumstances which determine whether the motion of water shall be direct or

- sinuous, and of the law of resistance in parallel channels. *Proceedings of the Royal Society of London*, 35, 84-99.
- REYNOLDS, O. 1895. On the dynamical theory of incompressible viscous fluids and the determination of the criterion. *Philosophical Transactions of the Royal Society of London. A*, 186, 123-164.
- RILEY, S. 1985. *Three-Dimensional Boundary Layer Transition*. PhD Thesis, University of Liverpool.
- SARIC, W. S., REED, H. L. & KERSCHEN, E. J. 2002. Boundary-layer receptivity to freestream disturbances. *Annual Review of Fluid Mechanics*, 34, 291-319.
- SARIC, W. S., REED, H. L. & WHITE, E. B. 2003. Stability and transition of three-dimensional boundary layers. *Annual Review of Fluid Mechanics*, 35, 413-440.
- SARIC, W. S. & YEATES, L. G. 1985. Generation of crossflow vortices in a three-dimensional flat-plate flow. *Laminar-Turbulent Transition*. Springer.
- SAVILL, A. M. 1992. A synthesis of T3 test case predictions. *Numerical simulation of unsteady flows and transition to turbulence*, 404-442.
- SCHLICHTING, H. 1933. Berechnung der Anfachung kleiner Störungen bei der Plattenströmung. *ZAMM*, 13, 171-174.
- SCHLICHTING, H. 1968. *Boundary-Layer Theory* Sixth Edition, (1968). McGraw-Hill Book Company, New York, London.
- SCHLICHTING, H. 1979. *Boundary Layer Theory: Seventh Edition*, McGraw-Hill.
- SCHLICHTING, H. & GERSTEN, K. 2000. *Boundary-Layer Theory: Eighth Edition*, Springer Verlag.
- SCHMID, P. J. & HENNINGSON, D. S. 2001. *Stability and transition in shear flows*, Springer Verlag.
- SCHRADER, L. U., BRANDT, L., MAVRIPLIS, C. & HENNINGSON, D. S. 2010. Receptivity to free-stream vorticity of flow past a flat plate with elliptic leading edge. *Journal of Fluid Mechanics*, 653, 245-271.
- SCHUBAUER, G. B. 1935. Effect of humidity in hot-wire anemometry. *Journal of the Franklin Institute*, 220, 789-790.
- SCHUBAUER, G. B. & KLEBANOFF, P. S. 1955. Contributions on the mechanics of transition.
- SCHUBAUER, G. B. & SKRAMSTAD, H. K. 1947. Laminar boundary-layer oscillations and transition on a flat plate. *J. Res. Nat. Bur. Stand*, 38, 251-292.
- SHAW, R., ENG, B., HARDCASTLE, J. A., RILEY, S. & ROBERTS, C. C. 1985. Recording and analysis of fluctuating signals using a microcomputer. *Measurement*, 3, 33-39.

- SOMMERFELD, A. 1908. Ein Beitrag zur hydrodynamischen Erklärung der turbulenten Flüssigkeitsbewegungen. *Atti del*, 4, 116-124.
- STEELANT, J. & DICK, E. 1996. Modelling of bypass transition with conditioned Navier–Stokes equations coupled to an intermittency transport equation. *International journal for numerical methods in fluids*, 23, 193-220.
- STEMMER, C. 2010. *Three-Dimensional Boundary Layers* [Online]. Technische Universität München. Available: http://www.aer.mw.tum.de/fileadmin/tumwaer/www/pdf/lehre/grenzschicht/lectures/lecture_07.pdf.
- STEWARTSON, K. Further solutions of the Falkner-Skan equation. Proc. Camb. Phil. Soc, 1954. Cambridge Univ Press.
- TEMPELMANN, D. 2011. *Receptivity of crossflow-dominated boundary layers*. KTH.
- TEMPELMANN, D., HANIFI, A. & HENNINGSON, D. 2010. Spatial optimal growth in three-dimensional boundary layers. *Journal of Fluid Mechanics*, 646, 5.
- TENNEKES, H. & LUMLEY, J. L. 1972. *First course in turbulence*, MIT press.
- TOLLMIE, W. 1929. Über die Entstehung der Turbulenz. *Ges. Wiss. Göttingen Math. Phys. Klasse*, 21.
- TSANIS, I. K. 1987. Calibration of hot-wire anemometers at very low velocities. *Dantec Information (ISSN 0900-5579)*, Feb. 1987, p. 13, 14., 1, 13.
- URANGA, A., PERSSON, P.-O., DRELA, M. & PERAIRE, J. 2011. Preliminary Investigation Into the Effects of Cross-Flow on Low Reynolds Number Transition. *20th AIAA Computational Fluid Dynamics Conference. 27 - 30 June 2011, Honolulu, Hawaii*.
- VALIDDYNE 2013. Validyne Engineering: Validyne Pressure Transducer Range Chart.
- VERSTEEG, H. K. & MALALASEKERA, W. 2007. *An introduction to computational fluid dynamics: the finite volume method*, Prentice Hall.
- VON KARMAN, T. 1930. Mechanische Ähnlichkeit und turbulenz. *Nachrichten von der Gesellschaft der Wissenschaften zu Göttingen, Mathematisch-Physikalische Klasse*, 1930, 58-76.
- WHITE, F. M. 1991. *Viscous fluid flow - Second Edition*.
- WILCOX, D. A. 1994. Simulation of transition with a two-equation turbulence model. *AIAA Journal*, 32, 247-255.
- WILCOX, D. C. 1998. *Turbulence modeling for CFD*, DCW industries La Canada.
- WILLS, J. A. B. 1962. The correction of hot-wire readings for proximity to a solid boundary. *Journal of Fluid Mechanics*, 12, 388-396.

- WYGNANSKI, I., SOKOLOV, M. & FRIEDMAN, D. 1976. On a turbulent 'spot' in a laminar boundary layer. *Journal of Fluid Mechanics*, 78, 785-819.
- YOKOTA, K., TAGAWA, M., OHMAE, N. & WELLS, C. S. 1967. Effects of freestream turbulence on boundary-layer transition. *AIAA Journal*, 5, 172-174.
- ZOGRAFAKIS, G. 2013. *Transition Modelling for Helicopter Flows*. PhD Thesis.
- ZURIGAT, Y. H. & MALIK, M. R. 1995. Effect of cross-flow on Görtler instability in incompressible boundary layers. *Physics of Fluids*, 7, 1616.

10 Appendix A – OpenFOAM and ANSYS Fluent Receptivity

Although a successful method of quantifying the receptivity has already been provided in Chapter 5 significant effort was expended attempting to provide similar results with both the OpenFOAM and ANSYS Fluent general purpose CFD codes. For brevity and owing to the relatively excessive numerical dissipation experienced with Fluent, only the OpenFOAM case set-up and results are discussed.

10.1 Derivation of Real Inflow Velocity Components

The unsteady velocity components, in complex form, are as follows for each waveform;

$$u = u_1 e^{i(\omega_x x + \omega_y y + \omega_z z + \omega t) - \beta x} \quad \text{Equation 10-1}$$

$$v = v_1 e^{i(\omega_x x + \omega_y y + \omega_z z + \omega t) - \beta x} \quad \text{Equation 10-2}$$

$$w = w_1 e^{i(\omega_x x + \omega_y y + \omega_z z + \omega t) - \beta x} \quad \text{Equation 10-3}$$

Continuity (Equation 10-4) must be satisfied, regardless of the solution orientation;

$$(i\omega_x - \beta)u_1 + i\omega_y v_1 + i\omega_z w_1 = 0 \quad \text{Equation 10-4}$$

For a $u'v'$ solution ($w_1=0$), therefore;

$$u_1 = \frac{1}{i\omega_x - \beta} \text{ and } v_1 = \frac{-1}{i\omega_y} \text{ such that continuity is satisfied and for a } v'w' \text{ solution } (u_1=0) \text{ so}$$

$$\text{therefore; } v_1 = \frac{1}{i\omega_y} \text{ and } w_1 = \frac{-1}{i\omega_z}$$

The full procedure, hereafter, is shown only for $u'v'$ solutions because those solution results from OpenFOAM are discussed in the remainder of this appendix, nevertheless a similar procedure can be followed for $v'w'$.

Firstly at $x=0$;

$$u = \frac{e^{i(\omega_y y + \omega_z z + \omega t)}}{i\omega_x - \beta} \quad \text{Equation 10-5}$$

and from the general equation (Equation 10-6) for the division of two complex numbers;

$$\frac{a+bi}{c+di} = \left(\frac{ac+bd}{c^2+d^2} \right) + i \cdot \left(\frac{bc-ad}{c^2+d^2} \right) \quad \text{Equation 10-6}$$

the real part of u , i.e. $\left(\frac{ac+bd}{c^2+d^2} \right)$, at $x=0$ is as per Equation 10-7;

$$u = \frac{\omega_x \sin(\omega_y y + \omega_z z + \omega t) - \beta \cos(\omega_y y + \omega_z z + \omega t)}{\omega_x^2 + \beta^2} \quad \text{Equation 10-7}$$

where the same procedure also yields Equation 10-8;

$$v = -\sin(\omega_y y + \omega_z z + \omega t) \quad \text{Equation 10-8}$$

These equations are then manipulated such that fluctuations of unit magnitude are produced for all spatial frequency combinations, resulting in the following equations (Equation 10-9 and

Equation 10-10) for a $u'v'$ solution;

$$u = \omega_y \frac{\omega_x \sin(\omega_y y + \omega_z z + \omega t) - \beta \cos(\omega_y y + \omega_z z + \omega t)}{(\omega_x^2 + \beta^2)^{\frac{1}{2}} (\omega_x^2 + \omega_y^2 + \beta^2)^{\frac{1}{2}}} \quad \text{Equation 10-9}$$

$$v = -\left(\frac{(\omega_x^2 + \beta^2)^{\frac{1}{2}}}{(\omega_x^2 + \omega_y^2 + \beta^2)^{\frac{1}{2}}} \right) \sin(\omega_y y + \omega_z z + \omega t) \quad \text{Equation 10-10}$$

These are then scaled (to Equation 10-11 and Equation 10-12) so as to result in a turbulence intensity of 1% on the inlet face (where $U_\infty = 10$ m/s and $u_{rms} = 0.1$ m/s) and the streamwise velocity, U_∞ , is added to the streamwise component;

$$u = U_\infty + \omega_y(\sqrt{2} * u_{rms}) \left(\frac{\omega_x \sin(\omega_y y + \omega_z z + \omega t) - \beta \cos(\omega_y y + \omega_z z + \omega t)}{(\omega_x^2 + \beta^2)^{\frac{1}{2}} (\omega_x^2 + \omega_y^2 + \beta^2)^{\frac{1}{2}}} \right) \quad \text{Equation 10-11}$$

$$v = -(\sqrt{2} * u_{rms}) \left(\frac{(\omega_x^2 + \beta^2)^{\frac{1}{2}}}{(\omega_x^2 + \omega_y^2 + \beta^2)^{\frac{1}{2}}} \right) \sin(\omega_y y + \omega_z z + \omega t) \quad \text{Equation 10-12}$$

10.2 OpenFOAM Case Library Files

The topology of the mesh is identical to that of Figure 5-1 which was used for the numerical receptivity calculations written in Fortran. However the mesh generated for OpenFOAM was composed of four sub-sections, or blocks as they are referred to in the OpenFOAM structured meshing utility blockMesh, as can be observed from Figure 10-1. The boundary conditions on the mesh are also colour co-ordinated in the figure less, that is, the spanwise boundary condition which comprised all parallel faces in the spanwise direction displaced by unit depth in this case.

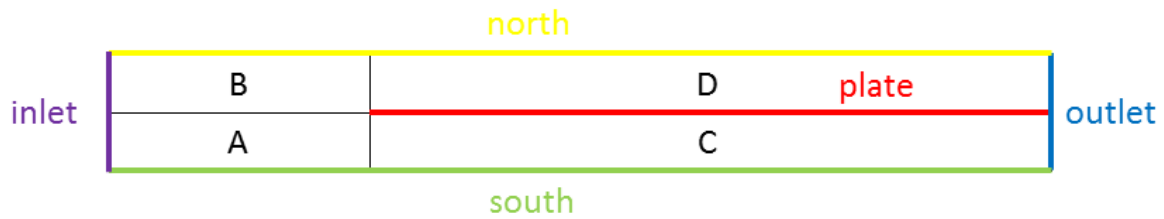


Figure 10-1 - OpenFOAM multi-block structured grid with colour co-ordinated boundary conditions

The following script is an OpenFOAM dictionary file which prescribed all 24 vertices of each of the 4 blocks, in addition to the names of the boundaries/patches. All overlapping faces are fused by default as interior faces unless requested otherwise. The interfacing faces of block C and D were programmed to opt out of this default treatment such that a wall (i.e. the plate) could be assigned as

a boundary condition. As an initial consequence of this opt-out approach the patch will be named 'defaultFaces' by default once blockMesh has completed execution and assigned patch type 'empty', these parameters are subsequently revised to 'plate' and 'wall' in the 'boundary' polyMesh dictionary file.

```
/*-----*- C++ -*-----*\
|=====|
| \ / Field | OpenFOAM: The Open Source CFD Toolbox |
| \ / Operation | Version: 2.2.1 |
| \ / And | Web: www.OpenFOAM.org |
| \ / Manipulation |
\*-----*/
```

FoamFile

```
{
    version 2.0;
    format ascii;
    class dictionary;
    object blockMeshDict;
}

// ***** //
```

convertToMeters 1;

vertices

```
(
    (0 0 0)
    (25 0 0)
    (25 10 0)
    (0 10 0)
```

(25 20 0)

(0 20 0)

(550 0 0)

(550 10 0)

(550 20 0)

(25 10 0)

(550 10 0)

(0 10 0)

(0 0 1)

(25 0 1)

(25 10 1)

(0 10 1)

(25 20 1)

(0 20 1)

(550 0 1)

(550 10 1)

(550 20 1)

(25 10 1)

(550 10 1)

(0 10 1)

);

blocks

(

hex (0 1 2 3 12 13 14 15) (25 200 1) simpleGrading (1 1 1)

hex (11 9 4 5 23 21 16 17) (25 200 1) simpleGrading (1 1 1)

hex (1 6 7 2 13 18 19 14) (525 200 1) simpleGrading (1 1 1)

hex (9 10 8 4 21 22 20 16) (525 200 1) simpleGrading (1 1 1)

```
);
```

```
edges
```

```
(
```

```
);
```

```
patches
```

```
(
```

```
  patch inlet
```

```
  (
```

```
    (0 12 15 3)
```

```
    (11 23 17 5)
```

```
  )
```

```
  patch outlet
```

```
  (
```

```
    (6 18 19 7)
```

```
    (10 22 20 8)
```

```
  )
```

```
  patch north
```

```
  (
```

```
    (5 4 16 17)
```

```
    (4 8 20 16)
```

```
  )
```

```
  patch south
```

```
  (
```

```
    (0 1 13 12)
```

```
    (1 6 18 13)
```

```
  )
```

```
  empty spanwise
```

```
  (
```

```

    (12 13 14 15)
    (13 18 19 14)
    (23 21 16 17)
    (21 22 20 16)
    (0 1 2 3)
    (1 6 7 2)
    (11 9 4 5)
    (9 10 8 4)
)
wall gap
(
    (3 2 14 15)
)

wall shadow
(
    (11 9 21 23)
)
);

mergePatchPairs
(

    ( gap shadow )

);

// ***** //
```


In OpenFOAM the boundary and initial conditions are specified in more dictionary files (FoamFile) which then propagate with the solution file properties as they are written. Hence, for example, one can modify the boundary conditions from a converged solution file and use it as the starting point for further analysis. This is analogous to the base flow and unsteady flow approach that was adopted in Chapter 5 with the Fortran codes. The boundary condition files for pressure and velocity were constrained as follows;

```
/*-----*- C++ -*-----*\
|=====|
| \ / Field | OpenFOAM: The Open Source CFD Toolbox |
| \ / Operation | Version: 2.2.1 |
| \ / And | Web: www.OpenFOAM.com |
| \ / Manipulation |
\*-----*/

FoamFile
{
    version 2.0;

    format ascii;

    class volScalarField;

    object p;
}

// *****

dimensions [0 2 -2 0 0 0];

internalField uniform 0;
```

boundaryField

```
{  
    inlet  
    {  
        type        fixedValue;  
        value        uniform 0;  
    }  
    outlet  
    {  
        type        fixedValue;  
        value        uniform 0;  
    }  
  
    north  
    {  
        type        fixedValue;  
        value        uniform 0;  
    }  
    south  
    {  
        type        fixedValue;  
        value        uniform 0;  
    }  
    spanwise  
    {  
        type        empty;  
    }  
    plate  
    {  
        type        zeroGradient;
```

```

    }

}

// *****

/*-----*- C++ -*-----*\
|=====|
| \ / Field | OpenFOAM: The Open Source CFD Toolbox |
| \ / Operation | Version: 2.2.1 |
| \ / And | Web: www.OpenFOAM.org |
| \ / Manipulation |
\*-----*/

FoamFile
{
    version 2.0;

    format ascii;

    class volVectorField;

    object U;
}

// *****

dimensions [0 1 -1 0 0 0];

internalField uniform (10 0 0);

boundaryField
{

    inlet
    {
        type groovyBC;

```

```

    valueExpression
"vector(vinf+unsteady*(wnorm/(a*b))*(wst*sin(wnorm*pos().y+wspan*pos().z+wtemp*time())-
beta*cos(wnorm*pos().y+wspan*pos().z+wtemp*time())),-
unsteady*(a/b)*sin(wnorm*pos().y+wspan*pos().z+wtemp*time()),0)";

    variables
"vinf=10;unsteady=0.1*sqrt(2);visc=0.01;wst=0.00125661421594;wnorm=3.00003;wspan=0.300001;
beta=sqrt(((vinf*vinf)/(4*visc*visc))+wst*wst+wnorm*wnorm+wspan*wspan)-
(vinf/(2*visc));wtemp=(-
1)*(vinf+2*beta*visc)*wst;a=sqrt(wst*wst+beta*beta);b=sqrt(wst*wst+wnorm*wnorm+beta*beta);
";

    timelines ();

    value uniform (10 0 0);

}

north
{
    type        zeroGradient;
}

south
{
    type        zeroGradient;
}

outlet
{
    type        advective;
}

spanwise
{
    type        empty;
}

plate
{

```

```

        type      fixedValue;
        value      uniform (0 0 0);
    }
}

// ***** //

```

In OpenFOAM it is possible to numerically solve any governing equations which transport parameters with whichever dimensions are specified by the user. Here the pressure field is identified as a scalar quantity with a dimension array of 0, 2, -2, 0, 0, 0, 0. This dimension array refers to SI properties, as per Table 10-1. Therefore the dimensions of the pressure field were in m^2/s^2 rather than $\text{kg}/\text{m}\cdot\text{s}^2$ – hence a kinematic pressure field. Similarly velocity was solved in m/s , only velocity is a vector and as such the boundary conditions are quantified in three Cartesian components.

For the velocity field a third party utility - groovyBC, as part of the swak4foam suite, is used to specify the components of the inlet boundary conditions with respect to their derivation in subsection 10.1. The spatial frequencies (wst, wnorm and wspan) are then set to specify how the waveforms oscillate on the inlet boundary. Note that these frequencies have been scaled such that the turbulence intensity on the inlet equates to 1% so as to maintain linearity in the approach. The initial conditions for the velocity and pressure fields correspond to the steady inlet velocity for the former and zero for the latter. These parameters, in theory, only affect solution speed and potentially stability if they deviate too much from the actual solution.

Table 10-1 - SI base units

Array Index	Property	Unit	Symbol
1	mass	kilogram	kg
2	length	metre	m
3	time	second	s
4	temperature	kelvin	K
5	substance amount	moles	mol
6	electric current	ampere	A
7	luminous intensity	candela	cd

```

/*-----*- C++ -*-----*\
| ===== |
| \ \ / F ield | OpenFOAM: The Open Source CFD Toolbox |
| \ \ / O peration | Version: 2.2.1 |
| \ \ / A nd | Web: www.OpenFOAM.com |
| \ \ / M anipulation | |
\*-----*/

FoamFile
{
    version 2.0;
    format ascii;
    class dictionary;
    location "constant";
    object transportProperties;
}

// *****

nu nu [ 0 2 -1 0 0 0 0 ] 0.01;

```

```
// ***** //
```

```
/*-----*- C++ -*-----*| ===== |  
|  
| \ / F i e l d | OpenFOAM: The Open Source CFD Toolbox |  
| \ / O p e r a t i o n | Version: 2.2.1 |  
| \ / A n d | Web: www.OpenFOAM.com |  
| \ / M a n i p u l a t i o n | |  
\*-----*/
```

FoamFile

```
{  
    version 2.0;  
    format ascii;  
    class dictionary;  
    location "system";  
    object controlDict;  
}
```

```
// ***** //
```

application icoFoam;

startFrom startTime;

startTime 0;

stopAt endTime;

endTime 2000;

deltaT 0.1;

```
writeControl  timeStep;
```

```
writeInterval  1;
```

```
purgeWrite  500;
```

```
writeFormat  ascii;
```

```
writePrecision 12;
```

```
writeCompression uncompressed;
```

```
timeFormat  general;
```

```
timePrecision 12;
```

```
runTimeModifiable yes;
```

```
libs ( "libOpenFOAM.so" "libgroovyBC.so" );
```

```
// ***** //
```

```
/*-----*- C++ -*-----* | ===== |  
|  
| \ / Field | OpenFOAM: The Open Source CFD Toolbox |  
| \ / Operation | Version: 2.2.1 |
```


| \ / A n d | Web: www.OpenFOAM.com |

| √ M a n i p u l a t i o n |

-----/

FoamFile

{

version 2.0;

format ascii;

class dictionary;

location "system";

object fvSchemes;

}

// ***** //

ddtSchemes

{

default backward;

}

gradSchemes

{

default fourth;

grad(p) fourth;

}

divSchemes

{

// default Gauss linearUpwind Gauss linear;

div(phi,U) /*Gauss linearUpwind*/ Gauss upwind;

}

laplacianSchemes

```
{
    default      Gauss cubic corrected;

    laplacian(nu,U) Gauss cubic corrected;

    laplacian((1|A(U)),p) Gauss cubic corrected;
}
```

interpolationSchemes

```
{
    default      linear;

    interpolate(HbyA) linear;
}
```

snGradSchemes

```
{
    default      fourth;
}
```

fluxRequired

```
{
    default      no;

    p            ;
}
```

```
// ***** //
```

```
/*-----* C++ -*-----* | ===== |
|
```

```
| \ / F i e l d | OpenFOAM: The Open Source CFD Toolbox |
```

```
| \ / O p e r a t i o n | Version: 2.2.1 |
```

| \ / A nd | Web: www.OpenFOAM.com |

| \ / M anipulation |

-----/

FoamFile

{

version 2.0;

format ascii;

class dictionary;

location "system";

object fvSolution;

}

// ***** //

solvers

{

p

{

solver PCG;

preconditioner DIC;

tolerance 1e-6;

relTol 0;

}

U

{

solver PBiCG;

preconditioner DILU;

tolerance 1e-8;

relTol 0;

}

```
}
```

PISO

```
{
```

```
    nCorrectors    2;
```

```
    nNonOrthogonalCorrectors 0;
```

```
    pRefCell      0;
```

```
    pRefValue     0;
```

```
}
```

```
// ***** //
```

Prior to a case being executed the mesh is divided into sub domains using ‘decomposePar’ such that the solution can be executed in parallel and take advantage of the multi core architecture which is common in modern computing. Thereafter the solution files can be read in parallel or restored as serial solution files with reconstructPar. This option is certainly a major advantage of using general purpose CFD codes as multithreading is readily available and can considerably reduce the solution time.

Please note that the ‘icoFoam’ solver executed as part of the OpenFOAM analysis produces solution files which utilise a kinematic pressure field. That is to say the momentum equation balances are divided throughout by the density, with the effect that the kinematic (as opposed to the dynamic) viscosity of the working fluid is specified and therefore the density is effectively embedded in the pressure scalar field. This is acceptable practice where the approximation of incompressibility holds, i.e. for flows with Mach numbers less than 0.3, which is very much the case for all flows considered in this thesis.

10.3 OpenFOAM Results

Results from one of the test cases evaluated in OpenFOAM are presented in this sub-section using the open source ParaView post-processor. One of the three spatial frequencies, however, does not comply with the streamwise frequency codes of Table 5-2. The frequencies chosen were $\omega_x = 0.0012566$, $\omega_y = 3.00003$ (G0) and $\omega_z = 0.300001$ (80) which were known to be reasonably receptive $u'v'$ frequencies for a two dimensional base flow – i.e. no steady crossflow. Unlike Chapter 5 this approach relies on marching the solution through time where, once a solution was considered to be statistically steady, 50 keyframes spanning exactly one period of the incoming waveform were analysed. The rationale, therefore, for deviating from the frequency code convention was simply because, with these frequencies, one period of the wave corresponded to an integer number – 500 ms.

Some plots of the solution files are demonstrated in the following figures. Figure 10-2 shows a frame of velocity magnitude contours (in m/s) at a snapshot in time (980 ms). The contours have been clipped to the peak and trough of the waveform added to the mean inlet velocity of 10 m/s. This contour clipping provides a visual representation of the boundary layer, owing to the fact that all velocities below 9.85858 m/s are coloured blue. More importantly, however, the contour thresholds clearly illustrate the waveform orientation as it propagates through the domain. Given that the streamwise frequency is small, whereas the frequency in the normal direction is large, the inclination of the waves, for this combination of spatial frequencies, is almost horizontal.

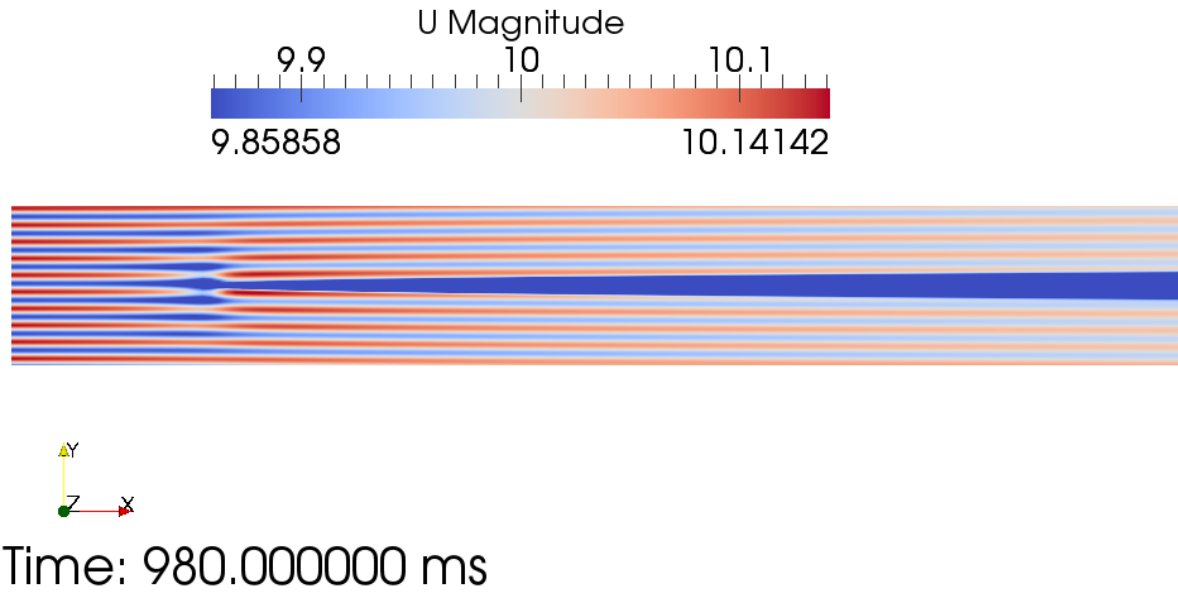


Figure 10-2 - OpenFOAM $u'v'$ receptivity example of instantaneous velocity magnitude contour plot after 980 ms of solution time

Once the final target solution time of 2000 ms was reached the final 50 solution files, written to disk, (1510 – 2000 ms) were then processed for temporal statistics (time average and standard deviation) in ParaView. Thereafter the ratios of the standard deviation and averages were processed for turbulence intensity which has been displayed in Figure 10-3. Firstly the turbulence intensity is seen to be 1% on the inlet face, as intended to maintain linearity of the solution unsteadiness. Secondly one can observe that the turbulence intensity decays in the freestream, as one would expect. The rate of the decay is somewhat moderate (β is approximately 0.0091). Thirdly this combination of spatial frequencies is seen to be receptive near the wall, given that the near wall turbulence intensities are higher than those in the freestream.

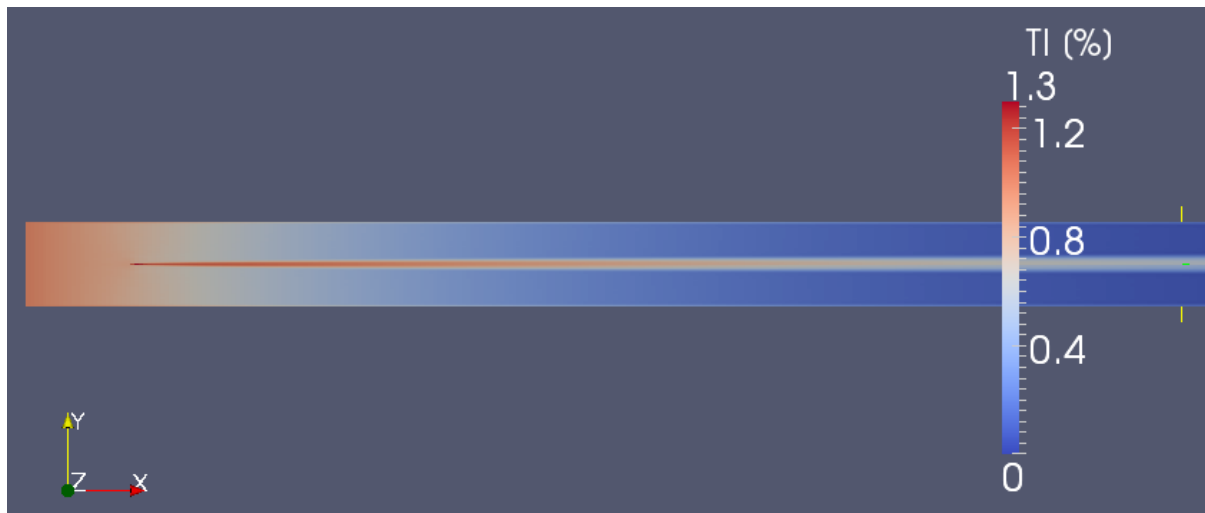


Figure 10-3 - Turbulence intensity contours time-averaged over one wave period for OpenFOAM u'v' receptivity example

The indications from the results presented in this appendix are that OpenFOAM could prove to be a viable method for analysing the receptivity of unique freestream waveforms in a similar manner to that which has been achieved in Chapter 5 in Fortran. There are problems to overcome, however, when it comes to scaling the problem up for the multitude of frequencies which were analysed in Chapter 5 – i.e. 2106 frequency combinations per pressure gradient. Each frequency combination would have its own corresponding wave period which would have to be accounted for when quantifying the time step and writing frequency in OpenFOAM. Furthermore, one must also ensure no individual time step across the frequency array enacts unstable CFL numbers – see Courant et al. (1967), i.e. CFL/Courant numbers which are high enough to allow solution instability.

In addition, the approach of using the HTCondor system to solve each frequency combination concurrently on a pool of computers could be utilised if Linux machines with OpenFOAM were brought into the University of Liverpool HTCondor pool. As of the present, the pool comprises Windows machines which operate in the HTCondor ‘vanilla universe’. Nevertheless, given that OpenFOAM is an open source code, it is possible to compile or cross compile the source code for the icoFoam solver (as well as the third party utilities used to impose the fluctuating boundary condition) into a binary form which will execute on a Windows machine. The availability of MPI

(parallel processing) in conjunction with OpenFOAM, offers the opportunity to utilise multi-threading on a single multi-core machine, clusters and high-throughput facilities such as HTCondor.

10.4 NACA 0002 Test Case

The principal objective of extending the receptivity analysis process to general purpose CFD codes was so as to be able to study receptivity on a wide range of topologies, without having to adopt an exhaustive programme of code (notably Fortran) development. Such code development, in the case of a 2-D mesh of a NACA 0002 aerofoil for example, would have to include a method of first meshing the topology with curvature (in a manner that was readable for the steady and unsteady codes) and additionally solution methods which compute fluxes through skewed faces in non-orthogonal cells which aren't equally distributed through space. These problems have already been largely overcome with many commercial and open-source general purpose CFD codes and, as such, further undertakings would likely prove to be duplicated and unnecessary effort. The following illustrates both the potential to conduct such analyses, but also highlights some of problems which have to be overcome.

Firstly a NACA 0002 aerofoil was selected for analysis. A NACA 0002 profile was selected on the basis that it is a symmetrical aerofoil, with the maximum thickness occurring at 30% chord, and provides the closest aerofoil approximation to that of a flat plate, being the thinnest viable option considered in the series, from the perspective of reliably meshing the leading edge. Given that this aerofoil has no camber the positive and negative of the thickness distributions (Equation 10-13) are added on either side of the chord line, where the chord line is a straight line connecting the leading and trailing edges.

$$y_t = \frac{t}{0.2} c \left[0.2969 \sqrt{\frac{x}{c}} - 0.126 \left(\frac{x}{c} \right) - 0.3537 \left(\frac{x}{c} \right)^2 + 0.2843 \left(\frac{x}{c} \right)^3 - 0.1015 \left(\frac{x}{c} \right)^4 \right] \quad \text{Equation 10-13}$$

This NACA profile was then modelled in Gambit 2.4.6 within the dimensions of the schematic of Figure 10-4. Note that, relative to the flat plate, the leading edge has been displaced further downstream and the domain made taller, for reasons which are discussed later. Note that the chord of the aerofoil was equivalent to that of the flat plate (525 mm).

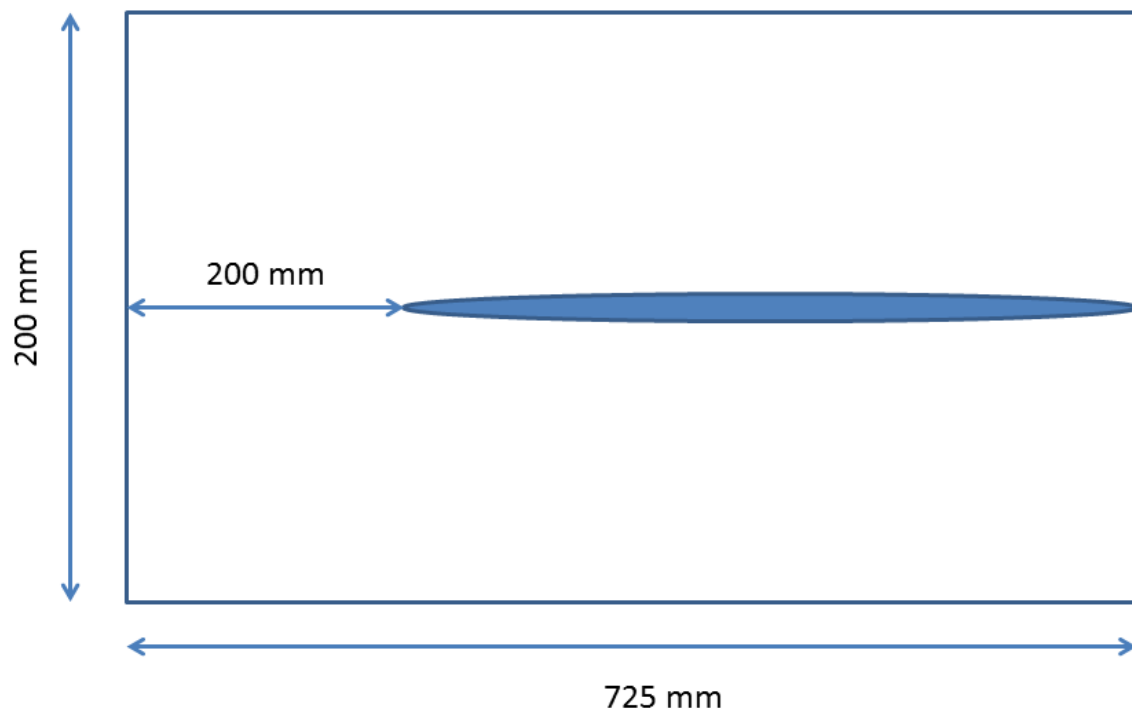


Figure 10-4 - Schematic of NACA 0002 2-D mesh

This was meshed, as per Figure 10-5, first by using a boundary layer mesh (50 cells deep) around the aerofoil with a growth rate of unity (i.e. constant height) and a cell height of 0.1 mm. Thereafter a mesh of paved quadrilateral elements was fitted and smoothed onto the remaining fluid domain. A detailed view of the mesh at the leading edge is included in Figure 10-6 illustrating the high quality of the mesh proximal to the aerofoil and the quadrilateral elements in the freestream. The spacing of the boundary layer cells are reduced around the leading edge such that the curvature is well resolved and to account for the spreading caused by the curvature itself as the boundary layer cells penetrate back towards the main paved mesh.

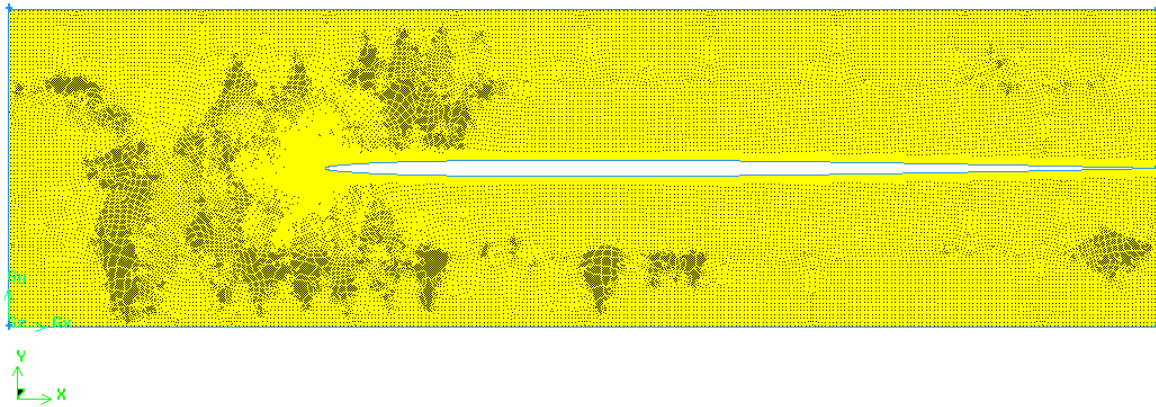


Figure 10-5 - NACA 0002 2-D Gambit mesh

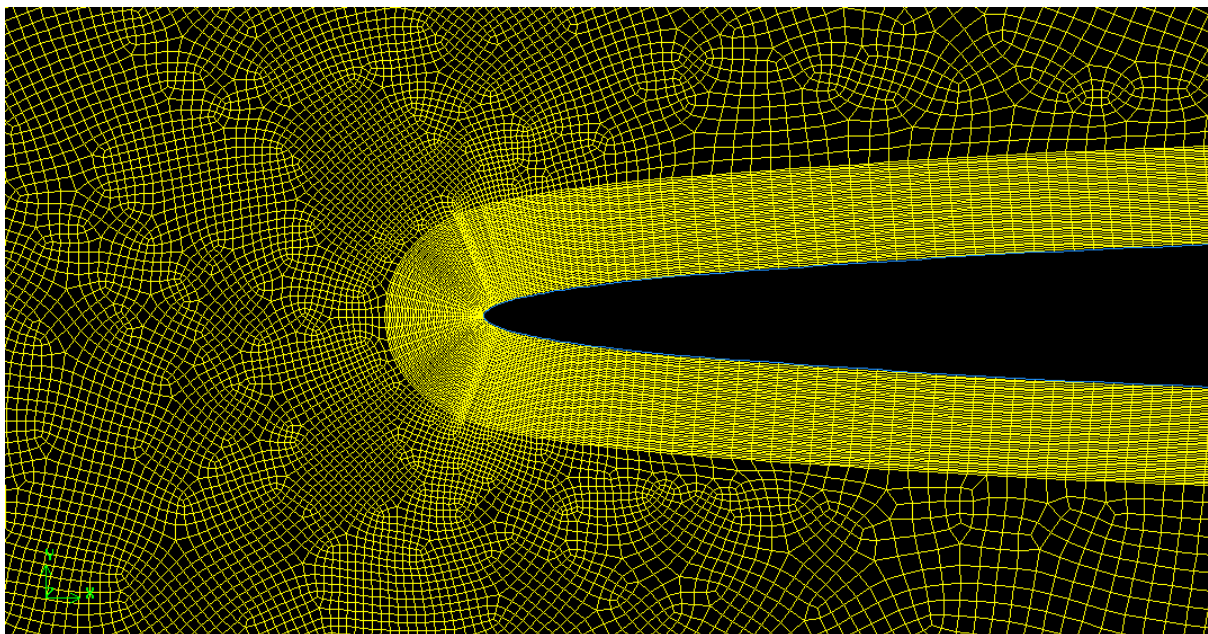


Figure 10-6 - NACA 0002 mesh detail at leading edge

Following the meshing of the domain the exported mesh (containing 207,875 cells) was then converted from an ANSYS Fluent format to OpenFOAM format using the `fluentMeshToFoam` conversion utility. Thereafter the NACA 0002 case was solved with exactly the same boundary conditions, dictionary and solution files as the flat plate case.

The velocity magnitude contour plot of Figure 10-7 when compared to that obtained (similarly scaled - Figure 10-8) for the flat plate boundary layer appears to demonstrate the presence of a far

larger stagnation region which appears to strongly suppress the incoming fluctuations as observed in Figure 10-9.

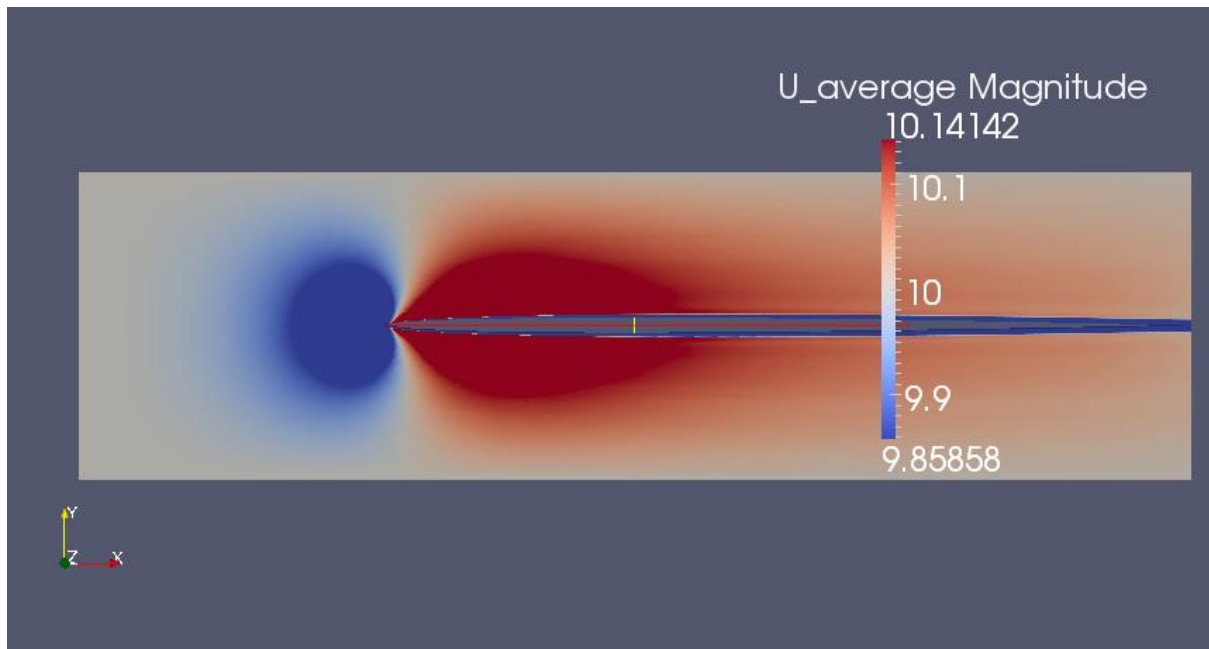


Figure 10-7 - Cropped average velocity magnitude contours (NACA 0002)

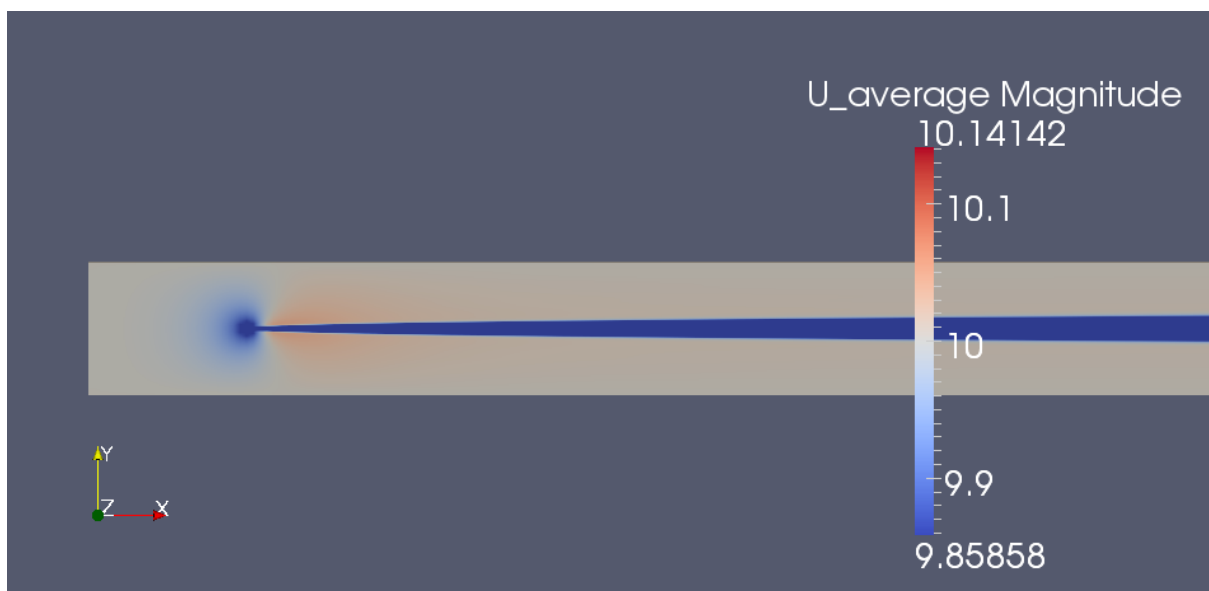


Figure 10-8 - Cropped average velocity magnitude contours for infinitesimally thin flat plate

Figure 10-10 provides a turbulence intensity line plot in the streamwise direction from the inlet to the tip of the leading edge which appears to back up the theory that the fluctuations are strongly attenuated by the large stagnation region. This problem could perhaps be circumnavigated by having a coincident leading edge and inlet boundary, hence modelling only one side of the plate but this would most likely involve developing a pseudo boundary layer profile on the inlet face and scaling the fluctuations accordingly. Other alternatives include using higher order momentum discretisation schemes and increasing the turbulence intensity at the inlet. However with the former the danger, particularly when reverting to unbounded schemes, is inducing oscillations such as checkerboard oscillations and the latter may result in a deviation from the applicability of the linear assumption.

This suppression of the inlet turbulence intensity constituted the main reasons for displacing the leading edge further downstream and increasing the height of the domain. Nevertheless, even with these compromises instigated the results were the same.

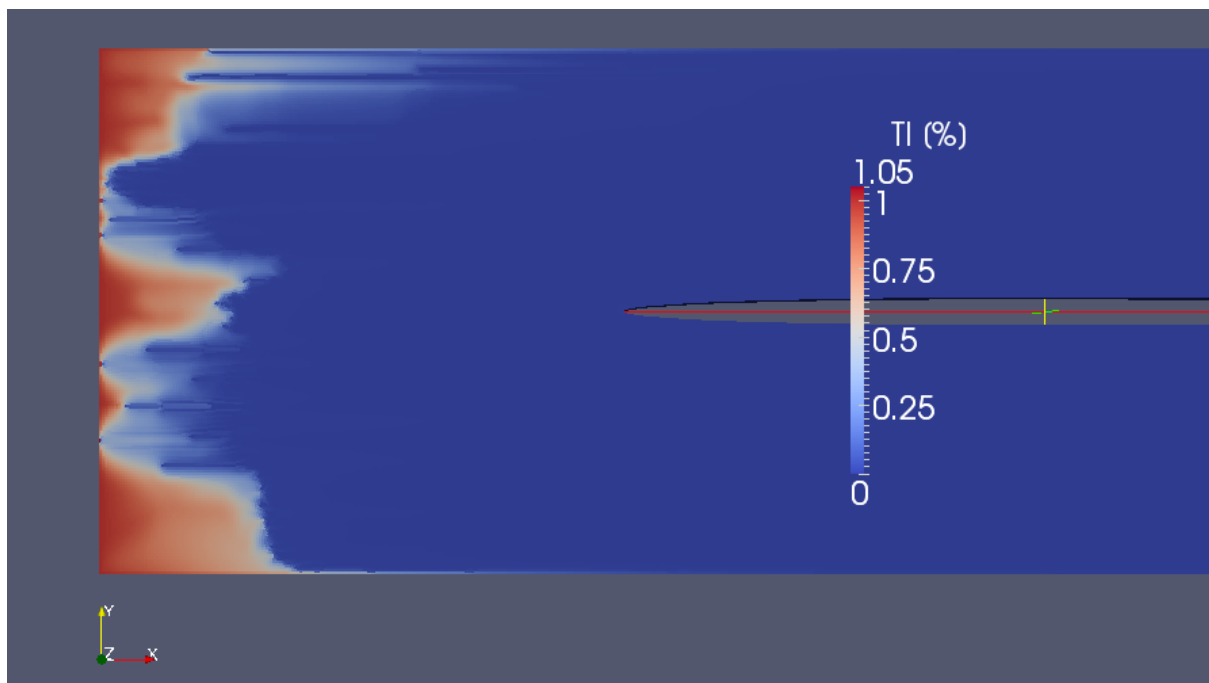


Figure 10-9 - NACA 0002 turbulence intensity contours

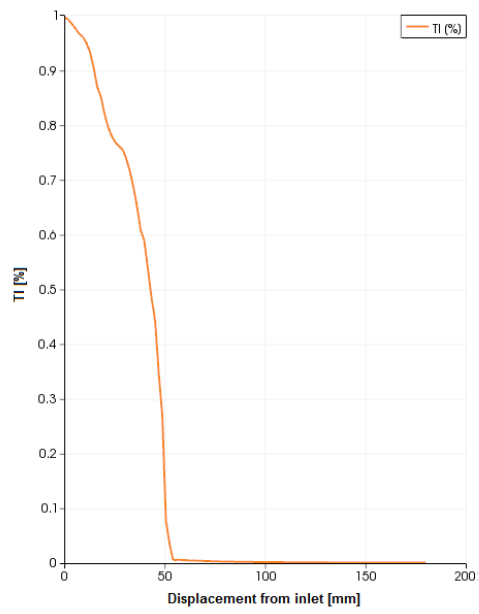


Figure 10-10 - Turbulence intensity line plot from inlet to leading edge (NACA 0002)

11 Appendix B – LabVIEW Codes (Experimental)

This appendix provides some of the graphical LabVIEW codes for completeness, and occasional commentary, all of which have been discussed in the main body of the thesis.

Firstly the vernacular of National Instruments/LabVIEW is discussed, further to what has already been covered in section 3.13. LabVIEW is a dataflow programming language which compiles graphical code, developed in its native front and back panel development interfaces, into G code. The G code executes natively within the LabVIEW environment for which it has been compiled and it will also run natively in any equivalent or subsequent release version but backwards compatibility, however, is not supported. Furthermore any G code can be compiled into a stand-alone executable through LabVIEW, however these executables require the relevant run time engine to be executed. More common languages, such as C, also require the equivalent of run time engines, but these are compliant with third party standards (such as ANSI) and therefore tend to thrive on universal embedded support from operating systems.

In LabVIEW there are VI's (virtual instruments) and sub-VI's, which can be considered as being the analogue of programs and sub-routines. Both are capable of being saved in storage and when opened in a LabVIEW environment are compiled into G code. Assuming that the code has been sufficiently well written, such that there are no compile errors, then it can be run/executed just like any 'normal' compiled or interpreted code, such as C++ or Java.

11.1 Record Wire Velocities and King's Law with Temperature Correction

A convenient example illustrating the execution of VI's and the calling of sub-VI's is demonstrated in conjunction with Figure 11-1 and Figure 11-2. Figure 11-1 represents the graphical code used to record the hot-wire voltages as velocities through calling the King's law (with temperature

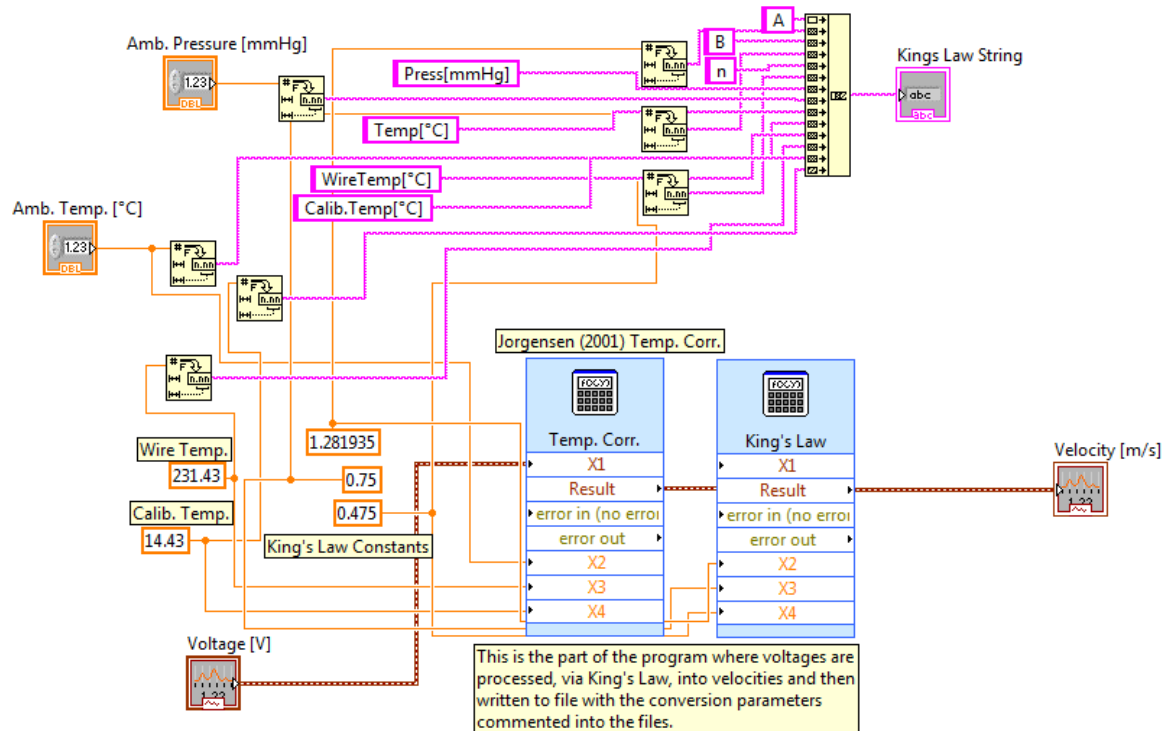


Figure 11-2 - LabVIEW graphical code for Kings law (with Jørgensen (2001) temperature correction) sub-vi

11.2 U and Delta Seek

The code in Figure 11-3 represents the algorithms used in LabVIEW to determine the boundary layer thickness and freestream velocities. It could be argued that freestream velocity should equate to the point which should be taken from the traverse is the one further away from the wall, i.e. point 100, but such an approach would not take account of the scatter associated with such recordings. Hence, an algorithm was implemented to effectively average across any scatter, such to minimise the uncertainty in determining the freestream velocity and therefore to hopefully minimise the error experienced thereafter in the integral parameters.

There are three inputs; number of measuring locations (100) and both the u and y arrays of measured velocities. The algorithm works by averaging the last 5 points of the traverse, computing 98% of that value and then summing all points greater than this temporary freestream velocity and computing the average of those as the freestream velocity. This algorithm was tested by

numerically superimposing random fluctuations, quantitatively similar to those measured on the wind tunnel, on a Pohlhausen zero pressure gradient velocity profile and then computing the resulting shape factor. This algorithm, in comparison with other alternatives considered, was found to be very consistent and accurate. Thereafter the boundary layer thickness was trapped as being the linear interpolation of the point where the local mean velocity first intersects with 99% of the designated freestream velocity. These two values, U and δ , are then displayed on the front panel or passed as outputs to be utilised elsewhere if executed as a sub-VI.

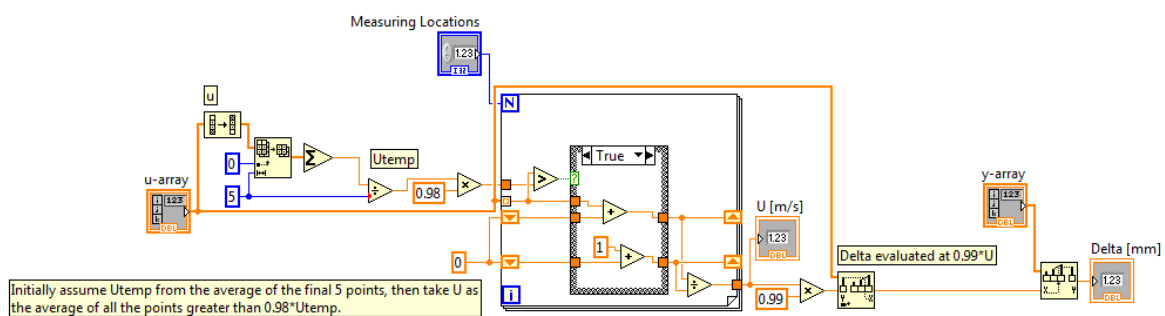


Figure 11-3 - LabVIEW sub-vi graphical code for seeking freestream velocity and boundary layer thickness from y and u arrays

11.3 Intermittency

Next the evaluation of intermittency is discussed in relation to Figure 11-4 and Figure 11-5. Figure 11-4 represents the graphical code used to calculate the intermittency (γ_1) of the raw waveform with respect to the U , δ and sampling frequency input parameters. The manner in which this code discriminates, and the relevant criteria thereof, has already been discussed in section 3.14. The γ_1 (g_1 sub-VI) is actually called twice, these being before and after the Wills' correction method is implemented, resulting in γ_2 (γ_2) as can be observed from Figure 11-5. In reality the difference between γ_1 and γ_2 is negligible, except in the near wall region where Wills' correction is exerts significant influence, but even here there the differences are not particularly substantial and

the trustworthiness of hot-wire measurements in the near wall region tend to be somewhat suspect in any case.

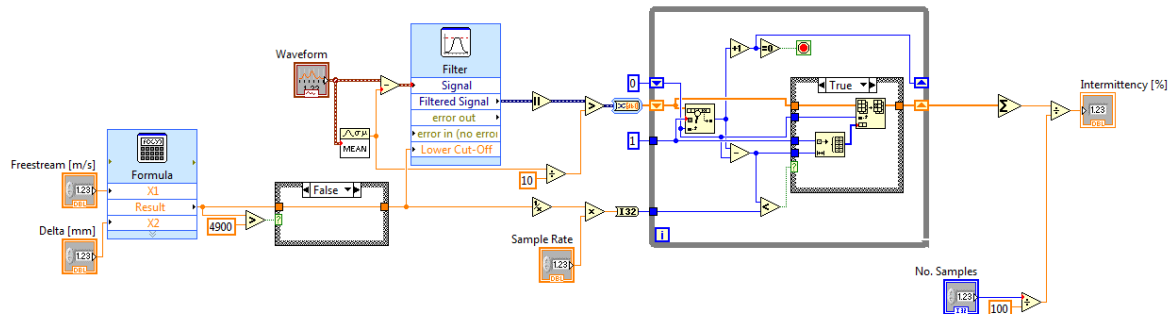


Figure 11-4 - LabVIEW graphical code for gamma1 sub-vi - intermittency processing

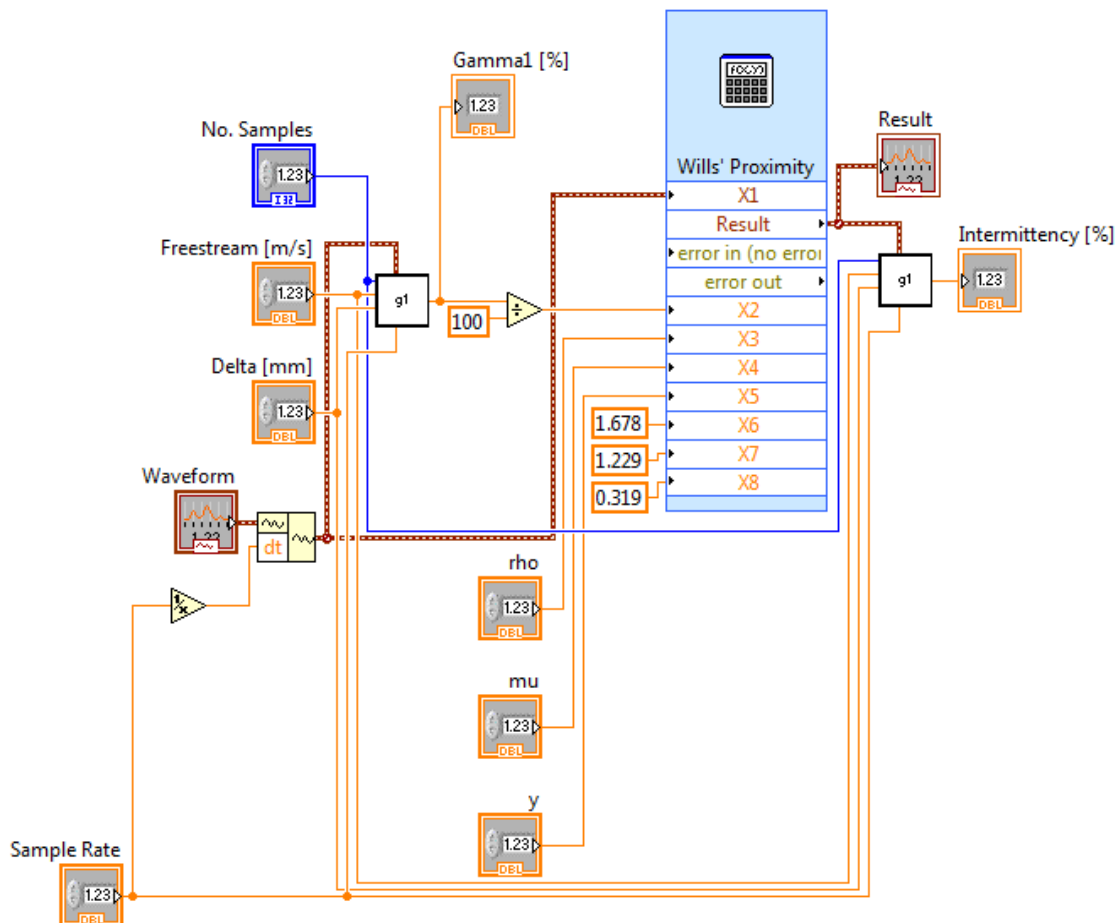


Figure 11-5 - LabVIEW graphical code for gamma2 sub-vi - intermittency processing plus Wills correction Wills (1962)

11.4 Integral Parameters

Figure 11-6 provides the graphical code for the manner in which the integral parameters are calculated (through strip integration) and then demonstrates how they are converted from doubles into strings and thereafter concatenated into an output string which is separately called and written to the output summary files. The aforementioned output summary files are written in the manner of Figure 11-7 in conjunction with all of the other arrays and the King's law string which details the calibrations coefficients etc.. With the benefit of greater experience some of the codes, with hindsight, are capable of being improved upon. For example in Figure 11-7 the for loop is superfluous and results in additional code so as to not write the comment string for every measurement location (i.e. 100 times). Simply put it would have been better coding practice to write all of the arrays directly to file, rather than sequentially writing every index of each array to file consecutively.

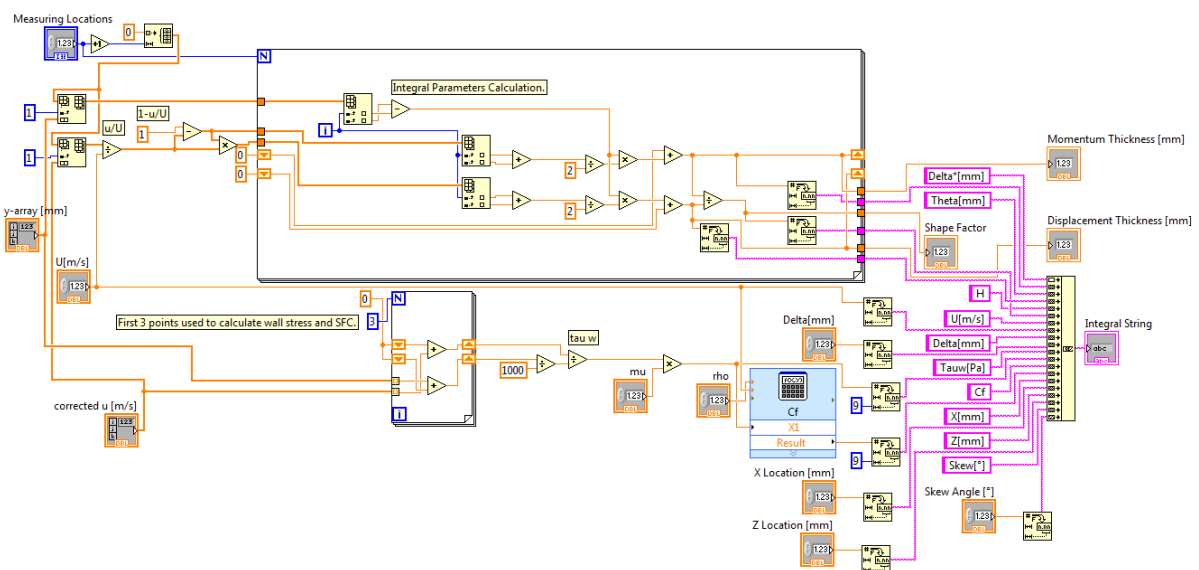


Figure 11-6 - LabVIEW integral parameters graphical code for sub-vi

quantifying whether or not the minimum voltage in the hot-wire signal was less than or equal to 1 Volt. The number of cumulative pulses were also tracked in the main while loop. This value would typically reach 850 for the same target voltage at two different locations on the plate. 850 pulses similarly corresponded to the total cumulative pulses away from the plate during the experiments themselves, hence one would expect an equivalent number of pulses when traversing in the opposite direction when seeking the default home position close to the plate. Any deviations from 850 cumulative pulses were attributed to ambient drift causing the target voltage to be attained earlier and local surface irregularities in either the probe location and or where the elliptical traverse body is sucked onto the plate. Nevertheless deviations from 850 were limited to ± 1 pulse and, in any case, the zero flow correlation algorithm would provide a reliable indication of the proximity.

Attempts were made to maintain proximity at around 0.1 mm and if the probe reached its target voltage at 0.16 mm (for example) then the probe would be manually nudged by another pulse closer to the plate. Consistency across the various skew angles, with the initial proximity at 000, was one of the main considerations and was thought to be more important than attempting to obtain the absolute minimum proximity possible, which carried with it the risks of inflicting probe damage. The procedures were designed to operate in quiescent conditions (zero flow) but were the probe to be tripped by residual revolutions from the blower fan or a gust of wind, for example, then this would be clearly observable through either visual inspection, a large disparity in the number of cumulative pulses, strongly unsteady voltage time history or erroneous estimates for proximity. Overall this semi-automated approach was found to be highly reliable and successful.

